

**Numerical modelling of the aluminium extrusion process and  
comparison with results obtained from industrially extruded  
complex sections**

**Kjell Einar Nilsen**

**A thesis submitted in partial fulfillment of the requirements of  
Bournemouth University for the degree of Doctor of Philosophy**

**February 2014  
Bournemouth University**

## **Copyright Statement**

This copy of the thesis has been supplied on condition that anyone who consults it is understood to recognise that its copyright rests with its author and due acknowledgment must always be made of the use of any material contained in, or derived from, this thesis.

## **Abstract**

**Kjell Einar Nilsen**

### **Numerical modelling of the aluminium extrusion process and comparison with results obtained from industrially extruded complex sections**

This thesis reports the analysis of extruded products by Forge2009® and EBSD produced by the investigator in the BOAL plant. The 3D FEM module was used to study the required load, the temperature evolution, surface formation of the extrudate and material flow during the process. The effect of varying process conditions on the selected geometries were investigated and verified by means of experiment. Considering the difficulty in performing the experiments (high temperature and high strain rates) the simulation results can be considered to be acceptable.

The simulations were performed with the implicit finite element code Forge2009® with user input written in Visual Fortran®. Alloy EN AW-6082 was selected on the basis that is a commonly used extrusion material in industry. A range of simulations were designed which would produce differing structures to those experienced within the industry.

The effect of variation of the bridge design for hollow dies and the effect of variation of the sink in for solid dies was investigated. 3D simulations were performed to investigate the effect of these variations in the design features on extrusion process parameters. The process parameters which are likely to be affected are load, deflection, velocity and temperature. The results indicated that the design of the die affected the process parameters.

The microstructure evolution during the extrusion process was investigated for the selected complex geometries. The following microstructure features were included in the investigations: Recrystallised grain size, subgrain size, misorientation, dislocation density and volume fraction recrystallised. Simulations were performed using physically-based mathematical microstructure models integrated into FEM through its Fortran® subroutine interface. Experiments were performed to investigate the effects of varying process conditions on the

microstructure. For hollow section, the emphasis was placed on the study of the complicated metal flow and the seam welding quality. EBSD analyses were performed to investigate the substructure. Surface cracking was modelled and compared with experiments. The agreement between the predicted microstructures using associated models and experimental measurements were acceptable. Predicted cracking show good correlation with experimental results.



## Contents

<b>Copyright Statement.....</b>	<b>1</b>
<b>Abstract.....</b>	<b>2</b>
<b>Contents.....</b>	<b>4</b>
<b>List of symbols.....</b>	<b>8</b>
<b>List of figures.....</b>	<b>14</b>
<b>List of tables.....</b>	<b>20</b>
<b>Acknowledgement.....</b>	<b>21</b>
<b>Author’s declaration.....</b>	<b>22</b>
<b>1. Introduction.....</b>	<b>23</b>
1.1 Aluminium and the extrusion process.....	23
1.2 Modelling the extrusion process.....	29
1.3 Objective of the research.....	30
<b>2. Literature review.....</b>	<b>32</b>
2.1 Thermo mechanical modelling.....	32
2.1.1 Physical parameters influencing the modelling of the extrusion process.....	32
2.1.2 Extrusion pressure .....	35
2.1.3 Heat transfer and temperature.....	38
2.1.4 Yield criterion.....	39
2.1.5 Viscoplastic model.....	40
2.1.6 Material flow investigations .....	41
2.1.7 Surface cracking criteria.....	47
2.2 Extrusion die design.....	50
2.2.1 Optimisation of solid die design.....	54
2.2.2 Optimisation of hollow die design .....	59
2.2.3 Extrusion process optimisation .....	64
2.3 Microstructure modelling.....	67
2.3.1 Development of structure during extrusion.....	68
2.3.2 Empirical models for structure prediction.....	69
2.3.3 Physically-based internal variable methods.....	72

2.3.4 The internal state variable formalism.....	72
2.3.5 Dislocation substructure evolution.....	75
2.3.6 Dislocation density evolution modelling.....	76
2.3.7 Subgrain size modelling.....	77
2.3.8 Misorientation change modelling.....	78
2.3.9 Recrystallised grain size.....	79
2.3.10 Volume fraction recrystallized.....	81
2.3.11 Time to 50% recrystallization.....	82
2.3.12 Grain boundary mobility.....	82
2.3.13 Grain boundary surface area per unit volume.....	84
2.3.14 Nucleation sites per unit volume.....	86
2.3.15 Stored energy.....	88
2.4 FEM Modelling.....	89
2.4.1 The equilibrium equation in FE simulations.....	89
2.4.2 Finite element kinematical description.....	90
2.4.3 Finite element discretisation and element type.....	91
2.4.4 Mesh generation.....	92
2.4.5 Mesh refinement.....	93
2.4.6 Re-Meshing.....	94
2.4.7 Contact Conditions.....	94
2.4.8 Finite element discretisation and increment approach.....	95
2.4.9 Microstructure modelling of aluminium extrusion.....	96
2.4.10 Finite Element Model.....	97
2.4.11 Thermo-mechanical process modelling using the Finite Element Method.....	99
<b>3. Experiments.....</b>	<b>101</b>
3.1 The extrusion press.....	101
3.2 Material.....	103
3.3 Extruded sections.....	104
3.4 Die designs.....	106
3.5 Extrusion experiments.....	107

3.6 Examination of extrudates.....	108
2.6.1 Optical microscopy.....	108
3.6.2 Electron microscopy.....	109
3.6.3 EBSD analysis method.....	110
<b>4. FEM Modelling.....</b>	<b>112</b>
4.1 Techniques used in the FEM simulation.....	112
4.2 Finite element models.....	115
4.3 Constitutive equation used.....	117
4.4 Data file and user sub-routine.....	118
4.5 The user sub-routine and its integration with Forge2009® solver.....	119
4.6 Extrusion simulations.....	121
4.6.1 Thermo mechanical simulations.....	121
4.6.2 Structural simulations.....	122
4.6.3 Microstructure prediction.....	123
4.7 Hollow die simulation.....	123
4.8 Solid die simulation.....	134
4.9 Conclusions.....	139
<b>5. Results and analysis mechanical.....</b>	<b>140</b>
5.1. Introduction.....	140
5.2 Simulation results.....	140
5.2.1 Temperature distribution.....	142
5.2.2 Strain.....	147
5.2.3 Strain rate.....	150
5.2.4 Load analysis.....	152
5.2.5 Material flow simulations.....	158
5.2.6 Surface cracking experiments.....	160
5.2.7 Surface cracking simulations.....	165
5.3 Conclusions.....	170
<b>6. Results and analysis structural.....</b>	<b>171</b>
6.1 Deformation during extrusion.....	171
6.2 Subgrain size and misorientation.....	172

6.2.1 Optical micrograph investigation.....	172
6.2.1.2 Effect of extrusion temperature.....	173
6.2.1.3 Effect of ram speed.....	176
6.2.1.4 Effect of section geometry.....	178
6.2.2 EBSD investigations.....	182
6.2.2.1 EBSD results.....	187
6.2.2.2 Effect of extrusion temperature .....	188
6.2.2.3 Effect of ram speed .....	198
6.2.2.4 Effect of section geometry.....	204
6.3 Simulation results.....	208
6.4 Dislocation density.....	215
6.5 Volume fraction recrystallised.....	218
6.4 Precipitation.....	223
6.5 Conclusions.....	230
<b>7. Conclusions and further research.....</b>	<b>232</b>
7.1 Conclusions.....	232
7.2 Further research.....	234
<b>8. Appendices.....</b>	<b>235</b>
8.1 Appendix 1.....	235
8.2 Appendix 2.....	237
8.3 Appendix 3.....	241
<b>9. References.....</b>	<b>252</b>

## List of symbols

$A$	material constant
$A_E$	cross sectional area of the extrudate
$A_C$	cross sectional area of the container bore
$\alpha$	constant
$B$	material constant
$B_n$	linear operator
$b$	magnitude of Burgers vector
$C$	constant
$C_1$	constant for the effect of the wall thickness
$C_2$	constant for the effect of the distance to the container wall
$C_3$	constant for the sink in dimensions
$C_{cr}$	critical value for the material to be damaged
$C_d$	constant
$C_t$	constant
$c$	constant
$D_C$	diameter of the container bore
$D_E$	equivalent diameter of the extrudate
$D_O$	pre-growth grain diameter
$d$	constant
$d_{rex}$	recrystallised grain size
$d_0$	initial grain diameter
$E$	energy per unit length of dislocation line
$E_{el}$	elastic energy of distributed edge dislocation
$E_{sb}$	energy per unit length of low angle tilt boundary

$F_j$	point force
$G_O$	constant
$h$	height of the welding chamber
$J_1$	first invariant of the stress tensor
$J_2$	second invariant of the stress tensor
$J_3$	third invariant of the stress tensor
$k$	constant
$L_c$	length of dislocations annihilated
$L_0$	mean linear intercept at zero strain
$l$	welding path
$M$	Taylor factor
$M_{GB}$	grain boundary mobility
$M_m$	shape function for the nodal pressure
$M_o$	constant a linear factor for the grain boundary mobility
$m$	strain rate sensitivity index
$m_o$	constant
$m_1$	constant
$N_L$	number of boundaries per unit length
$N_n$	shape function
$N_V$	nucleation sites per unit volume
$n$	inverse of the temperature compensated strain rate sensitivity
$n_1$	tensor for the effect due to wall thickness
$n_2$	first tensor for the effect due to distance to container wall
$n_3$	second tensor for the effect due to distance to container wall
$n_4$	tensor for the effect due to sink in dimensions
$P$	pressure

$\Delta P$	average pressure
$P_t$	pressure effect due to wall thickness
$P_d$	pressure effect due to distance to container wall
$P_s$	pressure effect due to sink in dimensions
$P_D$	stored energy per unit volume
$P_i$	material properties invariant
$P_j$	body force
$p$	constant
$P$	pressure field
$P_m$	nodal pressure
$\dot{Q}_d$	heat generation rate due to deformation per unit volume
$Q_{def}$	activation energy for deformation
$Q_{GB}$	activation energy for grain boundary migration
$q$	constant
$R$	universal gas constant
$R_e$	extrusion ratio
$R_{pe}$	radius caused by excess dislocation of a given Burgers vector
$R_{\rho\delta}$	radius caused by misorientation across subgrain boundaries
$r$	constant
$r_0$	radius of dislocation core
$r_1$	outer cut-off radius
$S$	surface area of the calculated domain
$S$	general deformation matrix
$S_i$	state variables
$S_j$	value of a microstructure state variable

$S_{jo}$	value of the microstructure state variable microstructure state variable S before a change of deformation conditions
$S_{js}$	value of the microstructure state variable microstructure state variable S after a change of deformation conditions
$S_V$	grain boundary area per unit volume
$S_{Vo}$	grain boundary area per unit volume at zero strain
$T$	temperature
$T_j$	surface force
$T_m$	lowest melting point
$t_{50}$	time to 50% recrystallisation
$t$	holding time
$t_w$	contact time of the two metal streams
$U$	total stored energy per unit volume
$U_i$	energy per unit volume for internal dislocations
$U_{sb}$	energy per unit volume for subgrain boundaries
$u_j$	displacement
$V$	volume
$V_n$	nodal velocity field
$V_R$	ram speed
$v$	velocity field
$\bar{v}_m$	mean velocity of mobile dislocations
$v_{avg}$	average flow velocity of the metal in the welding chamber
$\widehat{W}$	virtual work resulting from the strain due to the virtual displacement
$w$	distance between the sites of cross-slip or climb events
$X_n$	coordinate vector



$X_V$	volume fraction recrystallised
$x$	displacement field
$Z$	temperature compensated strain rate parameter
$Z^*$	material constant
$\alpha$	material constant
$\alpha'$	material constant
$\beta$	constant
$\Delta H$	activation energy for hot deformation
$\delta$	subgrain size
$\delta_{ss}$	subgrain size at steady state
$\varepsilon$	mean equivalent strain or effective strain
$\bar{\varepsilon}$	mean equivalent strain or effective strain
$\dot{\varepsilon}$	strain rate tensor
$\dot{\bar{\varepsilon}}$	mean equivalent strain rate or effective strain rate
$\hat{\varepsilon}_{ij}$	virtual strain
$\varepsilon_{js}$	characteristic strain that controls the strain over which steady-state is reached
$\varepsilon_\theta$	characteristic strain for misorientation growth
$\varepsilon_\delta$	characteristic strain for subgrain growth
$\theta$	misorientation across subgrain boundaries
$\theta_c$	critical angle for high angle grain boundary
$\theta_{ss}$	misorientation across subgrain boundaries at steady state
$\Lambda_r$	mean distance travelled by the dislocation before it is stopped
$\lambda$	heat generation efficiency
$\mu$	friction coefficient
$\nu$	Poisson ratio
$\xi$	local coordinate vector
$\rho$	total dislocation density

$\rho_b$	boundary dislocation density
$\rho_e$	equivalent distributed dislocation density for a simple low angle tilt boundary
$\rho_g$	'geometrically necessary' dislocation density
$\rho_i$	internal dislocation density
$\rho_r$	`random dislocation
$\sigma$	flow stress
$\bar{\sigma}$	equivalent stress or effective stress
$\sigma_{N-H}$	Norton-Hoff flow stress
$\sigma_{Z-H}$	Zener-Hollomon flow stress
$\sigma_f$	friction stress
$\sigma_{ij}$	Cauchy stress tensor
$\sigma_m$	mean stress or hydrostatic stress
$\sigma_n$	normal stress
$\sigma_1$	the first principal stress
$\sigma_2$	the second principal stress
$\sigma_3$	the third principal stress
$\tau$	friction stress
$\omega$	semi-angle of the deformation zone in direct extrusio

## List of figures

Figure 1.1 Schematic presentation of direct (left) and indirect extrusion: 1 Ram, 2 Container, 3 Aluminum, 4 Die, 5 End block, 6 Product (Vaneker 2001).....	23
Figure 1.2 (a) Limit diagram (schematic) by), Sheppard (1982a).....	24
Figure 1.3 , the mode of recrystallisation in the extrudates, (a) Extruded at 350°C, 0.5h soak, longitudinal, (b) Extruded at 350°C, 0.5h soak, transverse, (c) Extruded at 450°C,0.5h soak, longitudinal.....	27
Figure 2.1 A typical tooling arrangement for aluminium hollow sections (Sheppard 1999a, p.359).....	42
Figure 2.2 A cross section of an extruded billet revealing the metal flow.....	44
Figure 2.3 Showing the symmetrical planes .....	44
Figure 2.4 The metal's flow and weld of neighbouring metal streams during tube extrusion.....	45
Figure 2.5 Dead metal zones in tube extrusion (a) and iso-surfaces (b) (Sheppard, Niu and Velay 2012c).....	46
Figure 2.6 Weld quality index, (Sheppard, Niu and Velay 2012c).....	47
Figure 2.7 Bearing, sink in configuration of a solid die (Li et al. 2003).....	55
Figure 2.8 The influence of bearing length (a) and bearing angle (b) on the average pressure, Lof (2000).....	56
Figure 2.9 The relation between the distance to the centre and the extrusion speed, Lof (2000).....	57
Figure 2.10 The effect increased extrusion speed (a) and increased wall thickness (b) on the average pressure, Lof (2000).....	58
Figure 2.11 Representation of the bridge geometry in a die core, Mooi (1996 pp4) .....	60
Figure 2.12 Arrows indicate deflection points when a load is applied (Mooi 1996 pp4)...	60
Figure 2.13 Defection of the core as a function of the distance to the edge, (Mooi (1996).61	
Figure 2.14 Two bridge shapes (a) torpedo bridge shape and (b) traditional bridge shape.62	
Figure 2.15 the effect of the welding chamber (a) and the diameter of the torpedo shaped bridge (b) on the average pressure (MN/m <sup>2</sup> ).....	63
Figure 2.16 Schematic representation of possible material flow for the traditional bridge (a) and the torpedo shaped bridge (b) .....	63

Figure 2.17 Limit diagram with optimum subgrain size for fracture toughness as a fracture toughness line Sheppard (1999a).....	65
Figure 2.18 Limit diagram according to (Parson et al. 1992).....	65
Figure 2.19 Schematic representation of the microstructure; cell diameter $\delta$ , cell wall thickness, $h$ , cell wall dislocation density $\rho_b$ and dislocation density within the cells $\rho_i$ , (Nes 1997) .....	75
Figure 2.20 Sub-boundary misorientation vs. strain (Nes and Marthinsen 2002) .....	79
Figure 2.21 Tetrakaidecahedron, (Zhu et al. 2007).....	84
Figure 2.22 (a) Midpoint penetration and (b) impenetrability algorithm.....	95
Figure 3.1 The press used in the experiments.....	101
Figure 3.2 Schematic overview of the press with the measurement instruments.....	102
Figure 3.3 Rectangular profile (dimension in mm) .....	104
Figure 3.4 U-shaped profile (dimension in mm) .....	105
Figure 3.5 Tube section (dimension in mm) .....	105
Figure 3.6 The dies used in the experiments .....	106
Figure 4.1 Symmetry and auto-trim used in 2D simulation .....	114
Figure 4.2 Symmetry and auto-trim used in a 3D simulation.....	115
Figure 4.3 FEM configurations prior to simulation for (a) rectangle, (b) U-shape and (c) tube, where part A is the ram, part B, the container, part C the billet and part D the die (orifice) and part E is the die bridge.....	116
Figure 4.4 Schematic for multi mesh boxes and auto-trim settings.....	117
Figure 4.5 The tube section used for simulation of the variation in bridge design.....	124
Figure 4.6 A cross section for a die core of a tube with a traditional shaped bridge (a) torpedo shaped bridge (b).....	124
Figure 4.7 A three dimensional view of the die core of a traditional die bridge (a) and a torpedo shape die bridge (b).....	125
Figure 4.8 The extrusion set up for the simulated die for tube extrusion.....	126
Figure 4.9 Three dimensional representations of the components such as container, billet, die core and die plate including the mesh used in the simulations.....	127
Figure 4.10 The simulated deflection (mm) in the extrusion direction for the die core with the traditional bridge design (b) and a torpedo shape bridge design (a).....	128

Figure 4.11 The temperature (°C) distribution along the core with the traditional bridge design .....	129
Figure 4.12 The load distribution (MN) for the simulation of the hollow tube with the die containing a traditional bridge shape. ....	131
Figure 4.13 A close up representation for the extruded part of the hollow extrusion.....	133
Figure 4.14 Solid section for simulation of the variation in sink in depth (mm).....	134
Figure 4.15 Tooling set up for a for a solid die extrusion simulation and a three dimensional representation for the extrusion of the solid section .....	135
Figure 4.16 Velocity in extrusion direction (mm/sec) for the simulation of the solid die with the 10mm (a) and the 5.5mm (b) deep sink in.....	136
Figure 4.17 Temperature distribution (°C) in the die with a 10mm (a) and a 5.5mm (b) deep sink in.....	137
Figure 4.18 The load distribution (ton) for the simulation of the solid section with the 5.5mm and the 10mm deep sink in design.....	138
Figure 5.1 Position at which the predicted temperature evolution is represented.....	142
Figure 5.2 Temperature evolution over an extrusion cycle.....	143
Figure 5.3 Temperature distributions of three different extruded shapes (Temperature T in °C).....	144
Figure 5.4 Temperature distributions in the cross section of the extruded samples (a), (b), (c), (d), (e), (f) and (g) (Temperature T in °C).....	146
Figure 5.5 Strain distributions for the three extruded shapes at 500°C and 12mm/s.....	147
Figure 5.6 Equivalent strain distributions in the cross section of the extruded samples (a), (b), (c), (d), (e), (f) and (g).....	149
Figure 5.7 Strain rate distributions in the cross section of the extruding samples (a), (b), (c), (d), (e), (f) and (g).....	151
Figure 5.8 The various stages in the extrusion of a solid section.....	152
Figure 5.9 Pressure evolution during an extrusion cycle.....	153
Figure 5.10 The various stages in the extrusion of a hollow section.....	154
Figure 5.11 Load versus ram travel for the rectangular shape at low temperature with varying speeds.....	155
Figure 5.12 Load versus ram travel for the rectangular shape at low temperature with varying speeds.....	155

Figure 5.13 Load versus ram travel for the rectangular shape at high temperature with varying speed.....	156
Figure 5.14 Load versus ram travel for the U-shape at varying temperatures with constant speed.....	157
Figure 5.15 Load versus ram travel for the hollow shape at varying temperatures with constant speed.....	157
Figure 5.16 Numerical initial grids for the three extruded section.....	158
Figure 5.17 The numerical grid deformation for the extruded sections.....	159
Figure 5.18 Surface quality and cracks at the beginning of the extrusion run.....	161
Figure 5.19 Surface quality and cracks at the end of the extrusion run.....	163
Figure 5.20 Surface quality at the beginning and the end of an extrusion run for all three geometries.....	164
Figure 5.21 The simulation results are presented together with the simulated value of the cracking parameter (550°C, 22mm/sec).....	167
Figure 5.22 Predicted values of Cockcroft and Latham criterion C-L2 (Peng and Sheppard 2004).....	168
Figure 5.23 The visible cracking on the rectangular section corners, together with the temperature simulation and a simulated crack. ....	169
Figure 6.1 Micrograph of rectangular sections, at 480 °C, 500°C and 520 °C at 12mm/s..	173
Figure 6.2 Detailed micrographs of rectangular sections, at 480 °C, 500°C and 520 °C at 12mm/s.....	175
Figure 6.3 Micrograph of a rectangular section, at 500°C at 6 mm/s, 12 mm/s and 22 mm/s.....	176
Figure 6.4 Detailed micrographs of rectangular sections at 500°C and 6 mm/s, 12 mm/s and 22 mm/s.....	177
Figure 6.5 Micrograph of the U-shaped and tube section, at 500°C and 12 mm//s.....	178
Figure 6.6 Detailed micrograph of the U-shaped section.....	179
Figure 6.7 Detailed micrograph of the tube section.....	180
Figure 6.8 EBSD map of sample 5E (500°C, 12mm/sec) with scan line in the larger blue (sub) grain (Courtesy of Hydro Aluminium Mr. John Rasmus Leinum).....	183
Figure 6.9 Misorientation along the scanned line in (Figure 6.3) of sample 5E (500°C, 12mm/sec) (Courtesy of Hydro Aluminium Mr. John Rasmus Leinum).....	184

Figure 6.10 Misorientation angle as a function of the number of fraction for sample 2E (500°C, 6mm/s) (Courtesy of Hydro Aluminium Mr. John Rasmus Leinum).....	185
Figure 6.11 Subgrain size as a function of the percentage for sample 2Eb and c (500°C, 6mm/s) (Courtesy of Hydro Aluminium Mr. John Rasmus Leinum).....	186
Figure 6.12 The location of the sample position for the EBSD investigations.....	188
Figure 6.13 EBSD graphs of the rectangular sections in the center with temperature increase. (Courtesy of Hydro Aluminium Mr. John Rasmus Leinum).....	190
Figure 6.14 Enlarged view of EBSD graph of rectangular section 480°C and 12mm/sec in the center of the sample. (Courtesy of Hydro Aluminium Mr. John Rasmus Leinum).....	191
Figure 6.15 Enlarged view of EBSD graph of the rectangular section 520°C and 12mm/sec in the center of the sample. (Courtesy of Hydro Aluminium Mr. John Rasmus Leinum) .	192
Figure 6.16 Enlarged view of EBSD graph of the rectangular section 480°C and 12mm/sec in the center of the sample. (Courtesy of Hydro Aluminium Mr. John Rasmus Leinum) .	193
Figure 6.17 Enlarged view of EBSD graph of the rectangular section 520°C and 12mm/sec in the center of the sample. (Courtesy of Hydro Aluminium Mr. John Rasmus Leinum)..	194
Figure 6.18 EBSD graphs of the rectangular sections in the edge with temperature increase. (Courtesy of Hydro Aluminium Mr. John Rasmus Leinum).....	195
Figure 6.19 (sub) grain size ( $\mu m$ ) distribution with increasing extrusion temperature (Courtesy of Hydro Aluminium Mr. John Rasmus Leinum).....	197
Figure 6.20 EBSD graphs of the rectangular sections in the center with ram speed increase. (Courtesy of Hydro Aluminium Mr. John Rasmus Leinum).....	198
Figure 6.21 EBSD graphs of the rectangular sections in the edge with ram speed increase. (Courtesy of Hydro Aluminium Mr. John Rasmus Leinum).....	199
Figure 6.22 Enlarged view of EBSD graph of the rectangular section 500°C and 22mm/sec in the center of the sample. (Courtesy of Hydro Aluminium Mr. John Rasmus Leinum)	200
Figure 6.23 Enlarged view of EBSD graph of the rectangular section 500°C and 22mm/sec in the edge of the sample. (Courtesy of Hydro Aluminium Mr. John Rasmus Leinum)	201
Figure 6.24 (sub) grain size ( $\mu m$ ) distribution with increasing extrusion speed (Courtesy of Hydro Aluminium Mr. John Rasmus Leinum).....	203
Figure 6.25 EBSD graphs of the U-shaped sections. (Courtesy of Hydro Aluminium Mr. John Rasmus Leinum).....	204

Figure 6.26 EBSD graphs of the tube sections. (Courtesy of Hydro Aluminium Mr. John Rasmus Leinum).....	205
Figure 6.27 show the (sub) grain size ( $\mu m$ ) distribution for the U-shaped section and the tube. (Courtesy of Hydro Aluminium Mr. John Rasmus Leinum).....	207
Figure 6.28 Graphical representations for all the EBSD results for grain size and subgrain size ( $\mu m$ ) from the center of the sample for the erimental geometries.....	209
Figure 6.29 Graphical representations for all the EBSD results for misorientation ( $^{\circ}$ ) from the center of the sample for the experimental geometries.....	211
Figure 6.30 simulated subgrain sizes ( $\mu m$ ) for the experimental samples.....	213
Figure 6.31 Dislocation density ( $\times 10^{13}$ ) for the experimental samples.....	217
Figure 6.32 Volume fraction recrystallised (%) simulation results for the experimental samples.).....	220
Figure 6.33 Micrographs at 1000x magnification using Backscatter Scanning Electron Microscope.....	224
Figure 6.34 Micrographs at 2000x magnification using Backscatter Scanning Electron Microscope.....	226
Figure 6.35 EDX analysis of sample 2E, 1) AlSiMnFe, 2) carbon, 3) Oxidised Mg <sub>2</sub> Si....	228
Figure 6.36 EDX analysis of phases in sample 5E: 5) Oxidized Mg <sub>2</sub> Si, 6) Oxidized Mg <sub>2</sub> Si with Mg-residue.....	229



## List of tables

Table 2.1 Constants for equation 2.21.....	70
Table 2.2 Mobility of high and low angle grain boundaries, Huang and Humphreys (1999).....	83
Table 2.3 Mobility of high and low angle grain boundaries Driver et al.(2005).....	84
Table 2.4 Basic element shapes .....	92
Table 3.1 The alloy composition used in the extrusion trials .....	103
Table 3.2 The experimental samples used in the research .....	108
Table 5.1 Extrusion parameters during the experiments .....	141
Table 5.2 Predicted peak loads for the rectangular shape .....	156
Table 6.1 Volume fraction recrystallised using the grid method.....	181
Table 6.2 EBSD results for subgrain size ( $\mu m$ ) and misorientation ( $^{\circ}$ ) for the rectangular sections with increased extrusion temperature.....	196
Table 6.3 EBSD results for subgrain size ( $\mu m$ ) and misorientation ( $^{\circ}$ ) for the rectangular sections with increased extrusion speed.....	202
Table 6.4 EBSD results for subgrain size ( $\mu m$ ) and misorientation ( $^{\circ}$ ) are presented for the U-shaped section and the tube.....	206
Table 6.5 The EBSD results for subgrain size ( $\mu m$ ) and misorientation ( $^{\circ}$ ) and simulated results for subgrain size.....	212
Table 6.6 EBSD and simulated results for subgrain size ( $\mu m$ ) with increased extrusion temperature.....	214
Table 6.7 EBSD and simulated results for subgrain size ( $\mu m$ ) with increased extrusion speed.....	214
Table 6.8 EBSD and simulated results for subgrain size ( $\mu m$ ) for the U-shaped section and the tube.....	214
Table 6.9 Simulated results for dislocation density ( $\times 10^{13}$ ) for all the geometries in the experiments.....	216
Table 6.10 Volume fraction recrystallized (%) for the experimental and simulated geometries.....	222

## **Acknowledgement**

Doing a part time PhD has been a challenging experience. Having a full time job makes time management very important since distractions are plentiful. It has only been possible to do the PhD thanks to the support of a lot of people. Many of those deserve a sincere thank you but it is impossible to mention them all.

I am very grateful to Professor Terry Sheppard, my first supervisor, for his supervision, guidance and encouragement throughout various stages of this thesis. I really appreciated the numerous conversations where his professional input has kept me on the right path.

Dr. Xavier Velay, my second supervisor, is much appreciated for his continuous enthusiasm and professional input. He provided a lot of practical assistance and emphasised the need for planning and discipline during the work for this thesis.

Professor Terry Sheppard and Dr. Xavier Velay certainly made my stay at Bournemouth a most enjoyable experience.

Dr. Longjang Niu is much appreciated for the help and assistance in performing the simulations.

Bournemouth University and the department of DEC are recognized for the use of the facilities.

I am very grateful to Hydro Aluminium and in particular to Mr. John Rasmus Leinum for performing the EBSD analysis.

Mr. Ronald Boers, CEO of the BOAL Group is much appreciated for his continuous support and the use of the BOAL presses to perform the experiments.

I am very grateful to my family and friends without whose support and encouragement I could not have completed this thesis and in particular to Martin van Rees without whose love, support, encouragement and patience it would have been impossible to do the work.

## **Authors' declaration**

The work contained in this thesis is the result of my own investigations and has not been accepted or currently submitted in candidature for any other award.

# 1 Introduction

## 1.1 Aluminium alloys and the extrusion process

Aluminium is abundantly available. Besides good mechanical properties, aluminium and its alloys have good physical properties, such as low density, high corrosion resistance, good electrical and thermal conductivity. This unique combination of properties and the ability to fabricate a wide range of shapes has resulted in an industry dedicated to producing extruded products.

The extrusion process can be performed by means of two basic methods, direct and indirect extrusion, see Figure 1.1, (Mueller et al. 2002), (Sheppard and Patterson 1982). The differences between direct and indirect extrusion have been extensively studied in the literature (Paterson 1981; Sheppard 1984; Sheppard and Paterson 1982). The major difference is that in indirect extrusion there is no friction between the billet and the container whereas in direct extrusion the outer shell of the billets move relative to the container as extrusion proceeds, resulting in considerable friction. Thus the extrusion load is greater. The main advantage of indirect extrusion is that the material will not be pushed through the container. The disadvantage of indirect extrusion is that the hollow ram is weaker this may limit the size of the profiles which can be extruded. There are, however, various modifications to the ram which can overcome this difficulty.

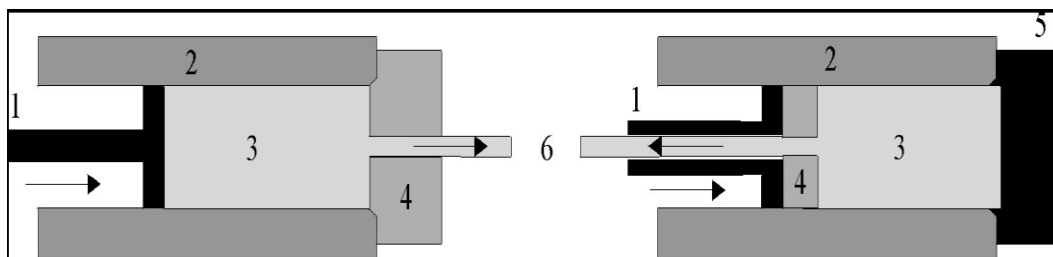


Figure 1.1 Schematic presentation of direct (left) and indirect extrusion: 1 Ram, 2 Container, 3 Aluminum, 4 Die, 5 End block, 6 Product (Vaneker 2001)

The process which needs to be optimized can be expressed using a limit diagram. Hirst and Ursell (1958) were the first researchers who investigated limitation factors of the extrusion process. They proposed a novel type of diagram which was able to represent these limitations in a graphical way such that they had produced a limit diagram. This identified the limitations to the extrusion process; they clearly identified the range of parameters which would be practical to use.

The application of these limit diagrams have since been extended such that almost any structural feature may be illustrated. Figure 1.2 show a limit diagram basically constructed according to the Hirst and Ursell premise (1958) but modified by including the temperature rise occurring during the process. Sheppard (1982).

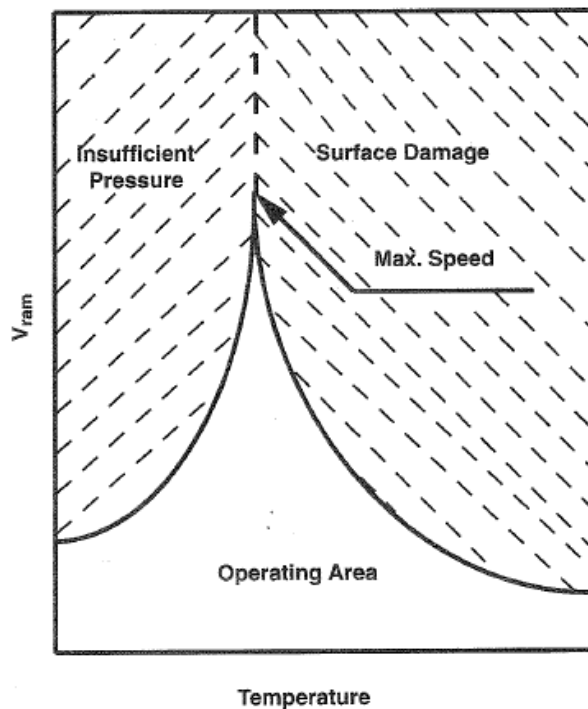


Figure 1.2 Limit diagram (schematic) by, Sheppard (1982)

It is clear that there is a locus indicating when the pressure would result in stalling of the press and one which would result in tearing of the surface. Inside these lines each point represents a suitable variation of parameters.

By careful control of alloying elements, an array of commercially available aluminium alloys can be produced. These aluminium alloys can be classified according to their suitability to specific manufacturing processes, based on whether they can be strengthened by work hardening only or also by heat treatment. Each alloy is described by a four digit number followed by a letter and a number indicating the temper or condition of the alloy. The work in this thesis is related to 6XXX series alloys. These alloys have Mg and Si as the main alloying elements and have good extrudability characteristics. All of the commercially used alloys contain Fe and Si as impurity dispersoids. They are mainly applied for structural, industrial and architectural applications since they have medium to high strength mechanical properties. Historically, mechanical working has been used as the primary means of changing the size and shape of materials while transforming the cast structure of an ingot into what is generally referred to as a wrought product. Extrusion is a typical process by which this can be achieved. Extrusion is typically conducted at relatively high temperatures because the lower flow stress of the material under these conditions permits larger reductions to be achieved. This results in lower load requirements and reduced processing times.

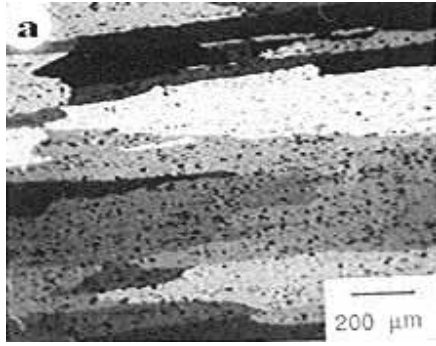
In order to model the deformation of materials it is important to recognize the structures and properties required in the final extrudate. Hence some background knowledge of the structure and properties is essential in order to ensure that the modelling results are sensible. Extrusion is a plastic deformation process in which a billet of cast and homogenized aluminium is forced to flow by applied compression through a die opening with the required geometry which is of a smaller cross section compared to the original billet.

The extrusion process must result in an engineered product satisfying geometric, appearance and mechanical property specifications. In order to achieve this extrusion involves the interaction between process variables and material characteristics. Process variables which can be used for process control are the extrusion ratio  $R$ , the ram speed  $V$  and the extrusion temperature  $T$ . The inherent stiffness or flow stress of the alloys is one of the limiting factors of the extrusion process. Flow stress may be defined as the relationship between load and strain at which a fully plastic condition may be assumed for a specific material. A further limitation is the maximum temperature which can be tolerated during extrusion.

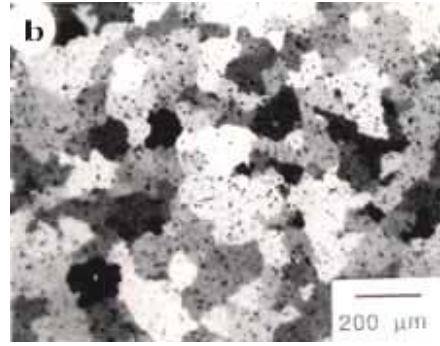
The way to control the final product properties is to investigate the relation between processing parameters, metallurgical response and final properties. Optimising the microstructure related to obtain the product properties require process control. For extrusion, thermo-mechanical process control will involve the following processing steps: billet homogenization, billet pre heat, extrusion (including solutionising where possible), cooling, stretching solution soaking and ageing. The resulting microstructure features are important in process control of extruded aluminium alloys: the coherency and distribution of strengthening precipitates, the degree of recrystallisation, the grain size and or subgrain size and shape, the crystallographic texture, size and distribution. We now should consider the structural features and the required properties generated by these features. In order to achieve the optimum mechanical properties in EN AW-6082, it is normal to solutionise during the extrusion process. In this alloy, the desired structure after solution soaking is usually one exhibiting as little recrystallisation as possible, but in some applications a structure with as small a grain size as possible is preferred.

The changes to the grain structure of directly extruded material after a solution soak are shown in Figure 1.3. Billets extruded at a temperature less than about 350°C assume a completely recrystallised structure after a necessary solution soak whilst the higher temperature extrudates appear to have retained much of the original grain structure, with a substantial subgrain substructure.

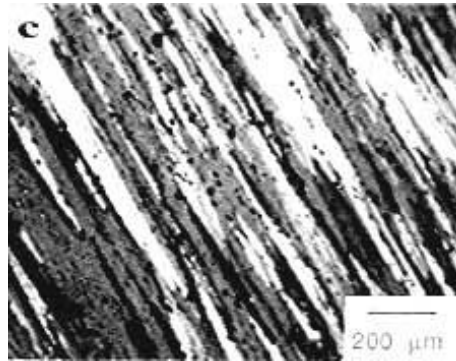
Figure 1.3 also illustrates the mode of recrystallisation in the extrudates; the elongated nature of the recrystallised grains in the extrusion direction is clearly due to the pinning of the boundaries by second phase particles (Figure 1.3a and 1.3b). Figure 1.3c indicates the absence of recrystallisation in the higher temperature extrudates. These specimens were extracted from extruded rod; similar micrographs would be obtained from extruded shapes. Although these structures may vary with alloy composition they indicate the complex problem to be analysed by FEM. These structures are of great importance because of the subsequent effect on properties. The evidence presented in these micrographs suggest that the extrusion conditions for 6082 alloy should be at the highest temperature possible consistent with maintaining a satisfactory surface.



(a) Extruded at 350°C, 0.5h soak,  
longitudinal



(b) Extruded at 350°C, 0.5h soak,  
transverse



(c) Extruded at 450°C, 0.5h soak, longitudinal

*Figure 1.3*, the mode of recrystallisation in the extrudates, (a) Extruded at 350°C, 0.5h soak, longitudinal, (b) Extruded at 350°C, 0.5h soak, transverse, (c) Extruded at 450°C, 0.5h soak, longitudinal

The structure of the extrudate is dependent on the total thermo-mechanical cycle but the most important consideration in terms of properties is the subgrain size and orientation which very much determines the metal response to the solution and ageing sequence. The subgrain size is related to the processing parameters and has been established for many alloys to be:

$$\delta^{-1} = A \ln Z - B \quad (1.1)$$

for direct extrusion. In this form  $\delta$  is the subgrain diameter and  $Z$  is the temperature compensated strain rate given by;

$$Z = \dot{\epsilon} \exp\left(\frac{\Delta H}{RT}\right) \quad (1.2)$$



Where  $\dot{\epsilon}$  is the mean equivalent strain rate and in practical terms is governed by the extrusion ram speed whilst  $\Delta H$  is the activation energy for the material and is a function of alloy content, dispersoid and precipitate distribution etc.  $R$  is the universal gas constant and  $T$  is the temperature of the billet at the relevant location. Thus once the homogenisation and preheat sequence have been completed structure control is largely dependent upon the extrusion conditions. There is a variation of structure longitudinally in the extrudate which could and should be eliminated by the control of press speed during the cycle. The importance of automation and computer control of presses becomes evident with the ideal combination being indirect extrusion with full automation of preheating and press facilities. The objective being the attainment of optimum, homogeneous and reproducible properties in each extrusion. These properties would vary with each alteration in die design, distribution of intermetallic particles and trace elements. Understanding the effects of these features on the properties of aluminium alloys will contribute to process control. The application of numerical methods can be used for quantitative predictions of microstructure during extrusion of aluminium alloys. This is also referred to as computational material science. The application of microstructure simulation into extrusion modelling is discussed in the present work.

Extrusion is a plastic deformation process in which a billet of cast and homogenized aluminium is forced to flow by applied compression through a die opening with the required geometry which is of a smaller cross section compared to the original billet. The extrusion process must result in an engineered product satisfying geometric, appearance and mechanical property specifications. In order to achieve this extrusion involve the interaction between process variables and material characteristics. The inherent stiffness or flow stress of the alloys is one of the limiting factors of the extrusion process. Flow stress may be defined as the relationship between load and strain at which a fully plastic condition may be assumed for a specific material. A further limitation is the maximum temperature which can be tolerated during extrusion. The way to control the final product properties is to investigate the relation between processing parameters, metallurgical response and final properties.

Optimising the microstructure related to obtain the product properties require process control. For extrusion, thermo-mechanical process control will involve the following processing steps:

billet homogenization, billet pre heat, extrusion (in some cases including solutionising), cooling, stretching and ageing. The following microstructure features are important in process control of extruded aluminium alloys: the coherency and distribution of strengthening precipitates, the degree of recrystallisation, the grain size and or subgrain size and shape, the crystallographic texture, size and distribution of intermetallic particles and trace elements. Understanding the effects of these features on the properties of aluminium alloys will contribute to process control. The application of numerical methods can be used for quantitative predictions of microstructure during extrusion of aluminium alloys. This is also referred to as computational material science. The application of microstructure simulation into extrusion modelling is discussed in the present work.

## **1.2 Modelling of the extrusion process**

The use of modelling opens up great opportunities for making maximum use of process data, for optimum co-selection of material and process, and for providing the designer with feedback on the likely influence of processing on the viability and cost of a design as well as indicating trial processing parameters (Sheppard and Velay 2007). At the beginning of the 1950's J. H. Argyris and Oleg C. Zienkiewicz at Imperial College commenced to publish work on Finite Element Method (FEM) (Zienkiewicz et al. 2005, p.2-3). By the early 80's most engineering problems could be solved by these methods and they continued to develop until the early 90's several commercial programs appeared specifically to deal with thermo-plastic problems. These are now available to the scientific community.

Bianchi and Sheppard (1987) were among the pioneers of applying FEM to extrusion calculation. So far process modelling has gained considerable impetus over the past few decades with the rapid increase in computational power. It has been mainly driven by industry to increase output with lower cost and better quality. Industrial modelling activity in metals and alloys extends to virtually every process from primary refining and casting processes through forming to fabrication and heat treatment (Grong and Shercliff 2002).

A complete analytical resolution of the extrusion process is presently impossible because of the complexities of the metal forming processes: large deformation, thermo-mechanically coupled, nonlinear boundary conditions and nonlinear material behaviour. Currently there are no other methods that are as convenient as the Finite Element Method (FEM) to approach all of these problems with the necessary precision. The main advantages of FEM, compared with other numerical methods and analytical techniques are:

- Predict the deformation information concerning strain, strain-rate, stress, temperature, velocity and the Zener Hillomon parameter,  $Z$ ;
- Consider the complex interactions between strain, strain rate, temperature, and microstructure;
- Use realistic models to represent real process behaviour, such as the coefficients of friction, heat transfer coefficients, and the flow stress;
- Visualise the deformation process with the ability to trace the history

The present work has concentrated on developing the ability to predict the range of structures which we could encounter when varying the Process parameters. When designing both the die and the process we aim to produce an unrecrystallised structure off the press giving increase strength and corrosion properties. Hence the Literature Review displays adaptations of relevant theory which can already be found. Chapter 4 reports on some experiments illustrating the possibilities of achieving control by die design, Chapter 5 concentrates on the macro and micro flow in extruding material and Chapter 6 discusses the simulation of physical properties and discusses the structure in terms of the micro factors involved.

The ultimate goal of FEM software is to replace the experimental phase partially or completely. For this reason a number of programmes modified to deal with deformation processes have become available commercially.

### **1.3 Objective of this research**

The research will focus on using simulations to model the hot extrusion of 6082 aluminium alloys of two solid and one hollow profile.

Since modelling of simple sections have been extensively studied, Sheppard and Wood (1980), Duan et al. (2004)), focus will be placed on the modelling and simulation of extrusion with more complex profiles such as U-shape (solid section) and tubular shape (hollow section). The effect of variations in design features for complex industrial extrusion dies will be investigated by means of simulation. Therefore the research objectives are as follows:

- Validate the FEM code by comparison with extrusion trials
- Investigate and develop suitable constitutive equations;
- Predict the extrusion pressure, temperature distribution and evolution;
- Predict the metal flow and surface generation during extrusion;
- Predict the microstructure evolution (subgrain size, volume fraction recrystallised);
- Investigate relevant design features for hollow and solid dies
- Predict the effect of die design in extrusion for hollow and solid dies

Thus the contribution to knowledge lies in the ability to describe the evolution of sub grain size and dislocation density distribution during the process and as a result of variations in process parameters; the ability to use these parameters to predict microstructure is also novel and of some importance. The ability to describe and predict, quantitatively, the effect of changes in die design is of equal importance.

## **2 Literature review**

### **2.1 Thermo mechanical modelling**

Extrusion is a relatively modern forming process. Other forming processes such as rolling and forging are much older. The process to produce aluminium, the electrolysis process, was developed into a workable process in 1886 concurrently by Hall and Heroult. Although extrusion is a complex process the ability to produce an enormous variety of complex shapes has enabled it to become established as a major industrial process, Sheppard and Raghunathan (1989). In this work the extrusion process has been modelled using the commercially available software Forge2009®.

#### **2.1.1 Physical parameters influencing the modelling of the extrusion process**

To a large extent most of the contents of this section may be calculated more accurately by utilising the FEM approach. Nevertheless the literature describing the use of equations developed to predict processing and the definition of the most commonly used terms is of some use to the processing engineer to understand or approximately calculate physical variables and arrive at an acceptable value. It also relates the history of the scientific growth of the subject. The reader should also be aware that FEM programming is excessively time consuming and is still, in effect, an Upper Bound.

##### **(a) Extrusion ratio**

The extrusion ratio is defined as the ratio of the initial billet cross-sectional area to the final cross sectional area. The effective extrusion ratio will range in industrial practice from 10:1 to 100:1. In conventional extrusion the extrusion ratio is denoted by  $R_e$  and is given by the expression:  $R_e = A_C / A_E$  where  $A_C$  is the area of the container cross section and  $A_E$  is the cross sectional area of the extrudate.

## (b) Plastic strain and strain rate

The Prandtl-Reuss equation describes all points of the nonlinear relationship between stress and strain. It is useful for metals which harden with plastic deformation, showing a smooth elastic-plastic transition. The Prandtl-Reuss equation relates an increment of stress to an increment of plastic strain for a metal undergoing plastic flow.

$$\frac{d\varepsilon_x^p}{\sigma'_x} = \frac{d\varepsilon_y^p}{\sigma'_y} = \frac{d\varepsilon_z^p}{\sigma'_z} = \frac{d\gamma_{yz}^p}{\tau_{yz}} = \frac{d\gamma_{zx}^p}{\tau_{zx}} = \frac{d\gamma_{xy}^p}{\tau_{xy}} = d\lambda \quad \text{or} \quad d\varepsilon_{ij}^p = \sigma'_{ij} d\lambda \quad (2.1)$$

Reuss assumed that the plastic strain increment ( $d\lambda$ ) in the equations are at any instant proportional to the instantaneous stress deviation and the shear stresses. The actual strain is obtained by integration as a logarithmic function.

The effective strain in direct extrusion can be roughly approximated as the fractional sectional area and is defined in an elementary notation as:

$$\bar{\varepsilon} = \ln \frac{A_C}{A_E} = \ln \eta R_e \quad (2.2)$$

Where  $\eta$  is the ration of the Perimeter of the extrudate divided by that of an equivalent ratio rod (Sheppard and Wood 1980).

The rate of straining is also an important parameter and very difficult to determine due to the complex flow pattern in the deformation zone. The material undergoes a rapid acceleration as it passes through the deformation zone. Therefore a mean equivalent strain rate  $\dot{\bar{\varepsilon}}$  has to be estimated for determination of the flow stress. Sheppard and Tutcher (1980) modified the equation proposed by Feltham by optimising an Upper Bound solution for the mean equivalent strain rate to read:

$$\dot{\bar{\varepsilon}} = \frac{6D_C^2 V_R (a + b \ln R_e)(c + d \tan \omega)}{D_C^3 - D_E^3} \quad (2.3)$$

Where a, b, c and d are constants,  $D_C$  is the container diameter,  $D_E$  is the extrudate diameter,  $V_R$  is the ram speed and  $\omega$  is the deformation cone semi-angle. A more accurate calculation of  $\dot{\epsilon}$  was obtained using FEM, (Bianchi and Sheppard 1987).

### **(c) Friction**

Generally hot extrusion of aluminium alloy is performed without lubricant. However a small amount of graphite based grease is sometimes used on the face of the die and dummy block (Sheppard and Raybould 1973). This is because the surface is an important feature of the product and is formed from the interior of the billet by the shear occurring in the conical zone adjacent to the die known as the dead metal zone.

Friction in aluminium extrusion is a complex and still not fully understood phenomenon (Donati et al. 2004) in the environment of hot extrusion (i.e. high pressure, high temperature and material flow) and the hostile environment prevents efficient investigation of the frictional interfaces. In direct extrusion (with a flat die) the friction occurs at four interfaces: (a) container-billet (b), die bearing-material (c), dead metal zone-material and (d), dummy block-billet. In indirect extrusion friction on a, b, and d, interfaces still exists. At the beginning of the extrusion the billet is upset in the container and the surfaces make first contact only at the highest points of the asperities. Consequently due to increasing pressure the contact area is increased. The asperities start to deform and the concentrated mechanical energy required to overcome frictional resistance is converted into heat energy. This eventually leads to sticking friction between the container and the billet and extrusion proceeds by shearing along the container wall. The thickness of the shearing layer is between 40 to 100  $\mu m$  (Jowett et al. 2000). When indirect extrusion it is considered there is a similar upsetting stage in the beginning as in direct extrusion. There is no friction between container-billet surfaces during the following stages of the extrusion process. On the other three interfaces friction still exists.

Due to the relatively small flow of material and the shearing of the discard, the dummy block-billet surface does not significantly influence the extrudate quality. Three laws are available in Forge2009® in order to define the friction between the deformable object and the rigid tooling: The viscoplastic friction law written in the following form:

$$\tau = -\alpha K(T, \varepsilon) \Delta V^{p-1} \Delta V \quad (2.4)$$

Where  $\tau$  is the difference in the shear stress vector,  $V$  is the velocity vector and  $\Delta V$  is the difference in velocity between the two solids,  $\alpha$  is the viscoplastic friction coefficient and  $0 \leq \alpha \leq 1$ ,  $p$  is the sensitivity parameter to the sliding velocity,  $K$  is the consistency of the material. The Tresca friction law can be written as:

$$\tau = -m \frac{\sigma_0 \Delta V}{\sqrt{3} \Delta V} \quad (2.5)$$

Where  $\sigma_0$  represents the yield stress,  $m$  is commonly referred as a friction factor. The range of  $m$  is  $0 \leq m \leq 1$ , when  $m=1$ , sticking friction occurs. The Tresca law treats the interface friction as pressure independent and relates the friction stress directly to the yield strength of the deformed material. The modified Coulomb friction law can be written as:

$$\tau = -\mu \sigma_n \frac{\Delta V}{\Delta V} \quad \text{if } -\mu \sigma_n < \frac{\sigma_0}{\sqrt{3}} \quad (2.6)$$

With this relationship the friction shear stress is equal to the normal stress  $\sigma_n$  multiplied by the friction coefficient  $\mu$ .

### 2.1.2 Extrusion pressure

The development of slip line field and upper bound techniques led to a plethora of semi-empirical equations to predict extrusion pressure.



In effect the first technique relies on the solution of hyperbolic shear or Slip-line deformation fields which are determined from observation of metal flow and is thus a solution built on stress minimisation which can only be achieved by trial and error. The field then describes the slip line field which must be consistent with a hyperbolic stress distribution. This solution must then be manually minimised and is a tedious and time consuming procedure. The upper bound solution assumes the material deforms by bulk movement of blocks of material bounded by velocity discontinuities in such a way that maximum energy is used and the solution is then minimised. In this case, however, it is possible to define the problem in a mathematical form such that minimisation can be programmed. Both techniques rely upon plane strain condition and perfectly plastic material. It would appear that following this route would not be productive. However, in the absence of any alternative, there is a plethora of equations to choose from. Such was the extent of study using these very approximate methods that there are texts available giving excellent coverage of these methods (Hill 1950) (Johnson and Kudo 1962). We should recall that FEM solutions are still easy to understand but use excessively long times. They are still upper bound solutions. The study of pressure during aluminium extrusion has been extensively reported over the years (Siebel and Fangmeir 1931), (Castle and Sheppard 1976), (Moe et al. 2003).

The pressure required for the process is the principal consideration in the selection of an extrusion press. The pressure can vary depending on the alloy and its condition, the extrusion ratio, diameter and length of the billet, temperature of the billet and tooling, ram speed and the shape of the extrudate (Sheppard 1993); (Sheppard 1999a, pp29).

An early equation derived by Siebel and Fangmeir (1931) suggested that;

$$P = \bar{\sigma} \ln R_e \quad (2.7)$$

In this equation  $\bar{\sigma}$  is the equivalent stress. Unfortunately this equation underestimates the real pressure by about 60%. It does not take into account the friction and the peak pressure.

Sheppard and Raybould (1973) has shown from observation and numerical analysis that the following equation can be derived;

$$P = \bar{\sigma}(a + b \ln R_e + cL) \quad (2.8)$$

Where  $a$ , is the contribution to redundant work,  $b$  is linked to the semi dead metal zone angle,  $L$  is the length of the billet and  $c$  is dependent on the friction coefficient. The application of slip-line fields or upper bound solutions produce similar forms of this equation.

Further work by Castle and Sheppard (1976b) have described that extrusion pressure could be viewed as consisting of four parts;

$$P = P_D + P_F + P_{RW} + P_B \quad (2.9)$$

Where  $P_D$  is the required pressure for the plastic deformation of the billet.

$$P_D = f(\bar{\sigma}, \bar{\varepsilon}) \quad (2.10)$$

In this equation,  $\bar{\varepsilon}$  is the mean equivalent strain and  $\bar{\sigma}$  is the flow stress,  $P_F$  is the pressure required to overcome the friction mainly at the container wall,  $P_{RW}$  is the pressure required to compensate for internal deformation work and  $P_B$  is the pressure required to overcome the higher number of dislocations present in the billet before steady state is reached.

FEM can give good predictions of the extrusion pressure (Peng 2005). FEM is also more flexible than other methods in particular when complex boundary conditions (complex shape) are encountered.

### 2.1.3 Heat transfer and temperature

Heat transfer is one of the most important phenomena to consider in extrusion as it decides the temperature parameter. This is one of the process variables which can be controlled. Temperature rise and distribution have been investigated by many researchers (Sheppard 1999) (Duan and Sheppard 2002b); (Libura et al. 2000). In general it has been shown that variations in temperature are mainly due to the extrusion ratio and ram speed. The flow stress and therefore the pressure can be reduced if the temperature is increased. However there is a risk of localized incipient melting with high ram velocity.

Heat transfer occurs throughout the extrusion process from the initial stage of homogenization to the following extrusion stage, during which heat transfers to the die (from the billet) and air (from the extrudate), then the stage of stretching and finally at the stage of solution treatment and ageing (Castle and Sheppard 1976b); (Chenot and Chastel 1996); (Sheppard and Wood 1980). The heat generation and heat transfer occurring during the extrusion are critical because they define the exit temperature of the extrudate. The temperature of the extrudate just leaving the die is important for product quality (dimensional stability and extrusion defects) and die life (wear and performance). Castle (1992) and Sheppard (1999b) divided the heat balance between the following processes:

Heat generation due to plastic deformation;

Heat generation due to friction at the container-billet, dead metal zone-material and die land-material interfaces;

Heat exchange between the billet and the tooling (container, pressure pad and die land)

Approximately 90-95% of the mechanical energy is transformed into heat. The heat generation rate due to per unit of volume  $\dot{Q}_d$  can be written as follows:

$$\dot{Q}_d = \lambda \sigma \dot{\epsilon} \quad (2.11)$$

Where  $\lambda$  is the heat generation efficiency ( $0.90 \leq \lambda \leq 0.95$ ).

### 2.1.4 Yield criterion

A yield criterion is a law which defines the limits of elasticity under any possible combination of stresses. It is expressed by;

$$f(\sigma_{ij}) = C \text{ (Constant)} \quad (2.12)$$

Where  $f(\sigma_{ij})$  is called the yield function and  $\sigma_{ij}$  is defined by the Cauchy stress tensor.

For isotropic materials, such as aluminium alloys, plastic yielding can depend only on the magnitude of three principal stresses  $\sigma_1, \sigma_2, \sigma_3$  and not on their directions. Thus any yield criterion can be expressed as follows:

$$f(J_1, J_2, J_3) = C \text{ (Constant)} \quad (2.13)$$

Where  $J_1, J_2, J_3$  are the three invariants of the stress tensor,  $\sigma_{ij}$ .

They are defined in terms of the principal components by the following relations:  $J_1 = \sigma_1 + \sigma_2 + \sigma_3$ ,  $J_2 = \sigma_1\sigma_2 + \sigma_2\sigma_3 + \sigma_3\sigma_1$ ,  $J_3 = \sigma_1\sigma_2\sigma_3$ . The first invariant ( $J_1/3$ ) represents the hydrostatic pressure. This pressure does not increase ductility except in extreme cases such as in brittle materials. Two differing forms of criteria are generally used.

The Tresca criterion, which postulates that yielding will occur when the largest shear stress reaches a critical value, and the Von Mises criterion which states that yielding will take place when second invariant  $J_2$  reaches a critical value. The Tresca criterion provides a practical approximation of yielding, however, the Von Mises criterion is usually preferred because it correlates better with experimental data.

### 2.1.5 Viscoplastic model

The theory of plasticity adequately describes materials with time-independent behaviour. However the theory of viscoplasticity more effectively defines the behaviour of materials which exhibit strain rate sensitivity such as in aluminium alloys. During hot extrusion the aluminium alloy's properties can vary considerably with temperature. The work piece (e.g. billet and extrudate) experiences temperature gradients. At elevated temperature, plastic deformation can increase the rate of phase transformations and modifications to grain structures. These metallurgical changes can, in turn modify the flow stress of the material as well as other mechanical properties. Thus, the flow stress  $\bar{\sigma}$ , can be expressed as a function of temperature, strain, strain rate, and state variables. At very high temperature ( $< 0.9T_m$ ), where  $T_m$  is the lowest melting point of the material. The influence of strain on flow stress is insignificant, and the influence of strain rate becomes increasingly important. Therefore  $\bar{\sigma}$  can be expressed as follows:

$$\bar{\sigma} = f(\dot{\epsilon}, T, S_i, P_i) \quad (2.14)$$

Two constitutive equations, the Norton Hoff law and the Zener-Hollomon formulation have been adopted in the FEM simulations of hot forming. However of the two constitutive equations, the hyperbolic sine function is the only one revealing the physical nature of the flow stress and has been found the most suitable for use. Duan and Sheppard (2003) made a comparative study concerning these three equations and their suitability for hot extrusion of aluminium alloys using FEM software Forge2009®. His results show that Zener-Hollomon formulation is the most accurate equation to represent the flow stress in hot extrusion of aluminium alloys in FEM simulation. Thus the Zener-Hollomon formulation was adopted in this research. The hot deformation of aluminium alloys is commonly described by the equations shown below (2.15, 2.16). Initially proposed by Zener and Hollomon (1944) and then subsequently rearranged by (Sheppard and Wright 1979). The flow stress is written:

$$\bar{\sigma} = \frac{1}{\alpha} \ln \left[ \left( \frac{Z}{A} \right)^{\frac{1}{n}} + \sqrt{\left( \frac{Z}{A} \right)^{\frac{2}{n}} + 1} \right] \quad (2.15)$$

Or

$$Z = A [\sinh(\alpha \bar{\sigma})]^n \quad (2.16)$$

Where the parameters  $\alpha, A, n$  are constants. Jonas et al. (1969) show that equation 2.17 reduces to a power law when  $\alpha \bar{\sigma} < 0.8$ , but approximates an exponential relationship when  $\alpha \bar{\sigma} > 1.2$ .  $Z$  is the temperature compensated strain rate parameter also called the Zener-Hollomon parameter. It is given by equation (2.18) below:

$$Z = \dot{\epsilon} \exp \left( \frac{\Delta H}{RT} \right) \quad (2.17)$$

Where  $T$  is the temperature,  $R$  is the universal gas constant ( $8.31451 \text{ J} * \text{mol}^{-1} * \text{K}^{-1}$ ), and  $\Delta H$  is the activation energy for hot deformation. Garofalo (1963) showed that the activation energy for creep in aluminium was identical to that for hot deformation increases with absolute temperature up to  $T \approx 0.5T_m$  whereupon it remains constant up to the melting point.

### 2.1.6 Material Flow Investigations

Metal flow during extrusion influences the formation of the microstructure and hence the mechanical properties of the section. The material flow during extrusion is to some extent generally understood. The material flow determines the location of surface defects and indicates the variations of structure which results in inhomogeneity. An important part of practical extrusion is the production of hollow sections and tubes in particular. To be able to produce these hollow sections a bridge die is required which usually follows the configuration of Figure 2.1.

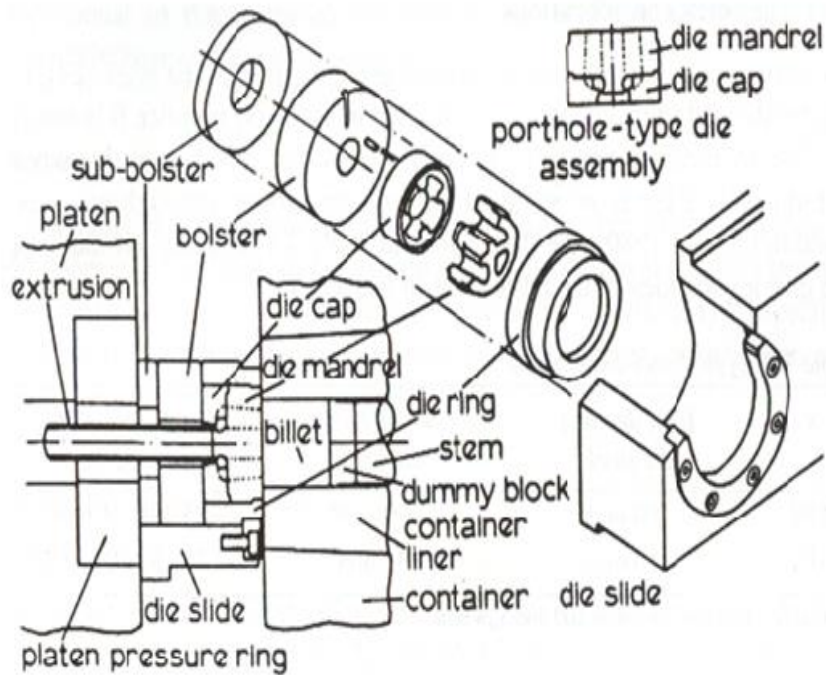


Figure 2.1 A typical tooling arrangement for aluminium hollow sections (Sheppard 1999a, p.359)

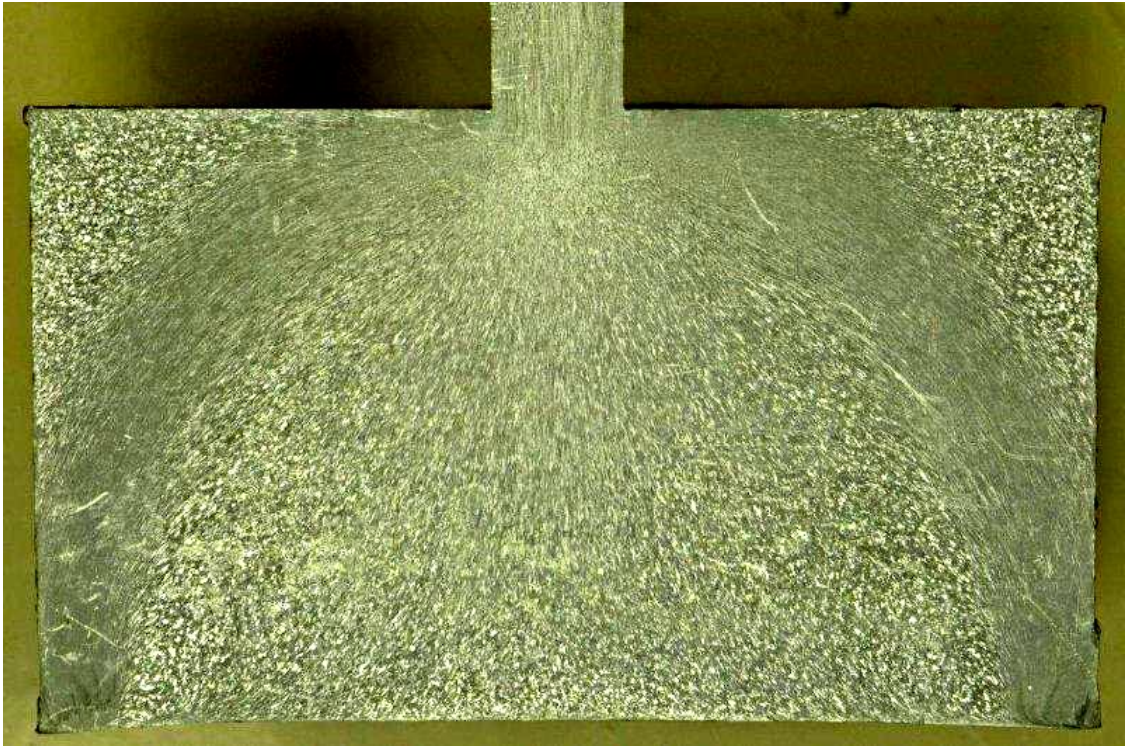
The required tooling to produce hollow dies consists of a die with a fixed core or mandrel. The mandrel is firmly kept in position by a number of bridges which form a web and are fixed to the back of the die. During extrusion the material is forced into the die ports and splits into separate flows across the die bridge resulting in a number of material streams around the mandrel support. When the material has passed the bridge and the mandrel the material is joined by welding in the welding chamber and becomes welded in the solid state by effect of pressure and temperature Bozzi et al. (2009). As a result the extruded sections, produced by means of these bridge dies have two or more weld seams in the longitudinal direction. Physical techniques have been used to describe metal flow in extrusion, (Valberg 1996, Sheppard & Wood 1980). These researchers have used techniques such as gridded billets, introducing a grid into the as cast billet followed by polishing and etching the surface after the extrusion. Recently numerical techniques were applied to study the metal flow (Liu et al. 2008).

These techniques were able to give a better description of but metal flow during extrusion but none of them gave a comprehensive insight to understand the flow across a hollow die bridge. The formation of a longitudinal weld seam is unique to hollow extrusion across a die bridge since the material will have to weld after it passes the die bridge. High pressures and temperatures prevent practical measurements. Physical methods have been used to try to describe the weld seam quality (Valberg 2002), numerical methods have been applied by Bourqi et al. (2002) and Donati & Tomesani (2004). From this work it can be concluded that weld seam formation is a solid-state pressure-bonding process.

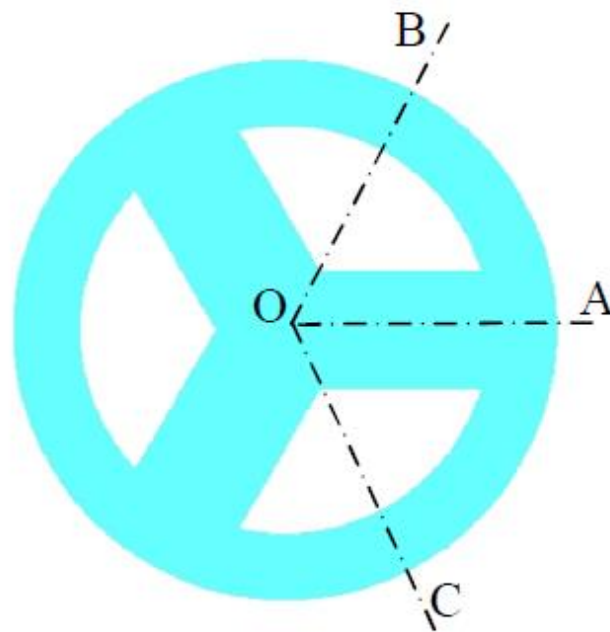
The formation of a longitudinal weld seam is unique to hollow extrusion across a die bridge since the material will have to weld after it passes the die bridge. High pressures and temperatures prevent practical measurements. The main parameters which influence the quality of the weld seam are pressure and contact time between the materials from neighboring metal streams. Understanding self-contact in welding material flows across the die bridge is the challenge.

Figure 2.2 is a macrograph of a partially extruded billet which illustrates the material flow. In general direct extrusion can be characterized by a rapid flow of the centre material toward the die whereas the peripheral parts of the billet are restrained by friction along the container wall. In combination with friction on the die surface this leads to the development of dead metal zones. The peripheral shear zone with the as-cast surface including contaminations is compressed in front of the dummy block. The rapid flow of material from the centre of the billet produces a lack of material in the centre at the end of each billet. Metal flow from the peripheral zone is then pulled to the centre by the inverse flow.



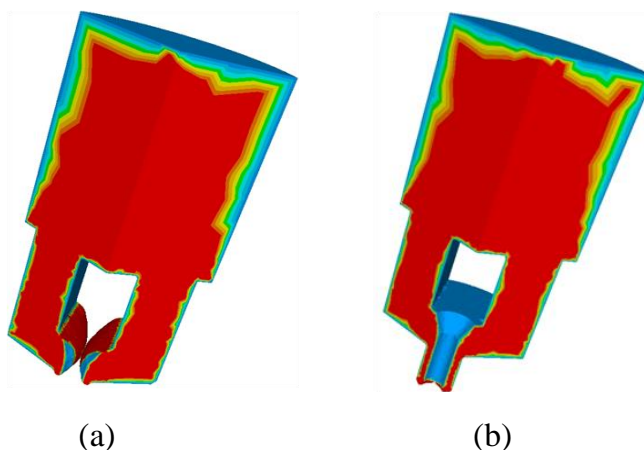


*Figure 2.2* A cross section of an extruded billet revealing the metal flow



*Figure 2.3* Showing the symmetrical planes

Observing the symmetrical nature of the flow in Fig 2.2 will allow us to set up our FEM simulation in 1/3<sup>rd</sup> or 1/6<sup>th</sup> symmetry. This will determine the number of elements to be used: an important feature of FEM modelling. This can also help in understanding the complex metal flow in hollow die extrusion across a bridge and can help to minimise the number of elements required for the simulations. The greatest advantage regarding minimising elements can be obtained when one sixth of the geometry is applied (see Figure 2.3). One sixth of the geometry avoids self-contact of elements in the simulations and will result in half of the feeder hole and half of the bridge being included in the simulation (see Figure 2.4). In the case of one third symmetry self-contact of elements is unavoidable. In this case the whole feeder hole will be included in the simulations and half of both adjacent die bridges, see Figure 2.3. This case would permit examination of the weld seam area including self-contact. In the one third symmetry model some self-contact mechanism will have to be triggered during simulation since two weld streams will meet to bond and form a closed tube. On application of the extrusion cycle and after the sequence described above the material will flow across the bridges to fill the ports until it reaches the welding chamber and the load will increase until it reaches the maximum value. From this point the section is extruded where a drop in pressure can be observed due to the reduced container friction until the extrusion process reaches the steady state. FEM is able to reveal two metal streams and weld completion between ram displacements of 28mm and 31mm.



*Figure 2.4* The metal's flow and weld of neighbouring metal streams during tube extrusion.

Sheppard et al. (2012c) has stated that there is a clear advantage when investigation one third symmetry with respect to investigation the aspect of self contact. The disadvantage being the double number of elements required in the simulations. Niu (2010) concludes that when considering statistically designed analysis, involving many runs, it is only practical to design using 1/6<sup>th</sup> symmetry.

From these observations we may conclude that in any practical problem the system dictates that the fewest elements possible will be selected. We should then realise that some accuracy will be surrendered: the acceptance of the results must then be considered. Niu (2010) showed that if detail of material flow or specific structural details were required the 1/3rd symmetry model was required. This allowed the identification of the metal flow, dead metal zones and the weld seam surface as shown in Figure 2.5.

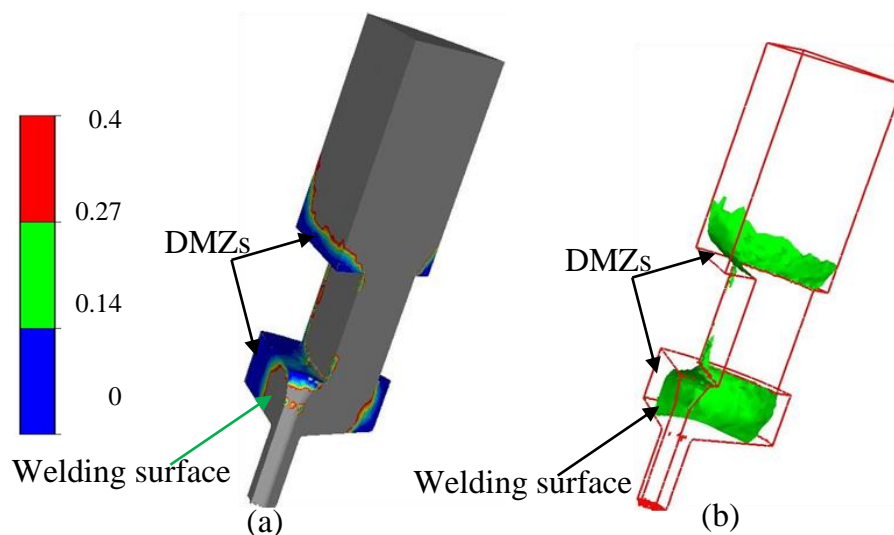


Figure 2.5 Dead metal zones in tube extrusion (a) and iso-surfaces (b) (Sheppard, Niu and Velay 2012c).

### 2.1.7 Surface Cracking Criteria

The pressure in the welding chamber and the contact time between the adjacent material streams are the most important factors which influence the weld quality. Weld seam quality can be evaluated using the Oyane damage law. The outer surface area of the tube extrudate should have better weld seam quality than the inner surface; from Sheppard and Niu (2010)

Weld seam quality can be evaluated using the Oyane damage law. The outer surface area of the tube extrudate would have better weld seam quality than the inner surface. Figure 2.6 shows the weld seam quality as predicted by FEM.

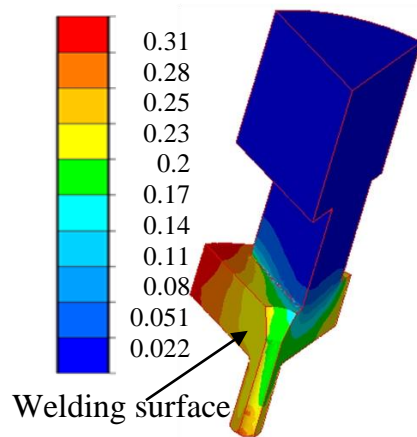


Figure 2.6 Weld quality index, (Sheppard, Niu and Velay 2012c).

Surface cracking is generally recognized as one of the main defects occurring during the process of aluminium extrusion, especially in the case of the relatively hard aluminium alloys such as EN AW-6082. Previous experiments suggest that this type of defect is caused by the rise in temperature as the process proceeds. Some experiments indicate that the surface quality is good even though the temperature may be high during extrusion. It is also well known that crack criteria have been developed to explain the cracking that occurs in extrusion, blanking and rolling, etc.

The finite element method (FEM) may be used to predict surface cracking during hot extrusion. The cracking criteria are integrated into the FEM code Forge2009®. The effectiveness of these criteria in predicting surface cracking in the case of hot extrusion is discussed.

In order to assess the implication of cracking on the extrusion one can distinguish two situations: Cracking occurring partly during the extrusion run and cracking occurring over the full extrusion run.

There are a number of cracking criteria for assessing rupture in metal forming process. They are all based upon experimental work which utilizes a deformation process related to actual industrial applications (Peng and Sheppard 2004). The initiation of ductile fracture in metals depends strongly on the stress and strain histories. Many ductile fracture criteria have the form that fracture occurs when the value of a damage parameter, which is given as an integral form of stress and strain, reaches a particular value. Peng and Sheppard (2004) compared a number of existing cracking criteria:

Oyane (1)

$$\int_0^{\varepsilon_R} \left( 1 + A \frac{\sigma_H}{\sigma_{eq}} \right) d\varepsilon_{eq} \geq C1 \quad (2.18)$$

where  $A$  and  $C1$  are constants,  $\sigma_H$  is the hydrostatic stress,  $\sigma_{eq}$  is the equivalent stress and  $\varepsilon_{eq}$  is the equivalent strain. The process by which fractures occur in metal forming has been widely modelled as void initiation and growth, followed by coalescence to form a crack. Based on this hypothesis, criteria for ductile fracture have been suggested by McClintock et al.(1996) Oyane (1980) Cockroft and Latham (1986).

Cockroft and Latham (2)

$$\int_0^{\varepsilon_R} \sigma^* d\varepsilon_{eq} \geq C2 \quad (2.19)$$

$$\sigma^* = MAX(\sigma_1, \sigma_2, \sigma_3) \quad (2.20)$$

where  $C2$  is a constant  $\sigma^*$  is the maximum principal stress. Cockroft and Latham (1986) considered the effects of the maximum principal stress over the plastic strain path to fracture.

Cockroft and Latham normalized (3)

$$\int_0^{\varepsilon_R} \frac{\sigma^*}{\sigma_{eq}} d\varepsilon_{eq} \geq C3 \quad (2.21)$$

where  $C3$  is a constant. This criterion has a dependence on hydrostatic stress.

Ayada (4)

$$\int_0^{\varepsilon_R} \left( \frac{\sigma_H}{\sigma_{eq}} \right) d\varepsilon_{eq} \geq C4 \quad (2.22)$$

where  $C4$  is a constant.

Generalized work criterion (GW) or Freudenthal criterion (5)

$$\int_0^{\varepsilon_R} \sigma_{eq} d\varepsilon_{eq} \geq C5 \quad (2.23)$$

or

$$\int_0^{\varepsilon_R} \left( \sigma_1 \dot{\varepsilon}_1 + \sigma_2 \dot{\varepsilon}_2 + \sigma_3 \dot{\varepsilon}_3 \right) \geq C5' \quad (2.24)$$

where  $C5$  and  $C5'$  are constants.  $\sigma_1$ ,  $\sigma_2$  and  $\sigma_3$  are the principal stresses and  $\dot{\varepsilon}_1$ ,  $\dot{\varepsilon}_2$  and  $\dot{\varepsilon}_3$

are the corresponding principal strain rates. Freudenthal proposed that energy is the critical parameter at fracture. With this criterion fracture occurs in a material when the rate of plastic energy dissipation reaches a critical value when integrated with respect to time, following the element as it travels through the die. This is the only criterion that accurately predicted the site of fracture initiation for all three metal forming processes considered: upsetting, extrusion and strip deformation in the work of Clif et al. (1996).

Temperature (6)

$$T \geq C6 \quad (2.25)$$

where  $C6$  is a constant. If the heat generation near the die land area increases the local temperature such that the applied stresses exceed the resistance to deformation then severe cracking at the surface may be expected. This temperature generation is a function of the alloy chemistry, extrusion speed, extrusion ratio, aspect ratio, container temperature and initial billet temperature. Much of the heat generated at the surface occurs through the dead metal zone and the deformation shear band, which terminates on the face of the die immediately ahead of the die land area. This results in a steep rise in the temperature as the material approaches the die land. According to the six criteria described above, when the constants  $C1-C6$  reach a critical value, the crack occurs.

## **2.2 Extrusion die design**

In die design, we try to optimize the demands the industry is dictating on extruded sections such as mechanical properties, appearance and productivity. This result is a search for optimum process conditions coupled to optimum die design. Process conditions and die design are strongly product dependent. Every profile section has unique optimum properties such as load requirements, extrusion ratio and mechanical properties. Die design plays a critical part in the production process since it can influence both productivity and product quality, Lotzenhiser (1977).

The efficiency of the die design and the quality of the dies has a major influence on the profitability of an extrusion plant. In a market in which the margins between the different extrusion companies are often small, improvement of the quality of the design may have a significant impact on the competitive position of a company. In general, the quality of a design can be described as its ability to fulfill its predefined purpose. The complex construction of the die is split up into more manageable design features. The effect of optimizing some of these features will be discussed in chapter 4. The main die features, their limitations and their effect on the performance of the die in practice are discussed in this chapter, (Lotzenhiser 1977).

Bridges (or arms, legs, webs) are used in porthole dies to support the core by connecting it to the mandrel. Due to the high pressure during extrusion the core might deflect or bend, which will result in deviating bearing positions. The design of the bridges cannot be separated from the design of the portholes. Increasing the width of the legs will decrease the size of the portholes, thus raising the pressure at the front side of the die. Equilibrium has to be reached between optimal flow of the aluminum (no legs) and optimal support of the core. A very basic design principle is the dimensioning of the legs according to the span. The classical shape of the bridges has a feed angle of  $10 - 20^\circ$  and a small nose radius. This should allow welding to take place just behind the bridge. Castle et al. (1988) Ingraldi (1992). But as dead metal zones form behind the bridges the flow path of the aluminum is not equal to the shape of the bridge. Other shapes have been tested to find bridge shapes with a better resistance to bending or a higher breakthrough pressure. Some practical results have been presented in Hamzah (2000) and some finite element calculations on bridge shape can be found in (Lof 2000) also. To avoid bending of the bridges to an extent that the sides of the bearing are no longer facing each other, the die design needs to be altered.

A circular shape of the feeder holes would be ideal. For a circle the ratio of feeding area to porthole surface is maximized. This will minimize the contribution of the portholes to the extrusion pressure. As it is usually not possible or desirable to use round portholes (it would use too large a surface area) the actual shape of the portholes approaches these round shapes as much as possible. In the direction of flow the outer walls of the portholes usually receive an inclination of a few degrees to relieve the material flow (Ingraldi 1992). Due to the high pressures in the portholes a residue of aluminium will stick to the walls of the portholes along



which the following material will flow. This aluminium on aluminium contact is favorable over an aluminium-steel contact and will improve material flow. Finally the portholes should be placed inside a circle of about 0.85-0.90 times the diameter of the container. This will ensure that the deteriorated surface material of the billet is left behind in the container and the best possible aluminium quality is used for the section (Castle et al. 1988).

The bridges in porthole dies divide the aluminium flow. Behind the bridges the aluminium is welded together again in the welding chamber. The location where the aluminium welds together on the profile is called the weld line. If the welding conditions are not optimal this weld line will result in reduced material properties. The welding chamber itself is divided over the mandrel and the die plate. This has a positive effect on the possible load before failure of the die. Two types of pressure welding can be found in aluminium extrusion sections; seam welds in hollow sections and charge welds (welds between successive billets) both in hollow and solid sections. Failure in these welds is caused by a decreased ductility of the weld. Best welding conditions for the longitudinal seam welds are guaranteed if a dead metal zone is formed behind the legs of the mandrel and if the welding occurs between fresh surfaces. Locating the entire welding chamber on the mandrel will weaken the core significantly. As a result, this solution is hardly ever used. The depth of the welding chamber is often divided over the mandrel and the die plate or the whole of the welding chamber is located on the die plate. (Hamzah 2000), (Valberg 1996), (Castle et al. 1988).

The die orifice defines the shape of the profile that will be extruded. The opening cannot exactly be shaped according to the dimensions of the profile, as it should take account of some effects that influence the shape of the extruded profile. A sunken face (sink in) is a decrease in the face of the die around the orifice. This feature pre-deforms the aluminium and reduces the pressure on the face of the die. This reduces the deflection of the tongue. (Lotzenhiser 1977); (Stockdale 1992). The orifice widens at the center of the die.

The mandrel is used to hold the inner contours of the bearing in the correct place. These bearings are located on the core, the shape of which is defined by the shape of the profile to be extruded. The length of the core is defined by the height of the bridges and depth of the welding chamber. Displacing the mandrel in the unloaded state can counteract this phenomenon. (Ingraldi 1992).

The undercut is a step in the core just prior to the bearing. It acts as a shear edge before the aluminium passes the bearing. With conventional straight mandrels, shear in the metal causes friction and generation of heat. This may result in deterioration of the metal surface. Undercutting the mandrel thus improves the flow of the material and the temperature distribution over the bearing.

The sink in and pre-chamber are features, created by sinking the face of the die around the contour of the profile. They both follow the shape of the profile to be extruded, although the sink in follows the profile more closely. The sink in can be used to avoid profiles with extremely long sides becoming convex or for improving the flatness of longer legs on a profile. (Ingraldi 1992) The sink in is located closer to the profile and can be used to fully control the flow characteristics of the die. Some authors (Machado 1992), propose to avoid modifications of the bearing as a means of controlling the exit velocity of the aluminium and exclusively rely on a variation of the width of the sink in.

The bearing on a flat die or a porthole die is the length of an orifice in the die with the approximate shape of the profile to be extruded. For porthole dies, part of the bearing is located on the mandrel and part of the bearing is located on the die plate. Choking the bearing (up to  $3.5^\circ$ ) slows down the flow, which improves the filling of sharp corners. Increasing the speed locally can be done at the backside of the bearing using an angle up to  $7^\circ$  (relieving the bearing). (Lotzenhiser 1977).

Die design can follow three basic rules for the design of parallel bearings (Miles 1996)

- The bearing is longer for wider sections
- The bearing is longer towards the centre of the die
- The bearing is shorter for sections with a high perimeter to area ratio.

Between different bearing lengths the bearing will be tapered. Ends of legs will generally take about 0.8 times the normal bearing length for a section of that width. Castle et al. (1988) proposes a similar function as (Lotzenhiser 1977).

A reference bearing length of 1.5 – 2.0 times the wall thickness with a minimum of 1.5mm is proposed. The general rule is to increase the bearing length to wall-thickness ratio by 0.25 for each 20mm reduction in radius from the centre of the die. Tips will carry a bearing length of 0.75 times the bearing length normal for a part of that width. Castle states that the above rules apply up to a wall thickness of 6 mm (Castle et al. 1988). Finally, on porthole dies the bearing length under the legs of the mandrel will be shortened slightly. Some attempts have been made to automate the bearing length assignment process, see for example (Stockdale 1992) equation 2.26, (Miles 1996) equation 2.27, (Miles 1997), (Thomma 1996), equation 2.28. They use;

$$B_1 = w \left( 2.0 + \frac{1}{80} (R_r - r) \right) \quad (2.26)$$

$$B_1 = w \frac{B}{W} \left( 1.0 + \frac{1}{80} (R_r - r) \right) \quad (2.27)$$

$$B_1 = \left( a^* w - \frac{r d_a}{20 d_b f} \right) \frac{k_1}{k_2 + s} \quad (2.28)$$

$B_1$  = bearing length,  $R_r$  = distance of the reference bearing,  $r$  = distance of the current part,  $w$  = width of the current part,  $B$  = bearing length of the reference bearing,  $W$  = width of the reference bearing,  $d_a$  = circumscribing circle of the profile(s),  $d_b$  = billet diameter,  $s$  = extrusion speed and  $a, f, k_1, k_2$  are constants to be set by the designer.

### 2.2.1 Optimisation of solid die extrusion

Critical to direct extrusion of aluminium alloys through solid dies, is metal flow through the die and the design of the sink in / bearing area. The aim is to achieve an optimized material flow through the die which results in a correct profile. In practice the effect on material flow which is due to section geometry will have to be compensated in the die design. In these cases where the extrusion ratio is large, the walls are usually small which often results in distorted profiles.

The variation of the material flow is influenced by the wall thickness (thicker parts of the section will flow faster than thinner parts), the container friction (areas near the centre of the die will flow faster than areas closer to the container wall), and the die design (Li et al. 2003). A simple bearing, sink in configuration is given in Figure 2.7 (Li et al. 2003).

Increased resistance to the material flow will reduce the extrusion speed. Extrusion temperature can be used as a control parameter by the operator to influence extrusion speed and surface quality. Li et al. (2003) have shown the effect of using a constant small bearing in combination with a sink in with constant depth and varying offset, see Figure 2.7.

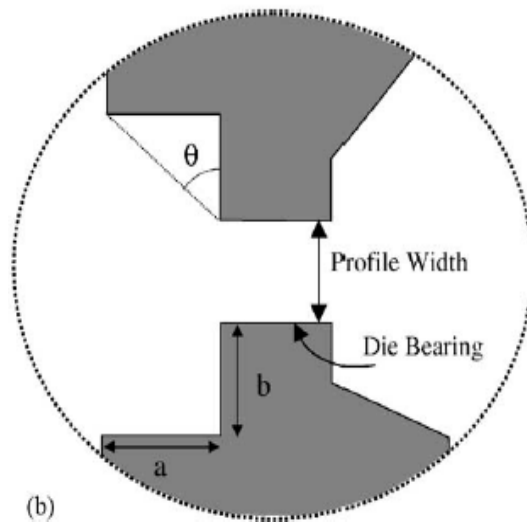


Figure 2.7 Bearing, sink in configuration of a solid die (Li et al. 2003)

They also investigated the effect of applying an angle in the sink in. Offsetting the sink in with a similar but enlarged shape of the profile geometry will offer an incomplete solution to possible flow problems. A sink in design with constant depth but varying offset dimensions can compensate for velocity differences caused by local wall thicknesses variations. The sink in is used as means to control extrusion of solid sections since it affects flow resistance and material flow by means of creating an additional dead metal zone.

A sink in is a pocket in front of the bearing. This pocket introduces extra resistance to the flow (*RI*).

The level of resistance introduced depends on the dimensions and shape of the sink in. In order to extrude profiles, an opening with approximately the shape of the required section has to be machined in the die. The aluminium will encounter flow resistance when passing through this orifice ( $R_2$ ). The level of flow resistance depends on the alloy used, the temperature, and the proximity of the container wall, the wall thickness and the shape of the pocket. In order to keep the exit velocity of the profile constant over the cross section, it is strived to keep the combined resistance ( $R_t$ ) of the profile orifice and the sink in at a constant level, ( $R_t = R_1 + R_2$ ). Lof (2000) proposed a possibility to determine  $R_1$  and  $R_2$ .

The Yield stress of aluminium is approximately 10.3MPa. Von Mises stresses below this value remain in the elastic domain. Von Mises stresses above 10.3MPa result in plastic deformation. The Von Mises stresses can be related to an equivalent plastic strain rate by applying the Prandtl-Reuss relationship. The material model includes elastic behavior. The parameters of the modified Sellars Taggart model were fitted to data from EN AW-6063 material based on experimental work from Akeret (1978) and the modeling work from Van de Langkruis (2000), at the Technical University Delft.

Lof used the Arbitrary Lagrangian Eulerian Code DIEKA for his simulations. Lof (2000) proposes a measure for the resistance of the bearing area. The average pressure on the inflow edge of the bearing is used as this measure. The average pressure can be defined as the sum of the forces in extrusion direction on all nodes on the inlet plane divided by the total surface of the plane.

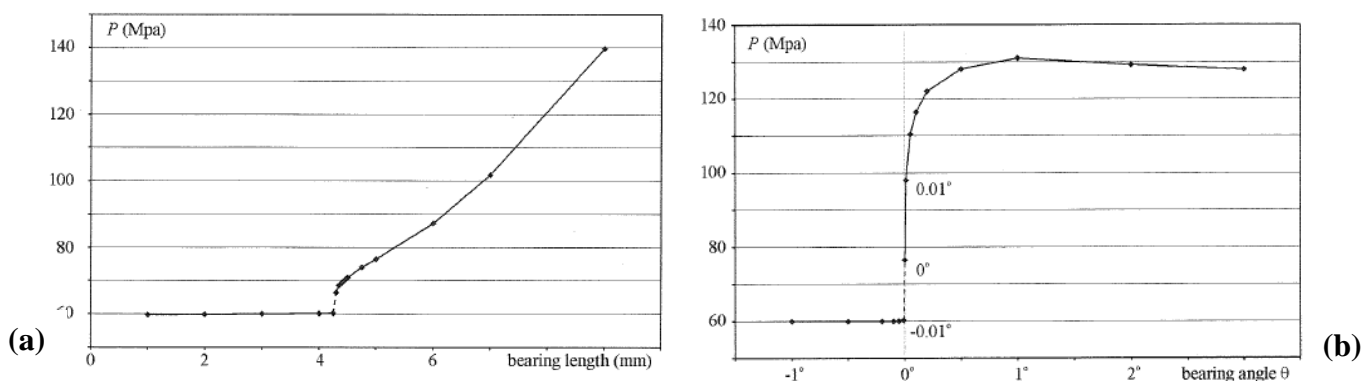


Figure 2.8 The influence of bearing length (a) and bearing angle (b) on the average pressure, Lof (2000)

According to Lof (2000), the average pressure is increased with increasing bearing length and with increasing bearing angle, see Figure 2.8. Small bearings with a length <4mm show marginal influence on the average pressure but bearings >4mm show a significant increase in average pressure with increasing bearing length, (Figure 2.8a).

In extrusion we assume parallel bearings. The influence of a relieved bearing angle is limited but a chocked bearing angle has an increasing effect on the average pressure, (Figure 2.8b). If we assume parallel bearings, flow resistance is very sensitive to small changes to the bearing angle. This would imply no manual interfering with the bearing. In practice a parallel bearing is usually manufactured with an accuracy of less than  $0.01^\circ$ . This implies that variations in pressure can only be controlled to a degree. Figure 2.8a and b shows the effect of the bearing length and the bearing angle on the average pressure.

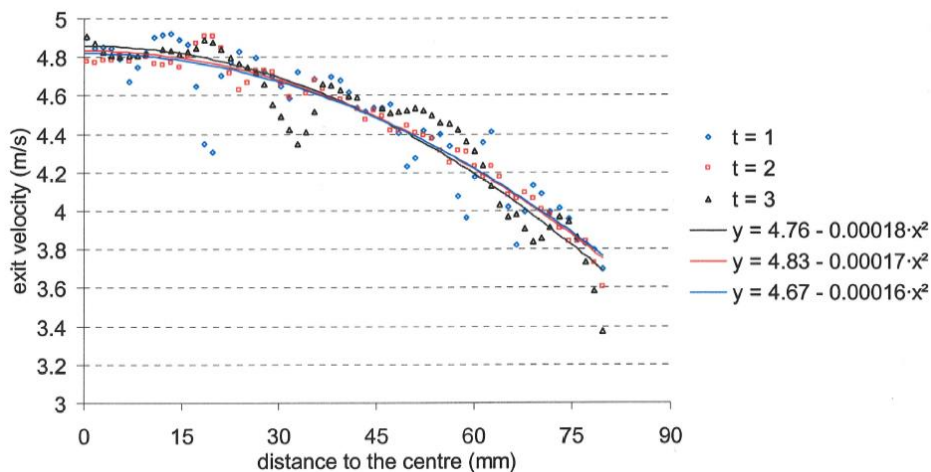


Figure 2.9 The relation between the distance to the centre and the extrusion speed, Lof (2000)

The influence of the distance to the container wall on the extrusion velocity was simulated by Lof (2000) using a wall thickness  $t$ , of 1, 2 and 3mm. Figure 2.9 shows the relation of the distance to the container and the extrusion velocity. Lof (2000) has stated that the dimensions of the sink in have an effect on the average pressure. Increased off set has a reducing effect on the average pressure. An increase in extrusion speed will have an increasing effect on the average pressure whilst an increase in wall thickness reduces the average pressure. Figure 2.10a show the effect of increased extrusion speed on the average pressure and Figure 2.10b show the effect in increased wall thickness on the average pressure.

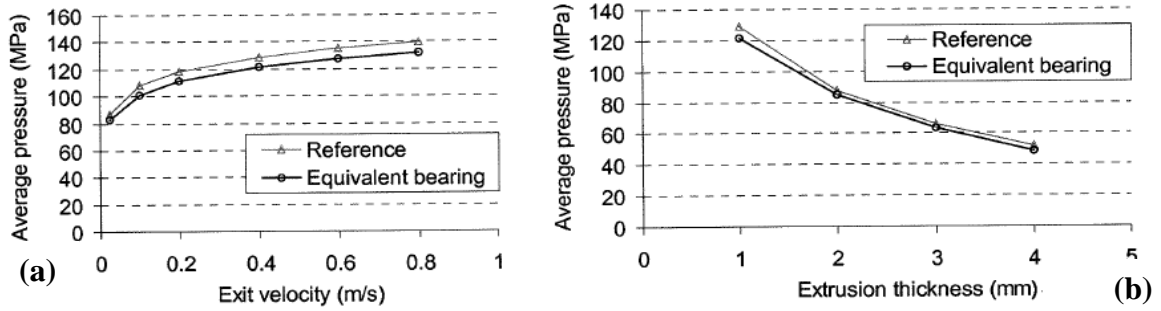


Figure 2.10 The effect increased extrusion speed (a) and increased wall thickness (b) on the average pressure, Lof (2000)

Lof (2000) proposed an equation to optimise the influence of the sink in on the flow resistance, equation 2.33. The basic idea of this equation is that the resistance in the bearing can be expressed as a pressure in front of the bearing. It is assumed that effects which influence the exit velocity can be described with this equation. The total average pressure  $\Delta P$  can be described as the sum of the influence of the wall thickness  $P_t$ , the effect of the sink in dimensions  $P_s$  and the effect of the distance to the container wall  $P_d$ . The average pressure is an equivalent pressure since the parameters have no unit. The total average pressure  $P$ , according to Lof (2000) can be described as:

$$\Delta P = P_t + P_s + P_d \quad (2.29)$$

The term to describe the effect of the profile thickness is:

$$P_t = C_1 t^{-n_1} \quad (2.30)$$

The term to describe the influence of the sink in is:

$$P_s = C_2 S T^{n_2} O^{C_3 T^{n_3}} \quad (2.31)$$

The term to describe the influence of the distance to the container wall is:

$$P = C_3 R_t^{n_4} \quad (2.32)$$

The total average pressure  $P$ , according to Lof (2000) can be described as:

$$P(O, R_t, S, T) = C_1 T^{n_1} + C_2 S T^{n_2} O^{c_3 T^{n_3}} + C_3 R_t^{n_4} \quad (2.33)$$

$P$  is the average pressure,  $O$  is the offset of the sink in,  $S$  is the sink in depth,  $R_t$  is the distance from the container wall,  $C_1, C_2, C_3$  are constants and  $n_1, n_2, n_3, n_4$  are tensors to be determined by means of simulations in combination with extrusion trials. If one would need to reduce the extrusion speed locally at the position of a bigger wall thickness, one could do this by reducing the offset of the sink in. This will have an increased effect on the average pressure. In practice, the control of the flow has been achieved by varying the length of the bearings. The length of the bearing is usually adjusted to compensate for variations in velocity. The disadvantage of this method is that it can contribute to local temperature increase caused by friction. In this research the effect is investigated of variations to the depth of the sink if applied to complex and wide solid sections with relatively small wall thicknesses. The offset of the sink in and the bearing geometry is kept the same.

## 2.2.2 Optimisation of hollow die extrusion

Extrusion of hollow sections is a complex process. Figure 2.11 gives a schematic representation of the material flow across the bridges of the hollow die core. Figure 2.11 shows all the important features of hollow die extrusion. The material flows through the feeder holes across the die bridges and welds in the welding chamber just in front of the bearing where the inside of the profile is formed.

Figure 2.11 shows the importance of the bridges since they will position the core in the die. Figure 2.12 shows an expanded view of the deflection area in the core when a load is applied.



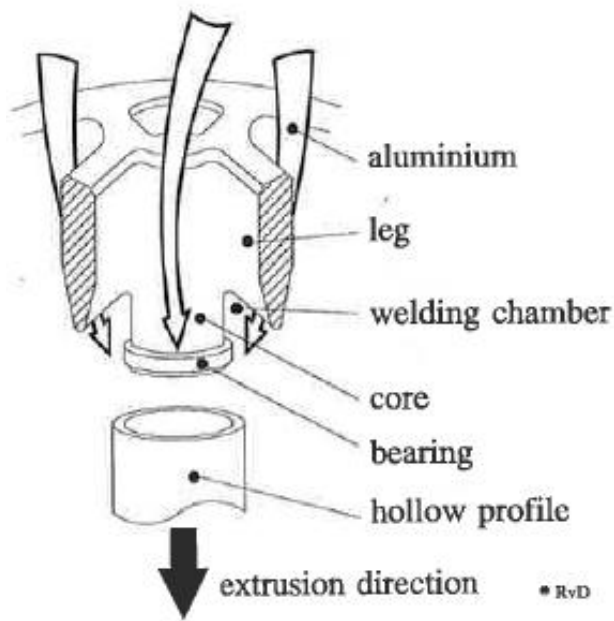


Figure 2.11 Representation of the bridge geometry in a die core, Mooi (1996 pp4)

Optimisation of hollow die extrusion requires control of the deflection of the die core.

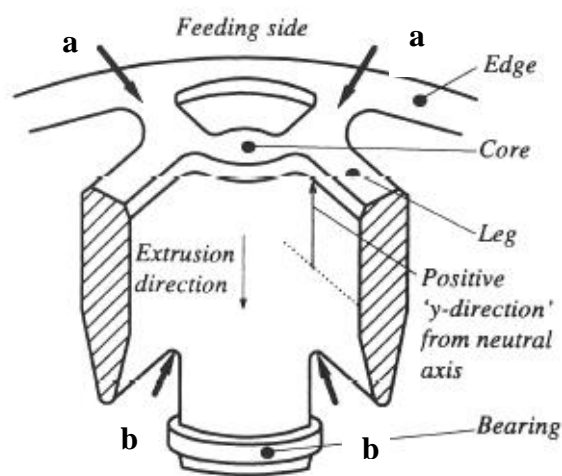


Figure 2.12 shows two deflection regions when a load is applied.

The first region is indicated by Figure 2.12a. This is the deflection region where the bridge is connected to the edge of the die. This area can be found at the position of all the bridges.

Figure 2.12 Arrows indicate deflection points when a load is applied (Mooi 1996 pp4)

Figure 2.12b shows the second area where the die bridge is pointed and the material welds. Figure 2.12 shows the cross section of a traditional bridge shape. Figure 2.13 shows the deflection, if a load is applied on a die core, Mooi (1996). This data is acquired from practical tests when a load is applied to a core and the deflection is measured. Figure 2.13 shows two steps in the deflection. A step in deflection can be seen where the bridge is connected to the edge and where the bridge is connected to the core.

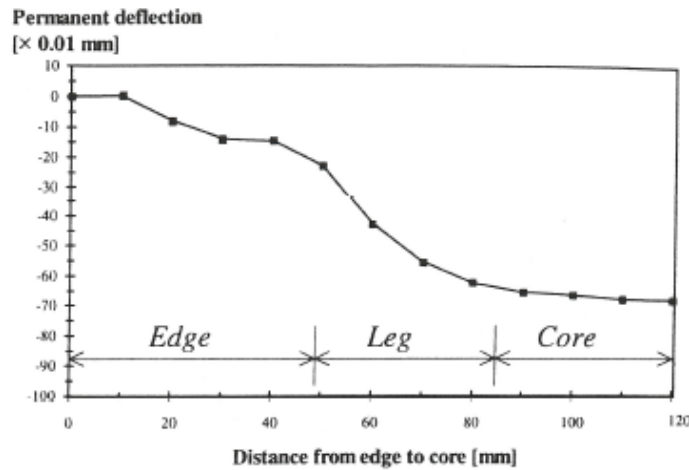


Figure 2.13 Deflection of the core as a function of the distance to the edge, (Mooi (1996))

The shape factor influences the strength of the construction. The resistance to bending is increased if material is “moved “to the outer “fiber” of the construction. Figure 2.14 shows two different bridge shapes.

Figure 2.14 shows two different bridge shapes (a) torpedo bridge shape and (b) traditional bridge shape including all relevant dimensions and the extrusion direction. The difference in the two geometries can be illustrated by the narrow tip at the welding point of traditional bridge shape in Figure 2.14b. The torpedo shape bridge is wider at the welding point which increases the resistance to bending because of the shape factor. Figure 2.14 shows the mass moment of inertia values for both geometries. The total height of the torpedo shaped bridge is 5mm less than the traditional bridge.

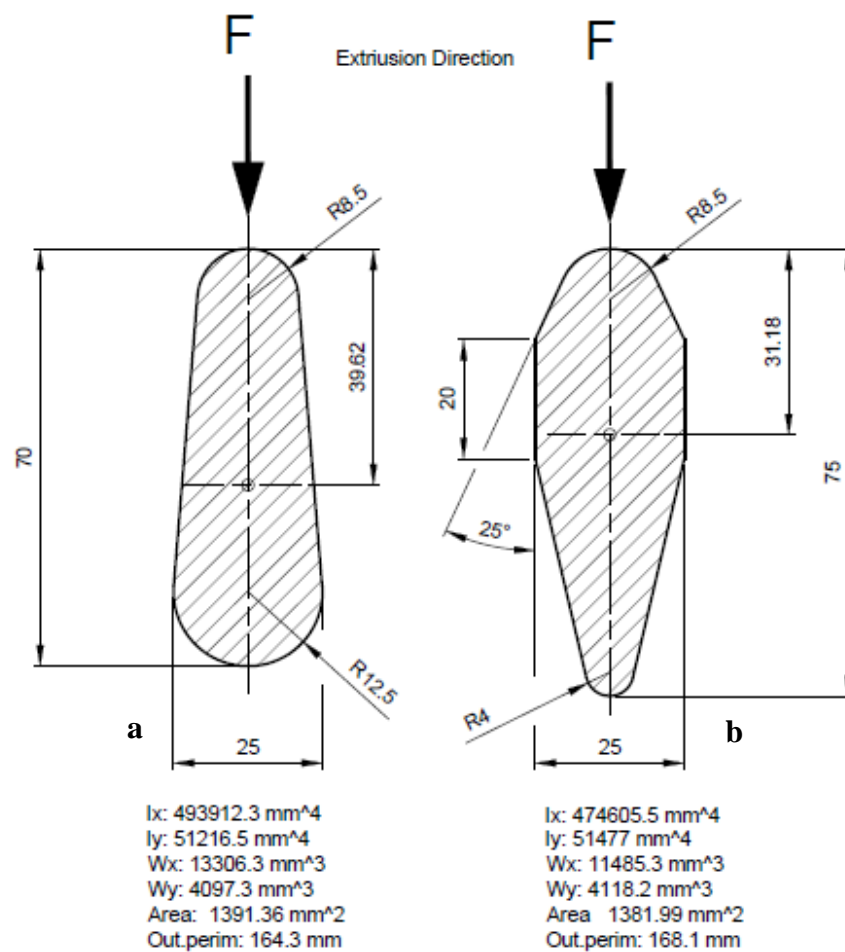


Figure 2.14 Two bridge shapes (a) torpedo bridge shape and (b) traditional bridge shape

The traditional shape of the bridge has a feed angle of 10 – 20° and a small nose radius, (Figure 2.14b). This should allow welding to take place just behind the bridge, Castle et al. (1988), Ingraldi (1992), Robbins (1996). But as dead metal zones form behind the bridges the flow path of the aluminum is not equal to the shape of the bridge. The final geometry of the torpedo shaped bridge will affect the average pressure.

Lof (2000) has investigated the effect of the height of the welding chamber and the effect of the diameter (width) of the torpedo shaped bridge on the average pressure. If the height of the welding chamber ( $w$ ) is increased the average pressure is reduced (Figure 2.15a). If the diameter  $d$  of the torpedo shaped bridge is increased the average pressure will also increase.

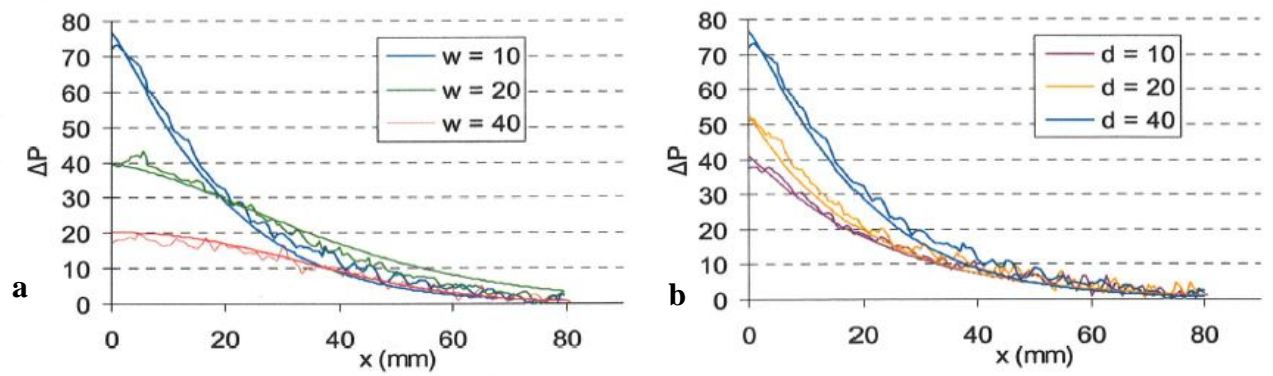


Figure 2.15 the effect of the welding chamber (a) and the diameter of the torpedo shaped bridge (b) on the average pressure (MN/m<sup>2</sup>)

Material flow will result in the formation of dead metal zones. Dead metal zones form behind the bridges and the flow path of the aluminum is not equal to the shape of the bridge. The traditional bridge shape is expected to generate a smaller dead metal zone than the torpedo shaped bridge.

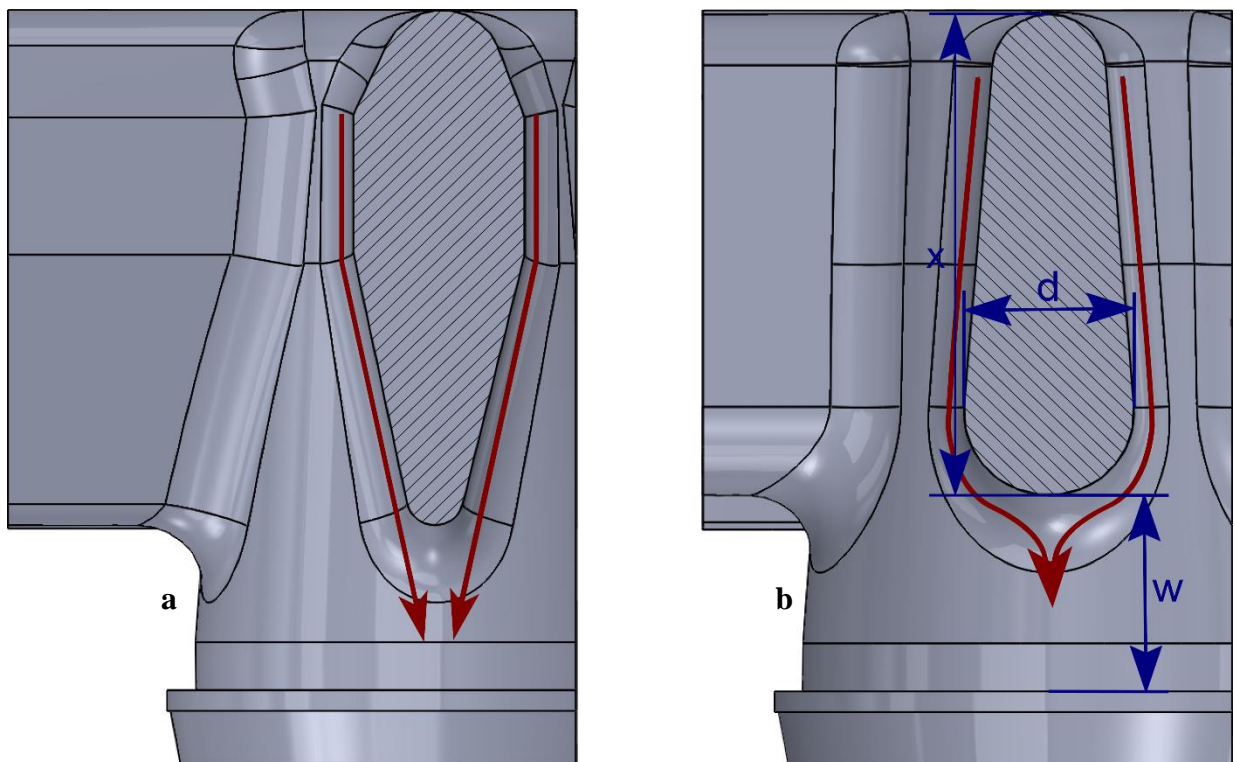


Figure 2.16 Schematic representation of possible material flow for the traditional bridge (a) and the torpedo shaped bridge (b)

The lower height of the torpedo shaped bridge increases the welding chamber allowing for a larger dead metal zone, Figure 2.16. In this research the effect is investigated of varying bridge shape whilst maintaining comparable static values and comparable dimensions for the welding chamber and the feeder holes. In the simulations two bridge shapes are compared. The first geometry is a traditional shape which follows the shape given in Figure 2.16a. The second geometry is a torpedo shaped bridge design which resembles the geometry which is represented in Figure 2.16b.

### **2.2.3 Extrusion process optimization**

Dies with unsuitable designs can lead to poor productivity and insufficient product specifications. Defects such as tearing, pick up and distortions can also occur. In hollow section dies the welding conditions strongly affect productivity. Process conditions such as billet temperature and extrusion speed influence the effectiveness of the extrusion process. The process which needs to be optimized can be expressed using a limit diagram. Hirst and Ursell (1958) were the first researchers who investigated limiting factors of the extrusion process. They proposed a graphical representation consisting of loci showing the pressure limit and the surface quality acceptance criterion. Such graphs became known as Limit Diagrams. Many researchers build upon the first version of the proposed limit diagram. Critical process parameters can be considered in relation to process limitations such as extrusion speed and surface quality. The limit diagram can be expanded to include other influencing factors such as volume fraction recrystallised, subgrain size, grain size and toughness. Examples of limit diagrams are given in Figures 2.17 and 2.18. The application of limit diagrams has been extended to more complex relations. Figure 2.17 show a limit diagram with a limitation for subgrain size and fracture toughness as a fracture toughness line, Sheppard (1999a). Figure 2.18 show a limit diagram by Parson et al. 1992.

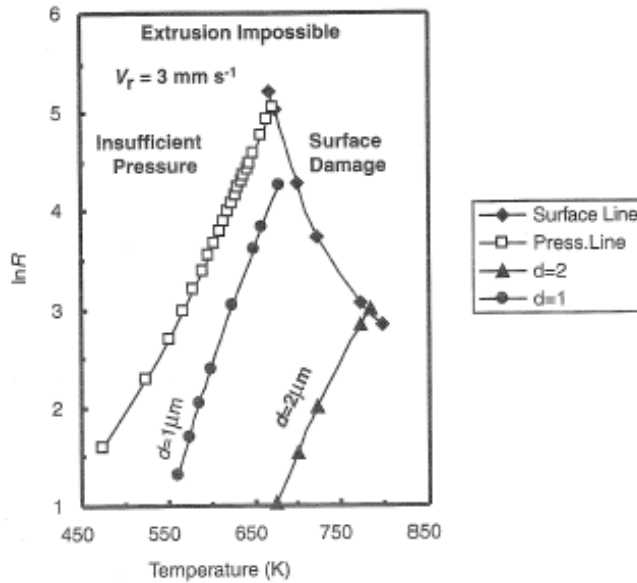


Figure 2.17 Limit diagram with optimum subgrain size for fracture toughness as a fracture toughness line Sheppard (1999a)

The process capability is plotted against a section temperature-production rate diagram. Hirst and Ursell (1958); Sheppard and Raybould (1973); Parson (1992); (Clode 1992) and Sheppard (1999a) have stated that this enables one to distinguish the main limitation parameters of the extrusion process.

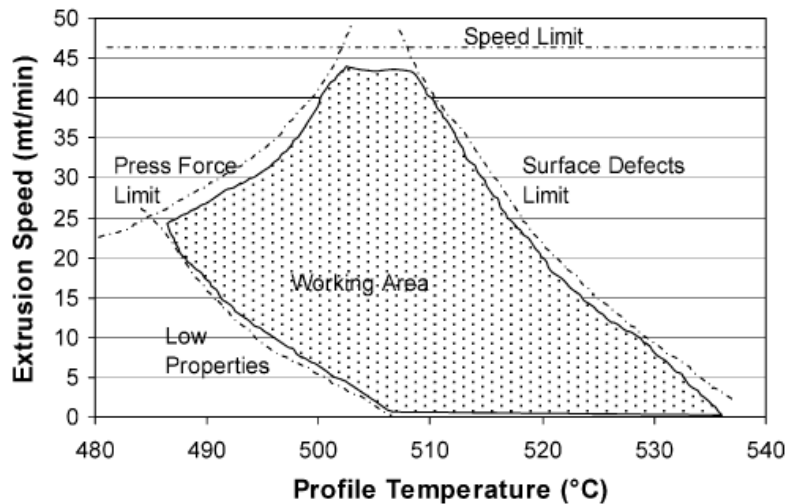


Figure 2.18 Limit diagram according to (Parson et al. 1992)

In Figure 2.21 the following limitations can be observed; pressure requirements and speed limits, mechanical properties and surface defects. These limits cannot be attributed to one single parameter (i.e. the process force limit is not only defined by press capacity alone), but can also be related to die design. The required pressure and the speed limit are mainly determined by the choice of press. Poor mechanical properties can mainly be attributed to low extrusion temperature and high speed Hirst and Ursell (1958) Sheppard and Raybould (1973) (Parson et al. 1992). Product defects however are a limitation to productivity and can be related mainly to die design. Different types of product defects may occur, tearing, pick up and poor weld. Tearing is caused by a succession of cracks which can be attributed to non-uniform speed or excessive extrusion temperature resulting in local melting of the secondary phase. (Hirst 1958) (Clode 1992) (Donati and Tomesani 2005). High extrusion temperatures can also be caused by high speed; hence the term speed cracking. Pick up is the result of adhesion between the extrusion die and the product surface. The results are usually a string of smaller deviations in the form of aligned defects. Pick up is not necessarily related to extrusion speed but often occurs at high speed prior to tearing. Poor welds are essentially related to insufficient pressure in the welding chamber. The extrusion ratio, extrusion parameters and the design of the die are the main contributors to poor welds and always have a temperature and pressure dependency. Dimensional and shape defects can mainly be attributed to die design.

The limit diagram in Figure 2.18 shows the possible working area and the zone with high productivity. Mechanical properties are limited by a critical extrusion temperature. The extrusion speed is limited by the extrusion force and the extrusion temperature. Surface defects can be controlled by controlling the extrusion temperature. For a given profile the actual working area can shift with actual die design. Donati (2005) has investigated the effect of varying feeder holes and welding chambers, thus resulting in different bridge geometries. Increased dimension of the welding chamber and the feeder hole can lead to increased output. Die design for aluminium extrusion has been, to a large extent, empirically based. This is amongst others caused by the lack of knowledge on the exact role of the different design characteristics used in manufacturing dies for the extrusion process. Low levels of automation in die design and die production, results in dies with varying design quality and poor

reproducibility. The poor predictability of the die design has led to increased testing and calibration cost since most of the dies will require a trial prior to production. For control reasons, Boal has chosen a feature based approach to die design. In this research the influence of two die features, the sink in area for solid dies and the die bridge for hollow dies, are investigated.

### **2.3 Microstructure modelling**

Observations of the structure developed by hot working have been made on a wide range of materials deformed either by forging, rolling, extrusion, compression, and torsion tests (Jonas, Sellars and McQueen 1969); (Nes et al. 1994); (Sheppard and Wright 1979); (Tibbetts and Wen 1998); (Van Geertruyden et al. 2006); (Zhu and Sellars 2001). In general, the results obtained using different modes of deformation are in good agreement and they indicate that there are two broad groups of metals and solid-solution alloys which may behave differently under hot working conditions. Aluminium and aluminium alloys, commercial-purity  $\alpha$ -Fe and ferrite alloys are observed to develop sub grains during deformation when specimens are cooled rapidly after either small or large amounts of deformation. The structural changes during hot working of this group of metals are similar to those during creep, and where activation energies have been observed to remain nearly constant over the whole range of strain rates and temperature, (Jonas et al. 1969).

The work in the present study concentrates on deformation of aluminium alloys and the microstructure evolution during the process which is dynamic recovery and recrystallisation after the process. Since the beginning of 1990's, much progress has been made in computer modelling of microstructure evolution during the hot deformation process. Excellent reviews of modelling of static recrystallisation (SRX) have been given by researchers (Doherty et al. 1997). There are several approaches to modelling microstructure evolution in hot deformation and subsequent annealing, the most commonly used methods include: (a), empirical methods (b), network methods (Humphreys 1992) (c), statistical methods (Crotaz et al. 2002) (d), physically based state variable methods (Grong and Shercliff 2002); (Sellars and Zhu 2000); (Sheppard and Duan 2002); (Peng and Sheppard 2004).



### **2.3.1 Development of structure during extrusion**

In forming processes such as extrusion complex shapes are produced at elevated temperatures. Recrystallisation involves the nucleation and growth of strain free grains in certain areas of the material, which grow by subgrains rotation to form other subgrains until they reach an orientation angle of  $15^\circ$  and they form grains. Materials which form the surface and subcutaneous layers of an extrudate experience large deformations when they traverse the die land. Deformation during extrusion leads to the existence of various metal zones. These metal zones and the dead metal zone in particular cause the distribution of structure to be inhomogeneous. Static recrystallisation has a significant influence on properties of the extrudate. As a consequence of the inhomogeneous structure, the recrystallisation and in particular the nucleation and growth will differ at various locations. In order to ensure optimum mechanical properties the EN AW-6082 alloy is usually solution treated during the extrusion process and aged subsequent to the extrusion process. Static recrystallisation has a significant influence on many of the properties of the extrudate. In this alloy, the desired structure after solution soaking is usually one exhibiting as little recrystallisation as possible. Material extruded at a temperature less than  $350^\circ\text{C}$  which is not likely fully solution soaked, will result in a completely recrystallised structure after solution soak. While high temperature extrudates appear to have retained much of the original structure, Sheppard and Tutchter (1980). The mode of recrystallisation in the extrudates, elongated in the extrusion direction, is due to the pinning of the grain boundaries by second phase particles. During the extrusion and soak cycle, the stored deformation energy within the extrudate ensures that some static recrystallisation occurs after the extrusion and during the soaking process. This static recrystallisation can extend to 100% of the material in some cases. Damage tolerance, fatigue crack propagation and corrosion, which are important features in structural applications of EN AW-6082 material, are significantly affected by the recrystallisation grain size and by the volume fraction recrystallised. The term recrystallisation temperature is in fact misleading as recrystallisation occurs over a range of temperatures. The recrystallisation temperature may be defined as being the temperature at which recrystallisation is complete (or completed to a percentage). There is no such thing as a single recrystallisation temperature. The recrystallisation temperature depends on the subgrain size obtained from the mechanical

working process. The structure of the extrudate is dependent on the total thermo mechanical cycle but the most important consideration in terms of properties is the subgrain size and orientation which very much determines the metal response to the solution and ageing sequence. During thermo mechanical processes at elevated temperatures, there is a competition between increasing and decreasing dislocation density in the material. Dislocations accumulate on second phase particles and grains as well as on subgrain boundaries. Hardening is the result of increasing dislocation density which is caused by deformation. During elevated temperatures dislocations eliminate each other which soften the material and at the same time are able to move freely through the material. The competition between hardening and softening mechanisms yields a dynamic equilibrium and therefore a steady state flow stress with a constant dislocation density can be observed in the material. In aluminium alloys with high stacking fault energy levels, the high efficiency of dynamic recovery is responsible for the classical nucleation mechanism for the formation of new grains which results in recrystallisation.

### 2.3.2 Empirical models for structure prediction

The inherent complexity of bulk metal forming modelling calls for a degree of pragmatism, so purely empirical models are used. Extensive experimentation is used as a pragmatic and traditional approach to describe microstructure and to capture the behaviour by empirical equations or graphs. The established empirical approach (Sheppard and Wright 1979) were the first to develop this form, (McLaren and Sellars 1992) on rolling, (Sellars 1990) to predict flow stress and subsequent recrystallisation is based on the Zener-Hollomon parameter, see equation (2.15). Flow stress in the above study is commonly described by an equation in the form of;

$$\sigma = \frac{1}{\alpha'} \arcsin h \left( \frac{Z}{Z^*} \right)^{1/n} \quad (2.34)$$

where  $\alpha'$ ,  $Z^*$  and  $n$  are material constants. Recrystallized grain size,  $d_{rex}$ , and the time to 50% recrystallisation,  $t_{50}$  (a common measure of recrystallisation kinetics), are described by power laws:

$$d_{rex} = k d_0^\alpha \varepsilon^{-b} Z^c \quad (2.35)$$

$$t_{50} = \beta d_0^\alpha \varepsilon^{-q} Z^{-r} \exp(Q_{def} / RT) \quad (2.36)$$

Where  $\alpha, \beta, k$  are constants,  $d_0$  is the initial grain size (Shercliff and Lovatt 1999), and  $\varepsilon$  is the Von Mises equivalent strain. The other parameters are empirical constants.

Other empirical models have been developed to describe:

(1) The relations between the sub grain size and grain size to processing parameters.

On the finer scale, the extrudate contains a well recovered sub grain structure whose sizes are modified by the presence of the inclusion and precipitates. The sub grain size is commonly given as reported in literature (Sheppard and Raybould 1973); (Paterson 1981); (Sellars 1990); as:

$$\delta^{-1} = A \ln Z + B \quad (2.37)$$

In which constants A and B have been given for various aluminium alloys for different forming processes, table 2.1.

Empirical equations were also given to relate the recrystallized grain size to the deformation conditions (Nes et al. 1994). Empirical models have also been combined with FEM to predict the final structure in rolling in previous studies (Sheppard and Duan 2002), (Duan 2003), (Herba and Mcqueen 2004)

Material	A	B	Process	Reference
EN AW-1100	0.0153	-0.196	Rolling	(Zaidi and Sheppard 1982)
EN AW-2014	0.096	-0.1747	Direct extrusion	(Vierod 1983)
EN AW-2014	0.085	-0.1586	Indirect Extrusion	(Vierod 1983)
EN AW-2014	0.0378	-0.5778	Direct extrusion	(Subramaniyan 1989)
EN AW-2024	0.0426	-0.6457	Indirect Extrusion	(Subramaniyan 1989)
EN AW-7075	0.023	-0.54	Direct extrusion	(Dashwood et al. 1996)

Table 2.1 Constants for equation 2.21

## (2) Volume fraction recrystallized factor

The volume fraction of a material  $X_v$  which recrystallizes in a time  $t$  during isothermal annealing produces a curve of sigmoidal shape as reported by Sheppard and Raghunathan (1989) and is consistent with the recovery, nucleation, and growth equation proposed by Johnson and Mehl and Avrami which takes the form:

$$X_v = 1 - \exp(-\beta t^n) \quad (2.38)$$

where  $\beta$  and  $n$  are constants for any fixed time and temperature conditions. Rearranging this equation yields:

$$\ln \ln \left( \frac{1}{1 - X_v} \right) = \ln \beta + n \ln t \quad (2.39)$$

## (3) Work hardening phenomena

Nes (1998) proposed various empirical equations for the prediction of proof stress. Sellars (1986) and Nes (1998) demonstrated the link between work hardening and the variation of subgrain size or the recrystallised grain size. Subsequently Marthinsen and Nes (2001) developed a physically based model.

By empirical means, a modest degree of prediction of microstructure can be achieved. For example by means of linking recrystallisation after deformation to the average process conditions. While at present this empirical methodology is applied with moderate success in industrial practice, the range of applicability and the accuracy of such predictions are limited due to the empirical nature of the microstructure models employed. Firstly, these empirical models do not disclose the underlying physical mechanisms of the microstructure evolution. Their applicability is confined within the boundaries in which they were obtained and hence they do not offer universal prediction capabilities. Secondly, they are usually of simple forms, while more complicated micro structural phenomena cannot be fully described using equations of such simple forms.

### **2.3.3 Physically-based internal variable methods**

Microstructure modelling has long been an important task for the physical metallurgist. However the complexity of industrial processing of commercial alloys had entailed the above-mentioned empirical methods and physically-based modelling with idealized alloys under controlled laboratory conditions. Until recently the great improvement of computation power, in particular the development of the Finite Element Method (FEM) and its application into metals processing made it possible for microstructural modelling to be integrated with modern Finite Element Analysis (FEA) and the results with considerable details can be extracted.

Theoretical modelling has long been an integral part of physical metallurgy applied to thermal or thermomechanical processing. This applies both to the evolution of microstructure with time or strain, and the dependence of properties on microstructure. Microstructural models attempt to describe the underlying phenomenon in terms of a small number of identifiable microstructural features (or ‘internal state variables’) (Grong and Shercliff 2002). It is widely acknowledged that a physically-based internal state variable method can predict the metal behaviour with more confidence compared to an empirical approach under conditions that have not been experimentally studied, (Chen et al. 1991); (McLaren and Sellars 1992); (Duan 2001b); (2000); (Talamantes-Silva et al. 2009); (Carron et al. 2010).

### **2.3.4 The internal state variable formalism**

Because the process conditions inevitably vary during industrial processing of metals, the internal state variable method was originally proposed to model the non-isothermal transformation behaviour. If the phenomenon of the microstructure evolution can be represented in the form of some differential equations about the state variables variation with respect to time, then using some appropriate numerical codes that have been developed and are available commercially, the process history, in principle, can be represented by these state variables whose values are calculated by integrating step-wise throughout the process.

Modelling of microstructure evolution explicitly in differential form has been the basis for most classical theories of work hardening and annealing. The internal state variables are now

physically meaningful quantities that can, at least in principle, be measured by electron microscopy (dislocation density etc.). Developments of this approach can now benefit from the recent advances in microscopy, such as semiautomatic Electron Back Scatter Diffraction (EBSD), which enables substructures to be quantified with far greater speed and precision. Differential physically based state variable models have the potential to follow complex process histories and provide a means of conveying microstructure explicitly from one processing stage to the next. Physically-based internal state variable models have been reported extensively by these research groups, Nes et al. at the Norwegian University of Science and Technology in Trondheim, Sellars et al. at the University of Sheffield, UK and Sheppard's group at Bournemouth University, UK, after establishment at Imperial College, UK). There are three separate modelling tasks: (a) describing the evolution of the deformation substructure, in particular the subgrain size, dislocation density and subgrain boundary misorientation; (b) relating substructure parameters to flow stress; and (c) predicting recrystallisation behaviour. The Trondheim group have proposed and further developed a three-parameter approach to model the metal plasticity (Marthinsen and Nes 1997), (Marthinsen and Nes 2001); (Nes et al. 2004); (Nes et al. 2005). Their result was concluded as a work hardening model during plastic deformation of FCC metals and alloys. Based on a statistical approach to the problem of thermal storage of dislocations, the model combines the solution for the dislocation storage problem with models for dynamic recovery of network dislocations and sub-boundary structures. Finally a general state variable description is obtained. The model includes the effects resulting from variations (a) stacking fault energy (b) grain size (c) solid solution content (d) particle size and volume fraction. Although the Trondheim group called their model a 'unified theory of deformation', controversy exists. Some workers Shercliff and Lovatt (1999) doubt their 'unified model' can be straightforwardly applied in a practical context because it introduces many adjustable parameters. Marthinsen and Nes (2001), (2002), later argued the large number of tuning parameters is not a problem and their model can deal with processing conditions under any combination of constant strain rate and temperature or more complex transient conditions. Paradoxically Marthinsen relies on the one set of data produced by this group to ascertain that  $\delta = A + B \ln Z$ : a misleading error which has appeared in a recognized journal.

Few researchers have adopted their model in the FE simulation. Only one paper can be found in a conference reference, Marthinsen et al. (2003), which unfortunately includes a serious error in which the formula for subgrain size is incorrectly written. It is safe to say too many adjustable parameters do hamper its wide application in its integration with FE simulation. Furthermore, it appears that any attempt to unify this theory with materials which dynamically recrystallise has not been successful.

The Sheffield group has approached hot working of aluminium alloys from a background of FE analysis of the transient nature of the deformation history in flat rolling, in terms of temperature, strain rate and strain path. Models for predicting the evolution of internal state variables such as internal dislocation density, subgrain size and misorientation between subgrains, as well as subsequent recrystallisation behaviour are developed for both constant and transient deformation conditions (Baxter et al. 1999); (Zhu and Sellars 2000). It should be noted that although great efforts have been invested by the Sheffield group to carry out experiments to get the mathematical expressions and to finally validate these models, they used an in house FEM which is not comparable with Forge in its structure prediction. They have recently begun to resolve real problems, mainly rolling (Talamantes-Silva et al. 2009); (Zhu et al. 2003).

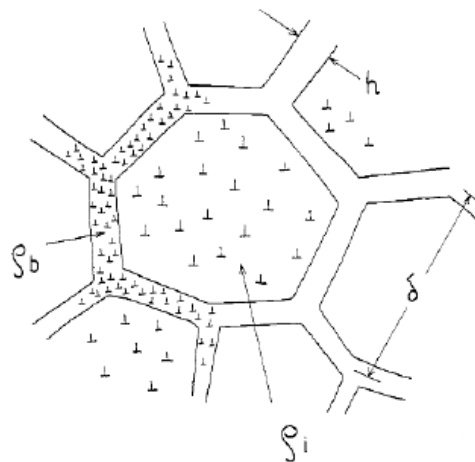
Despite the criticism that the physically based models from the Sheffield group have mainly been concentrated on a specific alloy (Al-1%Mg) and developed from experiments utilising plane strain compression (PSC), in which plastic strains greater than 2 are difficult to achieve and the interaction of recrystallisation and precipitation has not been considered in detail in the models (Jones and Humphreys 2003), the Sheffield models assisted researchers to study microstructure evolution because these models focus on the transient nature of the metal processing and they have the advantage of fewer tuning parameters which makes them more easily integrated into commercial FEM codes. Sheppard's group has done a considerable amount of pioneering work in this respect. After the success in applying these models into rolling simulation, Duan and Sheppard (2002), Sheppard and Duan (2002a) researching attention was turned to its integration with the FEM simulation of more complex extrusion process (Duan and Sheppard (2003), Peng and Sheppard (2004),

Sheppard and Velay (Sheppard 2007). In this work suitable models will be chosen and adapted for extrusion and its post treatment simulation by user-subroutine interface of the commercial FEM software Forge2009®.

### 2.3.5 Dislocation substructure evolution

Dislocation theory is an important tool to study the mechanism of metal plasticity. Dislocation substructure can be described by three internal state variables: dislocation density ( $\rho$ ), subgrain size ( $\delta$ ) and misorientation across subgrain boundaries ( $\theta$ ). To have a clear understanding of these variables, a schematic representation of substructure was taken from the literature (Nes 1997) see Figure 2.19.

During the early stage of deformation, dislocation multiplication occurs, and the total dislocation density  $\rho = \rho_i + \rho_b$  increases from  $10^8 \sim 10^{10} m^{-2}$  to  $10^{11} \sim 10^{12} m^{-2}$  at the commencement of macroscopic flow. Dislocations move and interact with one another to form tangles. This terminates in a cellular structure with the dislocations clustering tightly into the cell walls separating dislocation free region.



*Figure 2.19* Schematic representation of the microstructure; cell diameter  $\delta$ , cell wall thickness,  $h$ , cell wall dislocation density  $\rho_b$  and dislocation density within the cells  $\rho_i$ , (Nes 1997)



As deformation proceeds, dislocation density continues to increase and attains a constant value of approximately  $10^{14} m^{-2}$  when the steady state regime is reached. The cellular structures are replaced completely by the formation of subgrains due to the additional dislocation reactions. Subgrains can be regarded as an extension of a cellular structure in that the dislocations are arranged in the form of planar networks in subgrain boundaries, while the cellular boundaries consist of three-dimensional network and tangles of dislocation. The ability to form a cellular or subgrain structure depends on several factors: the stacking fault energy, the applied stress, the strain, the temperature and the presence or absence of obstacles.

A notable feature of subgrains is they are equiaxed and maintain their equilibrium size and shape in the steady state even at very large strains whereas the grains are always elongated in the direction of the extension. There are two interpretations for this phenomenon. The first considers that sub-boundaries are constantly migrating in such a way as to keep the substructure equiaxed. The second possible interpretation is by the repeated unravelling of the sub-boundaries and the subsequent reformation of new sub-boundaries at locations which keep their average spacing and dislocation density constant, termed ‘repolysionisation’ (Jonas et al. 1969).

### **2.3.6 Dislocation density evolution modelling**

For steady state deformation a generally accepted equation that represents the relation between the internal dislocation density and subgrain size is written as:

$$\rho_i^{\frac{1}{2}} \delta = C \text{ (constant)} \quad (2.40)$$

It was first proposed by Holt (1970) who showed the relationship to be valid by integrating results from other researchers. Holt proposed a method for the calculation of the dislocation density at steady state deformation. Different dislocation evolution models can be found in different work-hardening models such as the Mechanical-Threshold-Strength (MTS) model, the Microstructure Metal Plasticity (MMP) model and the Three Internal Variable (3IV) model reviewed by Holmedal et al. (Hirsch 2006).

But their purpose is to try to find a flow stress formulation that can include effects due to variations in solid solution level, particle contents, grain size, etc. from a microstructure view point, which inevitably involves many tuning parameters. The difficulty is increased in this problem because some of the parameters are not as yet defined so an intelligent guess must be utilised.

Sellars and Zhu's model (Baxter et al. 1999); (Sellars and Zhu 2000); (Zhu et al. 1997); which is developed from an FE background and doesn't have a large number of tuning parameters seems more suitable to be integrated with FEM. In their model, the internal dislocation density  $\rho_i$  has two components, that is, the so-called 'random' dislocation  $\rho_r$  and the 'geometrically necessary' dislocation density  $\rho_g$

$$\rho_i = \rho_r + \rho_g \quad (2.41)$$

The literature does not explain adequately how  $\rho_i$  and  $\rho_g$  can be calculated. The one attempted analysis was found not to be reproducible. Therefore in this work we should use equation 2.35 for the internal dislocation density. (Sellars and Zhu 2000).

### 2.3.7 Subgrain size modelling

It is generally accepted that the subgrain size  $\delta$  can be directly related to the temperature-compensated strain-rate or Zener-Hollomon parameter,  $Z$ , by the following equation

$$\delta_{ss}^m = A + B \ln Z \quad (2.42)$$

where  $A, B, m$ , are constants.

A good subgrain size fit could be obtained by varying exponent  $m$  within a range between -1.25 and -0.35 (Zaidi and Sheppard 1983). In fact, many researchers (Castle 1992); (Chanda et al. 2000); (Subramaniyan 1989); have chosen  $m = -1$  to produce accepted results.

This is because obtainable subgrain size ranges, under hot working conditions, are very small when compared with the total subgrain size range. It should also be emphasized that equation (2.26) is not valid for prediction of subgrain size in a transient deformation. In contrast with the well recognised relationship for subgrain size during steady-state deformation, there is still a lack of quantitative relationship to relate the subgrain density with the deformation parameters in transient deformation. Nevertheless, the Trondheim group (Marthinsen and Nes 1997) and Sheffield group (Sellars and Zhu 2000); (Zhu et al. 1997) have proposed their equations respectively to model the subgrain size evolution during transient state deformation. The Trondheim group approached the subgrain size problem including the effects of different microstructures which naturally need corresponding parameters to describe. As a result, to use this model those parameters must be derived from experimental data or from reasonable estimation, which greatly increased the difficulty in its integration with FEM. On the other hand, the model from the Sheffield group is calculated from a background of elementary analysis of the transient nature of hot deformation history in terms of temperature, strain rate and strain path. In their model, the subgrain size evolution has been explicitly expressed in a differential form, so even though its physical basis is limited to some extent, using this evolution law reasonable results have been achieved in hot working simulation, at least, in rolling simulation (Ahmed et al. 2005); (Duan 2001a). However there is some lack of research into prediction of subgrain development by FEM in aluminium extrusion. The few attempts (Dashwood et al. 1996); (Duan and Sheppard 2003); carried out on this topic either used only an empirical steady state equation or were limited to simple rod extrusion. This exactly highlights that using physically-based models to simulate complex shape extrusion is of significance.

### **2.3.8 Misorientation change modelling**

Misorientation could be the least well-characterised microstructure variable probably because of the obvious experimental technique constraints. Some work concerning high purity aluminium (in rolling condition) is shown in Figure 2.20 (Nes and Marthinsen 2002) which clearly shows that the average boundary misorientation increases rapidly with strain, reaching about  $3^\circ$  at a strain of about 1. After that it remains constant up to strain as high as 4.

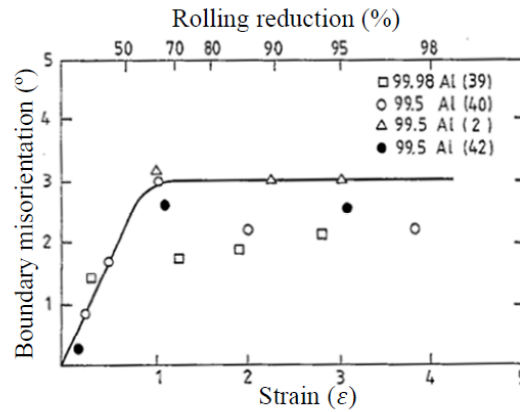


Figure 2.20 Sub-boundary misorientation vs. strain (Nes and Marthinsen 2002)

The Sheffield group (Zhu and Sellars 2000) have proposed another relationship for Al-1%Mg alloy during transient deformation conditions in differential form:

$$d\theta = \frac{1}{\varepsilon_{\theta}}(\theta_{ss} - \theta)d\varepsilon \quad (2.43)$$

where  $\varepsilon_{\theta}$  is a characteristic strain and  $\theta_{ss}$  is the misorientation across subgrain boundaries at steady state. In their study, the predicted results agree well with the experiments for the increasing and constant strain rate conditions while the discrepancy became larger during decreasing strain rate conditions. But this is not the case for extrusion; therefore, equation (2.38) has the potential to predict the misorientation.

### 2.3.9 Recrystallised grain size

Static recrystallisation can occur in extrusion after the material travels out of the die. Apart from the heavy worked outer region the substructure can be fully recrystallised, fibrous or a combination of both. Frequently the structure is a mixture of one or more of these types (Castle 1974).

In case of rod extrusion, Subramaniyan (1989) gives an empirical relationship in which the volume percentage recrystallisation is related to  $LnZ_i$ .

$$\text{Volume percentage recrystallisation} = a + b \ln Z_i \quad (2.44)$$

Where  $a$  and  $b$  are constants,  $Z_i$  is the Zener-Hollomon parameter calculated using the initial temperature:

$$Z_i = \dot{\varepsilon} \exp\left(\frac{\Delta H}{RT_i}\right) \quad (2.45)$$

Where  $T_i$  is the initial temperature,  $\Delta H$  is the activation energy for deformation,  $R$  is the universal gas constant.

Equation 2.46, can only be regarded as an approximation since the quench delay varies with the strain rate. Constants  $a$  and  $b$  vary significantly for different alloys and depend on forming conditions. Extrusion conditions such as initial billet temperature, ram speed and heat treatment have a great influence on the final structure.

The relationship between volume fraction recrystallised  $X_v$  and the holding time  $t$  is generally represented by the Johnson-Mehl and the Avrami (1939) equation. This equation predicts the relation between the volume fraction recrystallised and the holding time.

$$X_v = 1 - \exp\left\{-0.693\left(\frac{t}{t_{50}}\right)^k\right\} \quad (2.46)$$

Where  $t$  is the annealing time,  $k$  is the Avrami exponent with a commonly reported value of 2,  $t_{50}$  is the time to 50% recrystallisation. For calculation of  $t_{50}$  the physical model is generally regarded as the model revealing the mechanisms driving the transformation during recrystallisation. Sheppard and Duan (2002) have confirmed that the physical model will give better computed results than the empirical model.

### 2.3.10 Volume fraction recrystallized

In the years 1939 to 1941 Melvin Avrami (Avrami 1939), (Avrami 1940) (Avrami 1941), has attempted to describe the recrystallisation process. Since then further development has been based upon this model. In this model the recrystallised grain size is assumed to be proportional to time after incubation. The recrystallised grain size  $D_{REX}$  can be described as:

$$D_{REX} = \dot{G}(t - \tau) \quad (2.47)$$

In this equation the growth rate,  $\dot{G}$  is assumed not to change with time,  $t$  is the holding time and time after incubation is  $\tau$ . The recrystallised grain size  $D_{REX}$  is proportional to time after incubation. The nucleation rate in the non-recrystallised areas decreases exponentially with time.

The volume fraction recrystallised  $X_v$  can be described as:

$$X_v = 1 - \exp(-kt^n) \quad (2.48)$$

In this equation  $X_v$  is the volume fraction recrystallised,  $t$  is the holding time,  $k$  and  $n$  are constants. Time to 50% recrystallisation is designated  $t_{50}$ .

$$-k = \frac{\ln 0.5}{(t_{50})^n} \quad (2.49)$$

Combining (6.2) and (6.3) the most widely used Avrami equation can be formulated as:

$$X_v = 1 - \exp\left\{\frac{\ln 0.5}{(t_{50})^n} t^n\right\} = 1 - \exp\left\{-0.693\left(\frac{t}{t_{50}}\right)^n\right\} \quad (2.50)$$

According to Furu and i.e. Nes the Avrami exponent  $n$  has a value of 2 (Furu et al. 1999), (Shercliff 1997). The Avrami exponent for Al1Mn1Mg is reported to be 2.4 and for Al1Mn0.5Mg to be 1.6. These values correspond with values commonly found for recrystallisation. There would appear to be no theoretical reason why  $n$  should be alloy dependent.

### 2.3.11 Time to 50% recrystallization

The time which is required to reach 50% recrystallisation can be described by the physical model given in (2.52). It is generally regarded as describing the mechanics driving the transformation during recrystallisation. According to Vatne et al. (1996)  $t_{50}$  can be calculated using (2.52).

$$t_{50} = \frac{C_t}{M_{GB} P_D} \left( \frac{1}{N_V} \right)^n \quad (2.51)$$

In this equation  $\frac{C_t}{M_{GB} P_D}$  is considered as a constant for a given deformation and temperature and  $n$  is a constant with a value of  $\frac{1}{3}$  on the assumption that grain growth is three dimensional, Furu et al. (1999).

### 2.3.12 Grain boundary mobility

In 1864 Tresca had commenced a series of experiments designed to investigate the properties of materials in the plastic zone. From these studies Tresca proposed the yield criterion and also investigated the effect on recrystallisation of the surface grain boundary mobility  $M_{GB}$ . Tresca considered that grain boundary mobility was a thermally activated energy process. The most widely used equation, Huang and Humphreys (1999), Driver et al. (2005), for grain boundary mobility is:

$$M_{GB} = M_0 \exp\left(\frac{-Q_{GB}}{RT}\right) \quad (2.52)$$

There is some information available in literature for grain boundary mobility for super pure and commercially pure alloys containing small levels of Mn and Mg but there is no experimental data available in EN-AW 6082 alloys or any other specific alloys. Most of the attention was focussed on high purity alloys Huang and Humphreys (2000) see Table 2.2 and Driver et al. (2005) see Table 2.2. This is the case because it is more obvious to acquire quantitative and qualitative information regarding a certain solute on the grain boundary mobility and the influencing factor of the activation energy for grain boundary migration. Huang and Humphreys (1999) support the theory that such activation energy is controlled by the lattice diffusion of the solute atmosphere although they also admit that the situation may be more complex when it regards the effect of solutes on the migration of high mobility boundaries whereas Driver et al. (2005) argue that the activation energy for boundary migration is intermediate between that of solute diffusion in the lattice and along the grain boundaries.

Material	Misorientation	$M_0$ (m <sup>4</sup> /J s)	$Q$ (kJ/mol)
30C	2.6	0.0005	134
30C	3.8	0.0038	134
70C	3.7	0.0019	134
70C	4.6	0.010	134
70H	4.5	0.005	134
70H	5.6	0.028	134
All	40° (tilt)	251	152
All	40° (twist)	25	152

Table 2.2 Mobility of high and low angle grain boundaries, Huang and Humphreys (1999)

In the table 2.2, the symbol C stands for a low temperature and is 20 °C and H stands for high temperature and is 350 °C. In table 2.3, the results from Driver and et al. (2005) are given for the mobility of high and low angle grain boundaries.



		$V(\times 10^{-9} \text{ m s}^{-1})$	$P(\text{kJ/m}^3)$	$M(\times 10^{-14} \text{ m}^4/\text{J s})$	$M_0(\text{m}^4/\text{J s})$	$Q(\text{kJ/mol})$
Al-0.1 wt.% Mn	Standard Rex	141	370	38	2.71	136
	Slow Rex	3.7	370	1.0	75.33	168
	Rapid Rex	1260	370	340	-	-
Al-0.3 wt.% Mn	Standard Rex	6.6	440	1.5	0.09	135

Table 2.3 Mobility of high and low angle grain boundaries Driver et al.(2005)

In Drivers study the typical behavior of the majority of the grain boundary migration experiments is denoted ‘Standard Rex’. In some experiments the phenomenon that grain boundary migration is slower or even there is no recrystallisation at all was seen which he termed ‘Slow Rex’. Very fast recrystallisation is referred as ‘Rapid Rex. Obviously what concern us are the values about the more common ‘Standard Rex’ instead of the other two categories. However Driver’s data is only about HAGB while Huang and Humphreys’ data is more comprehensive and includes both HAGB and LAGB. Drivers HAGB results are similar to Huang and Humphreys’ mobility values of  $40^\circ \langle 111 \rangle$  representing the behaviour of ‘random’ high angle boundaries. Huang and Humphreys’ data are not similar to Sellars’ and Zhu’s (2000) estimated value of  $\frac{C_t}{M_{GB}}$ . From the information available it can be assumed that the data can be applied to EN AW-6082., Sheppard (2008).

### 2.3.13 Grain boundary surface area per unit volume

Tetrikaidecahedra have sections with good space-filling power that approximate closely to grain shapes observed metallographically, see Figure 2.21.

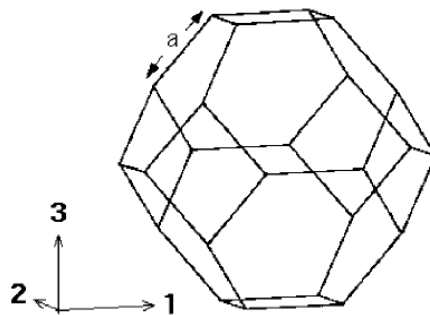


Figure 2.21 Tetrakaidecahedron, (Zhu et al. 2007)

A general deformation matrix (engineering strain)  $S$  acts on a vector  $u$  to give a new vector  $v$  as follows (Zhu et al. 2007)

$$\begin{pmatrix} S_{11} & S_{12} & S_{13} \\ S_{21} & S_{22} & S_{23} \\ S_{31} & S_{32} & S_{33} \end{pmatrix} \begin{pmatrix} u_1 \\ u_2 \\ u_3 \end{pmatrix} = \begin{pmatrix} v_1 \\ v_2 \\ v_3 \end{pmatrix} \quad (2.53)$$

According to Zhu's work, in axisymmetric tension deformation (like extrusion, wire drawing and rod rolling),  $S_{22} = S_{33}$  and volume conservation requires that  $S_{22} = \sqrt{S_{11}}$ . For the tetrakaidecahedron oriented as in Figure 6.2.

$$\frac{S_V}{S_{V_0}} = \frac{{}^{(3S_{11})/2} + \left(\frac{2}{S_{11}^2} + S_{11}\right)^{\frac{1}{2}} + \frac{1}{3} + \frac{1}{3}\left(\frac{2}{S_{11}^2} + 2S_{11}\right)^{\frac{1}{2}}}{1 + 2\sqrt{3}} \quad (2.54)$$

Where  $S_{V_0}$  is the grain surface area at zero strain.

$$S_{V_0} = \frac{3(1 + 2\sqrt{3})}{8\sqrt{2}a} \quad (2.55)$$

$$\varepsilon_{11} = \ln(S_{11}) \quad (2.56)$$

in which  $a$  is the length of the edge of the tetrakaidecahedron.

$$S_V = \frac{3(1 + 2\sqrt{3})}{16\sqrt{2}a} \{0.429 \exp(\varepsilon_{11}) + 0.571 \exp(\varepsilon_{22}) + \exp(\varepsilon_{33})\} \quad (2.57)$$

Equation 2.52 only applies for axisymmetric extrusion, which could not be used as an approximation for complex shape extrusions.

### 2.3.14 Nucleation sites per unit volume

During recrystallisation the phenomenon that the nucleation rate decreases so rapidly that all nucleation events effectively occur at the start of recrystallisation is termed site saturated nucleation (Humphreys and Hatherly 2004 , p233); (Cahn 1996). Near-site saturated nucleation applies to the recrystallisation after hot deformation of aluminium has been confirmed experimentally and applied into the modelling and simulation of its recrystallisation process (Daaland and Nes 1996; Vatne et al. 1996; Rossi and Sellars 1997; Furu et al. 1999). Most authors used compression techniques to accumulate these data but they refer to low strain rates. This theory is based upon dilute Al-Mg or Al-Mg-Mn alloys and has not been validated and calibrated in depth for EN AW-6000 series alloys nor that can it be applied to more complex deformation. But we proceed with caution. The nucleation per unit volume can be described as;

$$N_v = C_d \frac{S_v}{\delta^2} \quad (2.58)$$

Where  $\delta$  is subgrain size,  $S_v$  is the grain boundary area per unit volume,  $C_d$  is a constant which has been acquired by first using nucleation models from Vatne *et al.* (1996) and Sellars (1997) to get  $\frac{C_d}{\delta^2}$ , then substituting experimental data at a strain rate of 2.5/s to get  $C_d$ , whose value is  $1.48 \times 10^{-4}$  (Furu et al. 1999). Duan and Sheppard (2003) have used a value of  $2.6 \times 10^{-6}$  for  $C_d$  which they considered to be more suitable for extrusion simulation whilst they used 0.0004 for rolling simulation of aluminium alloy 5083 (Duan and Sheppard 2002a). Furu's values are derived from experiments on material with 1% Mg. This alloy can be related to EN AW-6082 material. The procedure of the estimation of  $C_d$  is from Vatne *et al.*'s work (1996)  $N_v$ ,  $S_v$  and  $d_{rex}$  are described as follows:

$$N_v = C_d f(\delta) S_v \quad (2.59)$$

$$S_V = \frac{2}{d_0} \{\exp(\varepsilon) + \exp(-\varepsilon) + 1\} \quad (2.60)$$

$$d_{rex} = \left( \frac{1}{N_V} \right)^n \quad (2.61)$$

Where  $f(\delta)$  is a function of subgrain size,  $d_{rex}$  is the recrystallised grainsize and  $d$  is the average grain size before deformation. Therefore at first,  $N_V$  can be achieved by the equation (2.54). Using measured  $d_{rex}$  from experiment. Secondly at a strain which is bigger than needed for the subgrain to reach a steady state (i.e. the subgrain size is a constant) when at a given strain rate, the  $f(\delta)$  and  $S_V$  would be constants, therefore  $C_D f(\delta)$  is obtained also as a constant.

Thirdly, Jonas, Sellars and McQueen (1969), calculated the steady state subgrain size  $\delta_{ss}$  at various strain rates from the empirical dependence on the Zener-Hollomon parameter  $Z$ , and suggested the following equation:

$$\frac{1}{\delta_{ss}} = A \ln Z - B \quad (2.62)$$

Where  $Z = \dot{\varepsilon} \exp\left(\frac{Q_{def}}{RT}\right)$  is the Zener-Hollomon parameter,  $\delta_{ss}$  is the steady state subgrain size, A and B are constants) to estimate  $\delta_{ss}$ ; finally a graph of  $\log(C_D f(\delta))$  against  $\log(\delta_{ss})$  was made, a relationship of  $f(\delta) = \left(\frac{1}{\delta_{ss}}\right)^2$  was assumed and, the constant  $C_D$  was determined.

### 2.3.15 Stored energy

The total stored energy per unit volume ( $U$ ) (Eshelby 1953) and later (Sellars 1997) is affected by the dislocation density ( $\rho$ ) and the energy per unit length of dislocation line ( $E$ ), and recovery can be considered to reduce stored energy as;

$$dU = Ed\rho + \rho dE \quad (2.63)$$

The first term arises from reduction of dislocation density, e.g. by growth of links and annihilation by dislocations of opposite sign. The second term arises from a reduction in energy per unit length by polygonisation, which can be simply estimated from the standard relationships for elastic energy of distributed edge dislocation (Dieter 1987).

$$E_{el} = E_o \ln\left(\frac{r_1}{r_0}\right) \quad (2.64)$$

where  $E_o = \frac{Gb^2}{4\pi(1-\nu)}$ ,  $G$  is shear modulus,  $\nu$  is Poissons ratio and  $b$  is Burgers vector.

Taking the outer cut-off radius,  $r_1$ , as  $0.5 \bar{l}$  ( $\bar{l}$  the mean link length  $\approx \rho^{-\frac{1}{2}}$ ) and the core radius as  $5b$  (Eshelby 1953); (Humphreys and Hatherly 2004), with the core energy  $\approx \frac{Gb^2}{10} \approx E_o$  (Dieter, 1987, p. 163) leads to a total energy per unit length for dislocations in the matrix. The total stored energy  $P_D$  per unit volume (Sellars and Zhu 2000) equals:

$$P_D \approx U_i + U_{sb} = \frac{Gb^2}{10} \left( \rho_i \left( 1 - \ln 10b\rho_i^{\frac{1}{2}} \right) + \frac{2\theta}{b\delta} \left( 1 - \ln \left( \frac{\theta}{\theta_c} \right) \right) \right) \quad (2.65)$$

## **2.4 FEM Modelling**

The most widely used finite element formulation in solid mechanics is the displacement approach. The displacement field within the element is defined in terms of assumed functions (interpolation functions) and unknown parameters at the nodes which are either displacements or displacement related quantities such as slopes and curvatures. For each finite element, a displacement function in terms of the element coordinates (x, y, z) and the nodal displacement parameters is chosen to represent the displacement field, and thereby the strain and stress within the element. A stiffness matrix relating the nodal forces to the nodal displacements can be derived through the application of the principle of virtual work or the principle of minimum total potential energy. The stiffness matrices of all the elements in the domain can be assembled to form the overall stiffness matrix for the system. After modifying the global stiffness matrix in accordance with the boundary conditions and establishing the force vector, the system of equations can be solved to yield firstly the nodal displacements, and subsequently the stresses at any point in each individual element.

### **2.4.1 The equilibrium equation in FE simulations**

Depending on the character of the material response to external and internal load, the material dynamics are conveniently described in terms of the ‘strong form’ of the differential equation of motion, the ‘weak form’ of the virtual work principle, or the stable equilibrium quantified by the ‘minimum mechanical energy’.

A simple straightforward approach to deriving the equations for displacement-based finite element codes starts from the general principle of virtual work. This is the work done by arbitrary small virtual displacements due to the forces and the moments acting on a solid body in accordance with continuity and displacement boundary constraints. For the most general cases this principle can be written as (Zienkiewicz and Taylor 2005, p.14):

$$\delta\widehat{W} = \iiint_v \sigma_{ij} \delta\widehat{\varepsilon}_{ij} dV = \iiint_v P_j \delta\widehat{u}_j dV + \iint_s T_j \delta\widehat{u}_j dS + \sum F_j \delta\widehat{u}_j \quad (2.66)$$

Where  $\delta\widehat{W}$  is the virtual work which results from the strain due to the virtual displacements  $\delta\widehat{\varepsilon}$  that acts on the stresses  $\sigma$ . This work equals the sum of the virtual work which results from the virtual displacements  $\delta\widehat{u}$  due to the body force  $P$ , to the surface force  $T$ , and to point forces  $F$ .  $S$  is the surface that encloses the volume  $V$ .

Equation (3.1) is generally valid for an arbitrary body. However, the finite element method decomposes the solid under investigation into a large number,  $n$ , of simply shaped volume elements which are connected at nodes. Thus equation (3.1) applies for each individual element under implicit consideration of equilibrium and compatibility. The course of the displacement is approximated in each finite element by interpolation polynomials that enter all  $n$  equations of the form of equation (3.1). This amounts to calculating the volume and surface integrals over each finite segment individually and subsequently summing up all elements. Assuming that the point forces are only applied at the nodal points, the equation (3.1) may then be rewritten

$$\sum_n \iiint_v \sigma_{ij} \delta\widehat{\varepsilon}_{ij} dV = \sum_n \iiint_v P_j \delta\widehat{u}_j dV + \sum_n \iint_s T_j \delta\widehat{u}_j dS + \sum_n F_j \delta\widehat{u}_j \quad (2.67)$$

#### 2.4.2 Finite element kinematical description

The algorithms of continuum mechanics usually make use of two classical descriptions of motion: the Lagrangian description and the Eulerian description. Lagrangian algorithms, in which each individual node of the computational mesh follows the associated material particle during motion, are mainly used in structural mechanics. The Lagrangian description allows an easy tracking of free surfaces and interfaces between different materials. It also facilitates the treatment of materials with history dependent constitutive relations. Its weakness is its inability to follow large distortions of the computational domain without recourse to frequent remeshing operations.

Eulerian algorithms are widely used in fluid dynamics. The computational mesh is fixed and the continuum moves with respect to the mesh. In the Eulerian description, large distortions in the continuum motion can be handled with relative ease, but generally at the expense of precise interface definition and the resolution of flow details.

Arbitrary Lagrangian-Eulerian (ALE) technique has been developed that, to a certain extent, succeed in combining the best features of both the Lagrangian and the Eulerian approaches. In the ALE description, the nodes of the computational mesh may be moved with continuum in normal Lagrangian fashion, or be held fixed in Eulerian manner, or be moved in some arbitrary specified way to give a continuous remesh capability. Because of this freedom in moving the computational mesh offered by the ALE description, greater distortions of the continuum can be handled than would be allowed by a purely Lagrangian method, with more resolution than that afforded by a purely Eulerian approach (Belytschko 2000, p.1(3-15); Bonet and Wood 1997, p.3.3).

### **2.4.3 Finite element discretisation and element type**

To divide the continuum or problem domain into valid finite elements is to discretise the problem domain involved. The number, size and shape of the elements are critical for a successful finite element analysis. The element should be small enough to give useful results and large enough to reduce the computational effort.

Depending on the problems studied different shapes of elements can be adopted. Basic element shapes are shown in Table 2.4. The shapes, sizes number, and configurations of the elements have to be chosen carefully such that the original body or domain is simulated as closely as possible without increasing the computational effort needed for the solution. Mostly the choice of the type of element is dictated by the geometry of the body and the number of independent coordinates necessary to describe the system.




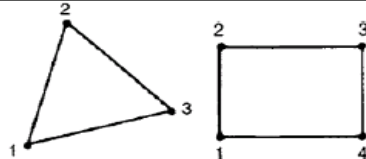
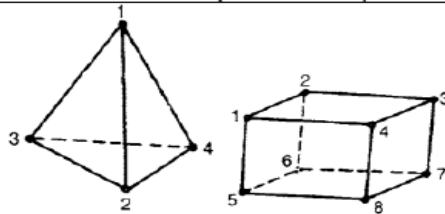
Dimension	Type	Geometry
Line (1-D)	Spring, beam	
Area (2-D)	2D solid, axisymmetric solid, plate	
Volume (3-D)	3D solid	

Table 2.4 Basic element shapes

One dimensional or line element can be used if the geometry, the material properties, and the field variable of the problem can be represented in terms of only one spatial coordinate while the configuration and other details of the problem can be described in terms of two independent spatial coordinates the two-dimensional elements can be used and likewise, three-dimensional elements have to be employed when the description of the geometry, material properties, and other parameters of the body needs three independent spatial coordinates.

#### 2.4.4 Mesh generation

Currently the most popular approaches for mesh generation are the Delaunay triangulation and the advancing front technique (Lee 2003) with the latter technique, also called the moving front method, the tetrahedral (or triangular) mesh is progressively generated by creating elements one by one. In this method an active frontal face is selected to define the position of the fourth node in order to create the best tetrahedron. This process is repeated until the whole volume is meshed. Although the advancing front technique generates very good quality meshes in terms of the element shapes, it requires a very large amount of computation time.

Therefore this technique is unsuitable for the simulation of extrusion where a large amount of re-meshing is necessary. The Delaunay triangulation generates tetrahedral (or triangular) meshes for a given set of nodes according to the Delaunay criterion (Weatherill and Hassan 1994). In this method the mesh is first generated on the boundaries of the volume (or the surface) and nodes are then inserted incrementally inside the mesh. The tetrahedrons (or triangles) are redefined according to the Delaunay criterion. Generally this method is used with specialised algorithms which force or recover the surface triangulation to match the original geometry. This is known as the ‘boundary constrained Delaunay triangulation’ (Weatherill and Hassan 1994). This is the preferred method for generating meshes for the workpiece in extrusion. The 3D geometries were modelled and meshed at the boundary using I-Deas (a CAD and FEA package). The surface meshes of the workpiece and tooling were then transferred to Forge2009® (Transvalor 2009a, 2009b). The software algorithm generated the internal mesh of the workpiece with tetrahedral elements and the surface meshes of the tooling with triangular elements.

#### **2.4.5 Mesh refinement**

Different global mesh edge lengths were defined and applied to the deformable parts (billet or feedstock). Mesh edge lengths were locally adapted depending on the local curvature. Mesh size distributions were imposed during computation by using ‘mesh boxes’. These boxes were fixed (i.e. they did not move with the material flow) and a local element length was defined within their surfaces (or volumes). As with every FEA, a fine mesh is required for those specific areas where accuracy is required. Therefore mesh boxes were implemented at die entries, die exits and sometimes at tooling boundaries. After several analyses, it was found that a minimum of four element edges should be used to define a fillet radius. It was also established that a minimum of 10 elements should be used to represent the extrudate thickness at the die land area.

#### **2.4.6 Re-Meshing**

Forge2009® (Transvalor 2009a, 2009b) automatically re-mesh the workpiece (or feedstock) at a given frequency or if the mesh has been degenerated. A mesh is considered degenerated if either some of the elements become too distorted, or if the contact surface of the workpiece does not correspond accurately to the tool surfaces. The element distortion is measured by the quality parameter,  $Q$ , in terms of the relative Jacobian between the reference element (with  $Q = 1$ ) and the distorted element. The time required to compute the numerical equations is highly dependant on the quality of the mesh. Coupez (1994) suggested that a good strategy with Forge2009® (Transvalor 2009a, 2009b) is to re-mesh as often as possible. However a good quality mesh is costly in terms of computational time and power. Therefore, to perform an efficient analysis, a compromise must be obtained between the degree of discretisation (i.e. use of mesh boxes), the frequency of re-meshing, the computing power and time available.

#### **2.4.7 Contact Conditions**

In the analyses used for this thesis the tools were considered rigid, i.e. non deformable Forge2009® (Transvalor 2009a, 2009b). The interior of the tools were not meshed and only the boundary surfaces were discretised. The number of equations to be solved simultaneously was therefore greatly reduced the mesh of the workpiece is updated at every step of re-meshing. The midpoint of each element boundary edge is tested. If a midpoint is found inside the tools then a node is created and the element is divided into two elements. Every node found inside the tools is projected onto the surface of contact by an impenetrability algorithm. Figure 2.22 illustrates this contact condition.

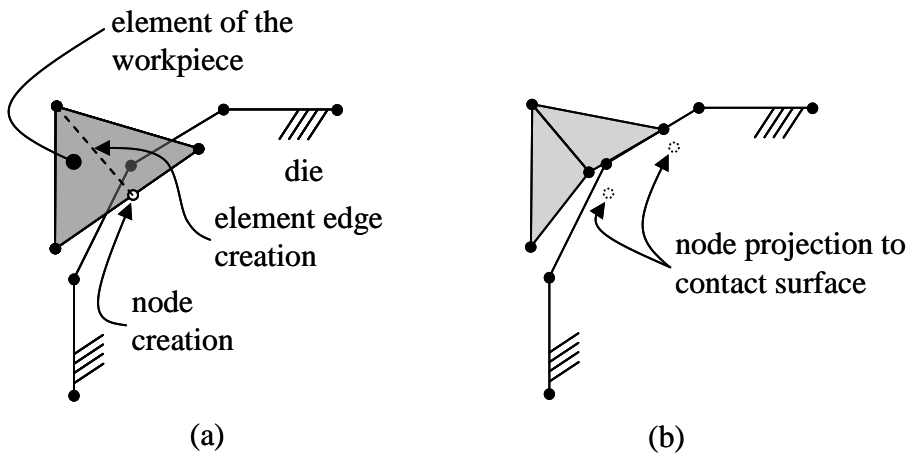


Figure 2.22(a) Midpoint penetration and (b) impenetrability algorithm

#### 2.4.8 Finite element discretisation and increment approach

The detailed theory of this topic can be found in many textbooks. Below is a concise description of it. Using isoparametric elements, the velocity field  $v$ , can be discretised in terms of the nodal velocity  $V_n$ , shape function  $N_n$  and local coordinate vector  $\xi$  as:

$$v = \sum_n N_n(\xi) V_n \quad (2.68)$$

The mapping with the physical space is defined by

$$x = \sum_n N_n(\xi) X_n \quad (2.69)$$

The strain rate tensor is computed with the help of the  $B$  linear operator

$$\dot{\epsilon} = \sum_n B_n V_n \quad (2.70)$$

The pressure field  $p$  is discretised in term of nodal pressure,  $P_m$ , with compatible shape functions,

$$p = n \sum P_m M_m(\xi) \quad (2.71)$$

For purely viscoplastic materials, the most popular scheme for nodal update can be performed with the Euler explicit scheme. Then if  $X_n^t$  is the coordinate vector, at time  $t + \Delta t$  the new coordinate vector

$$X_n^{t+\Delta t} = X_n^t + \Delta t V_n^t \quad (2.72)$$

A second order scheme was shown to improve the accuracy with a Runge and Kutta method or the semi-implicit scheme (Chenot et al. 1999):

$$X_n^{t+\Delta t} = X_n^t + \frac{1}{2} \Delta t (V_n^t + V_n^{t+\Delta t}) \quad (2.73)$$

#### 2.4.9 Microstructure modelling of aluminium extrusion

Traditionally, forming large models of systems has been via a mathematical model, which attempts to find analytical solutions to problems and thereby enable the prediction of the behaviour of the system from a set of parameters and initial conditions. While computer simulations might use some algorithms from purely mathematical models, computers can combine simulations with reality or actual events, such as generating input responses, to simulate test subjects which are no longer present. Whereas the missing test subjects are being modelled / simulated, the system they use could be the actual equipment, revealing performance limits or defects in long-term use by these simulated users. Note that the term computer simulation is broader than computer modelling, which implies that all aspects are being modelled in the computer representation. However, computer simulation also includes generating inputs from simulated users to run actual computer software or equipment, with only part of the system being modelled. Computer models can be classified according to several independent pairs of attributes, including:

- Stochastic or deterministic (and as a special case of deterministic, chaotic)
- Steady-state or dynamic
- Continuous or discrete (and as an important special case of discrete, discrete event)

Equations can be developed to define the relationships between elements of the model when the system is in equilibrium. Such models are often used in simulating physical systems, as a simpler modelling case before dynamic simulation is attempted. Dynamic simulations model changes in a system in response to (usually changing) input signals. Stochastic models use random number generators to model chance or random events; a discrete event simulation (DES) manages events in time. Most computer, logic-test and fault-tree simulations are of this type. In this type of simulation, the simulator maintains a queue of events sorted by the simulated time they should occur. The simulator reads the queue and triggers new events as each event is processed. It is not important to execute the simulation in real time. It's often more important to be able to access the data produced by the simulation, to discover logic defects in the design or the sequence of events. A continuous dynamic simulation calculates numerical solutions to differential equations or differential equations. Periodically, the simulation program solves all the equations, and uses the numbers to change the state and output of the simulation.

#### **2.4.10 Finite Element Model**

The finite-element method originated from the need for solving complex elasticity and structural analysis problems in civil and aeronautical engineering. While the approaches used by these pioneers are dramatically different, they share one essential characteristic: mesh discretization of a continuous domain into a set of discrete sub-domains, usually called elements.

The finite element method (FEM) (sometimes referred to as finite element analysis (FEA)) is a numerical technique for finding approximate solutions of partial differential equations (PDE) as well as of integral equations.

The solution approach is based either on eliminating the differential equation completely (steady state problems), or rendering the PDE into an approximating system of ordinary differential equations, which are then numerically integrated using standard techniques such as Euler's method, Runge-Kutta, etc. In solving partial differential equations, the primary challenge is to create an equation that approximates the equation to be studied, but is numerically stable, meaning that errors in the input data and intermediate calculations do not accumulate and cause the resulting output to be meaningless. There are many ways of doing this, all with advantages and disadvantages. The Finite Element Method is a good choice for solving partial differential equations over complicated domains when the domain changes (as during a solid state reaction with a moving boundary), when the desired precision varies over the entire domain, or when the solution lacks clarity.

The FEM software Forge2009® that is developed by Transvalor, a French company, and incorporates Forge®2 and Forge®3 is selected to be used in this research, because it has the ability to simulate thermo-mechanically coupled large deformation both in 2D and 3D, to re-mesh the FEM model automatically, to calculate the evolving contact and frictional interfaces and complicated temperature evolution, and most importantly, its user-subroutine interface offers users flexibility to incorporate their own material and structural evolution models into it. The procedure for a finite element analysis (FEA) has been well established and can be seen in many books (Reddy 2006); (Zienkiewicz et al. 2005). Reddy (2006), p.105, summarised the basic steps of an FEA as follows:

- 1) Discretisation (or representation) of the given domain into a collection of preselected finite elements (This step can be postponed until the finite element formulation of the equation is completed);
- 2) Derivation of element equations for all typical elements in the mesh;
- 3) Assembly of element equations to obtain the equations of the whole problem;
- 4) Imposition of the boundary conditions of the problem;
- 5) Solution of the assembled equations;
- 6) Postprocessing of the results.

#### **2.4.11 Thermal-mechanical process modelling using the Finite Element Method**

The simulation calculation of an extrusion sequence in an industrial environment consists principally of a thermo-mechanical analysis of the plastic deformation. Chenot pioneered the development of the Forge software which became a successful product for the simulation of forming processes (Chenot and Chastel 1996). Deform is also one of the main commercially available simulation software packages, however Ansys, despite its nonlinear functionality, is more suitable for generic nonlinear simulations. Huetink developed DIEKA which is used more as a research software. Modelling of thermo-mechanical processing of metals is one of a number of industrial modelling activities which has been reviewed in response to the technology foresight exercise (Shercliff 1997). This illustrated the breadth of industrial processes and alloys for which there are common underlying challenges in process modelling (Shercliff and Lovatt 1999). Modelling of thermo-mechanical processing of metals is one of a number of material modelling activities. The Finite Element Method is a general numerical means of obtaining approximate solutions in space-to-boundary and initial-value problems. It is based on generating the governing differential equations and the discrete algebraic counterparts of the problems under investigation using a variation formulation, the development of the state variable being approximated by appropriate interpolation functions. The application of numerical techniques to the continuum mechanics problem, developed over the last three decades (Iwata et al. 1972); (Liversley 1983); (Reinikainen et al. 1994). Schickora et al. (2008) has improved the capability for an integrated treatment of both tool-load demands and internal micromechanics.

Currently, computer modelling and simulation of the material forming process has been developed to the point where it may be used to solve industrial problems. Computer modelling is often treated as a universal tool in all problems of metal forming processes. Taking a general view of the present state of the art in terms of numerical modelling, it appears that the finite element method is most suited to the three-dimensional analysis of material forming processes. In fact the finite element method can take into account practical non-linearity in the geometry and material properties, besides producing accurate



predictions of stress, strain, strain rate and temperature throughout the deforming billet (Chanda et al. 2000); (Chenot and Chastel 1996); (Duan and Sheppard 2003); (Flitta et al. 2007); (Kobayashi et al. 1989). For many deformation processes, there is a view that continuum mechanics FEM is well established, both for simulating the manufacturing process itself and the less obvious task of modelling the 'standard test' used, for example, to determine constitutive behavior, Sheppard and Wright (1979). The greatest limiting factors at the continuum level in all metal-forming analyses are poor characterization of interfacial friction conditions (and to a lesser degree heat transfer), and the need for improved models of material constitutive behavior for complex deformation histories and for heterogeneous materials (Shercliff 1997).

### 3 Experiments

This chapter outlines the experimental processes used to perform the investigation. These processes and techniques include the extruded material, the dies and comments on die design. The extrusion press and instrumentation are described as well as the techniques and methods which are used in investigating the extruded sections.

#### 3.1 The extrusion press

The experiments were performed on a 5MN hydraulic horizontal press at BOAL Finex B.V. in the Netherlands. The extrusion ratio was approximately 26:1 for the rectangular section, 38:1 for the U-shape section and 42:1 for the tube section. Process parameters were varied following a constant set of parameters. The ram speed was set at 6mm/s, 12mm/s and 22mm/s. The initial billet temperatures were set at 480°C, 500°C and 520°C. The temperature of all dies was 450 °C. The billet length was 250mm and the diameter was 90mm.



*Figure 3.1* The press used in the experiments

These parameters were selected by the investigator who had special knowledge of the press and were meant to ensure minimum recrystallisation. Extrusion parameters were recorded during the experiments. Figure 3.2 show a cross section of the essential parts of the press with highlight to the most important parameter measurements. The pressure was recorded on the control console transducer attached to the main cylinder. It recorded the actual pressure in bar. The billet temperature was measured by means of contact thermo-couples in the billet oven. The exit temperature of the extruded profiles in the experiments were measured and recorded by means of a contactless Pyrometer which uses a dual wave infra-red signal. The pyrometer is made by 3T in Israel. The temperature readings were taken very close to the front plate where the material exits the press (T-exit). The distance between the measuring point and the die exit is 35cm. In the press mouth the temperature drop is very small because of the insulation of the front-plate. The extrusion speed usually allows the temperature readings to take place within one second after leaving the die. The temperature at this point will be very close to the temperature at die exit. In the day to day practise of extrusion the extruded sections are guided by a puller system for transport from the run-out to the table.

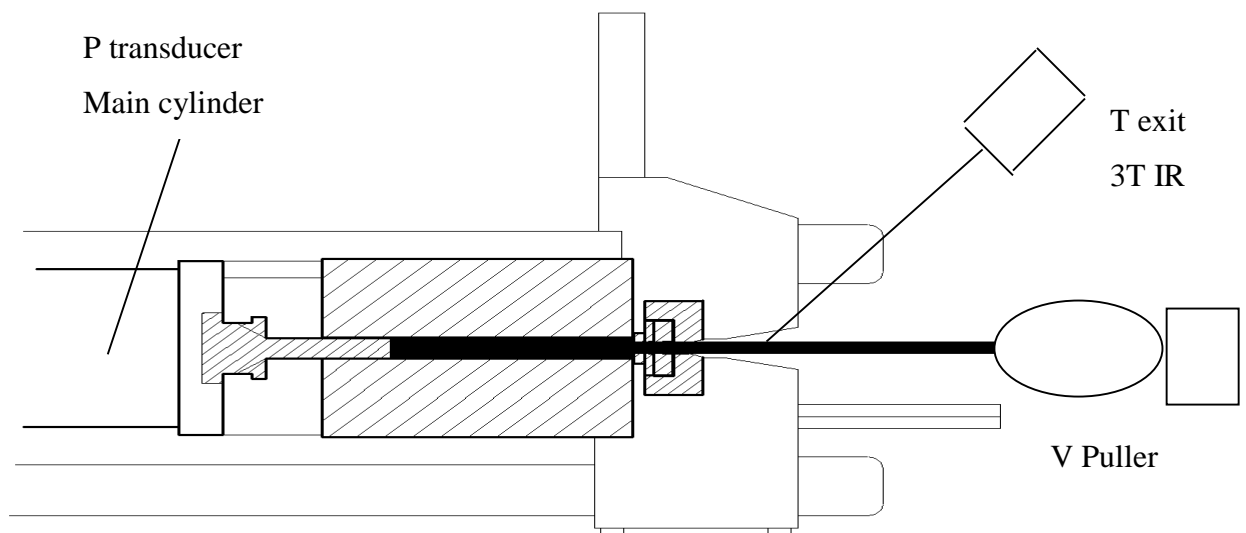


Figure 3.2 Schematic overview of the press with the measurement instruments

The position at which the exit temperature readings were taken is also the sample taking position. The gas heated billet oven which is commonly used does not allow for fast temperature variations. Therefore a compact convection oven was used to heat the billets to the required temperature, (within max 10°C variation). The billets were manually introduced to the mechanical billet conveyor system. From this point material handling was performed automatically according to the parameters set on the press. On the table the profiles were guided by means of a puller with 20-100N puller force. At the beginning of the table the sections were stretched. The extrusion speed was recorded by means of a speed and position measurement system which is attached to the puller.

### 3.2 Material

Table 3.1 gives the chemical composition of the materials used in the experiments.

Element	Concentration %
Si	0.90 - 1.14
Fe	0.15 - 0.25
Cu	0.05 - 0.10
Mn	0.40 - 0.54
Mg	0.60 - 0.74
Cr	≤ 0.05
Zn	≤ 0.14
Ti	0.005 - 0.054
Pb	-
B	≤ 0.001
<b>remainder</b>	
per element	≤ 0.05
total	≤ 0.15

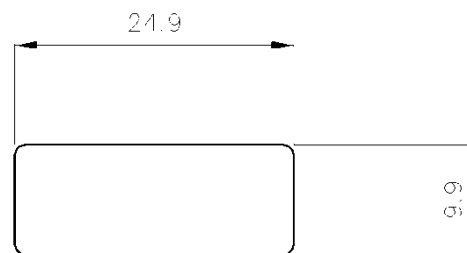
*Table 3.1* The alloy composition used in the extrusion trials

The material used is an alloy from the EN AW-6082 alloy range. The material was produced by Alsinta in Taiwan and homogenised. The composition of the alloy meets the

internal criteria for the alloy specification BC68 used at the BOAL Group. This alloy is commonly used for the extrusion of both hollow and solid sections at the extrusion presses in the BOAL Group. Table 3.1 gives the alloy composition used in the experiments. The material received a homogenizing heat treatment prior to extrusion at 580°C for 4 hours and was cooled by forced air to room temperature. The homogenizing heat treatment is generally performed to create a suitable structure for extrusion by re-distributing alloying elements, precipitates and inter metallic phases.

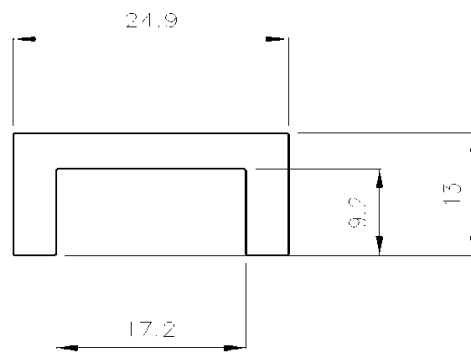
### 3.3 Extruded sections

There are three different profile geometries used in the experiments. The three different geometries are a rectangular section, a U-shaped section and a tube section. These geometries are selected for the experiments because they represent a cross section of geometries used in the practice of extrusion today.



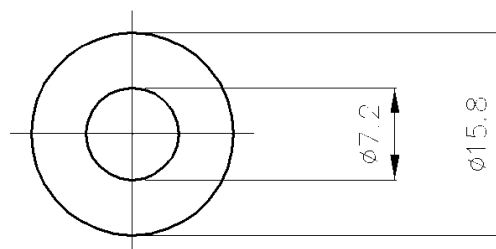
*Figure 3.3* Rectangular profile (dimension in mm)

The rectangular section, figure 3.3, is selected because it is likely to be extruded at a high extrusion speed. It is also relatively easy to take samples to allow for structure investigations but to reach solutionising temperature the billet temperature needs to be relatively high compared with the exit temperature. Because of the simple solid geometry the temperature rise during extrusion is relatively low. Potential variation in microstructure over the cross section of the sample can be observed with the selected sample dimensions.



*Figure 3.4* U-shaped profile (dimension in mm)

The U-shaped section, figure 3.4, is selected for the experiments because it has a small wall thickness and the legs of the U-shape are very sensitive to surface defects caused by variations in the extrusion speed or the extrusion temperature. Section complexity (i.e. level of details and surface to volume ratio) results in high temperature rise due mainly to friction. Good control of the extrudate temperature is critical for surface quality.



*Figure 3.5* Tube section (dimension in mm)

The tube section, figure 3.5, is selected because in practice hollow sections are widely applied. Hollow sections require a different die design. The die will consist of two parts a core and a plate to allow for the inner and outer part of the profile to be formed. During extrusion the material has to shear to flow across the web and subsequently weld in the welding chamber to form a closed hollow section. This complex flow process during extrusion will contribute to temperature increase of the extrudate. Hollow sections such as the tube are therefore very sensitive to variations in extrusion temperature and extrusion speed.

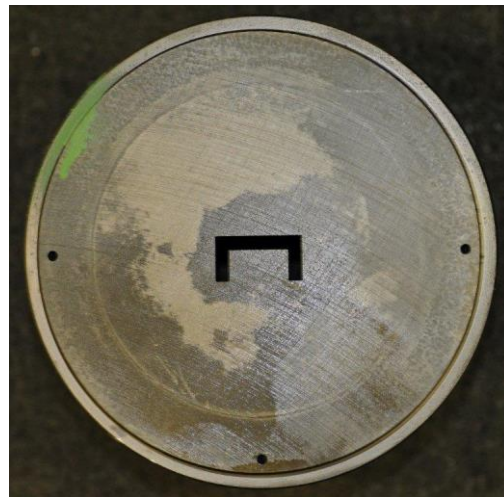
When extremes occur such as very low or very high temperatures or very slow or very fast extrusion they will have a direct effect on the integrity of the sections as well as on the structural properties of the profiles. The three selected shapes give a representative overview of potential practical problems related to extrusion.

### 3.4 Die designs

Design rules as outlined in chapter 2 have been applied to designs for the dies which were used in full scale production trials on one of the presses at BOAL. Figure 3.6 presents the dies used in the experiments.



A: die for rectangular shape



B: die for U-shape section



C and D: die consisting of two parts used for the Tube section

Figure 3.6 The dies used in the experiments

The approach in die design is feature based where the complex geometry of the die is split up into more manageable geometries. The die features which have been taken into account are; bridge, feeder hole, welding chamber, bearing, sink in and die orifice. The dies used are shown in Appendix 3.

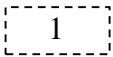
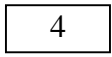
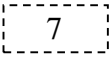
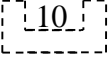

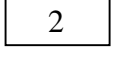
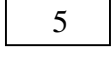
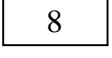
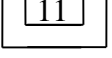

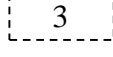
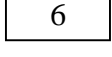
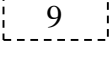
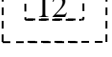

### **3.5 Extrusion experiments**

Full scale extrusion trials have been performed on a press at BOAL Finex B.V. in Helmond, the Netherlands. The press which was used had a capacity of 5MN. The extrusion speed was varied between approximately 6 and 22 m / sec. The profiles were stretched to about 0.5% of the extruded length above elasticity limit of the material. The extruded length is 1 billet per shape per temperature and per speed. The extrusion temperature of the 6082 billet is varied between 480 and 520°C. The profiles were air quenched with a cooling speed of more than 1°C / sec. Cooling rates were checked manually using hand held thermo-couples.

Temperature readings (T-exit) were taken using an infra-red meter (3T). Ram speed, pressure and billet temperature were taken from the pulpit display and records. The extrusion parameters are given in table 3.2.

In Full Scale Extrusion trial the three geometries have been extruded and temperatures and speeds have been varied. In the table 3.2 the selected samples are shown. For discussion a number of experiments which are displayed in the figure below have been selected. The temperature settings were the same for each horizontal row.



520°C					
500°C					
480°C					
	6 mm/s	12 mm/s	22 mm/s	12 mm/s	12 mm/s

*Table 3.2* The experimental samples used in the research

In view of the large number of experiments a statistical selection has been made to be used in simulations and structure investigations. The geometries given in Table 3.2 with a broken line are not included in simulations and structure investigations.

### 3.6 Examination of extrudates

Samples were collected for further examination. The samples were all collected at 1 meter from the end of the extruded length. This position ensures that steady state was reached and that all samples had reached the maximum extrusion temperature since the maximum extrusion temperature will be reached towards the end of the extrusion run. Therefore it is regarded as the most reliable and representative position for sample collection. The collected samples have been used for optical microscopy, electron microscopy and EBSD (Electron Backscatter Diffraction) analysis.

#### 3.6.1 Optical microscopy

Optical microscopy was partly performed by Hydro Research and Technology Development (RTD) in Sunndalsøra, Norway and partly performed by BOAL Beheer Laboratories in De Lier, Netherlands. Optical microscopy was used to determine particle size and distribution, macroscopic degree of recrystallisation and macroscopic degree of precipitation.

At Hydro RTD samples were prepared by grinding at 220, 320, 500 and 1200 mesh and polished with 3 $\mu$ m and 1 $\mu$ m diamond polish. After polishing the samples were anodised using a mixture of 95ml distilled water and 5ml 35% HBF<sub>4</sub>. The anodizing was performed in Struers Polectrol anodizing unit for 1-2 min at 20V, flow rate 4. Grain size measurements were done according to the line intercept method (ref. Metals handbook) using a Leica 5000M/CTR6000 stage controlled light optical microscope. A Qimaging Micropublisher 5.0 digital camera and ImagePro 7.0 software were used for imaging the grain structure.

At BOAL laboratories the samples were prepared by grinding at 220, 320, 500 and 1200 mesh and polished with 3 $\mu$ m and 1 $\mu$ m diamond polish. After polishing samples were etched using 10 grams of NaOH and 90 gram of water. Anodizing was performed by Tuckers' etchant, 45 parts of HCl, 15 parts of HNO<sub>3</sub>, 15 parts of HF and 25 parts of water for 10-15 sec. Images were taken by Leitz Metallux III Microscope, images were photographed by Leitz Collorview IIIu imaging system.

### **3.6.2 Electron microscopy**

Particle investigation was performed by electron microscopy at Hydro RTD. The samples were ground at 220, 320, 500 and 1200 mesh and polished with 3 $\mu$ m and 1 $\mu$ m diamond polish. The analysis was performed by Backscatter Electron Micrographs of the particle structure and was made using a Hitachi SU6600 Shottky Field Scanning Electron Microscope. Microscopic investigations were performed at positions in the various profile samples which are given in Figure 6.18 in chapter 6. Evaluation of recrystallisation is performed by the operator evaluation of the light optical micrographs of the grain structure. If the recrystallisation is inhomogeneous (i.e. nor 100% recrsytallised or 100% not recrystallised), the volume fraction recrystallised is estimated using the grid method in LOM over a representative area dependent on the sample cross-section.

### 3.6.3 EBSD analysis method

Subgrain size measurements and misorientation analysis were performed by means of EBSD analysis (Electron Backscatter Diffraction) method. The samples were ground at 220, 320, 500 and 1200 mesh and polished with 3 $\mu$ m and 1 $\mu$ m diamond polish. It is important to remove the prior deformation layer in each grinding and polishing step. After polishing, the samples were electro-polished in A2 electrolyte at 30V, flow rate 7 for 3-4 sec using a Struers LectroPol 5 electro-polishing unit with cooling (the sample was kept below 25°C. (A2 electrolyte consist of: 100 ml distilled water, 580ml ethanol, 83 ml butylcellosolve (C<sub>4</sub>H<sub>9</sub>OCH<sub>2</sub>CH<sub>2</sub>OH) – (ethyleneglycolmonobutylether) and 65 ml 70-72% HClO<sub>4</sub> (perchloric acid).

Sanples were collected from representative areas within the sample. Various samples were collected for different purposes such as overall grain structure over a cross section of the whole sample, detailed samples for subgrain size and misorientation. Further samples were collected for degree of precipitation.

Two 1mm<sup>2</sup> areas, one in the centre zone and one in the edge zone of the samples were analyzed in the rectangular profiles. One area of 1 mm<sup>2</sup> in the centre of the U-shaped and tube profile were analyzed. The locations of the sample area are given in Figure 6.20 in chapter 6 and are chosen to be representative with respect to the structure visible in the optical micrographs.

The EBSD acquisition was performed in a Hitachi SU6600 Shottky Field Emission Scanning Electron Microscope equipped with a Nordif Ultra-Fast detector and software. The EBSD data analysis, indexing and data processing were performed in TSL EBSD software.

The procedure which was used to determine the subgrain size and the misorientation is embedded in the EBSD software. The following steps can be identified: At first the particles size is measured. The program needs to be set with minimum step size to obtain

good resolution on the actual picture. Required for good resolution are at least 10 pixels in a small grain. Then the measurements are started which are based upon pixel numbers in each grain. These measurements are used in the calculations where grains and subgrains are identified based upon grain boundaries. Each pixel has a diffraction pattern which is used in the calculations. Subgrains are defined with low angle boundaries  $<15^\circ$ .

## **4 FEM modeling**

The most widely used finite element formulation in solid mechanics is the displacement approach. The displacement field within the element is defined in terms of assumed functions (interpolation functions) and unknown parameters at the nodes which are either displacements or displacement related quantities such as slopes and curvatures. For each finite element, a displacement function in terms of the element coordinates (x, y, z) and the nodal displacement parameters is chosen to represent the displacement field, and thereby the strain and stress within the element. A stiffness matrix relating the nodal forces to the nodal displacements can be derived through the application of the principle of virtual work or the principle of minimum total potential energy. The stiffness matrices of all the elements in the domain can be assembled to form the overall stiffness matrix for the system. After modifying the global stiffness matrix in accordance with the boundary conditions and establishing the force vector, the system of equations can be solved to yield firstly the nodal displacements, and subsequently the stresses at any point in each individual element.

### **4.1 Techniques used in the FEM simulation**

A successful aluminium extrusion simulation demands an FEM software that at least can handle the problems described by Bianchi and Sheppard (1987) and later more comprehensively by Chenot et al. (1999) as below;

- Large deformation both for 2D and 3D cases
- Remeshing
- Complicated temperature evolution
- Thermo-mechanical coupling
- Possible changes of microstructure of the work piece during deformation.

Haepf and Roll (1999) estimated that about 60 finite element (FE) software packages were used for the simulation of forming processes. In their study, initially three commercial

software packages were selected for their further investigation. Against the features listed above a technical evaluation was carried out by them using a T-section extrusion as the benchmark problem for the chosen software. Finally they were convinced that the French software Forge2® and Forge3® (currently the latest version is named Forge2009®) performed best during the T-section extrusion simulation.

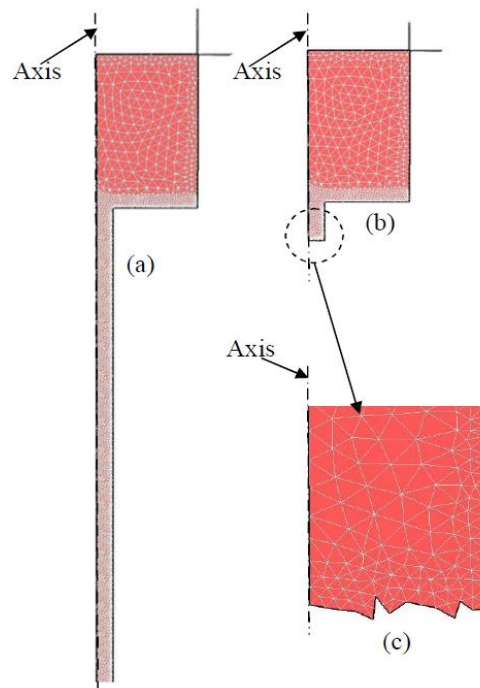
The French-developed FEM software Forge2009® that incorporates the 2D and 3D module is used in this study. Forge2009® is dedicated to the simulation of hot, warm and cold forging of both 3D parts and 2D geometry parts (axisymmetric (revolution) parts and parts with high length-to-width ratios.

FEM has long been proven to a powerful tool to aid engineers and researchers to solve problems in a wide range of fields and the hardware for computers have also been improved or even innovated greatly in the past decades. However it seems that it is still very difficult for these electronically technological developments to meet scientists' requirements due to their ambition for more realistic simulation for the reality. The most notorious problem is the unbearably long time needed for a complete three dimensional extrusion simulation with a complex shape.

The most common measure for a FEM software user to reduce computation time is to take advantage of the symmetry of the problem studied. If the configuration of the body and the external conditions (i.e. boundary conditions) can be regarded as symmetric, then only the repeated part of the structure needs to be modelled. There are three common types of symmetry encountered in engineering problems: reflective (or mirror) symmetry, rotational (or axial) symmetry and inversion symmetry.

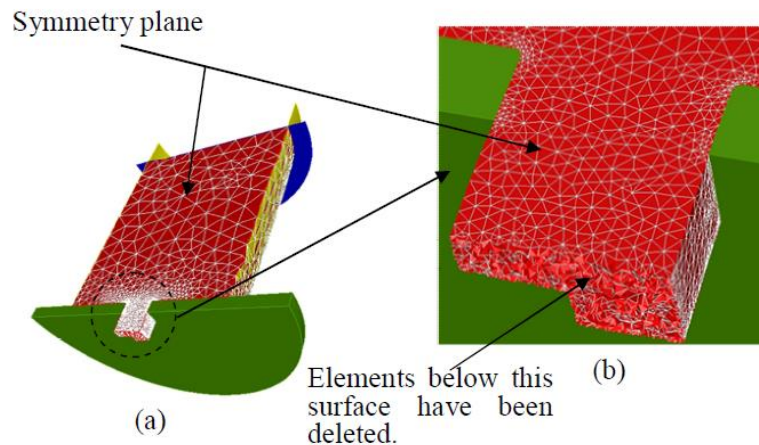
For an extrusion simulation, a very fine mesh has to be used in the areas of die mouth, die land and in the following extrudate. Therefore in a complete extrusion simulation, as the ram travels, many small elements in the extrudate will cause congestion, which makes the simulation practically impossible. To solve this problem and facilitate extrusion

simulation, an auto-trim technique that so far has not been found in other similar FEM softwares was invented with the collaboration between Sheppard's group and Transvalor. Auto-trim involves killing the elements that are some distance from the die orifice and does not affect the correct calculation, the number of elements in use are significantly reduced. Because auto-trim reduces the calculated elements, computation time will be saved and focus can be concentrated on the part of interest without having to waste elements in the material far away from die exit.



*Figure 4.1* Symmetry and auto-trim used in 2D simulation

Figure 4.1 shows a rod extrusion is simplified into a 2D axisymmetric FEM model. Figure 4.2 (c) is a magnified view of the extrudate after auto-trim.



*Figure 4.2* Symmetry and auto-trim used in a 3D simulation

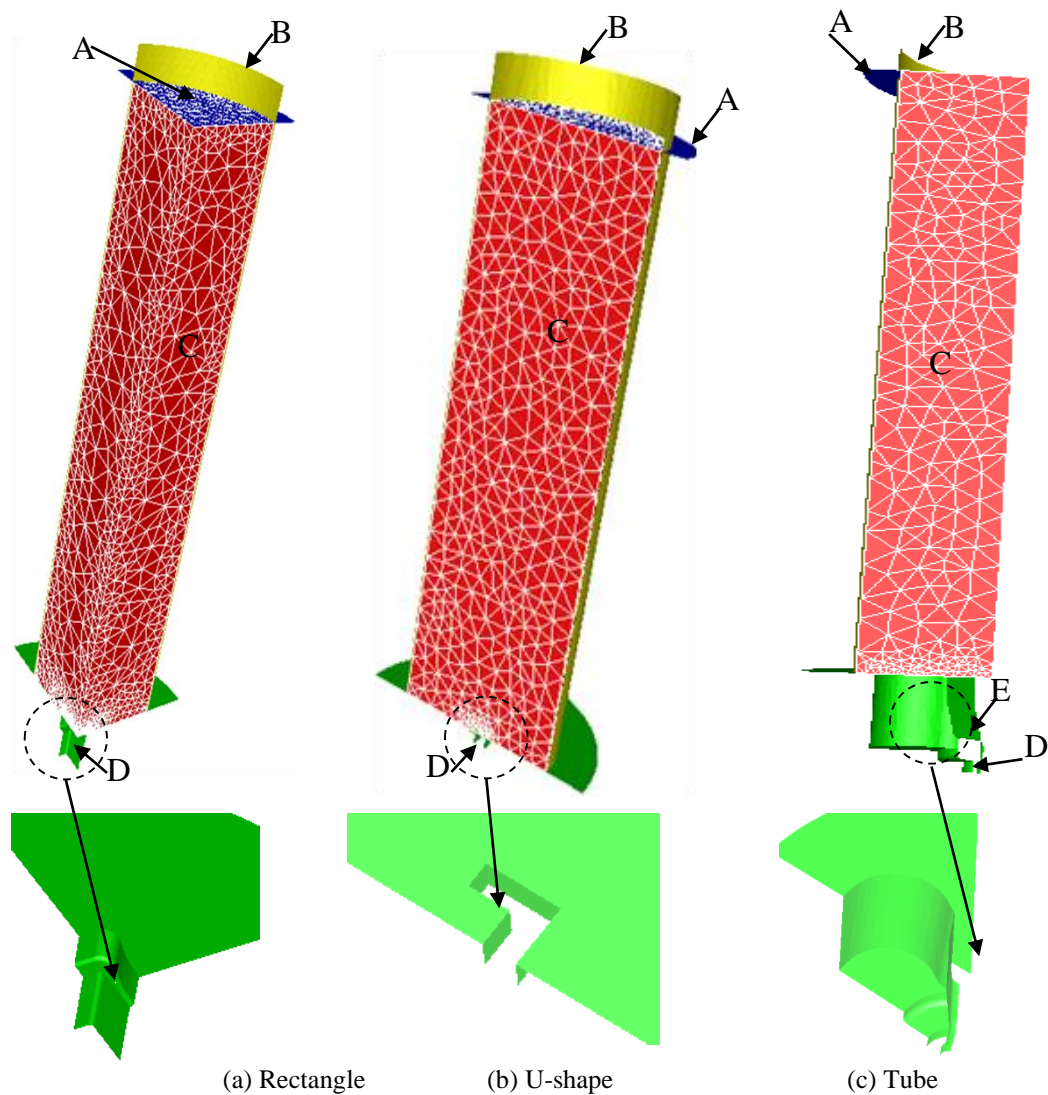
Figure 4.2 indicates a 3D simulation that utilises the mirror symmetry and auto-trim technique. It should be noted that excessive time is still required for a complete extrusion cycle simulation of a complex section even when the symmetry and auto-trim are employed. To further expedite the computation, a cluster version of Forge® software would be necessary.

#### **4.2 Finite element models**

Finite Element Models are used to create a simplified representation of the real problem under study, in this case the extrusion of a number of geometries.

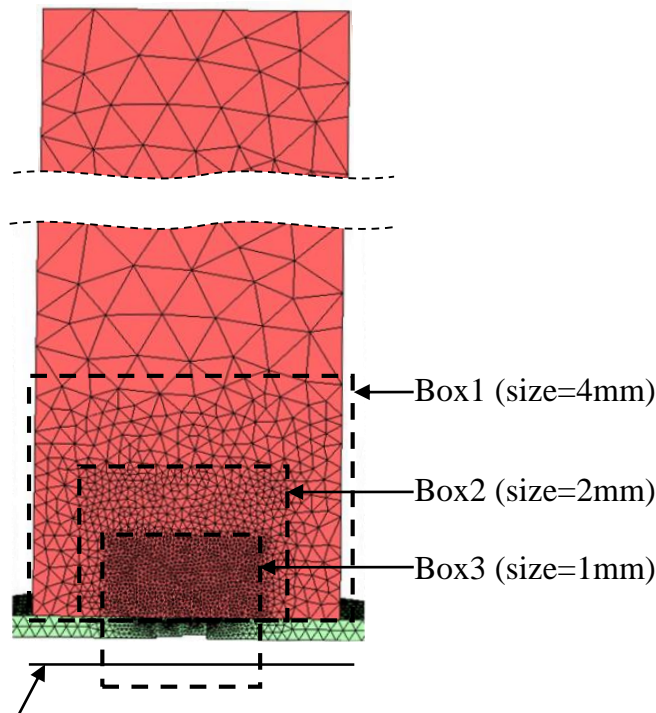
Figure 4.3 shows the Finite Element Models used in the simulations. The tools (ram, container, die including bridge die for tube extrusion) are regarded as rigid in the simulations without deformation. To facilitate the simulation the symmetry of the studied geometries was considered. The advantage of using symmetry of the geometries is to reduce calculation time by avoiding unnecessary repetitions. For the rectangular shape only one fourth of the real geometry was used. In this way the number of elements in the mesh which are needed to be calculated is reduced and therefore the calculation time is reduced.





*Figure 4.3* FEM configurations prior to simulation for (a) rectangle, (b) U-shape and (c) tube, where part A is the ram, part B, the container, part C the billet and part D the die (orifice) and part E is the die bridge

For the U-shape only half of the real geometry was used. For the Tube only one sixth of the geometry was used. To achieve reasonable accuracy and efficiency finer mesh near the areas with expected high deformation were applied and mesh boxes and auto trim techniques used. In Figure 4.4 the three mesh boxes were used. In Box1 the mesh size was the largest, in Box2 the mesh size was smaller and in Box3 the mesh was the finest. At the die exit we expect the largest deformation of the material.



Elements under this line that is 5mm from the die exit will be deleted.

*Figure 4.4* Schematic for multi mesh boxes and auto-trim settings

The auto trim technique is used to avoid a too large number of elements being required in the simulations. The horizontal line in figure 4.6 indicates any elements reaching this level will be deleted to save time without affecting the accuracy of calculations.

### 4.3 Constitutive equation used

The theory of viscoplasticity effectively defines a material behaviours which exhibits strain rate sensitivities such as in hot aluminium alloy extrusion. The Zener Holloman formulation has been shown to describe the hot deformation of aluminium alloys. The equation (5.1) initially proposed by Zener and Holloman (1944), later verified by Sellars et

al. (1972) and subsequently rearranged by Sheppard and Wright (1979) is given below.

$$\bar{\sigma} = \frac{1}{\alpha} \ln \left[ \left( \frac{Z}{A} \right)^{\frac{1}{n}} + \sqrt{\left( \frac{Z}{A} \right)^{\frac{2}{n}} + 1} \right] \quad (4.1)$$

Where the parameters  $\alpha, A, n$  are material dependent constants. In this study the value for EN AW-6082 material are as follows: ( $\alpha = 0.052 m^2 MN^{-1}$ ,  $A = 2.39 \times 10^8 s^{-1}$ ,  $n = 2.976$ )

Nes et al. (1994) showed that equation (4.14) reduces to a power law when  $\alpha \bar{\sigma} < 0.8$ , but approximates an exponential relationship when  $\alpha \bar{\sigma} > 1.2$ .  $Z$  is the temperature compensated strain rate parameter also called the Zener-Hollomon parameter and is defined as follows:

$$Z = \varepsilon \exp \left( \frac{\Delta H}{RT} \right) \quad (4.2)$$

In which  $T$  is the temperature,  $R$  is the universal gas constant ( $8.31451 J * mol^{-1} * K^{-1}$ ), and  $\Delta H$  is the activation energy for hot deformation.

#### 4.4 Data file and user-subroutine

Before starting a simulation, all the information needed for the simulation must be compiled and input into Forge2009®. This can be completed by using the graphic user interface of the pre-processor of the Forge2009® or modifying the formatted file (the data file) created by the pre-processor with specific syntax (usually for advanced users). The data file is composed of a certain number of modules into which the variables are entered using key words. These variables are naturally regrouped by themes into the same module. Depending on which options of Forge2009® are used the data file for Forge2® can provide up to 17 different modules while the Forge3® offers up to 13 modules. Each of the

modules presents a category of variables to define. Details of the structure of the data file can be found in the online documents of Forge2009® (Transvalor 2009a, 2009b). The main modules used in the simulations in this study are as follows:

- The Unit system module: This module allows the user to choose the unit system for the computation. The keyword ‘mm-MPa-mm.kg.s’ was used, which means the length unit is in mm, the stress and pressure in Mpa and the units for thermal quantities are the derivatives of mm, kg and second.
- The Rheology and Interfaces module: this module defines the thermomechanical characteristics and the contact conditions of the workpiece and the tools.
- The Thermal Computation module: it activates a coupled thermomechanical simulation; otherwise Forge2009® will only perform an isothermal simulation.
- The Tooling kinematics and setup module: it imposes general conditions linked to the dies.
- The Numerical Sensor module: Numerical sensors are used to follow the time evolution of several variables which are calculated by the software, which is also a powerful tool to investigate the material flow.
- The Remeshing module: If this block exists, the program will remesh the specific deformable object at a given frequency.

#### **4.5 The user subroutine and its integration with Forge2009® solver**

A good FEM software must have a user-friendly subroutine interface such that the software becomes an open system and its users can take best advantage of its flexibility and versatility to integrate the knowledge that is beyond the software’s original developers and finally, in turn, the feedback from the user can improve the software.

Using Forge2009®’s user subroutine, the user can incorporate his own material model, friction model and much more complicated models for structure evolutions during the whole forming process.

Forge2009® manages different types of computed variables, some are defined at the mesh nodes (nodal variables) and some are defined inside the volume elements at the volume

integration points or inside the surface elements at the surface integration points. The nodal variables number is fixed and limited to the simulation computation direct unknowns. For the thermal computation it is the TEMPERATURE and the temperature variation DELTA\_TEMP. For the mechanical computation it is the VELOCITY vector, the PRESSURE and some auxiliary variables like the previous increment pressure PREV\_PRESS and the DISPLACEMENT (Transvalor 2009c).

The detailed procedure to use the Forge2009® subroutines can be found in the online documents of the Forge2009® (Transvalor 2009c). Its basic steps are:

1. Creation of a new user law using a Fortran editor
  - 1.1. Choose the type of law to use among the existing ones (LOIV EVOL, LOIV MECA, LOIV UTIL etc).
  - 1.2. Start editing the Fortran file corresponding to the law type.
  - 1.3. Choose the law name (string with 16 characters maximum), define the parameters, DV and SV (with their respective dimensions) of the user law, in the order in which they will be read in the data file.
  - 1.4. Add the Fortran line: « elseif (nom.EQ.'MY\_LAW') then » in which “Nom” is the Fortran variable containing the name of the user law read in the data file and MY\_LAW is the user law name defined by the user.
  - 1.5. Write the Fortran code computing the values of gs\_var and gs\_eta (and gs\_etat\_point for the UTIL law type) as a function of gs\_par and the other values transferred to the routine by arguments.
2. Activation of the new user law in the data file: the user law MY\_LAW is activated in the datafile with the sub-module (in the .RHEOLOGIE module):
3. Compiling the new user routines. After the compilation, the user will find in the Forge2009® installation directories named “bin/ UserF2 and bin/UserF3” the newly created user dynamic link library;
4. Register the new solver using the new dynamic link library generated in step 3 through the Transvalor Solution Launcher;
5. Run a User solver: as soon as the user solver is registered, it may be chosen for computations by selecting its name in the Solver name field of the launch menu;

6. Using the Forge2009® post-processor to display the user created variables. The calculation of the grain boundary area per unit volume using tetrakaidecahedron grain model was briefly described in Appendix B to demonstrate the procedure to use the subroutine of the Forge2009®

## **4.6 Extrusion Simulations**

The FEM simulations in this research can be grouped in three different types:

Thermo mechanical simulations

Structural simulations

Microstructure prediction.

### **4.6.1 Thermo mechanical simulations**

These were used to predict temperature, strain, strain rate and load. The experiments were performed on a 5MN hydraulic horizontal press at BOAL Finex B.V. in the Netherlands. The extrusion ratio was approximately 26:1 for the rectangular section, 38:1 for the U-shape section and 42:1 for the tube section. Process parameters were varied following a constant set of parameters. The ram speed was set at 6mm/s, 12mm/s and 22mm/s. The initial billet temperatures were set at 480°C, 500°C and 520°C. The temperature of all dies was 450 °C. The billet length was 250mm and the diameter was 90mm. The material used is an alloy from the EN AW-6082 alloy range. The material was produced by Alsinta in Taiwan and homogenised. The composition of the alloy meets the internal criteria for the alloy specification BC68 used at the BOAL Group. This alloy is commonly used for the extrusion of both hollow and solid sections at the extrusion presses in the BOAL Group. Table 3.1 gives the alloy composition used in the experiments. The material received a homogenizing heat treatment prior to extrusion at 580°C for 4 hours and was cooled by forced air to room temperature. The homogenizing heat treatment is generally performed to create a suitable structure for extrusion by re-distributing alloying elements, precipitates and inter metallic phases. Experimental shapes are given in table 3.2. Niu (2010) used a Tresca friction factor of 0.4 on the ram/billet interface and 0.85 for the container/billet

interface. Therefore this study will use an overall Tresca friction factor of 0.6. The mesh of the billet had an average size of 4 mm, this was refined to 2mm and to 1mm near the profile exit area. The total number of elements is estimated at approximately 80,000. Simulation time for one run is approximately 72 hours. The heat transfer coefficient between the billet and tools (die, ram and container) is set as  $20000\text{Wm}^{-1}\text{K}^{-1}$ . The convective heat transfer coefficient is  $10\text{Wm}^{-1}\text{K}^{-1}$ . The emissivity is chosen as 0.05. Forge automatically re-mesh the workpiece at a given frequency (or time step) or if the mesh has been degenerated. A mesh is considered degenerated if either some of the elements become too distorted, or if the contact surface of the workpiece does not correspond accurately to the tool surfaces. The element distortion is measured by the quality parameter,  $Q$ , in terms of the relative Jacobian between the reference element (with  $Q = 1$ ) and the distorted element. The time required to compute the numerical equations is highly dependent on the quality of the mesh. Coupeuz (1994) suggested that a good strategy with Forge is to re-mesh as often as possible. However a good quality mesh is costly in terms of computational time and power, especially for the simulation of extrusion. Therefore, to perform an efficient analysis, a compromise must be obtained between the degree of discretisation (i.e. use of mesh boxes), the frequency of re-meshing, the computing power and time available.

#### **4.6.2 Structural simulations**

These simulations predicted the deformation of the die, the load on the die and the temperature evolution during an extrusion run. These simulations contribute to the optimisation of the die design. The dimension of the simulated dies is: diameter is 302mm and the thickness is 155mm. The dimensions of the section used in the simulation are; diameter 80mm and wall thickness 1,5mm. Figure 4.7 shows the geometry of the simulated profile. The initial billet temperature is  $450^{\circ}\text{C}$ . The billet diameter is 230mm and the billet length is 60mm. Ram speed is 30mm/sec and the applied ram travel is 40mm. The tool material is a steel referenced as X38CrMoV51, (DIN 1.2343 or H13) It is assumed to be isothermal at a constant temperature of  $500^{\circ}\text{C}$ . The behaviour of the steel is supposed to be isotropic and elastoplastic. Properties of the steel at  $500^{\circ}\text{C}$ , are; density =  $7800\text{kg}/\text{m}^3$ , Young Modulus =  $175000\text{MPa}$ , Poisson Coefficient = 0.3, Yield Strength =  $1050\text{MPa}$ .

The process which is used to calculate the stresses in the bridge die can be described as follows: The thermo-mechanical analysis generates a series of data for each performed iteration. One of these data sets comprises the pressure data on the surface of the work piece (i.e. the billet and the extrudate). In order to look at the structural integrity of the die it is necessary to extract the data file of pressure on the die when the pressure is at its highest level. The data file is then applied as input file of pressure on the 3D finite element model of the die. The simulation process is followed by a static FEA run in order to calculate the stresses and displacements in the bridge die using the pressure from the input file. The die is supposed to be rigid. At maximum pressure the load file is used as static input in the FEM on the deformable die. For these simulations the element types used are standards tetrahedron for static analysis. The mesh has been refined where areas of stress concentrations were expected.

#### **4.6.3 Microstructure prediction**

Subroutine application in user input, written in Fortran is used on the thermo mechanical simulations to predict macrostructural aspects such as: subgrain size, misorientation, volume fraction recrystallised and dislocation density.

Appendix 3 displays one of the subroutines with the values for all the necessary parameters.

#### **4.7 Hollow die simulation**

The parameters which were used in the simulations are the same for both bridge geometries. Figure 4.5 show the cross section of the hollow section used in the simulations. Figure 4.6 show a cross section of the die cores used to simulate the extrusion of a tube with a traditional bridge shape and a torpedo shape bridge.



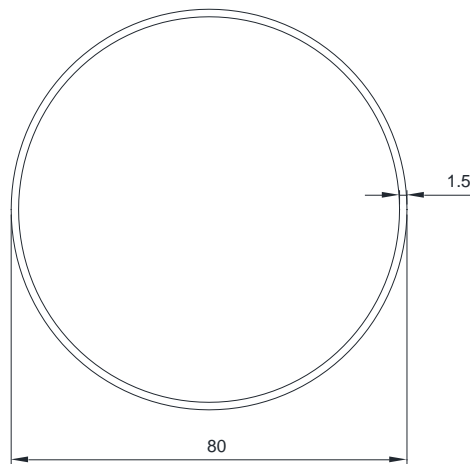


Figure 4.5 The tube section used for simulation of the variation in bridge design

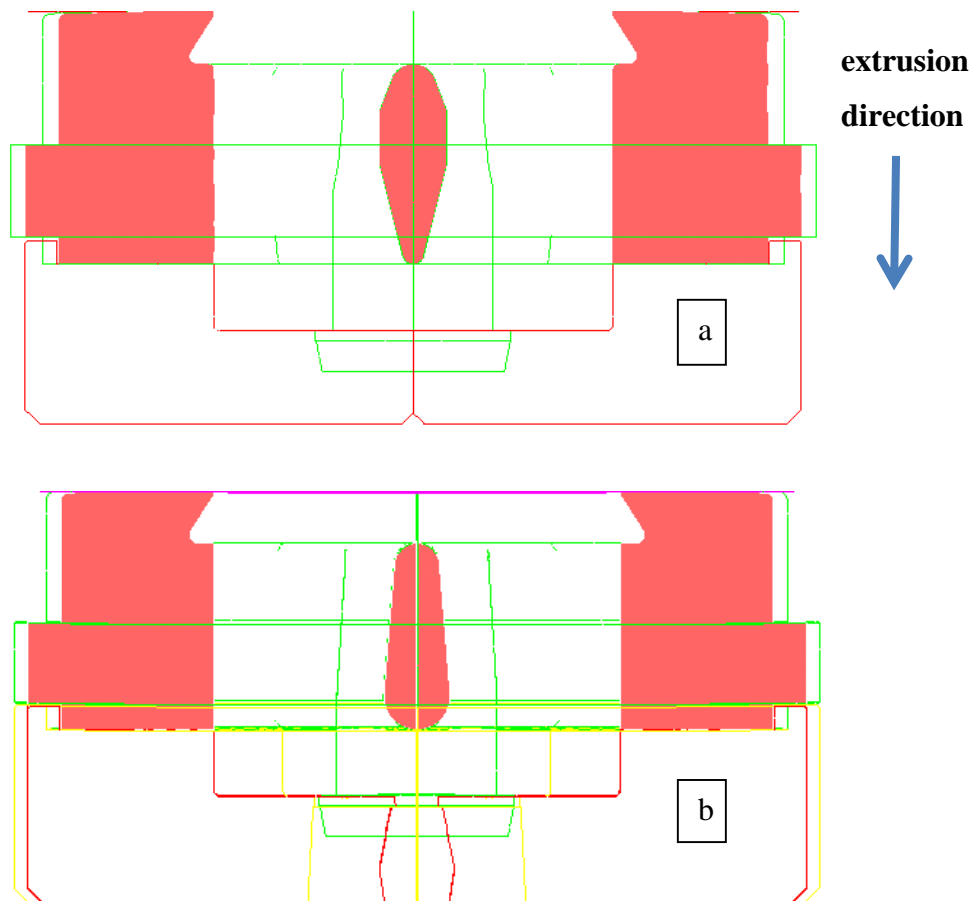
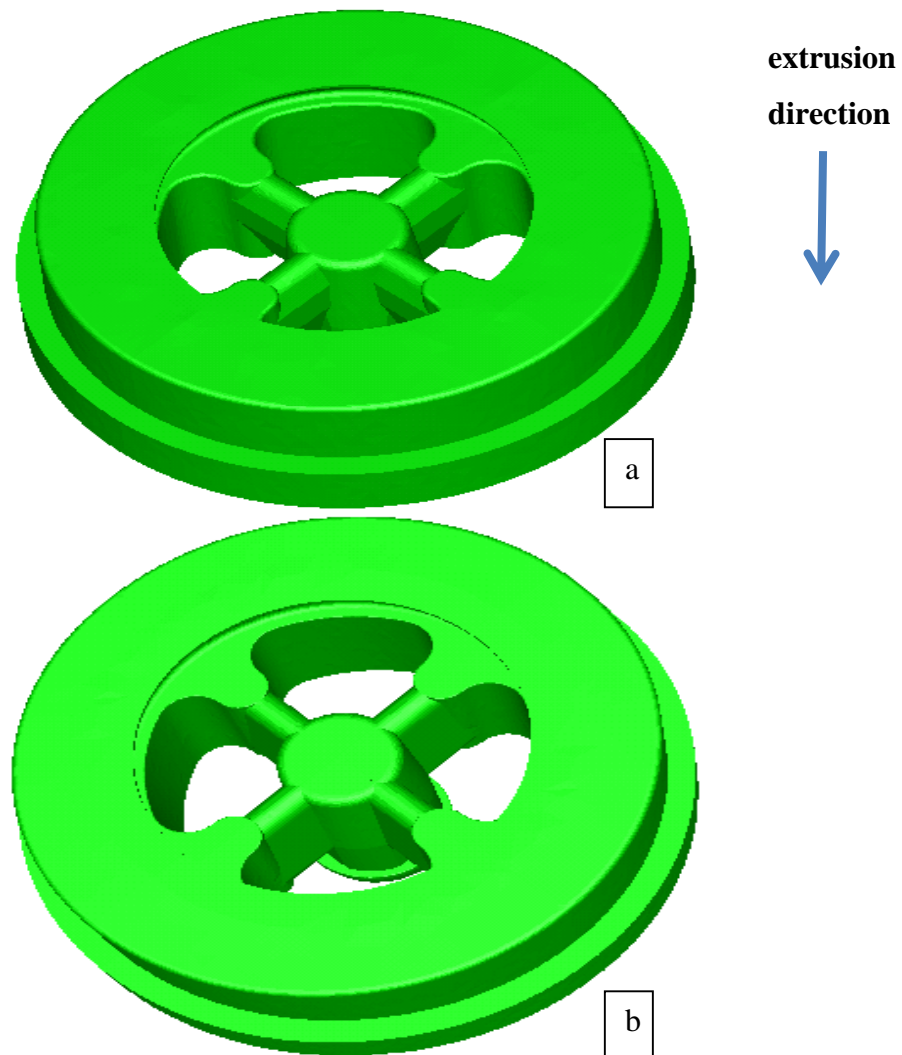


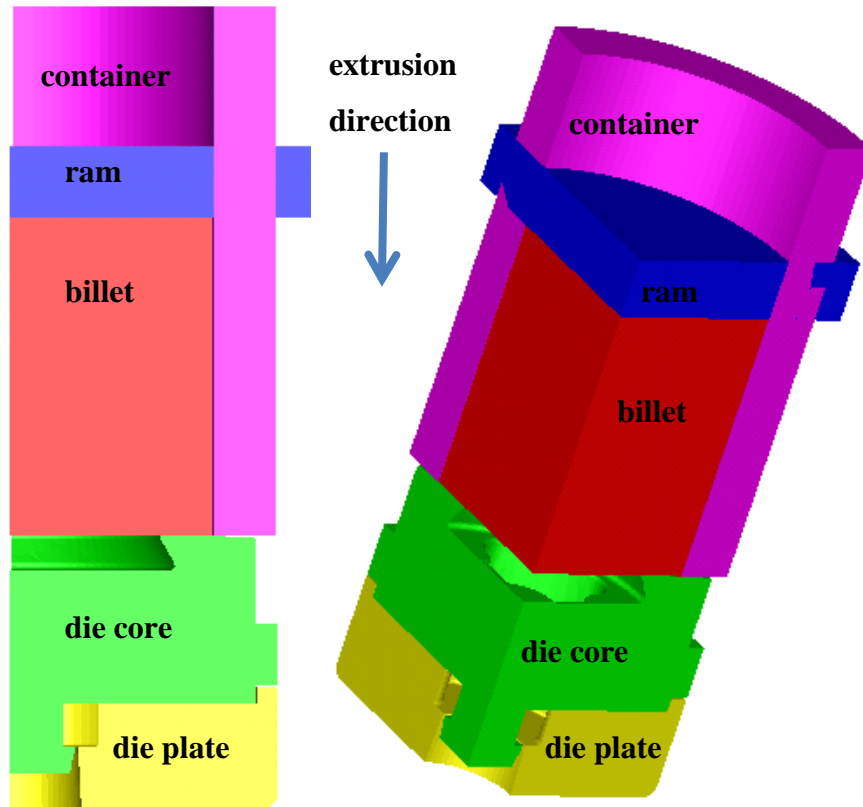
Figure 4.6 A cross section for a die core of a tube with a traditional shaped bridge (a) torpedo shaped bridge (b)

The die designs used in the simulations are in Appendix 3. The set up parameters used for the simulations represents the practical conditions which are applicable if it had been an industrial extrusion run. The bridge shape of the traditional bridge is wide at the position of the entrance of the material during extrusion and narrow at the welding point in the die. The shape of the torpedo shape bridge is narrow at the entrance and wider at the welding point.



*Figure 4.7* A three dimensional view of the die core of a traditional die bridge (a) and a torpedo shape die bridge (b)

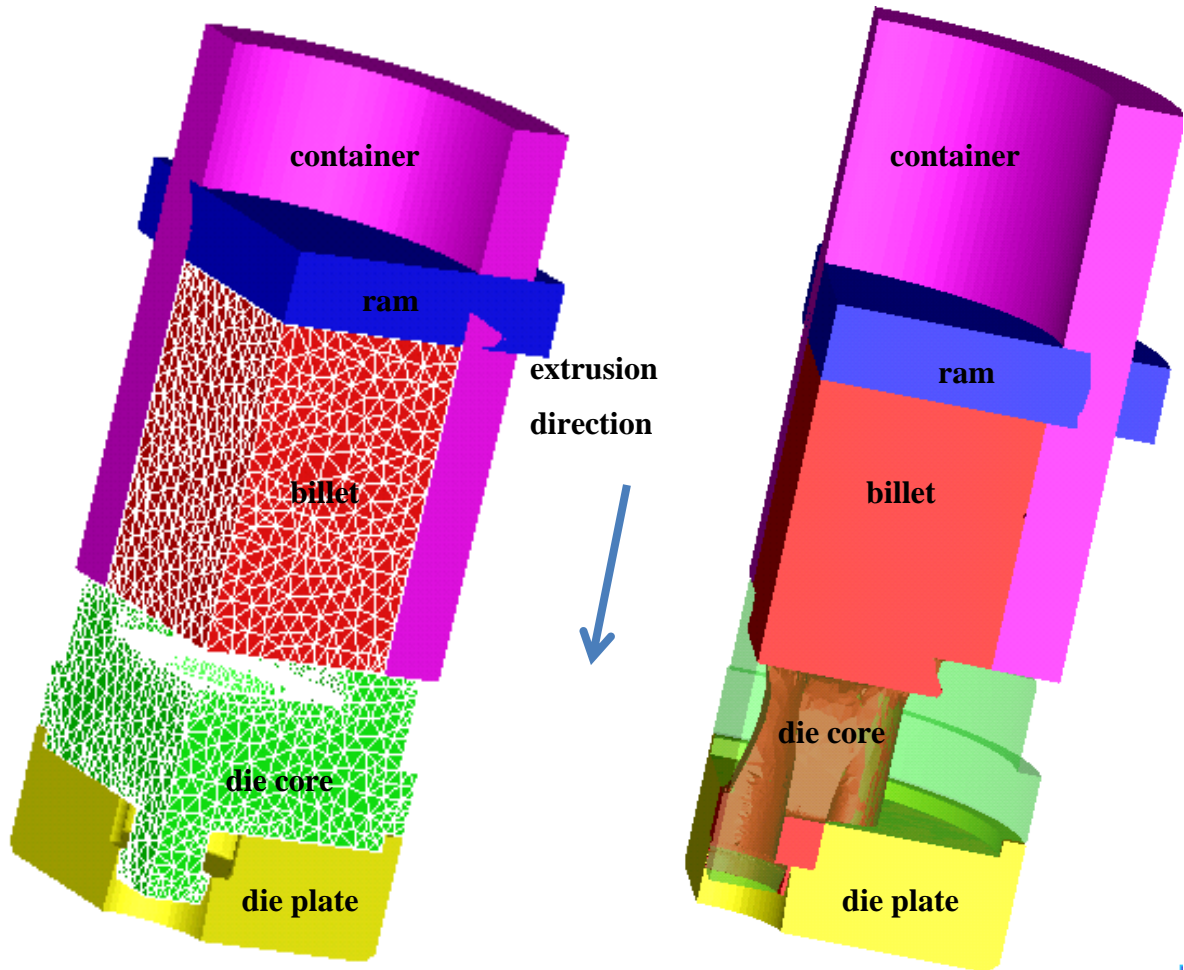
Figure 4.8 shows the extrusion set up for the simulated die for tube extrusion. Figure 4.9 describes the various parts of the extrusion set up such as container, billet, ram, die core and die plate. Die plate deflection is assumed to be minimal in relation to the core deflection.



*Figure 4.8* The extrusion set up for the simulated die for tube extrusion

The container is purple and the billet is red. The die for hollow extrusion consists of two parts. The core at which the inner part of the tube is formed is represented in green. The die plate which is used to form the outer part of the tube section is represented in yellow. Figure 4.9 shows a three dimensional representation of all the components such as container, billet, die core and die plate including the mesh used in the simulations. The purpose of the simulations is to verify the effect of variations in the design of the bridge on the deflection of the core and the effect of the bridge design on the total load of the die.

The die bridge is an important parameter in die design and can be used to control the average pressure on the die and the deflection of the die. It is important to keep the deflection within a predictable range. A die core which deflects parallel to the bearing of the die plate is likely to produce sections with shape deviations. This applies to situations where opposing bearings of the die plate and die bridges are no longer in parallel position compared to each other.



*Figure 4.9* Three dimensional representations of the components such as container, billet, die core and die plate including the mesh used in the simulations

Figure 4.10 shows the simulated deflection in the extrusion direction for the die with the traditional bridge design. Figure 4.10 show high deflection in the top part of the graph. This is the area which is called the baffle. During extrusion there is stick between the ram

and the aluminium in the die. An angle is applied to prevent the ram from emptying the die after a cyclical stroke. This area show high deflections at the edge of the baffle but is not expected to influence the total deflection of the core or the geometry of the section.

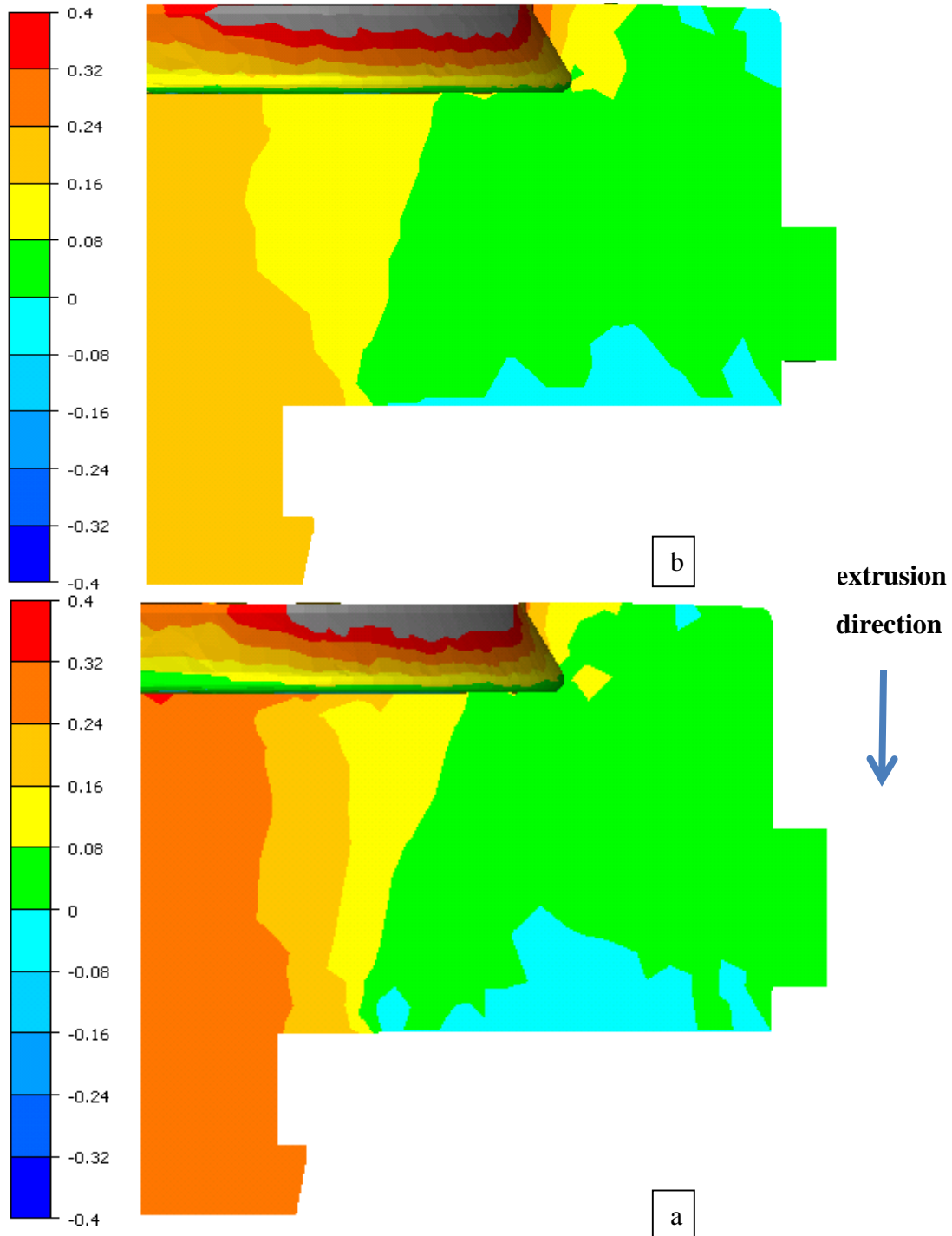


Figure 4.10 The simulated deflection (mm) in the extrusion direction for the die core with the traditional bridge design (b) and a torpedo shape bridge design (a)

The deflection in the extrusion direction (Figure 4.10) is 0.24mm for the traditional bridge shape and 0.16mm for the torpedo shape bridge. This means that the die core will move in the extrusion direction. The design of the die core is symmetrical with 4 bridges. Figure 4.11 show the temperature distribution in the die core with the traditional bridge design and a torpedo shape bridge design.

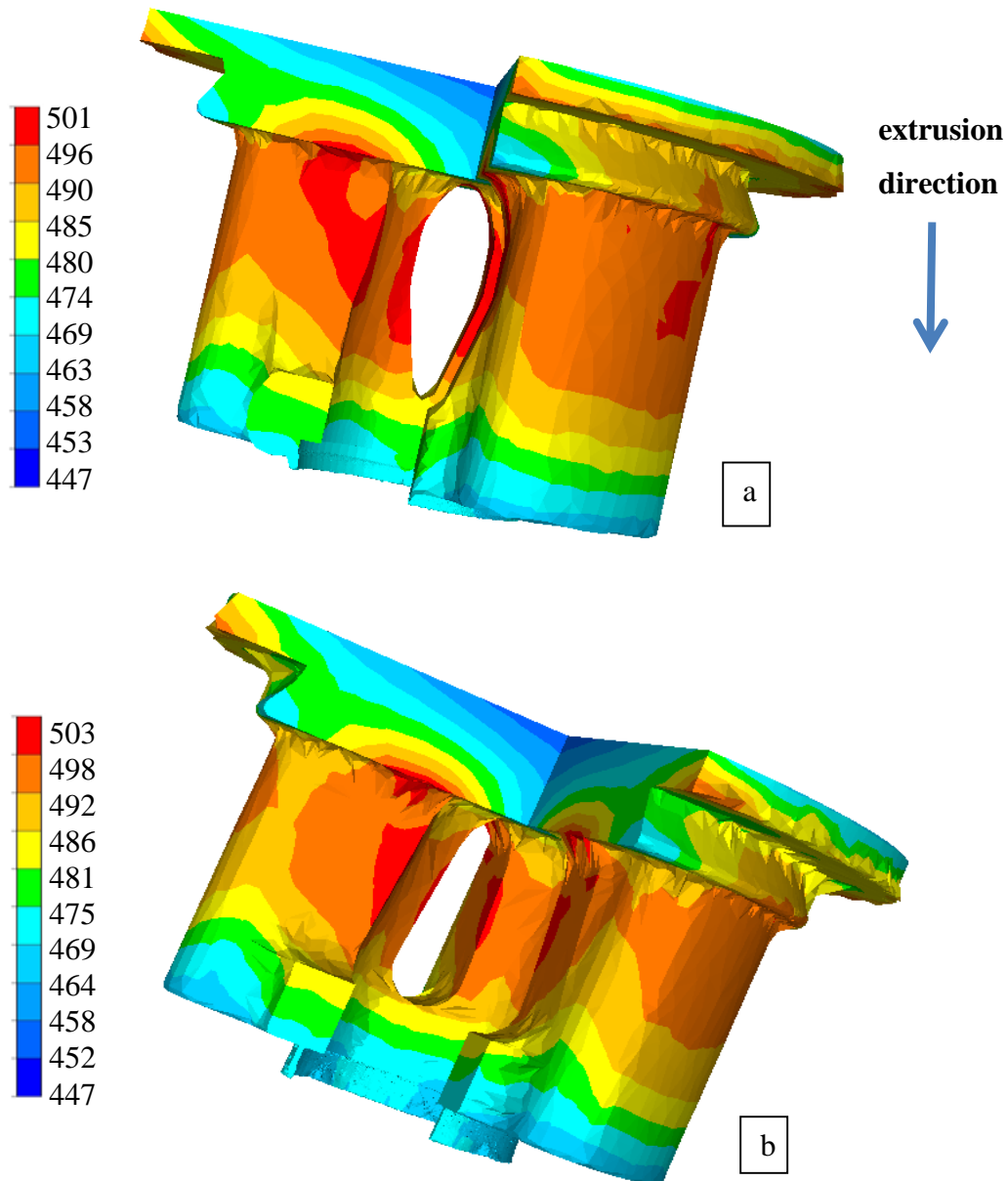
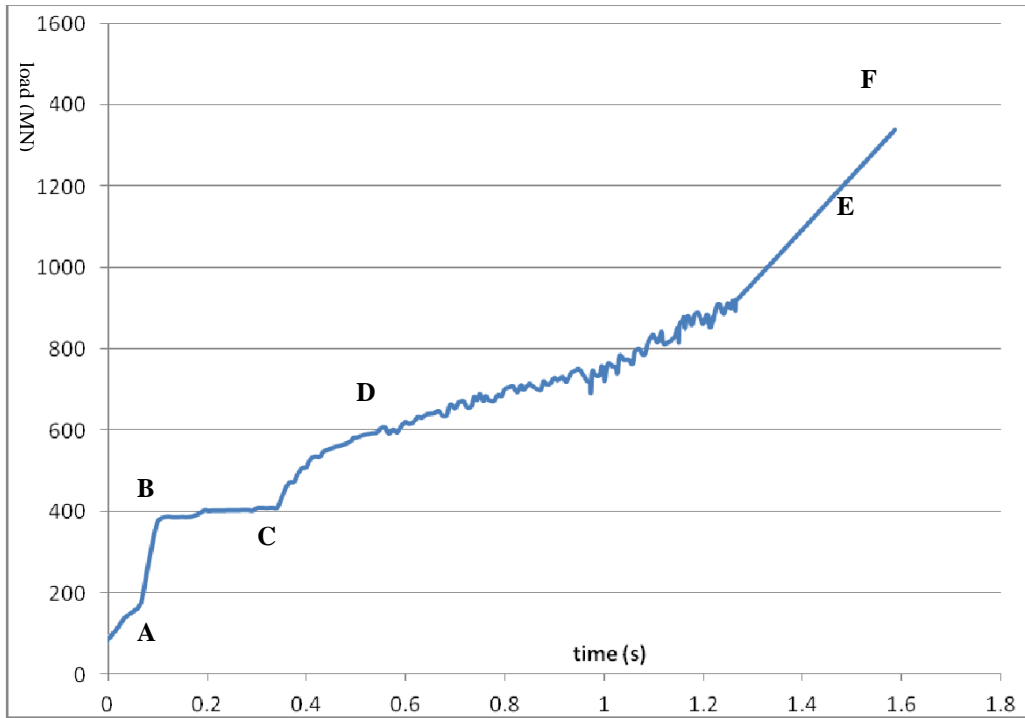


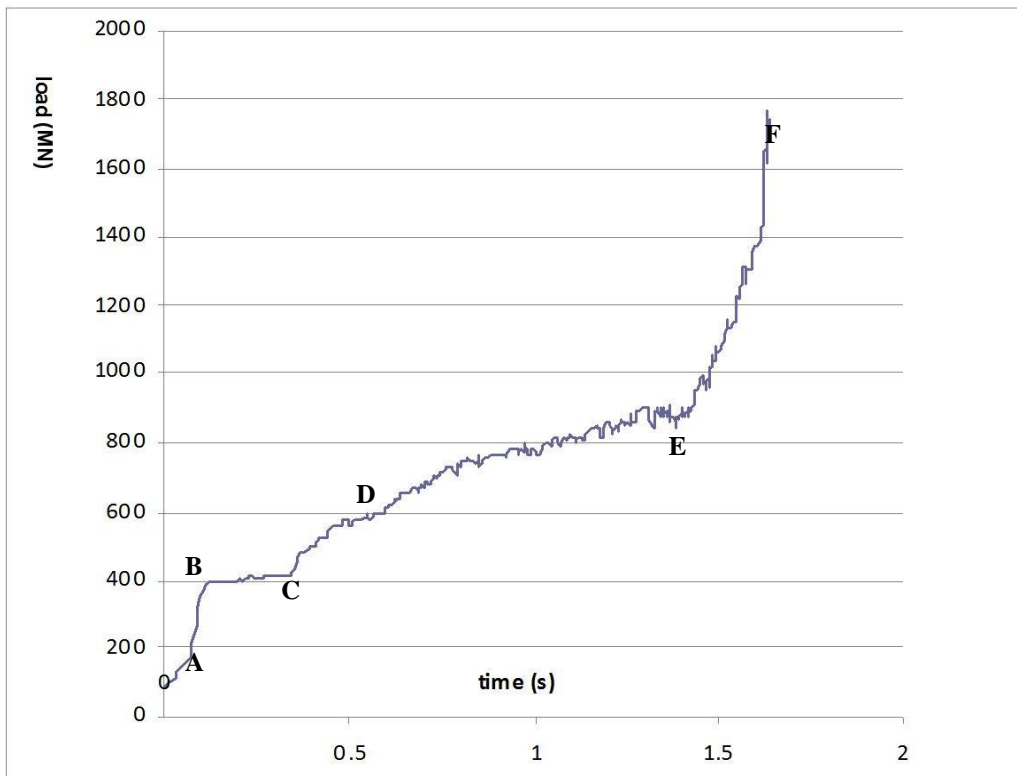
Figure 4.11 The temperature (°C) distribution in the die core with the traditional bridge design (a) and a torpedo shape bridge design (b)

The load is applied in extrusion direction. The load will lead to deflection of the core and will cause stresses in the die bridges during extrusion. The symmetry position of the 4 bridges will ensure that the core will move in the extrusion direction. The predicted deflection is a realistic value and corresponds with practical experience. The deflection of the torpedo shaped bridge is significantly less than the deflection in the traditional bridge shape.

The shape of the torpedo shaped bridge design results in a stiffer construction resulting in less deflection. The highest temperature (501°C) occurs at the bridge surface where it is to be expected due to high shear stresses. Temperatures are lower on most walls of the feeder holes. The highest temperature occurs at the bridge surface (503°C) where it is to be expected due to high shear stresses. The change in bridge design however does only marginally affect local temperature distribution. Temperatures are lower on the walls of the feeder holes compared to the torpedo bridge design. This is likely to be caused by less friction since the height of the bridge is considerable lower. . Figure 4.11 shows the temperature distribution in the die core of the die with the traditional bridge design.



a



b

Figure 4.12 The load distribution (MN) for the simulation of the hollow tube with the die containing a traditional bridge shape.



Figure 4.12 shows the load distribution (ton) obtained in the present work. The figure illustrates the load distribution of the simulation of the hollow tube with the die containing a traditional bridge shape. A number of process steps can be distinguished after the load is applied and the material is extruded. O-A is the billet upsetting stage in which the material began to fill the container. At stage A-B the container is completely filled. In stage B-C one can observe shear of the material over the ports in the die. In stage C-D the material fills up the separate ports of the die. At point D the discrete streams reach the bottom of the welding chamber. In stage D-E the load is increasing because the material is filling the welding chamber at point E the tubular product begins to form and the load required reaches the maximum. From point E the section is extruded. The drop in pressure to point F due to the reduced container friction is not yet observed since the process has not fully reached steady state. Figure 4.12 shows that steady state may not have been reached since the pressure drop is not visible. The total load is approximately 1800 ton. It is expected that the traditional design of the bridge will result in more deflection than the revised bridge design. Higher overall load is likely to result in a larger deflection of the core. The deflection in the extrusion direction (Figure 4.10) is 0.16mm. This means that the die core will move in the extrusion direction and that the maximum deflection is 0.16mm. This is significantly less than the die with the traditional bridge design. The shape of the torpedo shaped bridge design results in a much stiffer construction resulting in less deflection.

Figure 4.11 shows the temperature distribution in the die core. The highest temperature occurs at the bridge surface (503°C) where it is to be expected due to high shear stresses. The change in bridge design however does only marginally affect local temperature distribution. On the location of the feeder hole the material shows a direct flow and will have reached the bottom of the welding chamber without the obstruction of the die bridge. Temperatures are lower on the walls of the feeder holes compared to the torpedo bridge design. This is likely to be caused by less friction since the height of the bridge is considerable lower.

The total load evolution of the torpedo bridge die is comparable to the load evolution of the traditional bridge design. Simulation of both geometries has not fully reached steady state.

The total load cannot be obtained from these simulations. A lower bridge results in a smaller length over which friction will contribute to the load this will result in a lower maximum load. The expected total lower load of the torpedo bridge shape is likely to be achieved by the reduction of the bridge height which will result to less friction across the bridge. It is expected that the revised torpedo shaped design of the bridge results in less deflection.

The maximum deflection using the torpedo shape bridge is 0.16 mm and deflection using the traditional bridge design is 0.24 mm resulting in a 25% less deflection. A die design which results in less deflection is to be preferred. Less deflection of the die will contribute to better control of the shape of the extruded section. It is expected that reduced deflection leads to a reduction of scrap. The gross output may not alter but a reduction of scrap due to less deflection will increase net output. Figure 4.13 shows a close up representation for the extruded part of the hollow extrusion

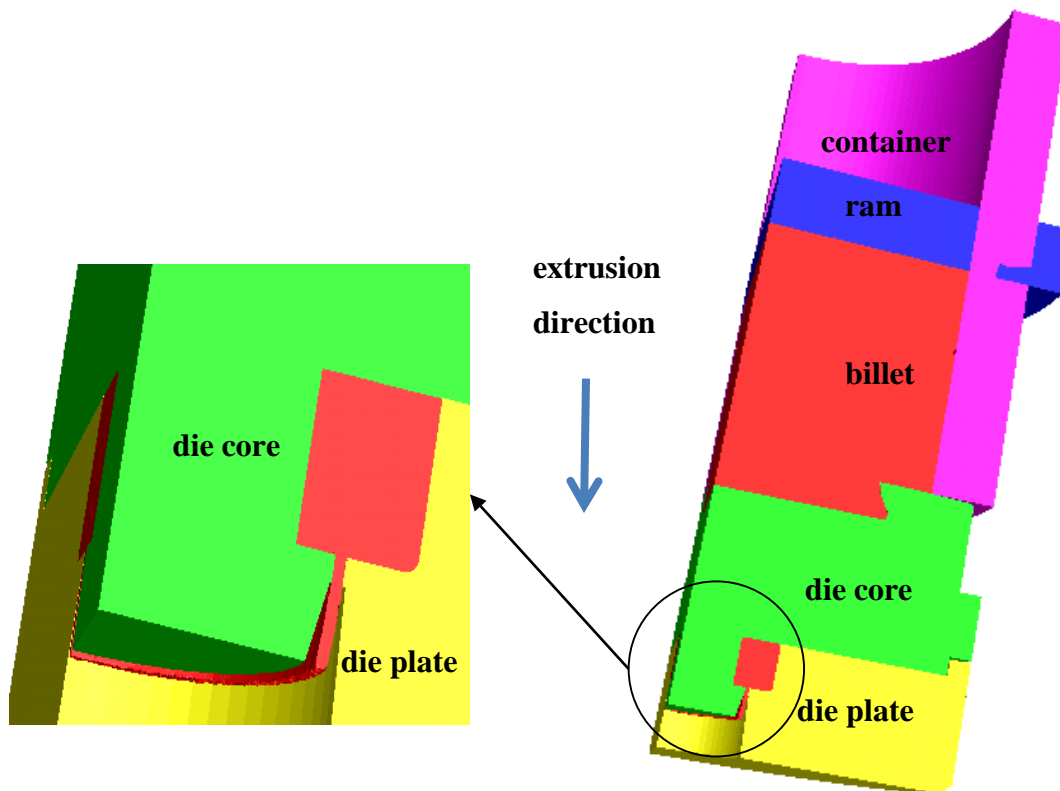


Figure 4.13 A close up representation for the extruded part of the hollow extrusion

#### 4.8 Solid Die Simulation

The sink in is an important feature to control the extrusion of solid sections. A sink in is usually applied as a means of protection to prevent damage to the bearing edge. The most widely applied sink in shape has a constant depth and a constant offset. The controlling possibilities in applying a sink in like this are minimal. In practice, control of the metal flow is performed by altering the bearing length with respect to local wall thicknesses and the distance to the container wall. Li et al. (2003) have indicated that the effect of increasing the offset parallel to the section geometry is limited. A better effect could be achieved by varying the offset whilst keeping the depth constant. In practice this results in limitations regarding the available surface area. In this chapter we will investigate the effect of increasing the volume of the sink in by increasing the depth. All other parameters are kept the same.

The initial billet temperature was 450°C. The billet diameter was 180mm and the billet length was 45mm. Ram speed was 30mm/sec and the applied ram travel was 10mm. This reflects the practical conditions which are applicable should it have been an industrial extrusion run. Figure 4.14 shows the solid section for simulation of the variation in sink in depth (dimensions in mm). Depth dimensions in mm.

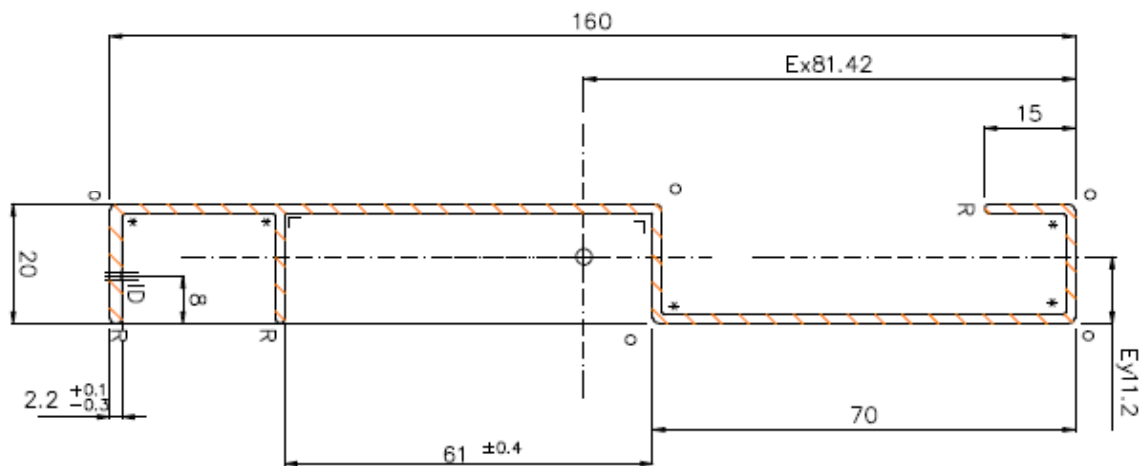
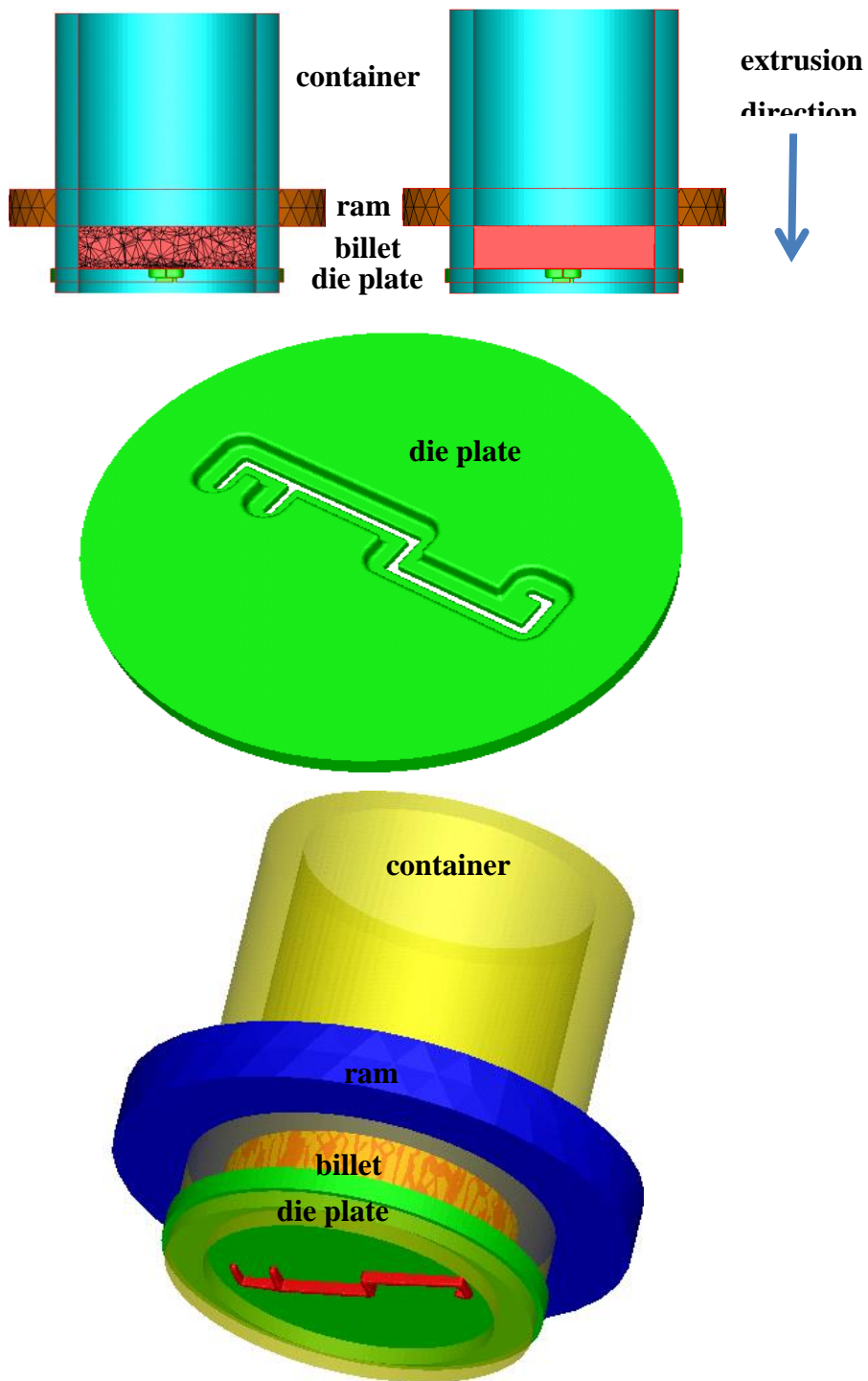
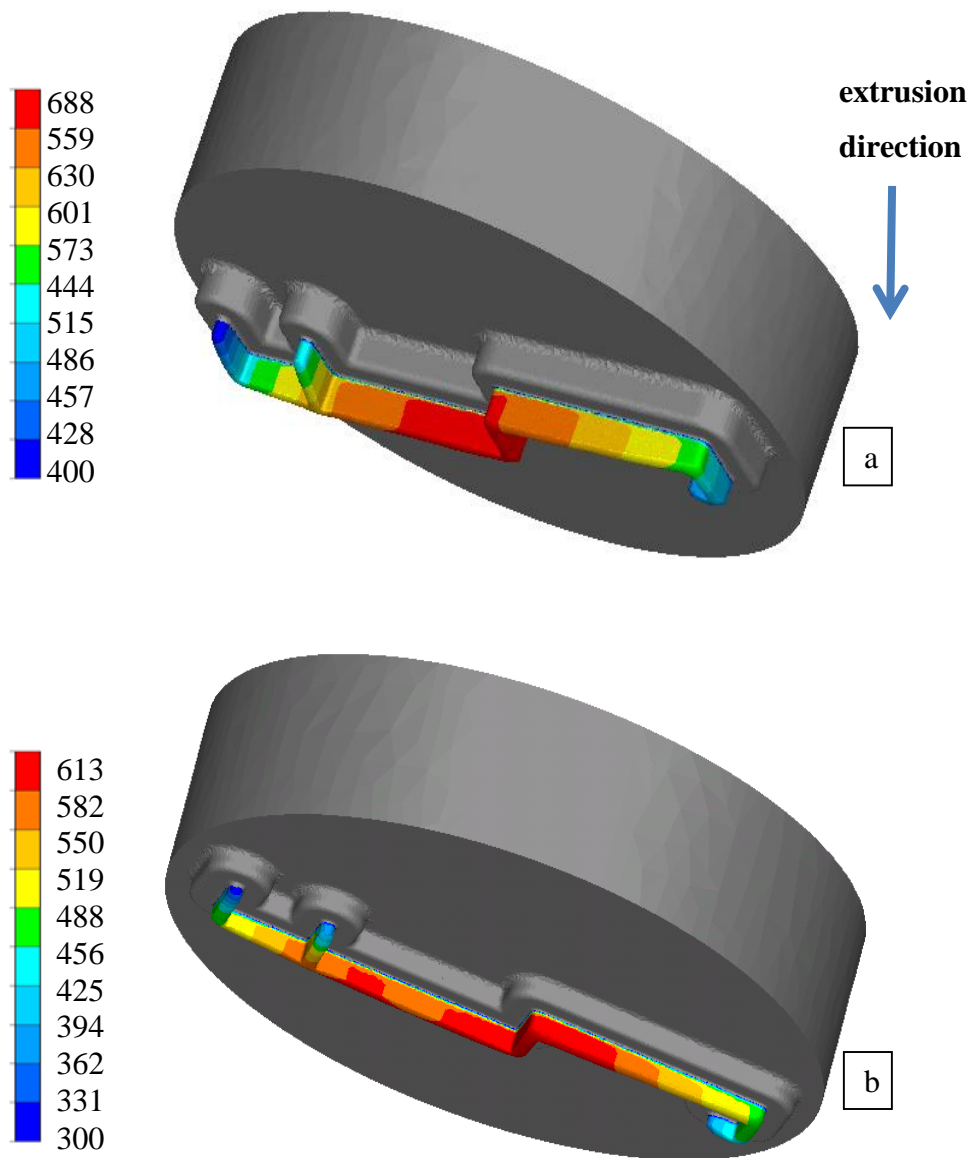


Figure 4.14 Solid section for simulation of the variation in sink in depth (mm)



*Figure 4.15* Tooling set up for a for a solid die extrusion simulation and a three dimensional representation for the extrusion of the solid section



*Figure 4.16* Velocity in extrusion direction (mm/sec) for the simulation of the solid die with the 10mm (a) and the 5.5mm (b) deep sink in

With the purpose of verifying the effect of altering the sink in depth, simulations have been performed and the results are presented in this section. In this chapter two variations of the sink in depth are investigated. At first a die with a sink in with a depth of 10mm is investigated followed by simulations of a die with a sink in of 5.5mm. Figure 4.16 shows the velocity results in extrusion direction for the two sink in depth variations.

The flow of material through a solid die is mainly controlled by means of adjusting the shape and dimensions of the sink in. Flow characteristics are determined by the wall thickness, the position and distance from the centre of the die and the shape and geometry of the sink in. Figure 4.15 shows the tooling set up for a for a solid die extrusion simulation. The various parts for extrusion are visible in this overview. The container with the billet can be seen in blue and red. The die for solid extrusion consists of one part. The die plate which is used to form the solid section is represented in green.

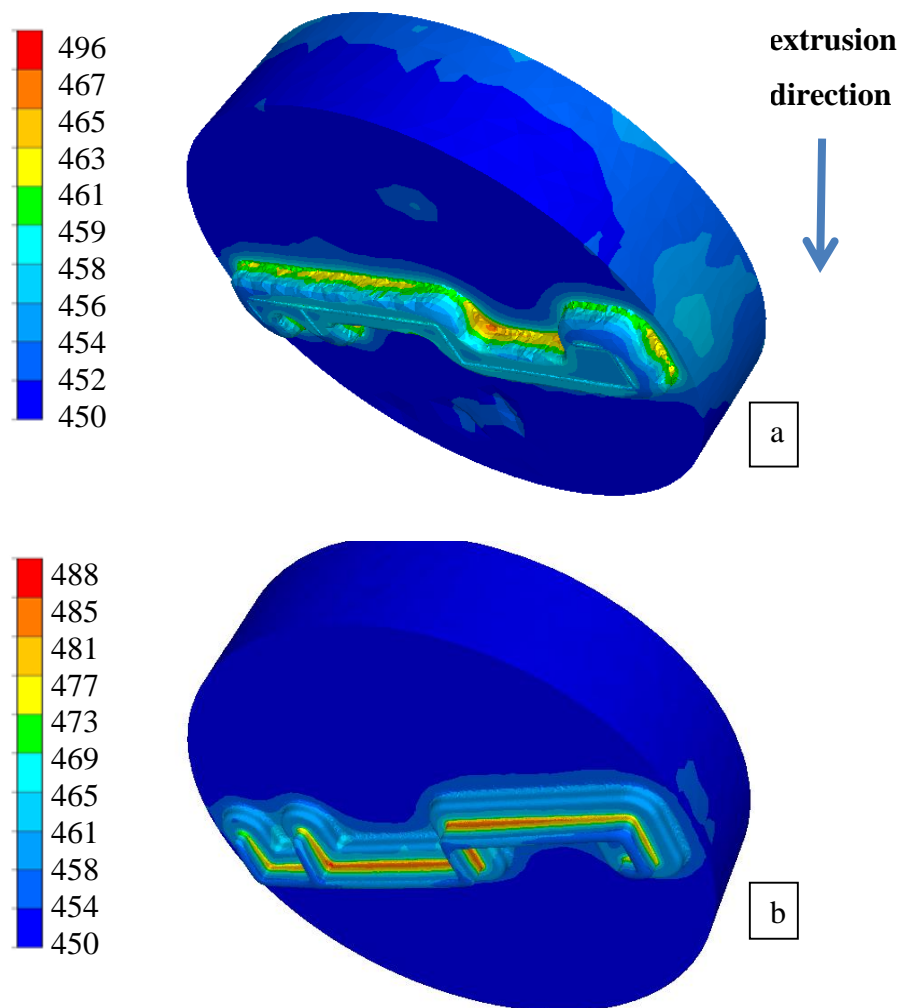


Figure 4.17 Temperature distribution ( $^{\circ}\text{C}$ ) in the die with a 10mm (a) and a 5.5mm (b) deep sink in

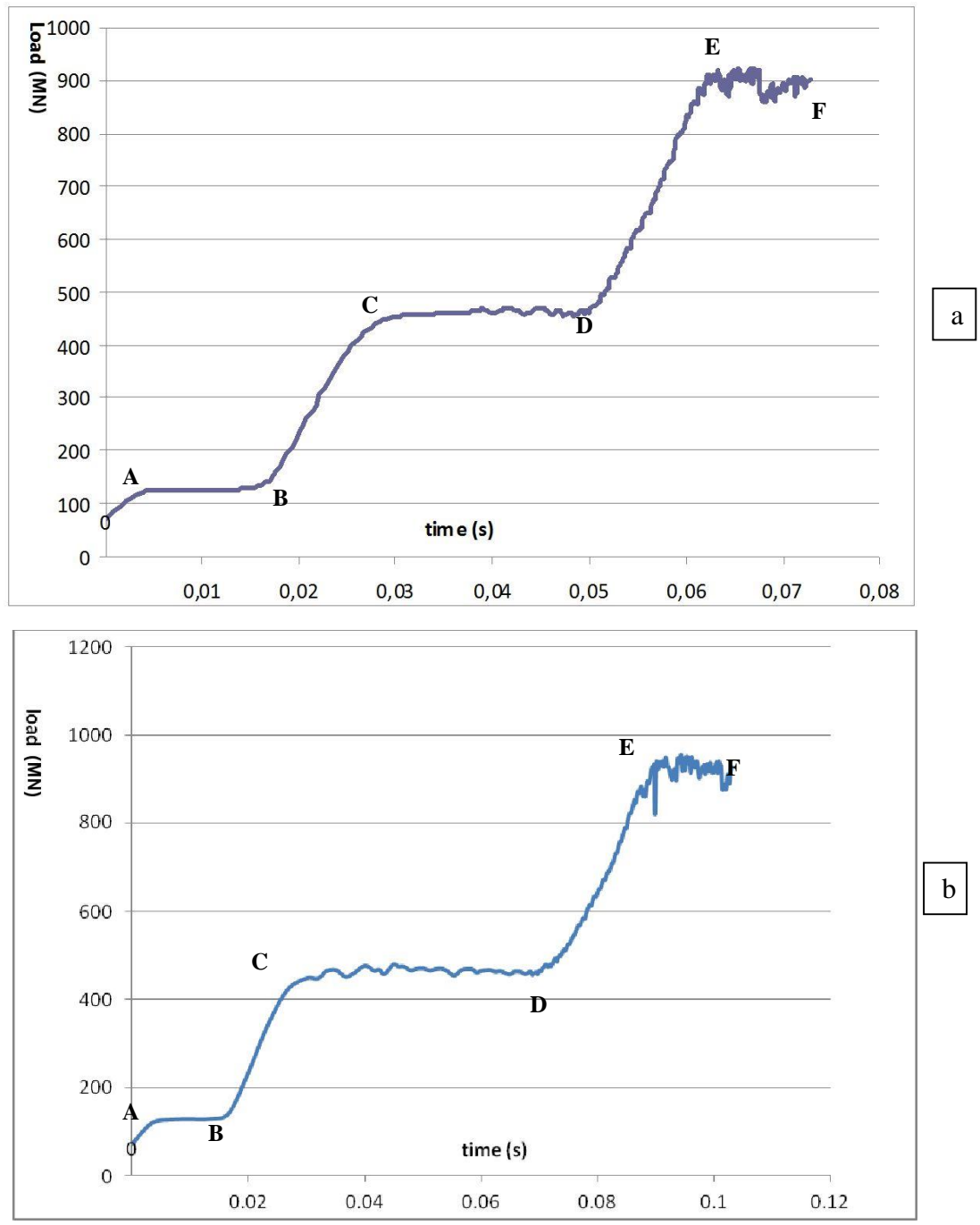


Figure 4.18 The load distribution (ton) for the simulation of the solid section with the 5.5mm and the 10mm deep sink in design

Figure 4.17 shows temperature distribution ( $^{\circ}\text{C}$ ) in the die with a 10mm (a) and a 5.5mm (b) deep sink in and Figure 4.18 shows the load distribution (ton) for the simulation of the

solid section with the 5.5mm and the 10mm deep sink in design. O-A is the billet upsetting stage in which the material began to fill the container. At stage A-B the container is being completely filled. In stage B-C the material is filling the die and pressure starts to build up. At point D peak load is reached. From point C-D the section is extruded where a drop in pressure can be observed. The maximum velocity depends on ram speed and extrusion ratio. Comparing the two sink in depths we can conclude that the speed differences within the profile section differ depending on the sink in depth. In the design with the 10mm deep sink in the maximum velocity variation within the section is varying from 400-559 mm/sec. The lowest speed can be found at the outer detail of the section and the higher speed can be seen in the centre of the die on a very small localised area. In the design with the 5.5mm deep sink in the maximum velocity variation within the section is varying from 300-582 mm/sec. The lower sink in will allow for higher extrusion speeds and less variation over a larger part of the section. The outer details close to the container wall are exhibiting larger differences compared to the centre part of the section. The increase of the volume of the sink in will lead to smaller speed differences within the extruded section but also to a lower overall speed. The maximum as well as the minimum speeds which occur in the section are both lower in the die with the deeper sink in. The control possibilities with variations in the depth of the sink in are limited. The deeper sink in shows less speed variation within the section but also shows a higher maximum load. Given the higher maximum load a compromise is probably required. This could be in the form of lower sink in depth combined with local sink in off set and local small variations in bearing length.

#### **4.9 Conclusions**

The material flow during the extrusion of complex shapes were predicted by the Forge2009® program. Hence the affect of die design variations could be investigated. It was observed that alteration in the cross section of a bridge during tube extrusion substantially influenced the material flow in the welding chamber which changed the optimisation of the processing parameters required. The extrusion of solid shapes were also affected by die design. Varying the depth of the sink altered the velocity profile across the extrudate providing the die designer with an extra tool to improve the performance of the die.



## **5 Results and analysis mechanical**

### **5.1 Introduction**

In the work presented we do not develop FE solutions. We devise and incorporate sub-routines into an experimental programme FORGE in order to solve complex geometries. We will introduce original sub routines, usually written in Visual Studio 2005 to achieve the modelling goal. These routines contribute significantly to the original work in this thesis.

In contrast with analytical techniques, finite elements can be applied to complicated shapes. The basic characteristic of the finite element method is the discretization of the domain of interest, which may have complex geometry, into an assembly of relatively simple shaped elements that are connected by nodes.

### **5.2 Simulation results**

Previous work by Peng and Sheppard (2004), Duan and Sheppard (2001) has shown that Forge2009® is able to deal with a wide variety of problems concerned with the metal forming process. Duan and Sheppard (2003) has shown that a very successful prediction of structural features is possible.

Extrusion simulations have been performed on the selected number of samples used in the experiments and highlighted in table 3.2. The rectangular samples were used with an extrusion temperature and extrusion speed variation. The Tube section and the U-shaped section were used with constant extrusion temperature and a variation in extrusion speed.

The extrusion experiments were performed for the three geometries where extrusion parameters were recorded. Differences between measured and simulated values are likely caused by practical issues during the collection of data. There was a potential time difference between the collection of data and the real event. Additionally, due to the deviating emissivity factor of aluminium, contactless temperature reading of aluminium could be inaccurate. Some of the inaccuracies could also have been generated by accumulations of

errors at each FEM increment. The estimated accuracies obtainable from these experiments are approximately plus and minus 5% for temperature and 7% for load measurements.

		billet temp °C	exit temp °C	simul temp °C	% diff	ram speed mm/sec	load MN	simul load MN	% diff
Rectangular	1	475	498			21	280	300	7.1
	2	478	499	536	7.4	12.5	260	275	5.7
	3	476	502			6.4	250	260	4.0
	4	505	514	519	1	22	260	275	5.7
	5	500	531	545	2.6	12.7	245	260	6.2
	6	510	534	559	4.6	6.3	210	220	4.7
	7	520	527			22	240	255	6.2
	8	518	535	553	4.1	12.5	215	230	7.1
	9	520	540			6.3	190	200	5.2
U-shape	10	480	518			20	260	275	5.8
	11	495	524	543	3.6	20	235	250	6.3
	12	510	535			10	225	240	6.6
Tube	13	478	514			20	320	340	6.2
	14	500	524	556	6.1	20	280	290	3.5
	15	520	532			20	265	280	5.6

*Table 5.1* Extrusion parameters during the experiments

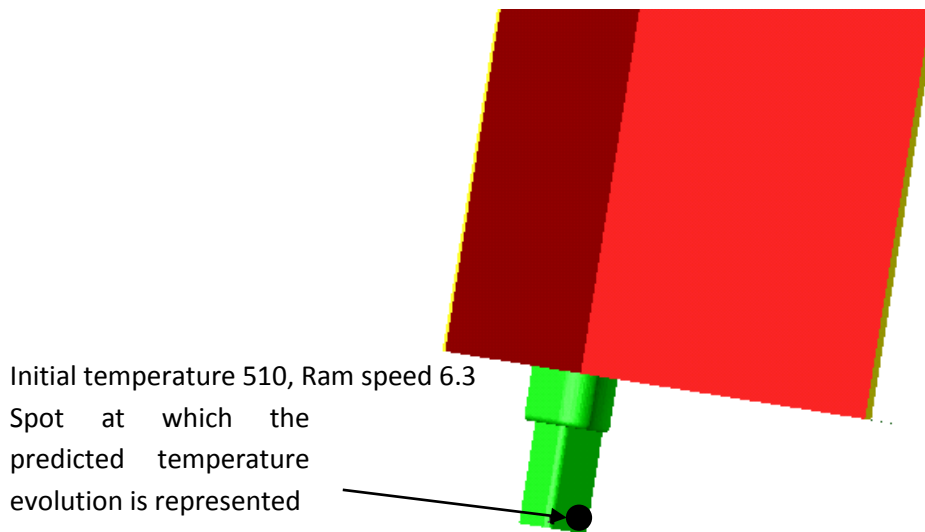
The predicted temperature and load correlate relatively well with the value from the experimental data. With regard to the temperature the high percentages of difference (7.4% and 6.1%) are for low and high temperature respectively. It is therefore difficult to find a correlation between inaccuracy and initial billet temperature. With regard to extrusion load again there is no apparent correlation between inaccuracy and initial billet temperature. There is also no apparent correlation between inaccuracy and ram speed.

### 5.3 Temperature distribution

The uncertainty in the temperature readings is in the order of magnitude of 25°C with an unquantifiable uncertainty in strain rate, but we will proceed with caution to predict histories in microstructure evolution recognising that the accuracy may be limited.

Temperature is an important parameter in extrusion. It has a great influence on the microstructure of the extruded product. Temperature is a pre-condition for successful extrusion as it influences the extrudability. Stress can influence strain negatively under the influence of temperature increase.

In Figure 5.1 the position at which the temperature is predicted is shown. The temperature evolution over the extrusion cycle is given in Figure 5.2. From Figure 5.2 it can be seen that during steady state the extrudate temperature distribution remains reasonably constant. However it will continue to rise in a limited fashion if the friction and flow stress factors are not in balance.



*Figure 5.1* Position at which the predicted temperature evolution is represented

In Figure 5.1 predicted and simulated load distribution over a billet cycle is presented.

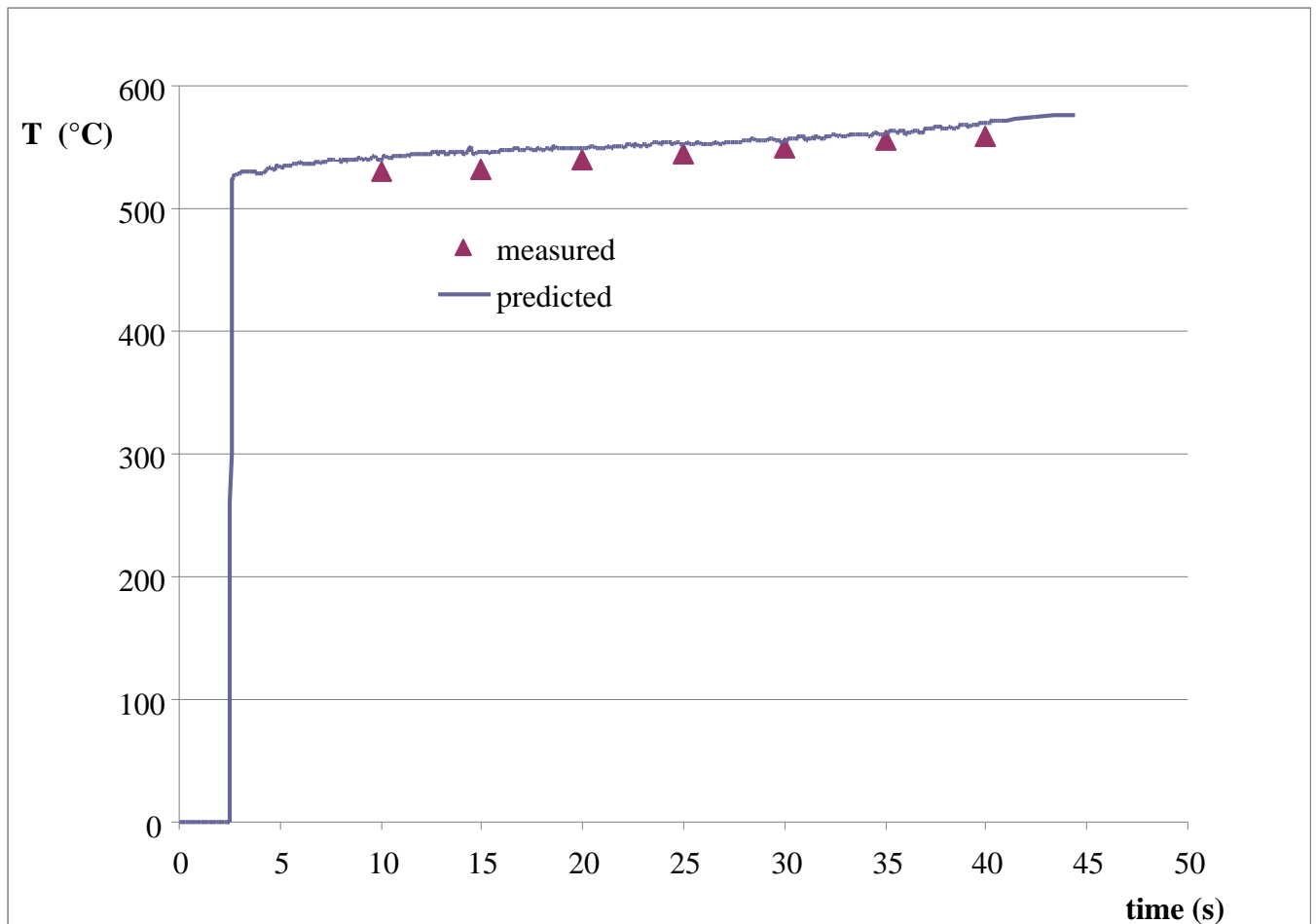


Figure 5.2 Temperature evolution over an extrusion cycle

The temperature evolution was performed in one experiment (550°C, 12mm/s), with the purpose of validating the simulation results. The simulated temperature evolution results were collected from a position at the die exit and are shown in Figure 5.3. It indicates that at this point, during one billet extrusion cycle, the temperature will increase from 537 to 567°C. The experimental readings were collected with a contactless pyrometer at a set position close to the press exit, see Figure 3.2. The measured temperature evolution curve shows a temperature increase from 530-559°C. The distance between the die exit and the pyrometer reading position is approximately 35cm. It can be noted that the predicted values are higher than the measured values. This could be caused by a temperature drop after the material passes the die exit.

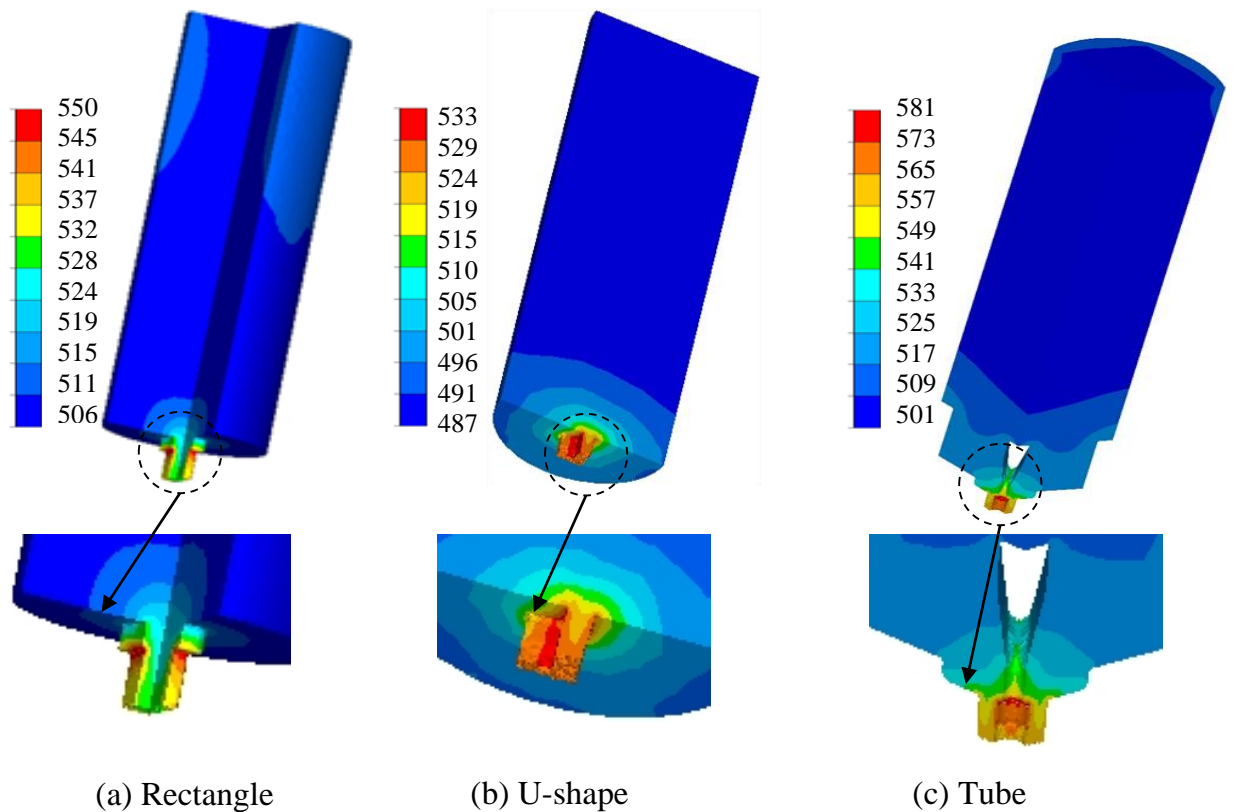


Figure 5.3 Temperature distributions of three different extruded shapes (Temperature T in °C)

Because five predicted overall temperature distributions for rectangular shape extrusion are similar for geometrical reasons only the one with the same ram speed and initial temperature is displayed in Figure 5.3 with the other two shapes. The lowest temperatures can be found further to the back of the container. In Figure 5.4 the temperature variations on the cross sections are given for all geometries used in the experiments. When the material passes through the die orifice the temperature increases significantly and it is very likely that the micro structure will mainly be determined by the conditions at the moment when the material passes through the die. The highest temperature is represented by the red color which happens in places where high deformation is expected which can be clearly seen in Figure 5.3. Figure 5.6 (a), (b), (c), (d), (e), (f) and (g) correspond to experiment numbers (2, 6, 5, 4, 8, 11 and 14) which can be found respectively in Figure 5.6. In all the extrusions the temperature of the cross sections, show a similar distribution pattern.

This pattern indicates that the higher temperature appears at the outside of the section and the lower temperature at the inside of the section. All the temperatures of the extruded sections show an increase from the initial temperature.

At the position of the corners of the sections it can be seen that due to higher deformation the temperature increase is also higher. This is likely the result of the combination of friction and deformation caused by local stress concentrations.

It can also be seen when other parameters are the same that a lower extrusion speed compared to higher extrusion speeds give a lower temperature increase in the extruded section. This is shown in Figure 5.4 (b), (c), (d). If the extrusion speed is very high there will be a shorter exposure time for the mechanical energy to be transformed into heat causing a higher temperature of the extrudate.

The phenomenon we can see are that with constant initial temperature a variation in extrusion speed will also have a significant effect on the extrusion temperature. Higher speed means a shorter time for the mechanical energy to be absorbed by means of deformation instead it will be released in the form of heat and affects the temperature of the extrudate. This can be seen in Figure 5.4 (a), (c), (e).

In Figure 5.4 (c), (f), (g), it can be seen that with constant extrusion parameters the dominant factor is the shape of the geometry. An increase in complexity, i.e. a hollow section, will give a higher extrusion temperature, as is to be expected.

The predicted temperatures in figure 5.4 show a reasonable correlation with the measured temperatures. The temperature simulation of the rectangular section shows a reliable temperature distribution.

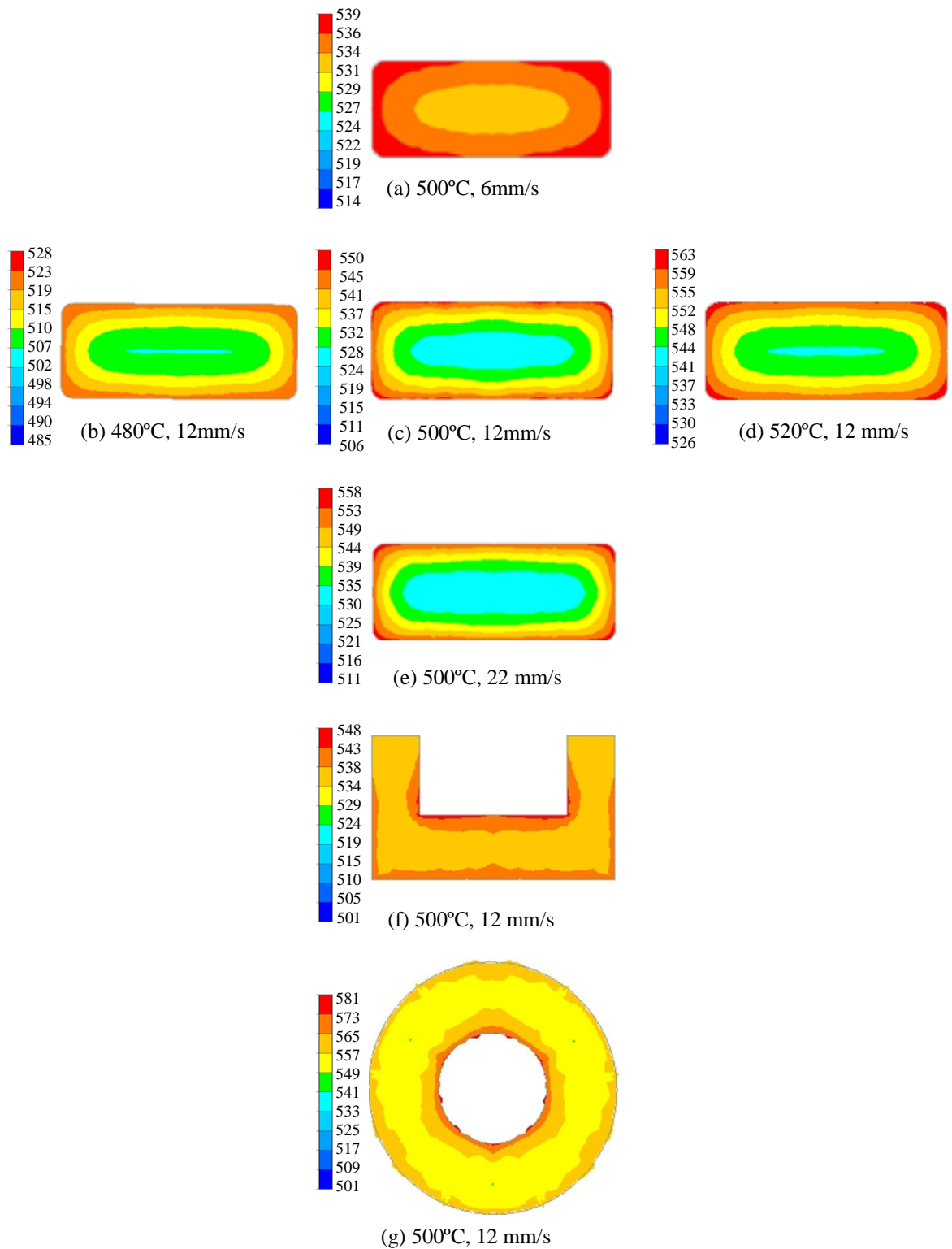


Figure 5.4 Temperature distributions in the cross section of the extruded samples (a), (b), (c), (d), (e), (f) and (g) (Temperature T in °C)

The U-shaped section shows a temperature increase on the corners caused by shape change which will increase friction and deformation. The tube section shows the highest temperature on the inner wall caused by material flow across the mandrel.

### 5.3.1 Strain

Strain is an important variable in micro structure prediction, in particular in grain boundary migration. The strain is the Von Mises equivalent Strain. The strain is useful in calculation of surface area per unit volume of the grain which is required for structural calculations. The predicted strains for the selected experiments are shown in Figure 5.5. The strain mainly affects the strain rate. The strain rate distribution is affected by the geometry condition imposed.

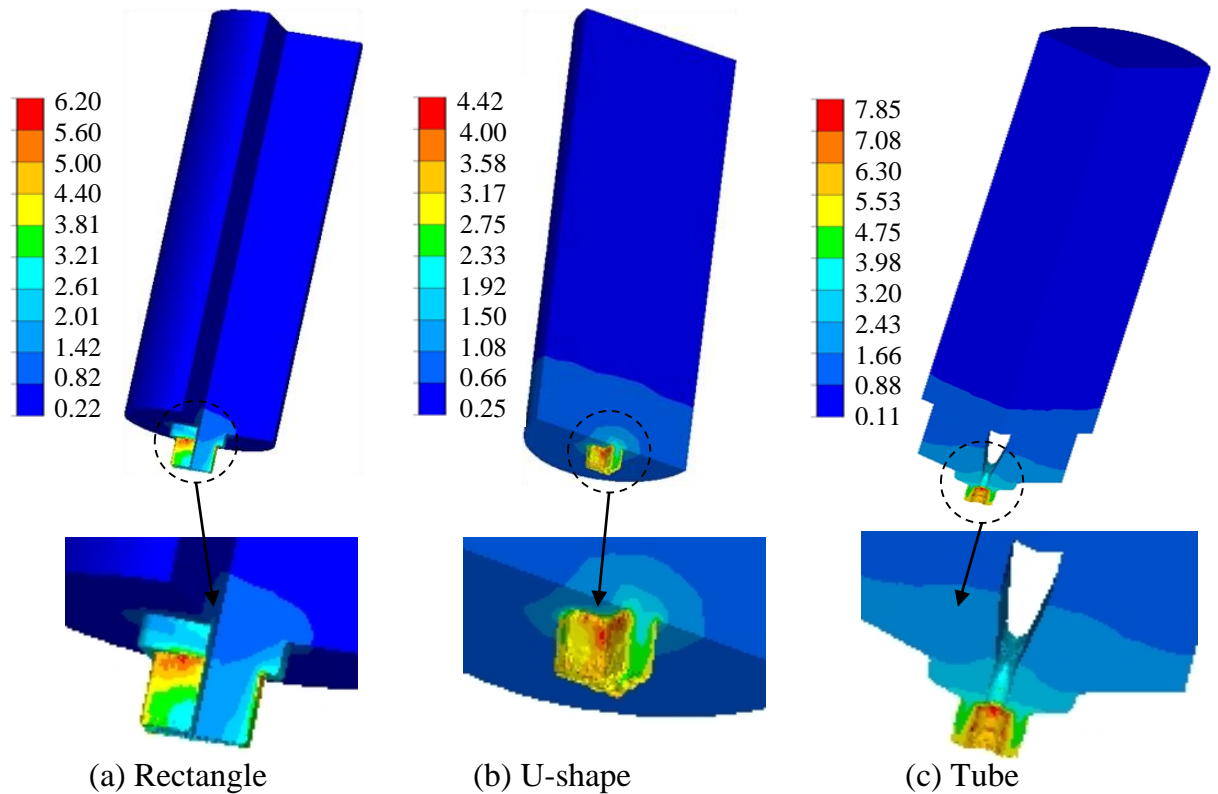


Figure 5.5 Strain distributions for the three extruded shapes at 500°C and 12mm/s ( $s^{-1}$ )

The U-shape section and the tube section have a more complex shape which results in



more inhomogeneous strain in the billet. The visualization of the predicted distribution of temperature and strain over the extruded sections is realistic. It seems that geometry influences the temperature increase the most. It can be concluded that the larger deformation results in higher strain. Together with the effect of friction between the die land and the billet, the deformation of the structure results in the temperature increase. All graphs are represented at a ram displacement of 35mm.

A large part of the billet has very low equivalent strain. When the material passes through the die orifice the equivalent strain increases significantly. The highest equivalent strain is represented by the red color which happens in places where high deformation is expected which can be clearly seen in Figure 5.6.

Figure (a), (b), (c), (d), (e), (f) and (g) correspond to experiment numbers 2, 6, 5, 4, 8, 11 and 14 which can be found respectively in Figure 5.6. In all the extrusions the equivalent strain of the cross sections, show a similar distribution pattern. This pattern indicates that the higher equivalent strains appear on the outside of the section and the lower equivalent strains at the inside of the section. The difference is compared to the temperature distribution for the five rectangular experiments, the temperature and initial ram velocity will not influence the equivalent strain distribution.

At the position of the corners of the sections it can be seen that due to higher deformation the equivalent strain increase is also higher. This is very likely the result of the effect of geometry. It can also be seen from Figure 5.6 (a), (b), (c), (d), and (e) that within the experiments of the rectangular section the equivalent strain patterns are quite similar. In general the higher values of strain appear at areas where the extruded section shows dimensional variation such as in corners and at the edge.

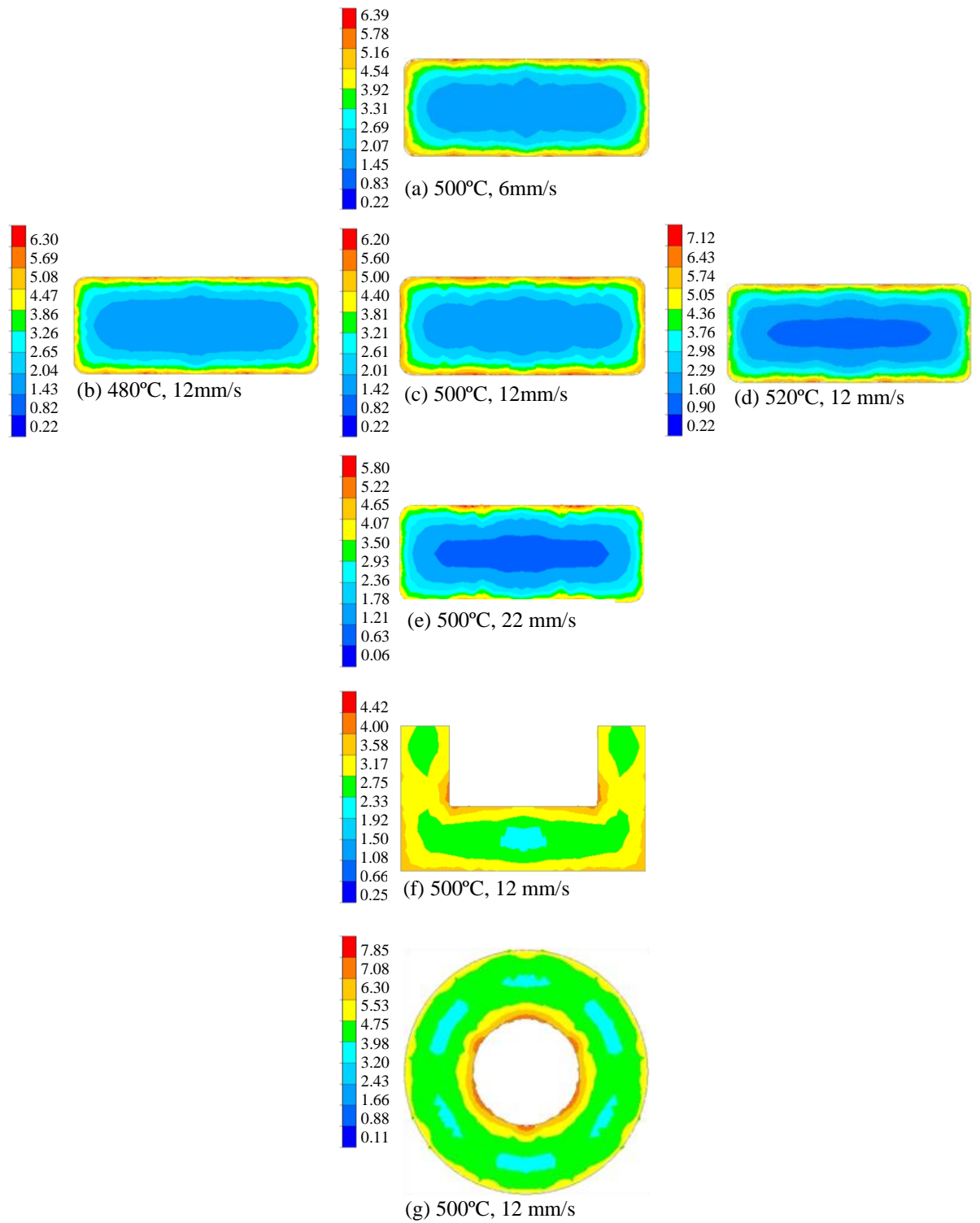


Figure 5.6 Equivalent strain distributions in the cross section of the extruded samples (a), (b), (c), (d), (e), (f) and (g)

In the rectangular shapes it can be observed that high strain areas occur at the edge of the geometry. The extrusion ratio influences the strain. In the rectangular shapes' extrusion ratios are the same and as a result the equivalent strains are similar. The tube section has a higher extrusion ratio resulting in higher strain. In this case there is also more surface area which leads to higher strain. Strain rate and temperature will not influence strain. Strain is mainly influenced by the extrusion ratio.

### **5.3.2 Strain rate**

During the steady state stage of the deformation the distribution of strain rate will not change significantly. In figure 5.7 an overall view of the strain rate in the extruded billet is given. We need to look in the die area to distinguish distributions. Only at the die exit (see Figure 5.7) it can be seen that equivalent strain is increased slightly which is caused by the pocket of the die. This is probably caused by the influence of the cut off mechanism.

The strain rate is a crucial parameter because it is critical in assessing the structure of the extrudate. Only strain rate distributions on the cross sections will be presented. During the steady state of the extrusion the strain rate is near zero for most of the billet in longitudinal direction. Only where the material approaches the die entry the strain rate values change dramatically. Once the material enters the die land the strain rate will be reduced rapidly to nearly zero again. For all the extrusions, Figure 5.7 show the strain rate on the cross section is nearly zero except at the edge around the section.

Strain rate is completely ram speed and section shape dependent which can be seen from Figure 5.7 (a), (b), (c), (d), and (e) where, for the same extrusion ratio, and even at different temperatures the strain rate increases with the increase of the ram speed. The strain rate is influenced by extrusion ratio. When extrusion ratios are similar it is mainly determined by the ram speed when other parameters are the same. It can be seen in the hollow section extrusion that the strain rate is higher because of the high extrusion ratio and a greater proportion of the cross section is slender.

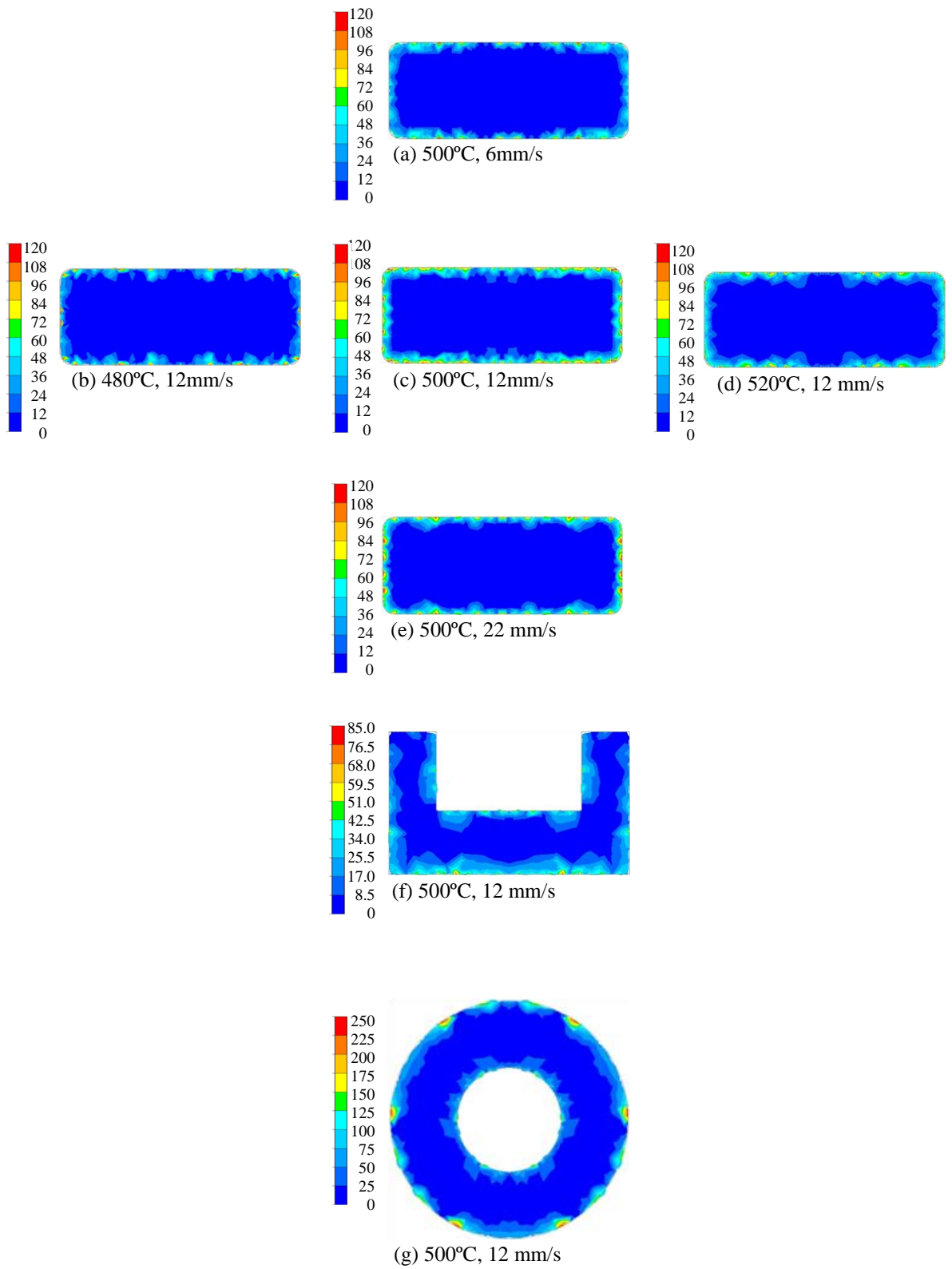


Figure 5.7 Strain rate distributions in the cross section of the extruding samples (a), (b), (c), (d), (e), (f) and (g)

With higher speeds, in a shorter time the mechanical work done on the billet cannot be accommodated by increased plastic deformation, thus producing higher temperatures. The course shape of the strain rate contour is a numerical artifact and will set a limit to the accuracy of the predicted microstructure distribution due to the sensitivity of flow stress to strain rate.

### 5.3.3 Load analysis

The pressure can vary depending on the alloy and its condition, the extrusion ratio, diameter and length of the billet, initial temperature of the billet and tooling, ram speed and the shape of the extrudate. (See Figure 5.8). Typical load versus ram travel curves for solid extrusion were acquired for all the rectangular extrusion simulations. Approximately 90-95% of the mechanical energy is transformed into heat. For the solid section in the experiments the load versus ram travel curve show the following separate stages; the curve for the rectangular shape  $T = 475C$  and speed is 21 mm/s is used as an example. Four stages can be seen in the extrusion from the curve. O-A is the billet upsetting stage in which the material began to fill the container. At stage A-B the container is being completely filled. In stage B-C the material is filling the die and pressure starts to build up. At point C peak load is reached.

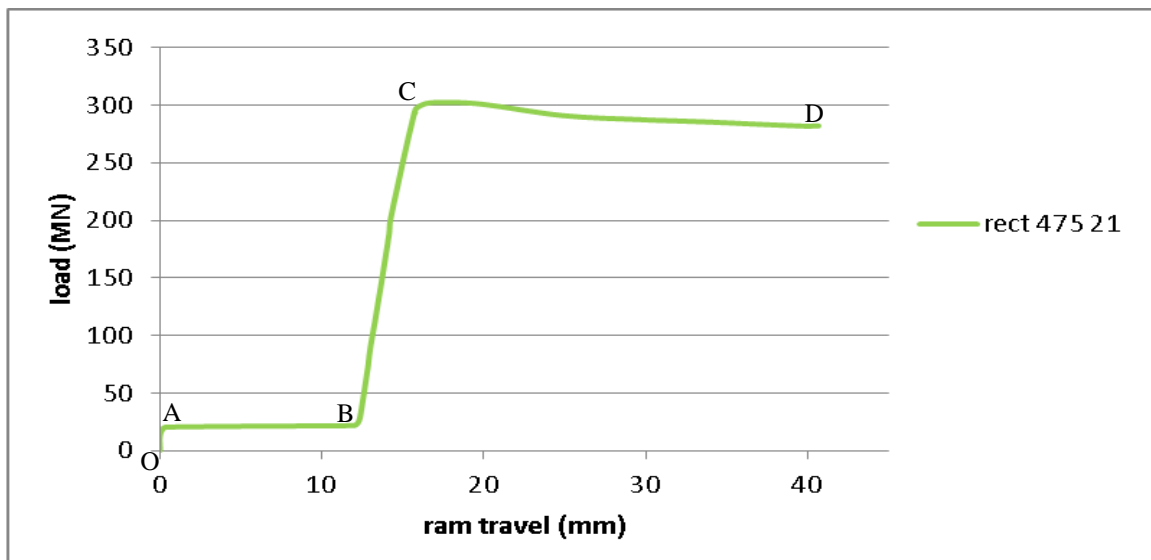


Figure 5.8 The various stages in the extrusion of a solid section

From point C-D the section is extruded where a drop in pressure can be observed due to the reduced container friction until the process reaches the steady state. It was recognised that the data collection method led to some inaccuracy in the data but the data quality is sufficient to demonstrate some correlation with predicted values (see Figure 5.9). One experiment (500C, 12mm/s) was used to show load evolution over an extrusion cycle and to compare it with predicted load evolution.

The simulated load evolution results were collected from a position at the die exit and are shown in Figure 5.12. It indicates that at this point, during one billet extrusion cycle, the load will increase to a peak load of 260 ton. After which it decreases to a level of 230 ton. The experimental readings pressure was collected with a pressure transducer in the main cylinder of the press, see Figure 3.2. The pressure readings are converted into load values. The measured load evolution curve is showing a load decrease from 236-218 ton. It can be noted that the predicted values are higher than the measured values. From the pictures showing both the temperature evolution (Figure 5.2) and the load evolution (Figure 5.9) display a consistent trend. This could be caused by inaccuracies during the collection of the readings. It is expected that higher predicted temperatures will result in lower predicted loads.

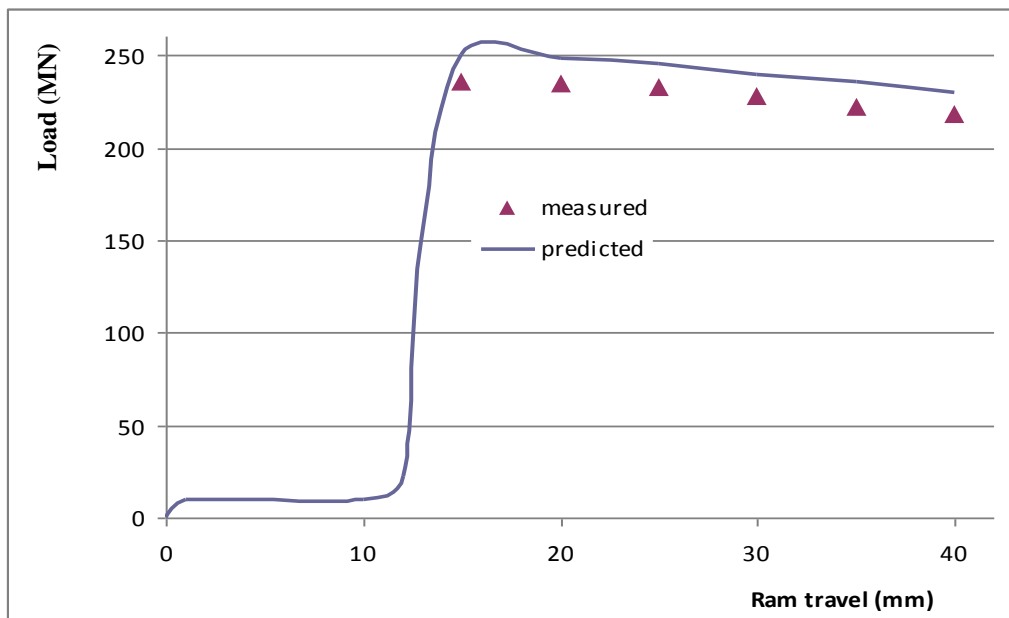


Figure 5.9 Pressure evolution during an extrusion cycle

Although there are some discrepancies, predicted values show a reasonable correlation to measured values and it is safe to say that these results are reliable and can be used in microstructure simulations.

For the hollow section in the experiments the load versus ram travel curve show the following separate stages; the curve for the rectangular shape T = 500C and speed is 12 mm/s is used as an example. Five stages can be seen in the extrusion from the curve. O-A is the billet upsetting stage in which the material began to fill the container. At stage A-B the container is completely filled. In stage B-C one can observe shear of the material over the ports in the die. In stage C-D the material fills up the separate ports of the die. At point D the discrete streams reach the bottom of the welding chamber. In stage D-E the load is increasing because the material is filling the welding chamber at point E the tubular product begins to form and the load required reaches the maximum. From point E-F the section is extruded where a drop in pressure can be observed due to the reduced container friction until the extrusion process reaches the steady state. (See Figure 5.10).

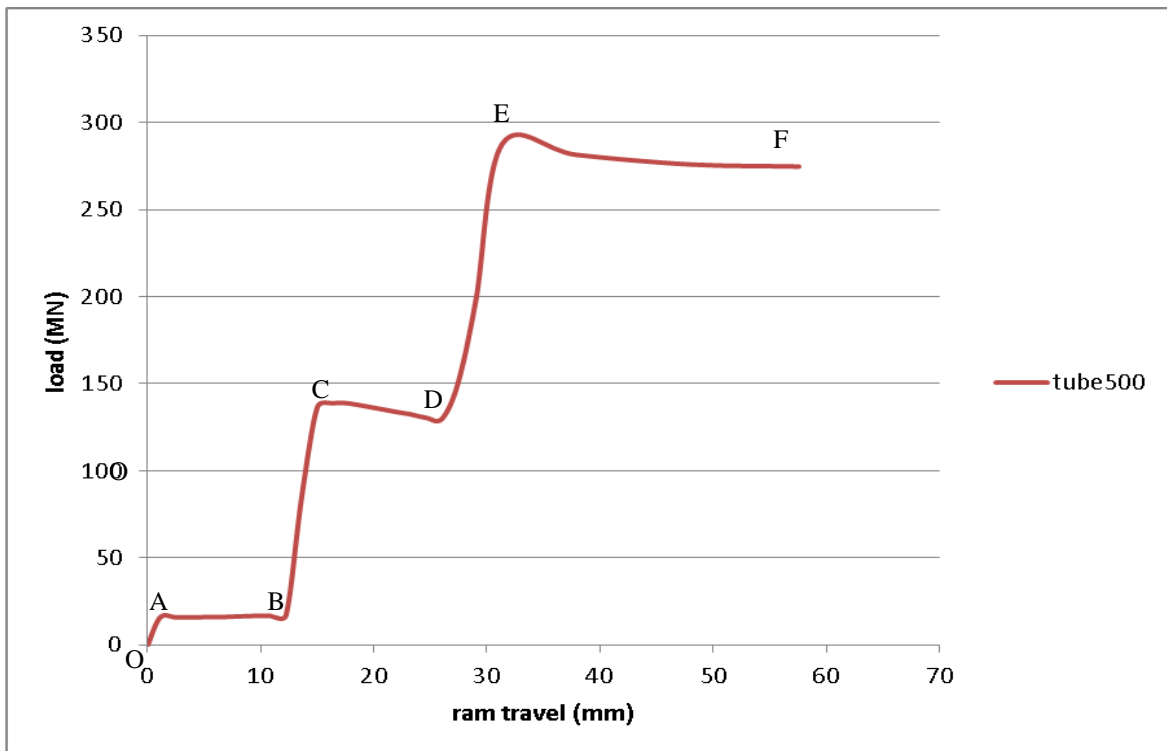


Figure 5.10 The various stages in the extrusion of a hollow section

The predicted load variations for different section extrusions are displayed in figures below. An increase of the extrusion speed results in higher peak load. This phenomenon applies to all the extruded shapes with similar initial temperatures.

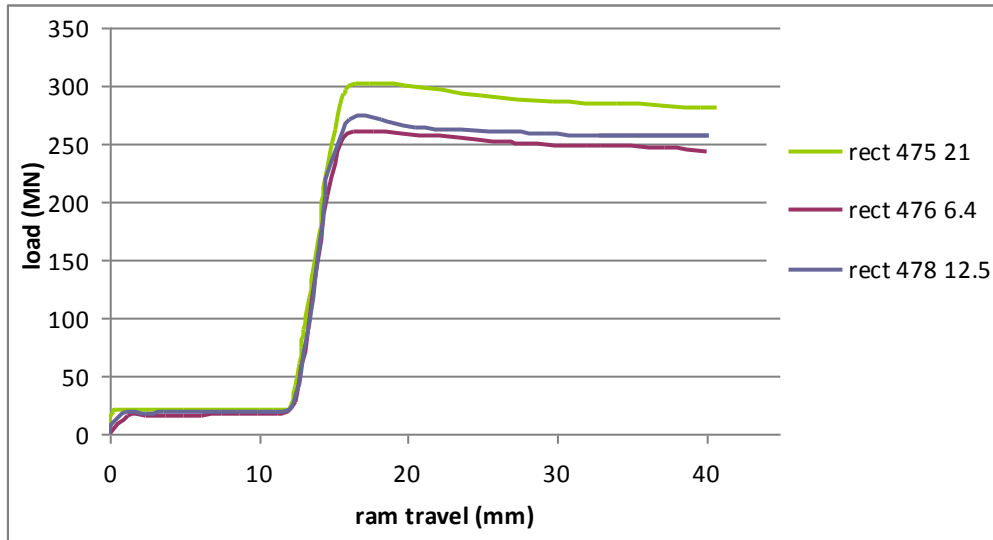


Figure 5.11 Load versus ram travel for the rectangular shape at low temperature with varying speeds

It can also be seen from table 5.11 when extrusion speeds are equal that there is an increasing effect on the peak load when the initial billet temperature is lower.

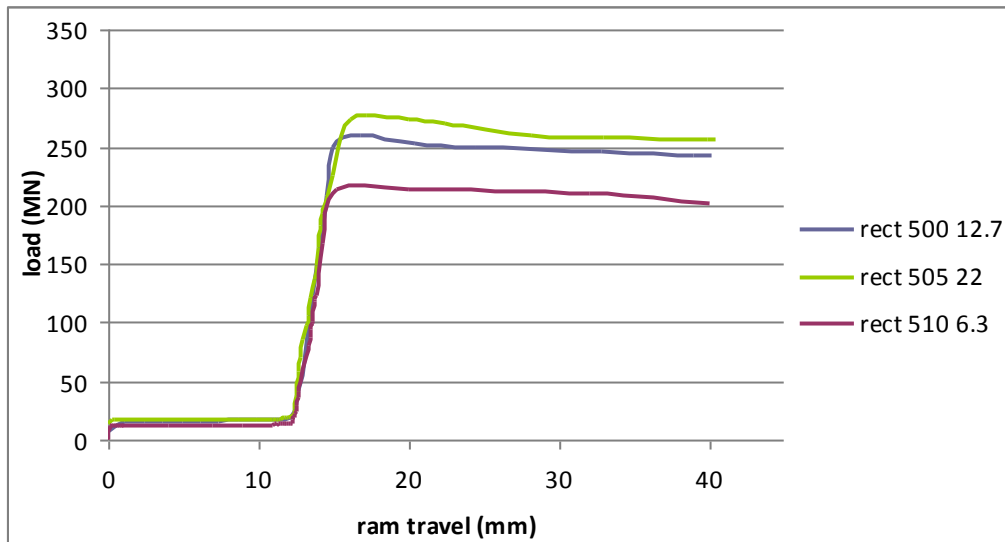


Figure 5.12 Load versus ram travel for the rectangular shape at low temperature with varying speeds



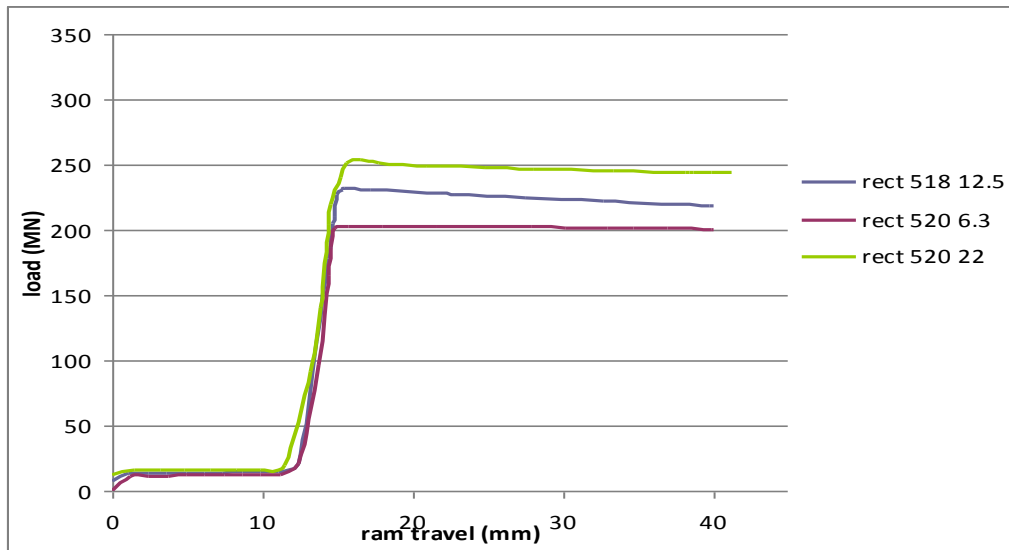


Figure 5.13 Load versus ram travel for the rectangular shape at high temperature with varying speed

set speed	set Temperature	Load(MN)
6	480	260
	500	220
	520	200
12	480	275
	500	260
	520	230
25	480	310
	500	275
	520	255

Table 5.2 Predicted peak loads for the rectangular shape.

The predicted load variations for U-shape section extrusions are displayed in the figure below. It can also be seen that when extrusion speeds are equal there is an increasing effect on the peak load when the initial billet temperature is lower.

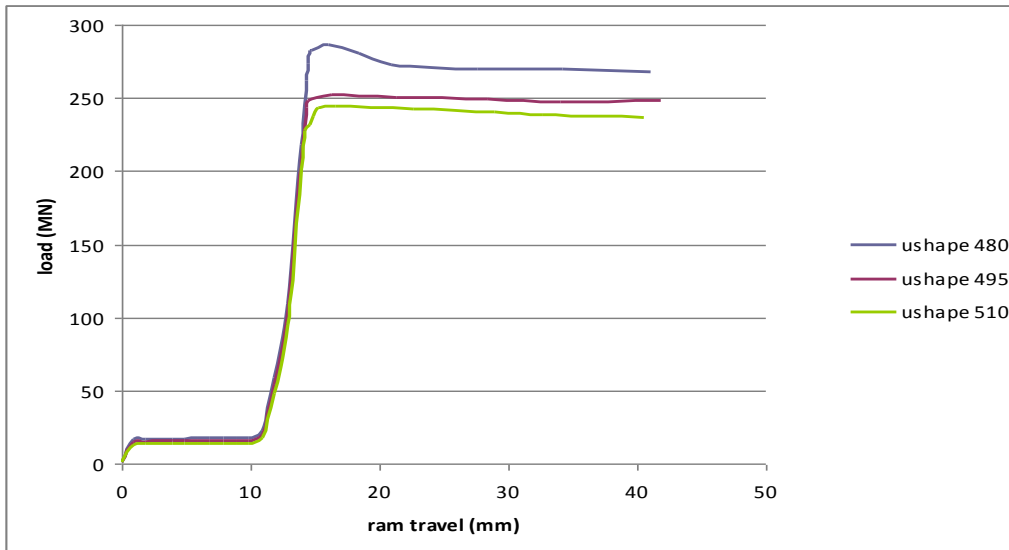


Figure 5.14 Load versus ram travel for the U-shape at varying temperatures with constant speed

The predicted load variations for hollow section extrusions are displayed in the figure below. It can also be seen that when extrusion speeds are equal that there is an increasing effect on the peak load when the initial billet temperature is lower.

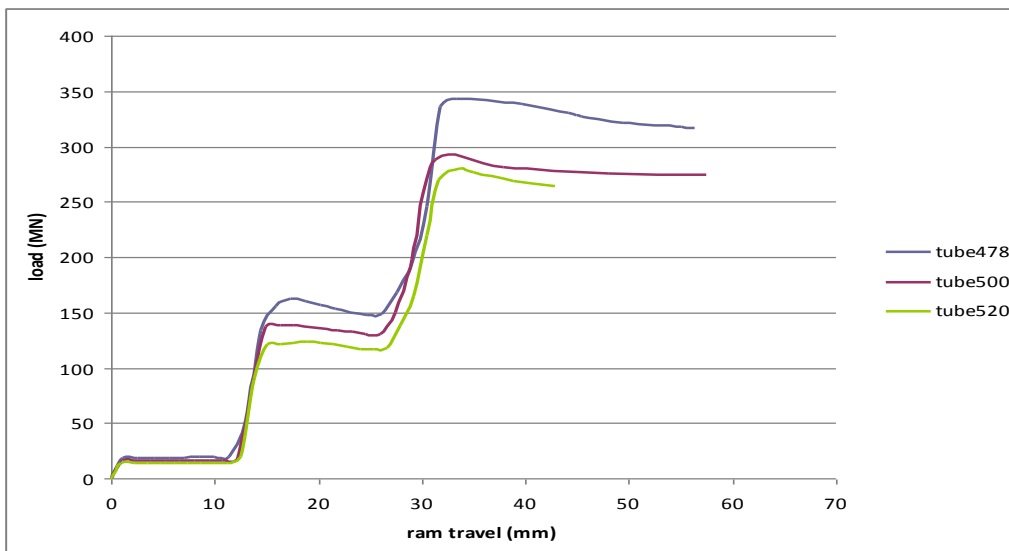


Figure 5.15 Load versus ram travel for the hollow shape at varying temperatures with constant speed

### 5.3.4 Material flow simulations

In order to study the metal flow, the grid method was used in simulations. The initial grid was the same for all the three different sections and can be found in figure 5.16.

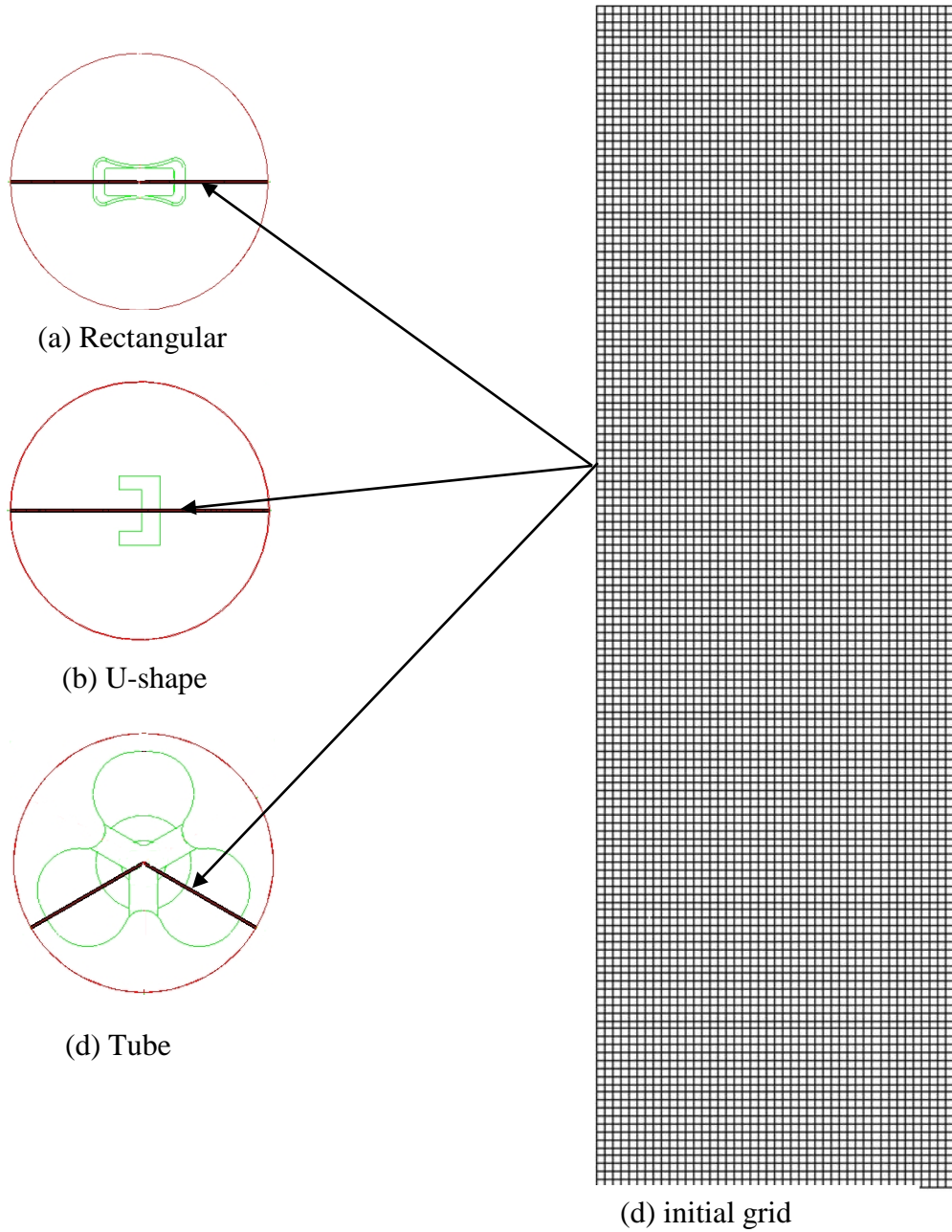
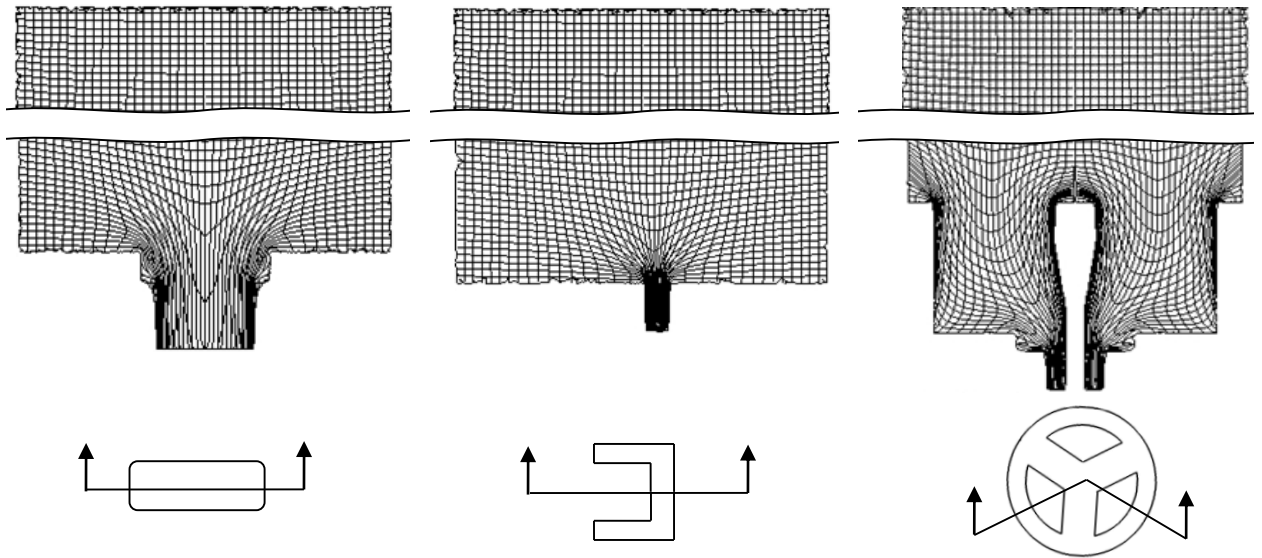


Figure 5.16 Numerical initial grids for the three extruded sections

In Figure 5.17 the grid deformation is shown for the three extruded sections. The simulated metal flow for the three geometries is given for the moment where peak load was reached.



*Figure 5.17* The numerical grid deformation for the extruded sections

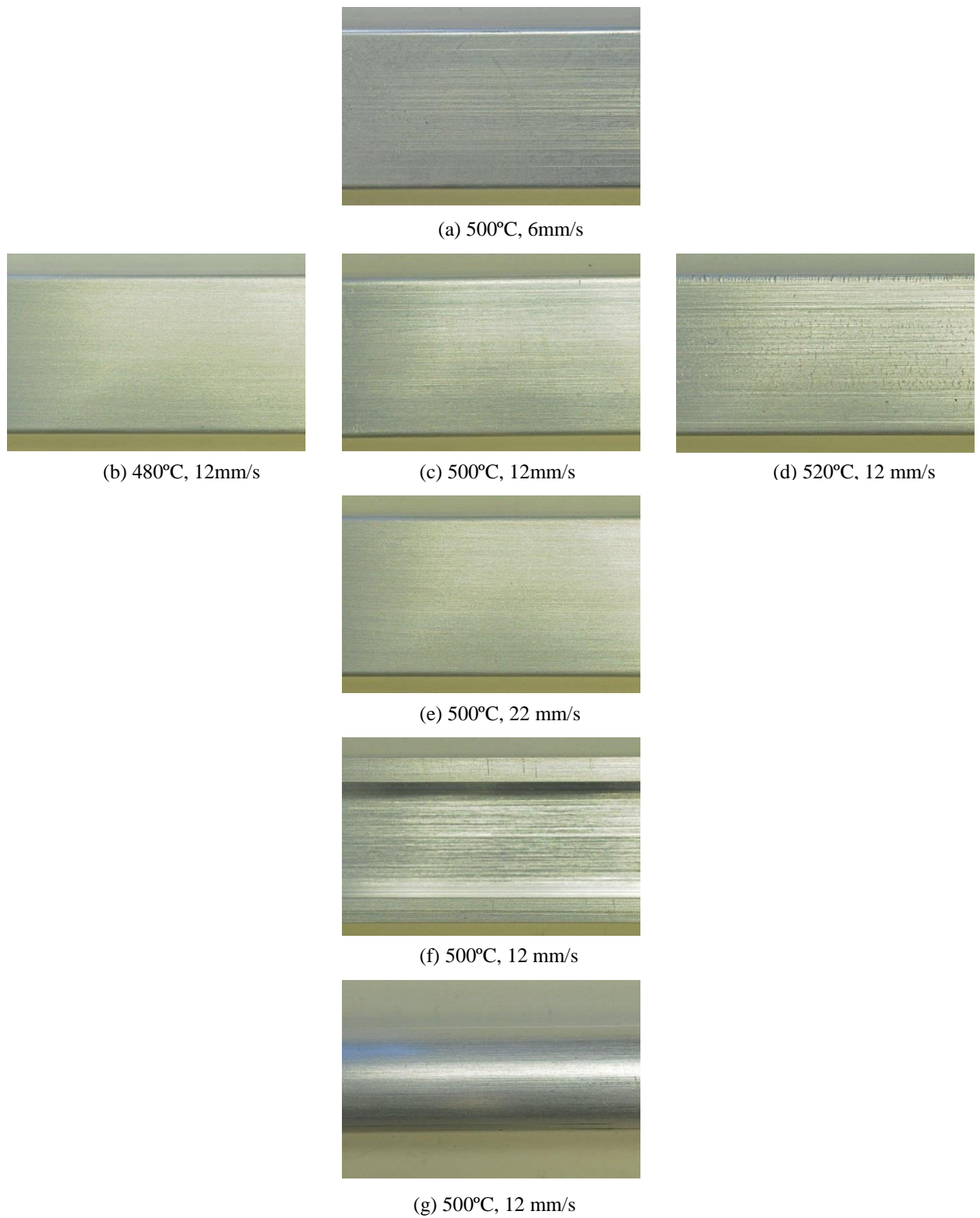
The billet length used in the experiments is quite long, 250mm, compared with its diameter of 90mm. During the extrusion most of the billet does not show much deformation. Only when the material reached the die orifice or the bridge of the tube die severe deformation took place. For the rectangular section we can observe a symmetric deformation of the grid. For the U-shape section we see an asymmetric deformation of the grid. For the Tube section you can observe the flow around the bridge before the material reaches the die exit.

The simulation of the metal flow of the three geometries show a flow pattern which is characteristic for these shapes and is what can be expected for these geometries. In figure 5.17 a number of flow characteristics can be observed. In the first place the areas with direct flow towards the die exit can be recognized as the centre flow. At the edge of the billet the dead metal areas can be identified in the corners. In between the central direct flow and the dead metal zones, areas with high shear can be observed as areas with strongly deformed structure which is visible as a concentration of extrusion lines close to each other. The metal flow of the rectangular shape (Figure 5.17) in direct extrusion can be characterized by a rapid flow of the centre material toward the die whereas the peripheral

parts of the billet are restrained by friction along the container wall and the areas around the sink in. There is symmetry to be observed which lead to even metal flow and will not contribute greatly to shape deviations in the section. Metal flow deviation usually has to be compensated through die design. The metal flow of the U-shaped section shows a quite similar flow pattern compared to the rectangular metal flow with the exception of the smaller wall thickness and the effect of asymmetry in the geometry of the section. The smaller wall thickness leads to higher concentration of areas with compact flow lines and high shear stress. These asymmetrical features will have to be compensated by die design. The similar flow is, however, not typical it stems from the sectioning of the diagram. The metal flow in the tube section is strongly influenced by the separation of the flow over the three die bridges. Within the separated metal streams over the die ports similar phenomena as with the rectangular and u-shaped section can be observed. The separation of metal flow will lead to further dead metal zone areas in the die area. Further there will also be more friction because of the larger surface area which is in contact with the metal. This will result in a higher required pressure. Observing symmetry can help in understanding the complex metal flow in hollow die extrusion across a bridge and can help to minimise the number of elements required for the simulations. The greatest advantage regarding minimising elements can be obtained when one sixth of the geometry is applied (see Figure 5.17). One sixth of the geometry avoids self-contact of elements in the simulations and will result in half of the feeder hole and half of the bridge being included in the simulation (see Figure 3.2D).

### **5.3.5 Surface cracking experiments**

When the material passes through the die orifice the temperature increases significantly and the surface quality will mainly be determined by the conditions at the moment when the material passes through the die. The highest temperature will occur on the edge of the material and more important on the corners of the section. In all the experiments the temperature of the cross sections reveals a similar distribution pattern.



*Figure 5.18* Surface quality and cracks at the beginning of the extrusion run

In Table 3.2 an overview is given for all the extruded shapes which were used in the experiments. In Figure 5.18 the surface quality is represented at the start of the extrusion run. It can be observed that the surface of the extruded sections is almost free of cracking. This pattern indicates that the higher temperature appears at the outside of the section and the lower temperature at the inside of the section. All the temperatures of the extruded sections show an increase from the initial temperature. At the position of the corners of the sections it can be seen that due to higher deformation the temperature increase is also higher. This is likely the result of the combination of friction and deformation as a result from local stress concentrations.

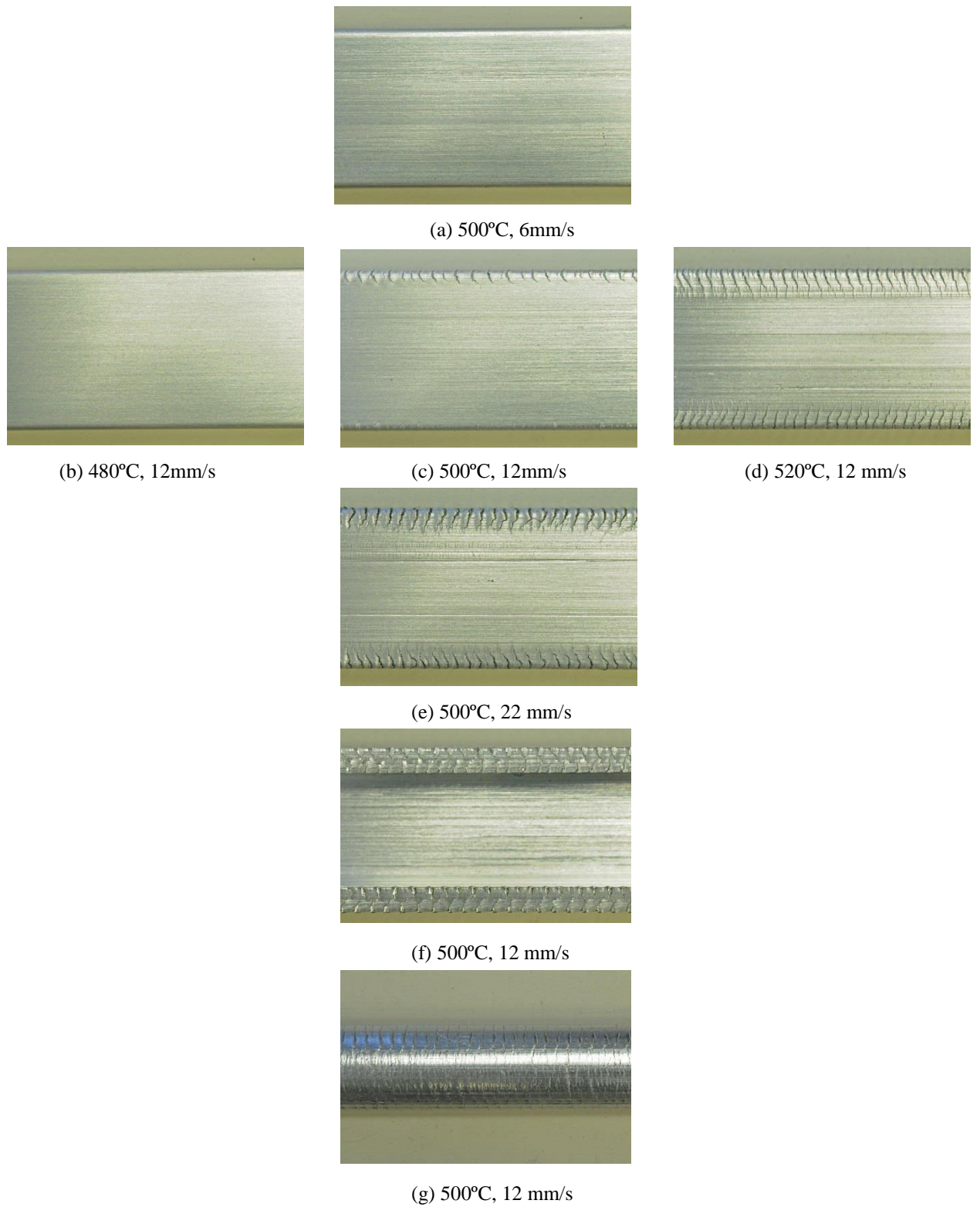
It can also be seen when other parameters are the same that a lower extrusion speed compared to higher extrusion speeds give a cracking increase in the extruded section. This can be seen in Figure 5.19(b), (c), (d).

If the extrusion speed is very high there will be a shorter time for the mechanical energy to be transformed into heat which will cause a higher temperature of the extrudate. Speed however is a limiting parameter in extrusion. Virtually all work hardening energy is transformed into heat.

The phenomenon we can see is that with constant initial temperature a variation in extrusion speed will also have a significant effect on the occurrence of cracking. This can be seen in Figure 5.19 (a), (c) and (e).

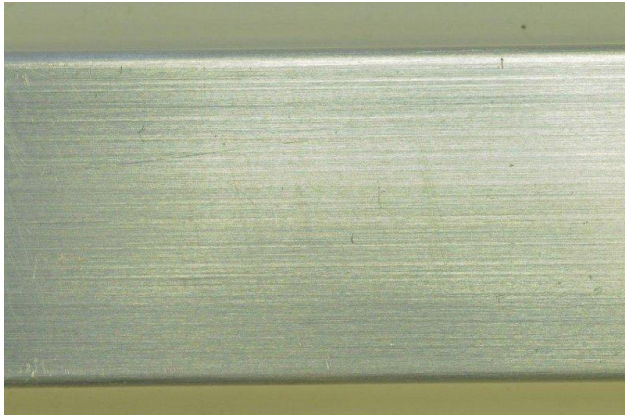
The cracking phenomenon which can be observed is that cracking will commence at some distance along the extrusion run.

In Figure 5.20 it can be seen that the specific distance along the extrusion run is dependent on the actual extrusion speed and extrusion temperature.

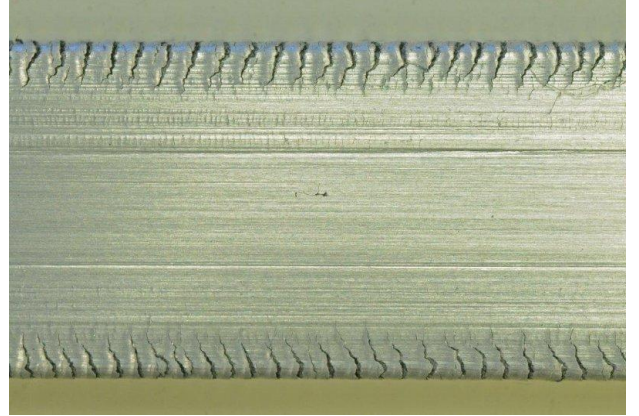


*Figure 5.19* Surface quality and cracks at the end of the extrusion run

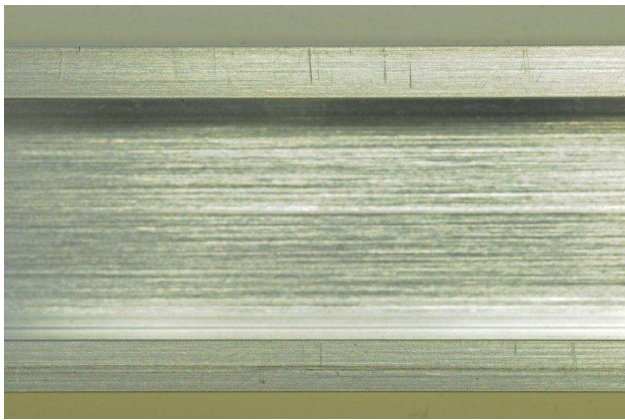




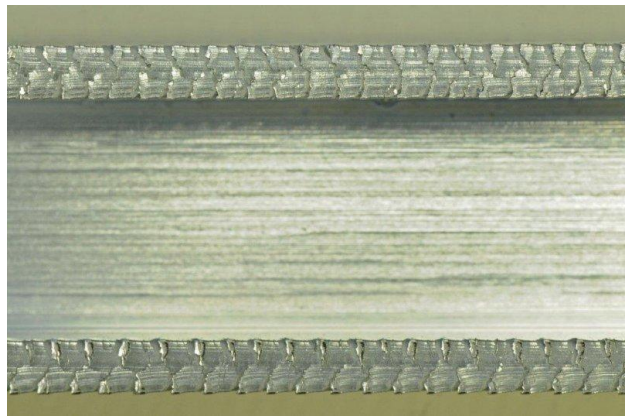
(b) 500°C, 12mm/s



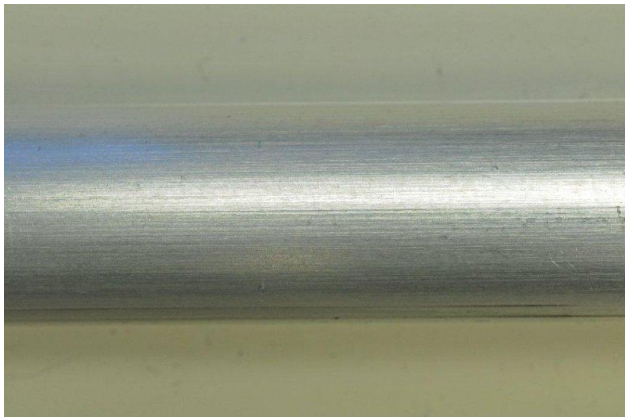
(d) 500°C, 12 mm/s



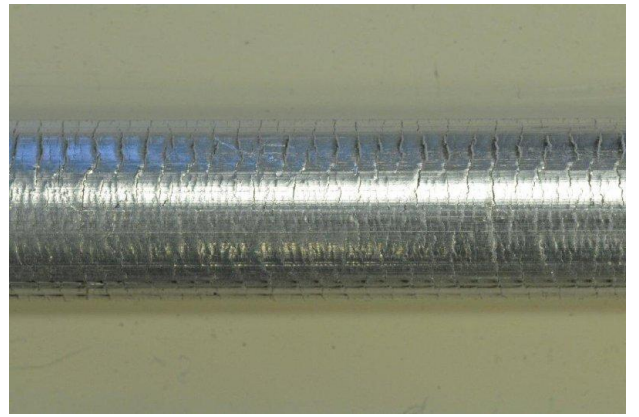
(a) 500°C, 12mm/s



(c) 500°C, 12mm/s



(f) 500°C, 12 mm/s



(e) 500°C, 22 mm/s

*Figure 5.20* Surface quality at the beginning and the end of an extrusion run for all three geometries

All the samples in Figure 5.19 are taken at 1 meter from the start of the extrusion. All the samples in Figure 5.20 are taken at a position at 1m from the end of the extrusion. It is clear that only two conditions provide a good surface quality: 500°C at 6mm/s (Figure 5.20a) and 480°C at 12m/s (Figure 5.20b). In figure 5.20 (c) cracking starts to appear due to the combination of increased temperature and increased extrusion speed.

In Figure 5.20 (d) and (e) the cracking is increasing to a level that would not be acceptable as a surface quality for extrusions. The U-shape geometry is showing severe cracking at the corners of the legs. The tube section showed cracking to such a degree during extrusion that the geometry disintegrated over the welding lines of the three bridges in the die.

### **5.3.6 Surface cracking simulations**

A suitable cracking criterion needs to be able to predict the cracking phenomenon which occurs during the extrusion experiments.

Peng and Sheppard (2004) have identified four cracking phenomena:

Phenomenon 1, occurs on the extrudate surface and is not seen at other locations

Phenomenon 2, the extrusion suffers serious surface cracking during extrusion at high initial temperatures and is not so detrimental at low initial temperatures.

Phenomenon 3, in some cases, surface cracking occurs during the middle period of the process and becomes more serious as the process continues.

Phenomenon 4, the severity of the cracking is less in the direct extrusion mode than in the indirect extrusion mode.

The most predominant factors governing the occurrence of surface cracking seem to be speed and temperature. Temperature distribution over the cross section of the profile is not constant. In Figure 5.6c it can be seen clearly that the highest temperatures occur at the section surface and in particular at the corners of the rectangular shape. From Figure 5.2 it can be seen that the temperature continues to increase over the extrusion cycle. Peng and Sheppard (2004) have indicated that the temperature at the centre of the extrudate rises faster than the temperature at the surface of the extrudate and that towards the end of the cycle temperature differences are small. Temperature distribution is showing a sharp gradient near

the surface area. This is of importance since it is the temperature which is critical for surface failure such as cracking. If surface cracking were to occur it would appear immediately on the surface of the extrudate after it leaves the die. Therefore it is evident that the die land area influences cracking phenomenon. The cracking criterion which according to Peng and Sheppard shows reliable results in predicting cracking for all cracking phenomena is the empirical one. In the experiments the cracking phenomenon which occurred could be described as; surface cracking which commences at some distance along the extrudate depending on the extrusion parameters.

Clif et al. (1996), Ko et al. (1996) and Domanti et al. (2002) have indicated that the Cockcroft and Latham criterion is the best amongst the various existing criteria for the prediction of fracture initiation for extrusion.

$$\int_0^{\varepsilon^R} \frac{\sigma^*}{\sigma_{eq}} d\varepsilon_{eq} \geq C3 \quad (5.1)$$

In which  $C3$  is the critical value,  $\sigma^*$  is the maximum principal stress and  $\sigma_{eq}$  is the equivalent stress,  $\varepsilon^R$  the effective strain at fracture. This criterion considers the combinative effect of maximum principal stress normalized by the equivalent stress and the equivalent strain during deformation. It is assumed that when  $C3$  reaches a certain value, crack will be initiated. Peng and Sheppard (2004) have indicated that the predicted value of the cracking criteria decreases from the edge to the centre of the material. Figure 5.21 shows the simulation results of a simulated crack together with the simulated value of the cracking parameter (550°C, 22mm/sec). The simulated section represents half of the rectangular section (11mm).

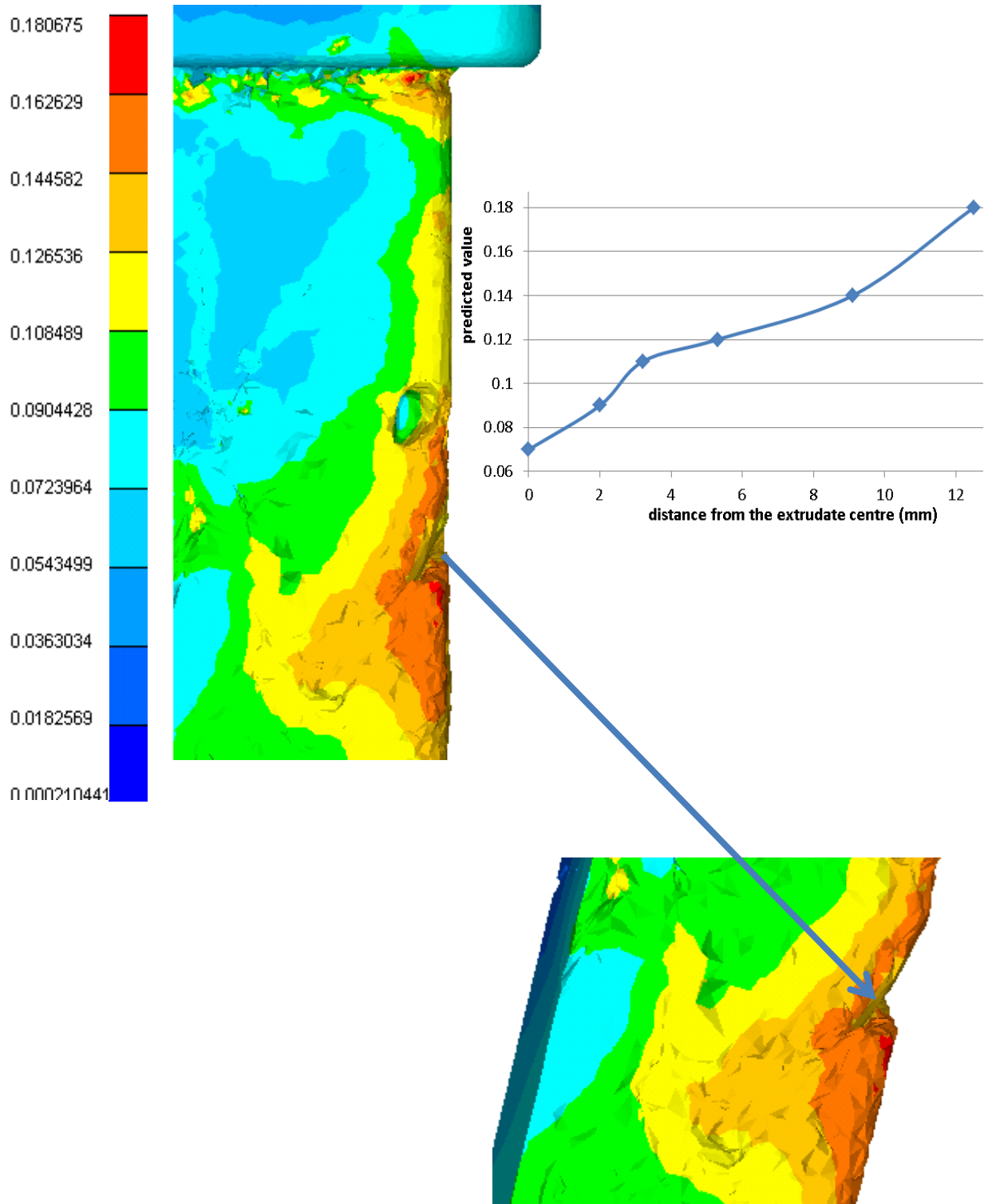
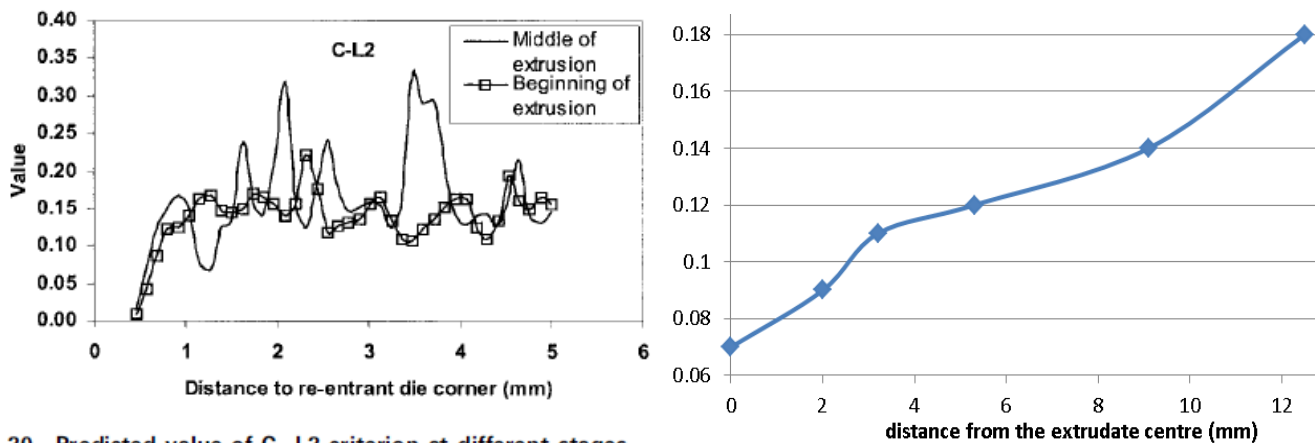


Figure 5.21 The simulation results are presented together with the simulated value of the cracking parameter (550°C, 22mm/sec)

Maximum values for cracking criteria are first reached near the surface and corner areas of the extrudate. If a cracking criterion can be determined this would first be reached on the surface and corner area. This is in agreement with the experiments.

Cockroft and Latham (1986) considered the effects of the maximum principal stress over the plastic strain path to fracture. Peng and Sheppard (2004) have indicated that principal stress occurring in extrusion of hot aluminium differs depending on the extrusion ratio. At the same time maximum stress on the extrudate surface is higher during low temperature extrusion compared to high temperature extrusion. This indicates that prediction of surface cracking would be possible by assuming Cockroft and Latham criterion C-L2.

Simulations have been performed on one rectangular shape using the Cockroft and Latham criterion. The predicted values of Cockroft and Latham criterion are in good agreement to the predicted values which were found in Peng and Sheppard (2004), see figure 5.22. The value of the simulated cracking parameter at a distance of 12 mm from the centre is 0.18. The values of the cracking parameter according to Peng and Sheppard (2004) is approximately the same.



20 Predicted value of C-L2 criterion at different stages

Figure 5.22 Predicted values of Cockcroft and Latham criterion C-L2 (Peng and Sheppard 2004)

Values at a distance from the centre of approximately 5mm vary from 0.14 – 0.17. See Figures 5.22 and 5.23. The simulated results for this rectangular geometry show values between 0.16 – 0.18.



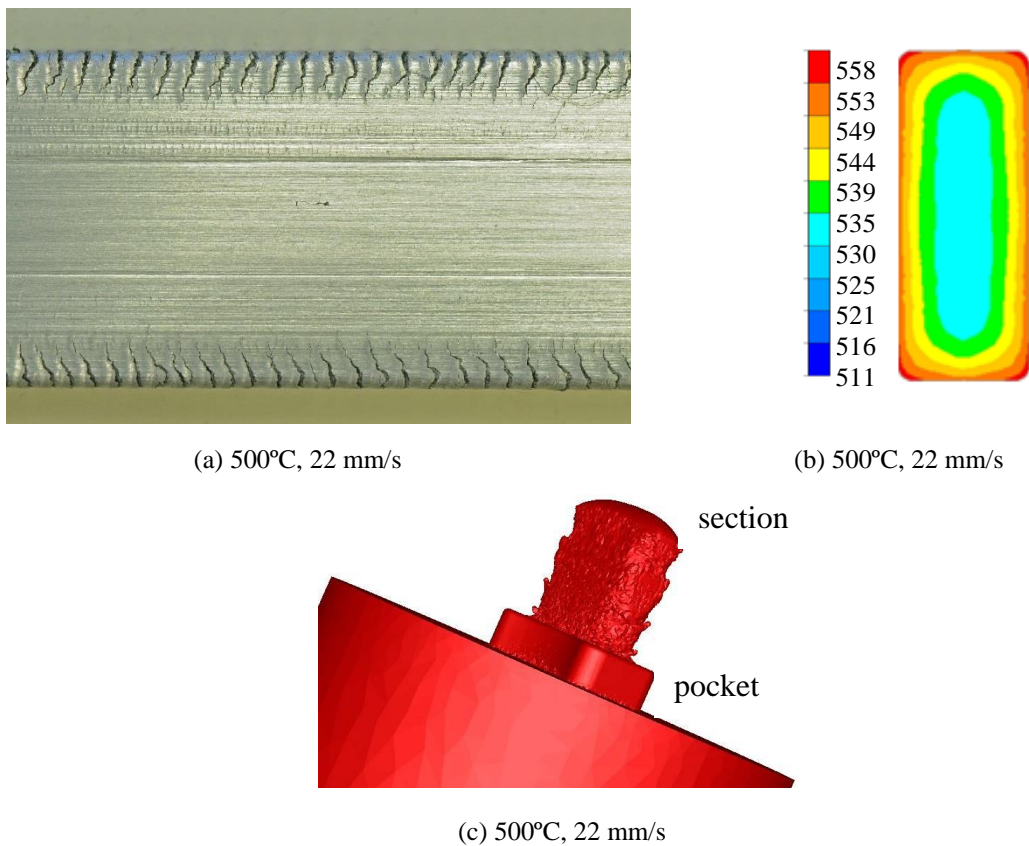


Figure 5.23 The visible cracking on the rectangular section corners, together with the temperature simulation and a simulated crack.

Figure 5.26 show the experimental sample with cracks in (a), the simulated temperature in (b) and a simulated crack on (c). The extruded section in figure 5.26 (c) is 10 x 22 mm. The extruded length is approximately 20 mm. Crack simulations are performed using element removal. The simulated crack does not represent an exact cracking situation. Due to FEM software limitation there is a difference between the real sample and the simulated crack. The crack frequency is different from the experiment due to the early breaking in the brittle phase at the end of an extrusion.

Surface cracking is closely related to the temperature rise during extrusion. If the heat generation near the die land area increases the total temperature in excess of the solidus point, localised melting can occur which can cause severe cracking of the surface. This

coincides with previous studies (Sheppard 1999b), (Paterson 1981), (Vierod 1983), (Sheppard, Tunnicliffe and Paterson 1982).

#### **5.4 Conclusions**

The load predicted by the simulation of the profiles used in the experiments was within 7 % of experimental results. The influence of the variation of extrusion parameters as well as section geometry on temperature and load was in reasonable agreement for the geometries investigated. The prediction of the extrusion temperatures was close to those predicted and within 3% of simulated values. Section geometry and extrusion ratio influenced the extrusion temperature and load.

Material flow throughout the ram stroke was well predicted using Forge2009®. Differences in metal flow for the various shapes could all be satisfactorily modelled using the program. The complex material flow across the bridge of a hollow die was modelled taking into account the inaccuracies due to temperature effects.

The cracking simulations were performed with the implicit finite element code Forge2009® with user input written in Visual Fortran®. Surface cracking experiments show that the speed and temperature had a significant influence on cracking phenomena during extrusion. Using these values and the induced stress state allowed preliminary prediction of surface deterioration. Increased section complexity was observed to enhance the occurrence of cracking.

## **6 Results and analysis structural**

### **6.1 Deformation during extrusion**

During the extrusion of aluminium, energy much of which is in the form of dislocations, is stored within the material. In materials such as aluminium, in which the incidence of stacking faults is high the rate of cross slip and climb of dislocations is enhanced. Movement of dislocation is thus enhanced and fairly stable subgrains are established. This strengthens the material in the as-worked condition. It is the basic relation between the sub-structural parameters and the deformation variables which enables control of the industrial process. It is therefore necessary to recognise the factors which may induce recrystallisation and static (as opposed to dynamic) recovery. Taking these factors into account and enabling the measurement and prediction of sub-grain size, subgrain misorientation, and the volume fraction recrystallized allows the basic structure and properties to be presented in mathematical form. Dynamic recovery is the process by which a decrease or increase of dislocation density occurs by motion and annihilation of individual dislocations. Recrystallisation can only occur after deformation but should be prevented by a sufficient rate of cooling. Further deformation (for example in a stretching operation) would lead to movements of the dislocations and aid recrystallisation by forming high angle boundaries. Dynamic recovery certainly occurs during deformation and hence the microscopic structure is more complex than it would be suggested by microscopic evaluations. The structure of the extruded section must be further investigated using EBSD techniques. The actual grain morphology at the various geometries used in the experiments must be analysed using EBSD techniques. The deformation of the original grain structure during extrusion will lead to a recrystallised structure after extrusion if not quenched sufficiently. The grain structure after extrusion can be made visible using light optical techniques. However for the detection of low angle grain boundaries and the accompanied formation of subgrains, the application of EBSD techniques is very suitable.

The structure of extrudates which had been quenched exhibited elongated grains. The structures of extrudates after extrusion at elevated temperatures and inadequate cooling were unstable and static recrystallisation was observed resulting in the loss of substructure. This was most obvious at the extrudate surface where the increased degree of deformation and



temperature variations provided the driving force for nucleation by coalescence and by migration of high angle boundaries. The substructure of extrudates at room temperature after rapid cooling from extrusion temperature, generally exhibited a dynamically recovered structure in which the original grains were elongated in the extrusion direction and usually contained smaller subgrains in the center. Subgrain size increased with extrusion temperature and the internal dislocation density reduces with increasing extrusion temperature. The surface of the extrudate was subjected to higher degrees of deformation which led to a recrystallised surface area, Clode (1992).

## **6.2 Subgrain size and misorientation**

The structure of the extrudate is dependent on the thermo-mechanical cycle but the most important topographical features of the substructure are the subgrain size and misorientation which determines the metal's response to any further exposure to increases in temperature and deformation. This might occur in processing such as a stretching operation and quite radical changes if subjected to solution soaking. In the remainder of this chapter the microstructural changes observed by using optical microscopy and electron microscopy will be reported and discussed. The subgrain size and misorientation was investigated using EBSD and predicted using the deformation model written into the commercial computer program Forge2009®.

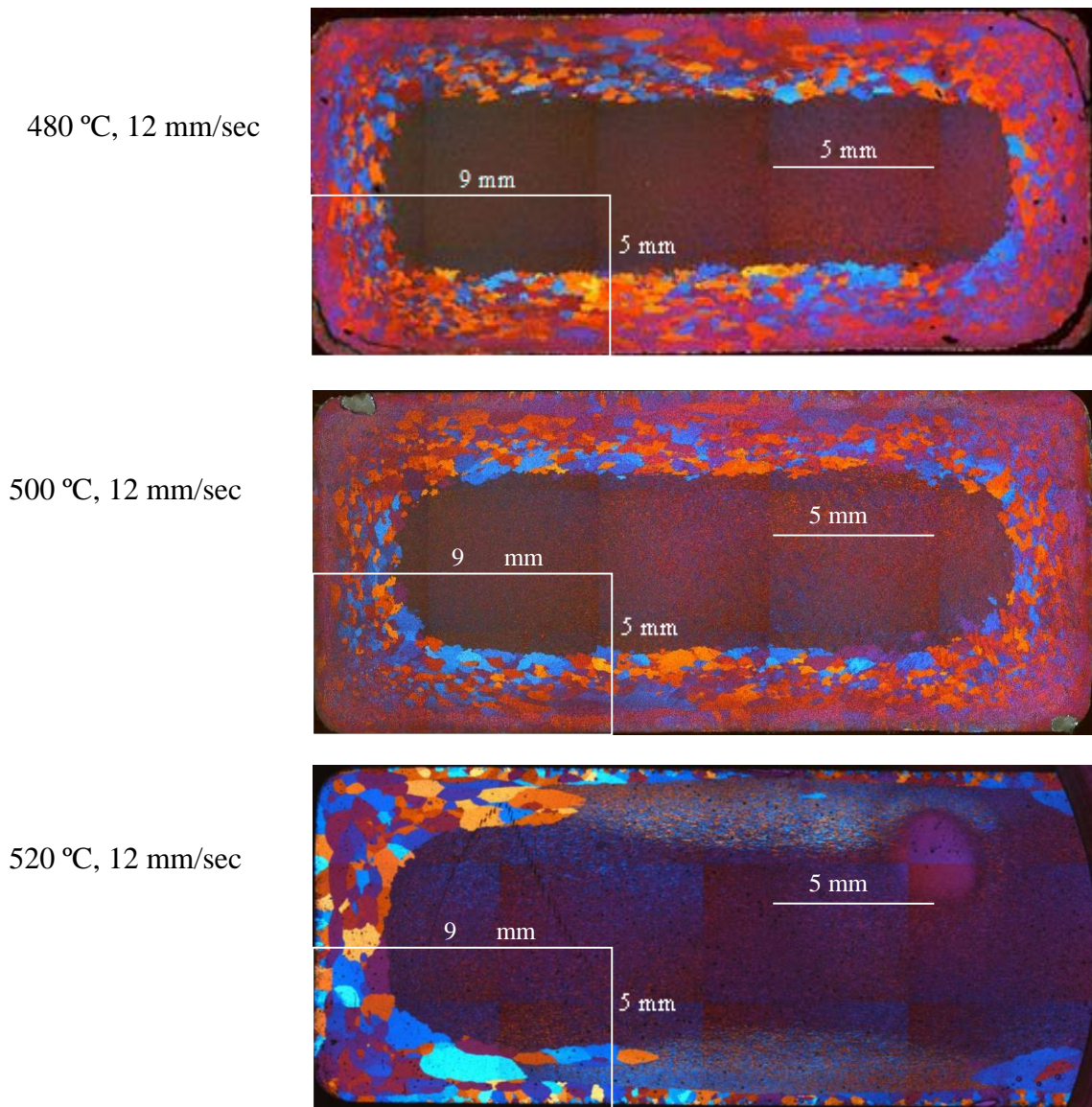
### **6.2.1 Optical micrograph investigation**

Grain structure of extruded alloys can have an impact on the performance of the final product. We might expect to see variations in damage tolerance, fatigue crack propagation, corrosion, and a number of other properties. The extrusion process may produce unrecrystallised fibrous grains, fully recrystallised grains, or a mixture of both. The desirable structure is one exhibiting zero recrystallisation. Optical micrographs were used to investigate grain size and distribution as well as orientation development. The micrographs of the rectangular sections were used to investigate the effect of the extrusion temperature and extrusion speed whilst the U-shaped section and the tube section were

used to investigate the effect of geometry on the grain size and distribution.

### 6.2.1.1 Effect of extrusion temperature

Figure 6.1 show that microscopic investigation of structure reveals a non-uniform partially recrystallized structure.



*Figure 6.1* Micrograph of rectangular sections, at 480 °C, 500°C and 520 °C at 12mm/s

The simulation results for the rectangular sections are shown in Figure 6.29. The reader should recall that in chapter 5 (Figure 5.8) it was shown that higher levels of strain were

observed at the surface of the section whilst lower levels of strain were associated with the center of the rectangular section.

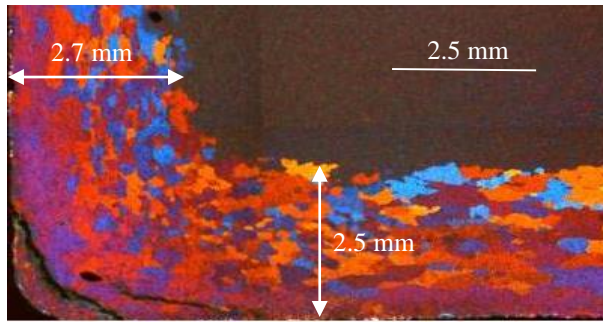
The optical micrographs of the three rectangular sections are similar but some variation can be observed with the changes in thickness of the recrystallised area in the section. All micrographs show the recrystallized region to be associated with the section surface. The grains predominantly have a shape which is not equiaxed indicating the non-uniform nature of the deformation.

The grains at the interface between the recrystallised and the unrecrystallised area are larger. As a general trend Figure 6.1 show an increase of the grainsize with increasing extrusion temperature. The temperature effect can be best observed revealing the larger grains in the micrograph with the highest extrusion temperature. This can be seen very clearly in Figure 6.1 which show the micrograph for 520 °C, 12 mm/sec.

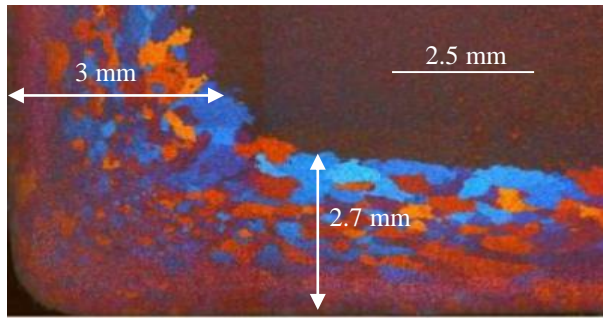
All micrographs in Figure 6.1 show to a certain degree the effect of a band with substantially smaller grains at the surface of the section. This effect is probably caused by the re-heating effect of the cooled sections. All extruded sections are cooled with air. When the section has passed the cooling stage the remaining heat in the center of the section will re-heat the outside of the section.

Figure 6.1 Micrograph, 520 °C, 12 mm/sec, show a deviating pattern most likely caused by ineffective cooling.

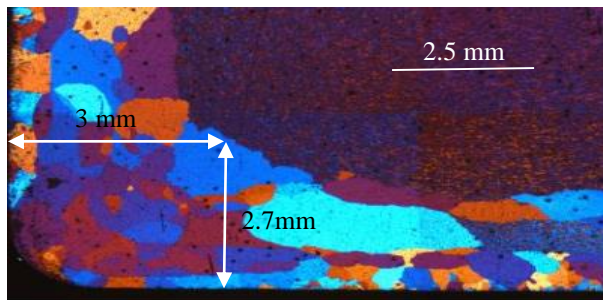
Figure 6.2 show enlarged micrographs of a detail of the rectangular sections. The investigated area is identified by a white rectangular in the micrographs of figure 6.1. The rectangular area show a detail of the micrograph (5x9mm) and allows for further investigation.



480 °C, 12 mm/sec



500 °C, 12 mm/sec



520 °C, 12 mm/sec

*Figure 6.2* Detailed micrographs of rectangular sections, at 480 °C, 500°C and 520 °C at 12mm/s

The details of the micrographs in Figure 6.2 clearly show the increased grain size with increasing extrusion temperature. This can be seen particularly well at 520 °C 12 mm/sec. This micrograph shows grains predominantly deformed in the lateral direction. Measurements of the recrystallised area show an increase of the thickness of this layer with increased extrusion temperature. The thickness of the recrystallized area increases 2.5 to 2.7mm on the width of the rectangular section and from 2.7 to 3 mm on the height of the rectangular section. This supports the theory that the depth of the recrystallised surface layer increases with increased extrusion temperature.



### 6.2.1.2 Effect of ram speed

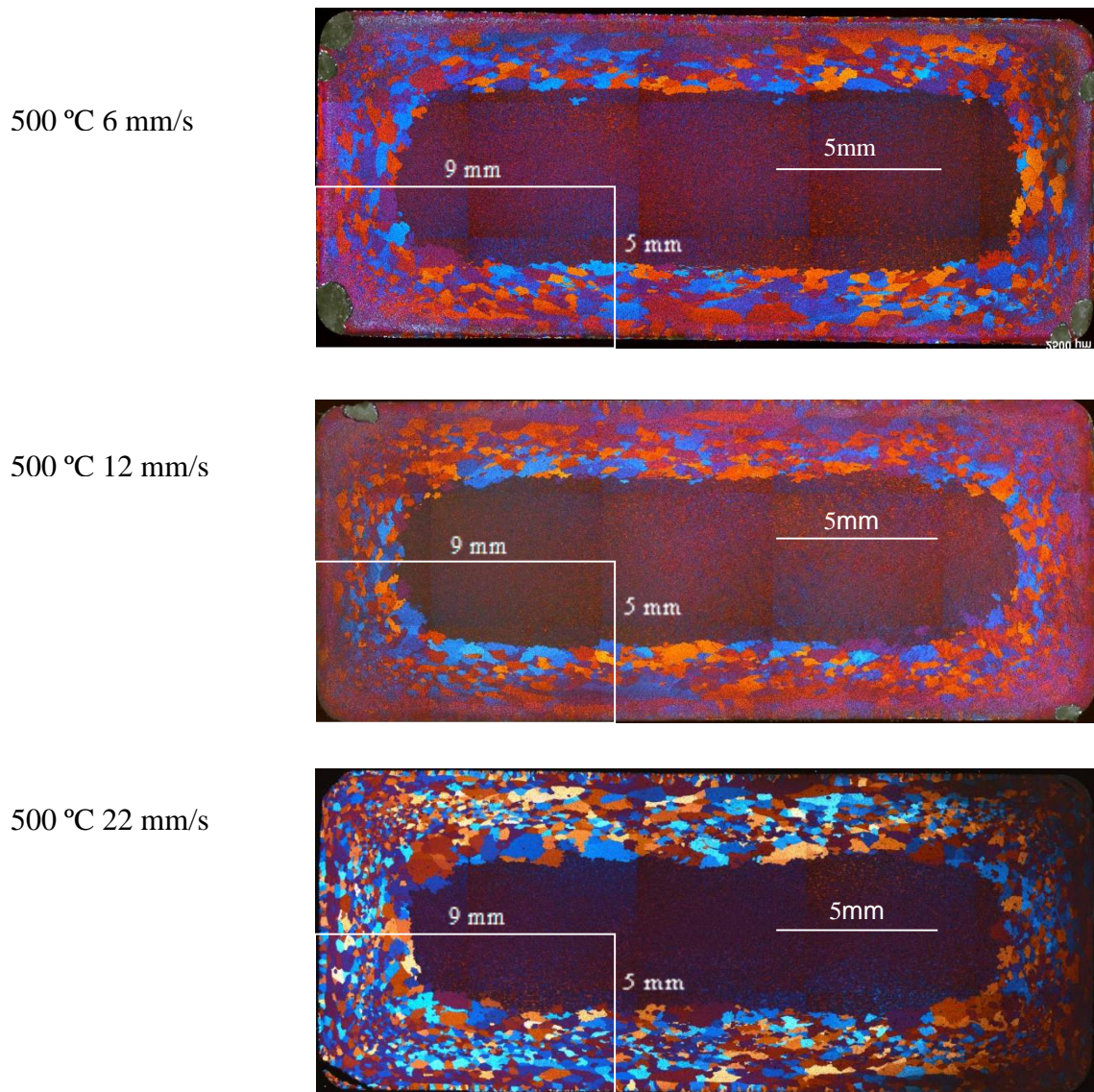
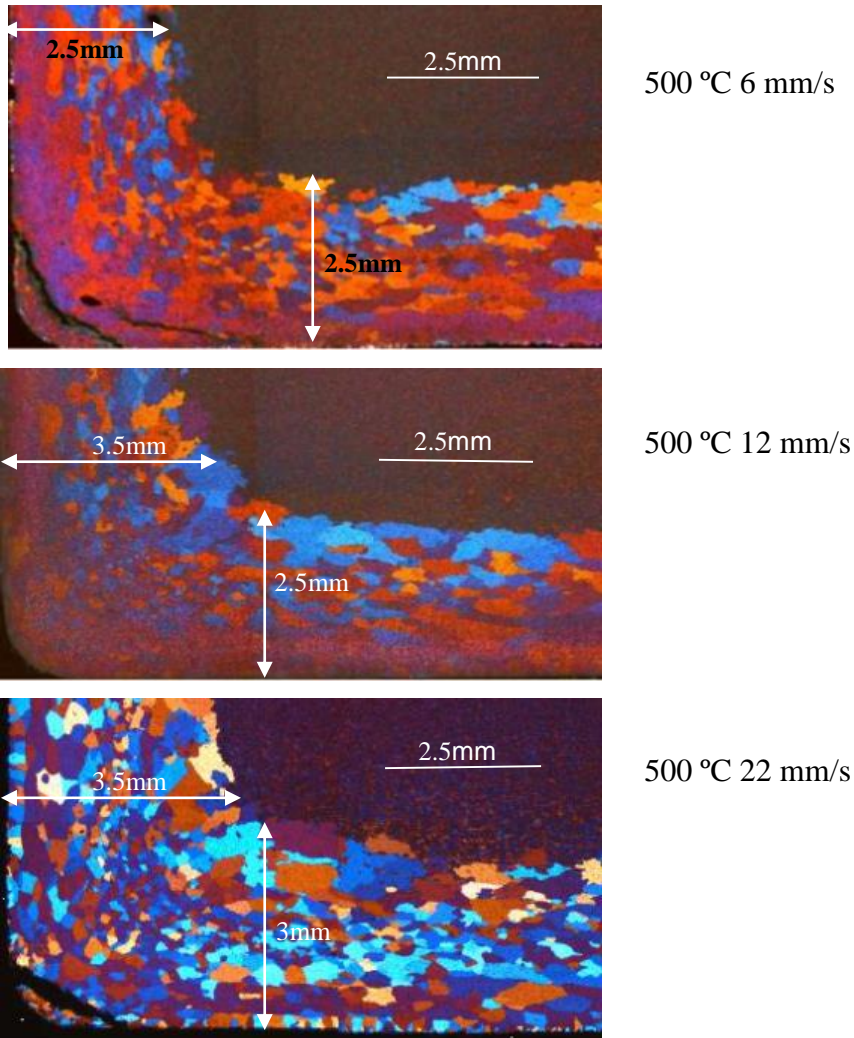


Figure 6.3 show the micrographs of the rectangular sections with increased extrusion speed.

*Figure 6.3* Micrograph of a rectangular section, at 500°C at 6 mm/s, 12 mm/s and 22 mm/s. The effect of extrusion speed increase will lead to a further temperature rise. High speed and high temperature both result in a more recrystallized structure but temperature is the predominant factor. The findings from increased extrusion temperature are to a large extent similar to those of an increased ram speed.

The larger recrystallised grains are predominantly visible at the high ram speed. All the recrystallised grains show a greater deformation in the lateral direction and an area of substantially smaller grains at the surface of the extrudate. Figure 6.4 show detailed micrographs of the rectangular sections with increased ram speed.



*Figure 6.4* Detailed micrographs of rectangular sections at 500°C and 6 mm/s, 12 mm/s and 22 mm/s

Figure 6.4 show enlarged micrographs of rectangular sections. The investigated area is marked as a white rectangular in the micrographs of figure 6.3 and show a detailed area of the micrograph (5x9mm) and allows for more detailed investigation. The detailed micrographs in Figure 6.4 support the observations from Figure 6.3. The increased grain size and depth of the recrystallised area is clearly shown in the detailed micrograph of

Figure 6.4 at 500 °C, 22 mm/s. The thickness of the recrystallized area increases 2.5 to 3mm on the width of the rectangular section and from 2.5 to 3.5 mm on the height of the rectangular section.

### 6.2.1.3 Effect of section geometry

Section features such as details and small wall thickness can have an effect on the profile complexity. A more complex geometry is generally expected to result in a higher extrusion temperature which will affect the recrystallised grain structure

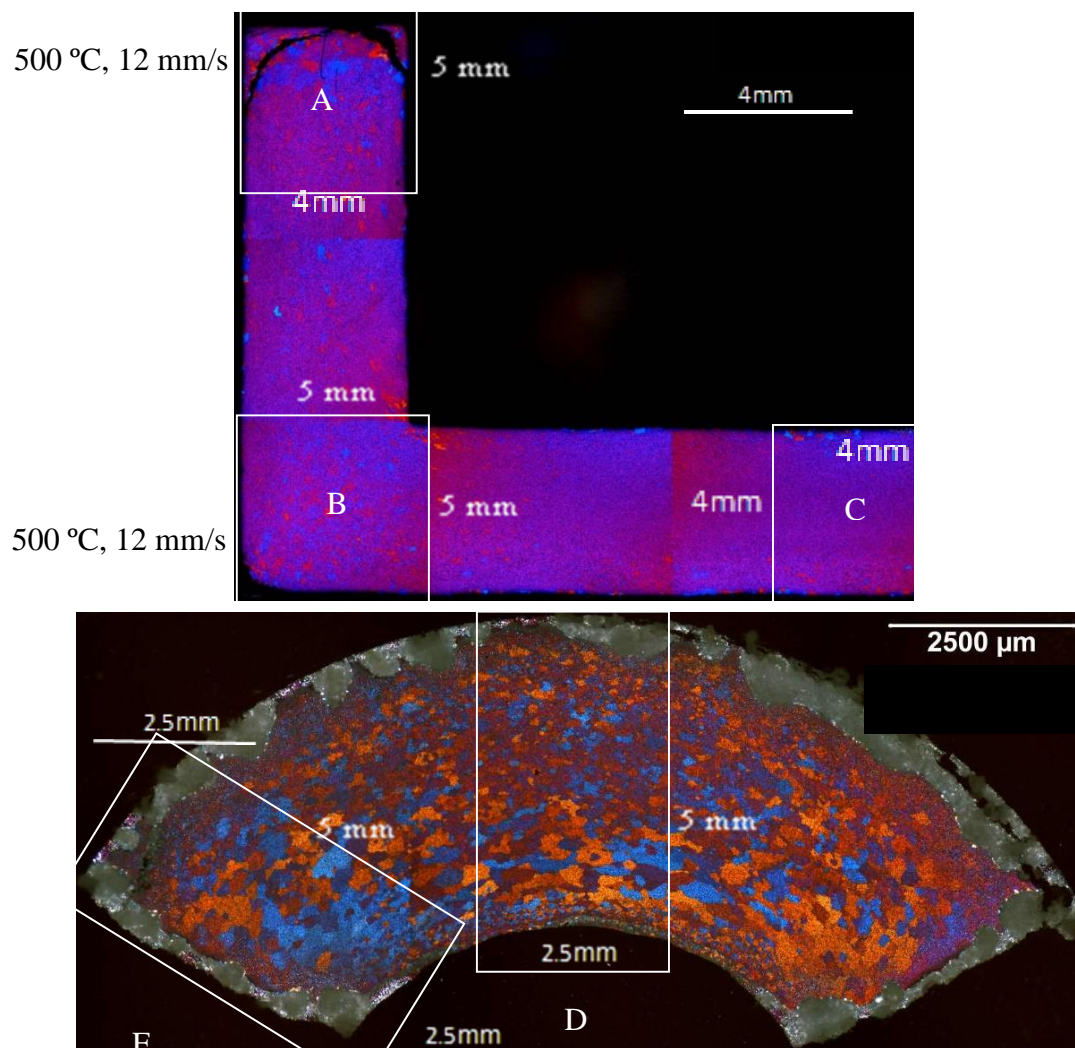
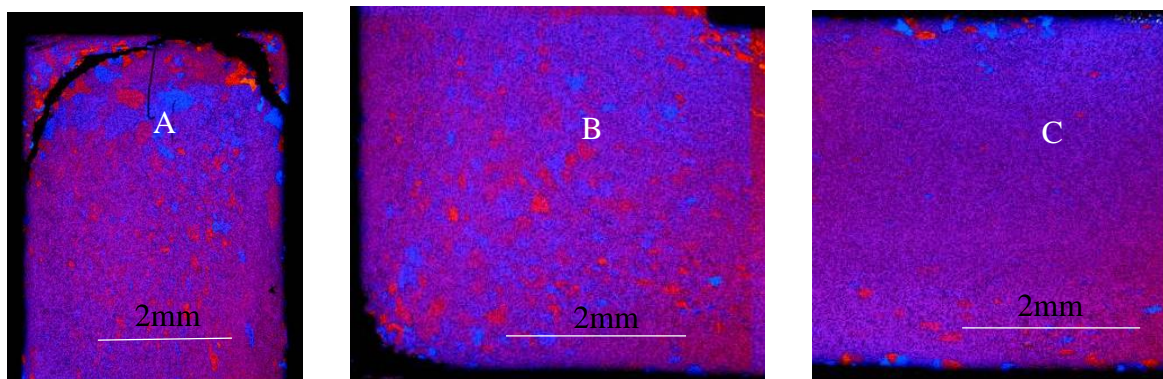


Figure 6.5 Micrograph of the U-shaped and tube section, at 500°C and 12 mm/s



The extrusion ratio is approximately 26:1 for the rectangular section, 38:1 for the U-shape section and 42:1 for the tube section. The wall thickness of the U-shaped section is 4mm and 4.5mm for the tube section. Figure 6.5 show the micrographs of the U-shaped and tube section, at 500°C and 12 mm/s.

A section with an increased surface area will contribute to more friction and influence recrystallisation. The micrograph of the U-shaped section show an overall recrystallised structure. In Figure 6.6 detailed micrographs of the U-shaped section are used to illustrate further details of the structure.



*Figure 6.6* Detailed micrograph of the U-shaped section

In Figure 6.6 details of the U-shaped section are presented: the top of the standing leg A, the corner of the U-base B and a part of the base of the section C. The overall impression of the structure of the U-shaped section is one of a fully or almost fully recrystallised structure. Observing the detailed micrographs A and B in Figure 6.6 show the presence of courser grains at the tip of the standing leg and at the corner of the U-shape. These section details contribute to differences of friction and strain Figure 6.7 show the micrographs of the tube section where details D and E are used to explain details of the microstructure.



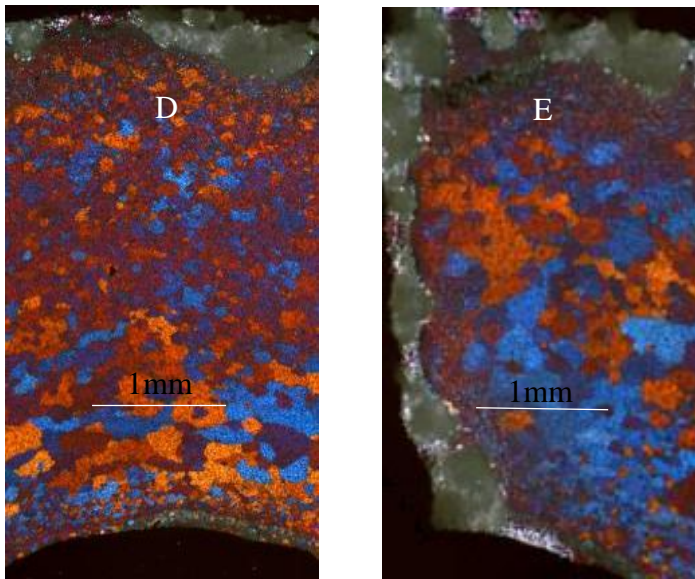


Figure 6.7 Detailed micrograph of the tube section

The extrusion of a hollow section is complex. The die consists of two parts, the core forms the inside of a hollow section and is build-up of a core and feeder holes. The outside of a hollow section is produced with a die plate. The material subsequently has to traverse the die bridges to form the closed hollow section. The welding of the material after the die bridge can contribute to temperature increase. The relative small wall thickness and the complex extrusion across the die bridge can lead to increased levels of strain rate and a higher temperature. At the position of the die bridge on the inner wall this is  $573^{\circ}\text{C}$ , see Figure 5.6. The micrograph of the tube section in Figure 6.5 show a fully recrystallised structure. Details of the tube section are given in Figure 6.7, where at the position D, a detail is shown of the tube section in the middle of the feeder hole and in E, a detail at the position close to the die bridge.

The micrograph of the tube section in figure 6.5 show a structure with larger grains towards the inner wall of the section and smaller grains toward the outside of the section. At the position of the inner wall a narrow band of smaller grains can be seen probably as a consequence of insufficient cooling of the inner wall of the tube. The cooling area is much less on the inside of the tube. The detailed micrograph of the tube section in Figure 6.7D, show the microstructure in the middle of the feeder hole. This detailed micrograph show a

symmetrical picture from left to right. The grain size is increasing from the outside of the section to the inside with the exception of a small band close to the inner wall where smaller grains are visible. This latter observation suggests the onset of secondary recrystallization.

In Figure 6.7E, the detail of the micrograph of the tube section is shown at the position of the die bridge. The die bridge is expected to contribute to a higher temperature which will lead to increased grain size at this position. Figure 6.7E show a coarse grain structure throughout the section with the exception of a very narrow band close to the section surface due to secondary recrystallization as a result of insufficient cooling.

Volume fraction recrystallised is evaluated by the operator of the light optical microscope. This microscope has a feature which enables the operator to estimate the volume fraction recrystallised. This estimate is made using the grid method where a grid is used to compare actual structure with historical data. This method has its limitations since it can only compare the visible grain structures and it cannot give a qualitative analysis of the structure. However the results obtained with this method can serve as an indication of the overall recrystallised structure.

Table 6.1 show the results of the volume fraction recrystallised using the grid method.

optical estimated volume fraction recrystallised			
section	extrusion condition	centre	edge
rectangular	480 °C, 12 mm/s	55	100
rectangular	500 °C, 12 mm/s	55	100
rectangular	520 °C, 12 mm/s	55	100
rectangular	500 °C, 6 mm/s	55	100
rectangular	500 °C, 12 mm/s	55	100
rectangular	500 °C, 22 mm/s	55	100
U-shape	500 °C, 12 mm/s	80	80
tube	500 °C, 12 mm/s	100	100

*Table 6.1* Volume fraction recrystallised using the grid method

The estimated values from the grid method for volume fraction recrystallised of the

rectangular sections all show a similar result. All the inner parts of the rectangular sections are regarded as 55% recrystallised using the grid method whilst the outer area is regarded as fully recrystallised. The U-shaped section is evaluated as being 80% recrystallised. The tube section is regarded as being fully recrystallised. The results of the recrystallised volume fraction values have to be regarded with some trepidation since they can only be used as estimates.

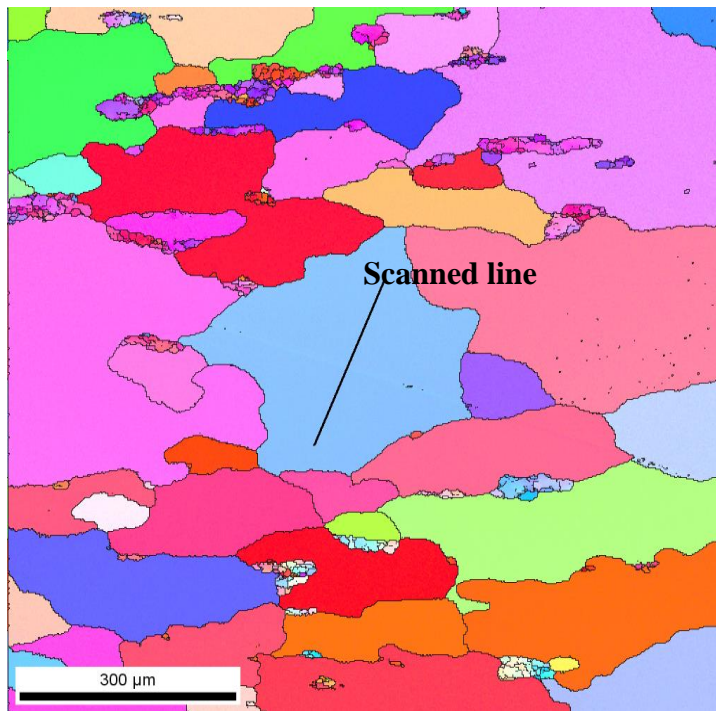
### **6.2.2 EBSD Investigations**

A grain boundary is illustrated on the EBSD map by a thick black line indicating a misorientation between grains. In the literature subgrains are usually described where misorientation between grains and subgrains is smaller than  $6^\circ$ . High angle boundaries can be represented as two crystallographic planes joined together. Low angle boundaries are arrays of dislocations. In the range greater than  $6^\circ$ , the dislocation structure changes to a high angle boundary structure. EBSD analysis is used to obtain detailed information regarding subgrain size and misorientation. The procedure of obtaining this data is outlined below.

Two  $1\text{mm}^2$  areas, one in the center zone and one in the edge zone of the samples were analysed in the rectangular profiles. One area of  $1\text{mm}^2$  in the center of the U-shaped and tube profile were analysed. The locations of the sample area are given in Figure 6.12 and are chosen to be representative with respect to the structure visible in the optical micrographs.

In the procedure, which was used to determine the subgrain size and the misorientation, the following steps can be identified: At first the grain size is measured. The program needs to be set with minimum step size to obtain good resolution on the actual picture. Required for good resolution are at least 10 pixels in a small grain. Then the measurements are started which are based upon pixel numbers in each grain. These measurements are used in the calculations where grains and subgrains are identified based upon grain boundaries. Each pixel has a diffraction pattern which is used in the calculations. Subgrains are defined with

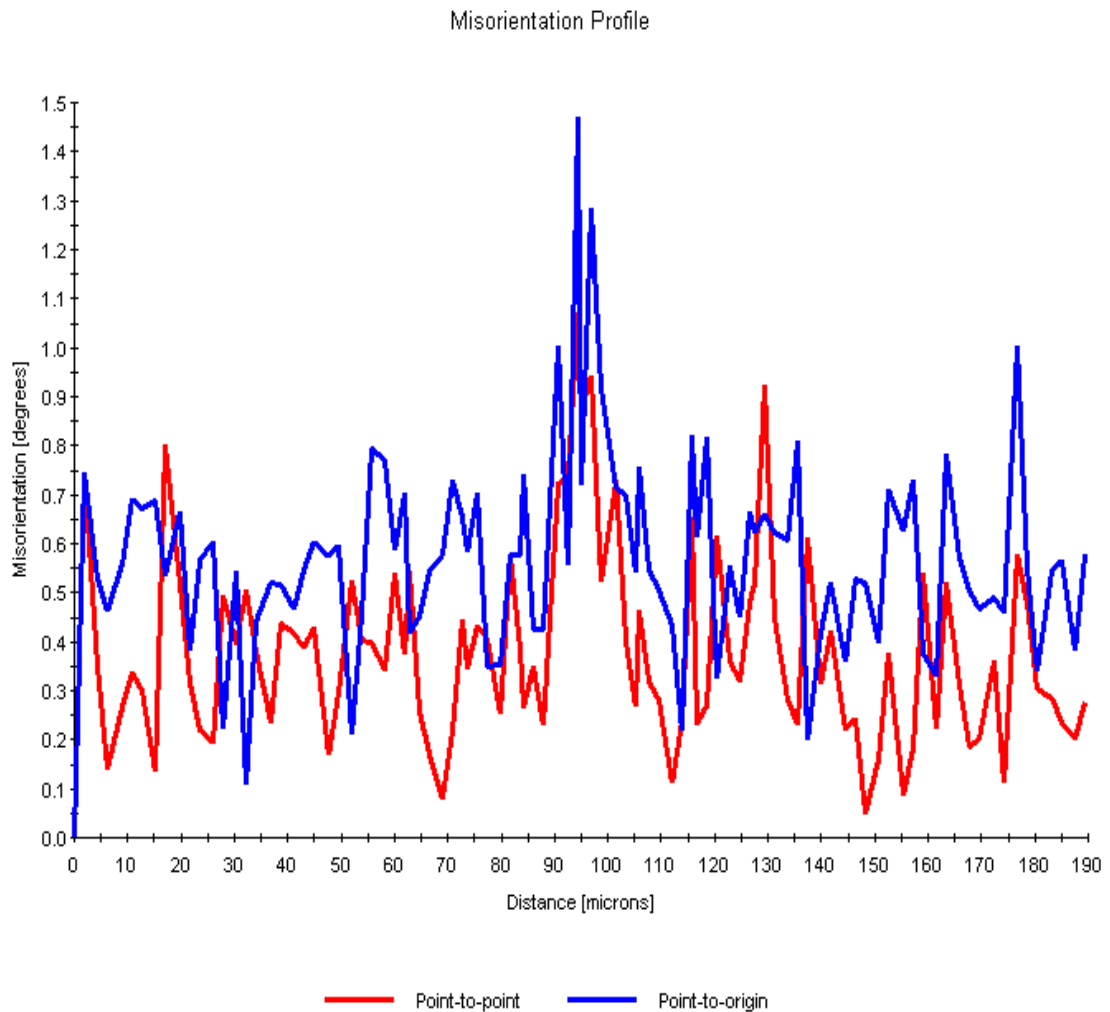
low angle boundaries  $<6^\circ$ . (Jonas, Sellars and McQueen, 1969). Within the designated sample area (highlighted as white squares in Figure 6.12) the average misorientation is determined for each (sub) grain. The method is verified by investigating the misorientation variation within some of the larger (sub) grains. The variation in misorientation is measured along the scanned line in Figure 6.8 and represented in Figure 6.9.



*Figure 6.8* EBSD map of sample 5E (500°C, 12mm/sec) with scan line in the larger blue (sub) grain (Courtesy of Hydro Aluminium Mr. John Rasmus Leinum)

Normally EBSD software automatically calculate (sub) grain size and misorientation and represent this graphically. This feature was not available in the present software. The results of the misorientation along the scanned line are represented in Figure 6.9. Figure 6.9 show a graphical representation of the EBSD results for the measured variation of the misorientation within the large subgrain along the marked line, highlighted in Figure 6.8. The representation includes misorientation measured from point to point and the misorientation measured from point to origin. The EBSD software calculates average (sub) grain size and misorientation for all the (sub) grains within each allocated sample area

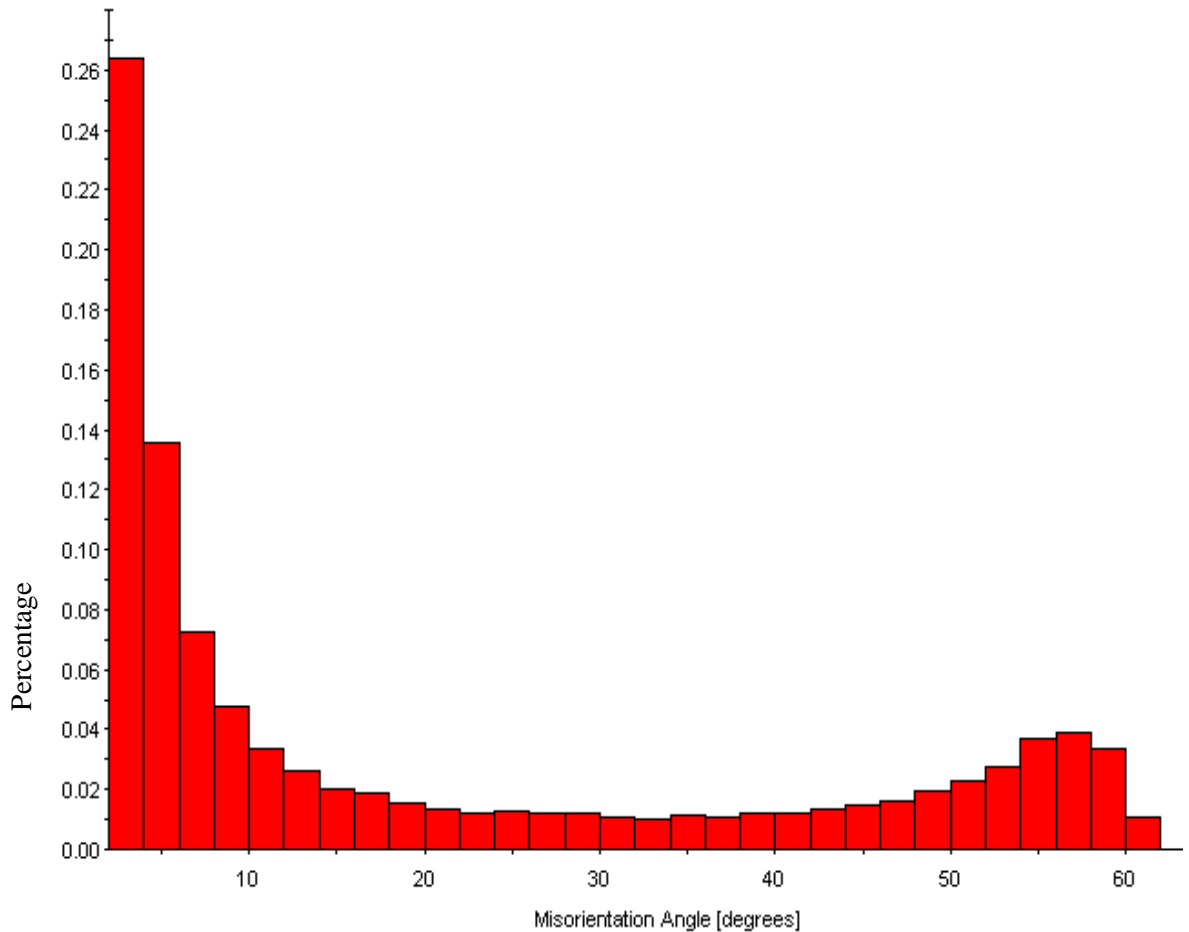
highlighted in Figure 6.8. An example of the result of the EBSD measurements of (sub) grain size and misorientation is represented in a graphical way in Figures 6.9 and 6.10.



*Figure 6.9* Misorientation along the scanned line in (Figure 6.3) of sample 5E (500°C, 12mm/sec) (Courtesy of Hydro Aluminium Mr. John Rasmus Leinum)

EBSD measurements are performed for the (sub) grains visible in the marked area in Figure 6.12. The EBSD software determines the average misorientation for all investigated (sub) grains within this marked area. For statistical reasons the misorientation results are graphically represented together with the percentage present in the sample area. This allows for the comparison of a specific misorientation range to the respective percentage in a specific (sub) grain. Figure 6.10 show an example of the graphical representation of the

misorientation measurements of sample 2E (500°C, 6mm/s). The graph in figure 6.10 show a large number of fraction for misorientation in the range  $<6^\circ$ . Approximately 47% of the investigated (sub) grains have a misorientation angle  $<6^\circ$ . The rest of the (sub) grains visible in sample 2E exhibit a misorientation  $>6^\circ$ .



*Figure 6.10* Misorientation angle as a function of the number of fraction for sample 2E (500°C, 6mm/s) (Courtesy of Hydro Aluminium Mr. John Rasmus Leinum)

A representation can also be made for the EBSD results for (sub) grain size. EBSD measurements are performed for the (sub) grains visible in the marked area in Figure 6.12. Figure 6.11 show the (sub) grain size as a function of the percentage for sample 2E (500°C, 6mm/s). The EBSD software determines the average (sub) grains for all investigated (sub)

grains within this marked area. For statistical reasons the (sub) grains results are graphically represented together with the percentage. This allows for the comparison of a specific (sub) grains range to the respective percentage in a specific (sub) grain. Figure 6.11 show an example of the graphical representation of the (sub) grains measurements of sample 2E (500°C, 6mm/s).

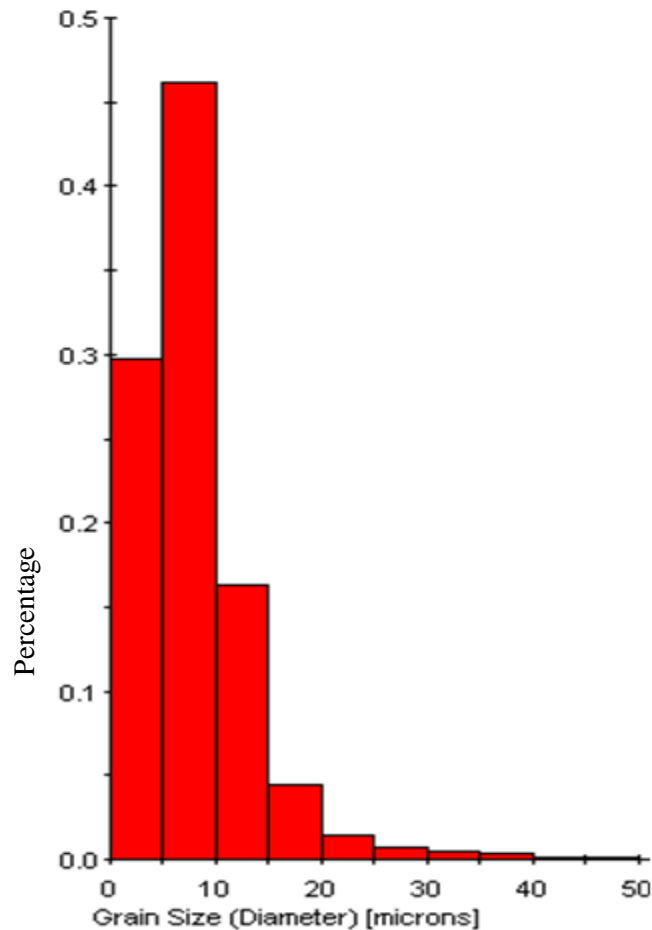


Figure 6.11 Subgrain size as a function of the percentage for sample 2Eb and c (500°C, 6mm/s) (Courtesy of Hydro Aluminium Mr. John Rasmus Leinum)

The graph in figure 6.11 show a large number of fraction of the (sub) grains in the range  $<10 \mu m$ . Approximately 30% of the investigated (sub) grains have a size smaller than or equal to  $5 \mu m$ .

Approximately 45% of the investigated (sub) grain size have a size of between 5 and  $10 \mu m$ . The rest of the (sub) grains visible in sample 2E (25%) exhibit a size  $>10 \mu m$ .

Statistical data provided by the EBSD software is used to calculate average (sub) grain size and misorientation angle. Grains are distinguished by high angle grain boundaries which have a misorientation angle higher than 6°. The calculation procedure for (sub) grain size is outlined in the paragraph below and the results for (sub) grains size from experiment and simulation are represented in Table 6.7, 6.8 and 6.9. Figure 6.29 show the results for simulated values of subgrain size. The calculation procedure to analyse the average subgrain size and the average misorientation per experiment sample is as follows:

- At first the total sum of the original fraction number (OFN) of all grains / subgrains and orientation angles is determined.
- The relative fraction number (RFN) is determined by dividing the OFN by the sum of OFN of all grains / subgrains and orientation angles.
- The product of the (particle size and orientation angle) and the RFN is determined.
- All products (particle size and orientation angle) are summarised.
- Finally the sum of all (particle size and orientation angle) is divided by the number of sizes and the number of angles to obtain average (sub) grain size and misorientation.

### **6.2.2.1 EBSD Results**

Processing parameters such as extrusion temperature and speed influence the structure of the final product. Optical micrographs show that section geometry will also have an effect on structure. EBSD was used to investigate this effect. EBSD techniques support qualitative and quantitative analysis of the samples. Optical micrographs indicate a non-uniform structure. The desired structure would be one exposing none or as little as possible recrystallisation. Analysis of the optical micrographs of the rectangular samples lead to the conclusion that there are two areas to be identified: one fully recrystallised outer zone and a un-(or partly) recrystallised inner area. EBSD techniques can be used to further investigate the sub structure of the samples involved. The test program was set up to investigate the effect of temperature increase and speed increase on the subgrain size and the misorientation for the rectangular section. The U-shaped section and the tube were used to investigate the effect of geometry.



In Figure 6.12 the location of the sample position for the EBSD investigations are highlighted.

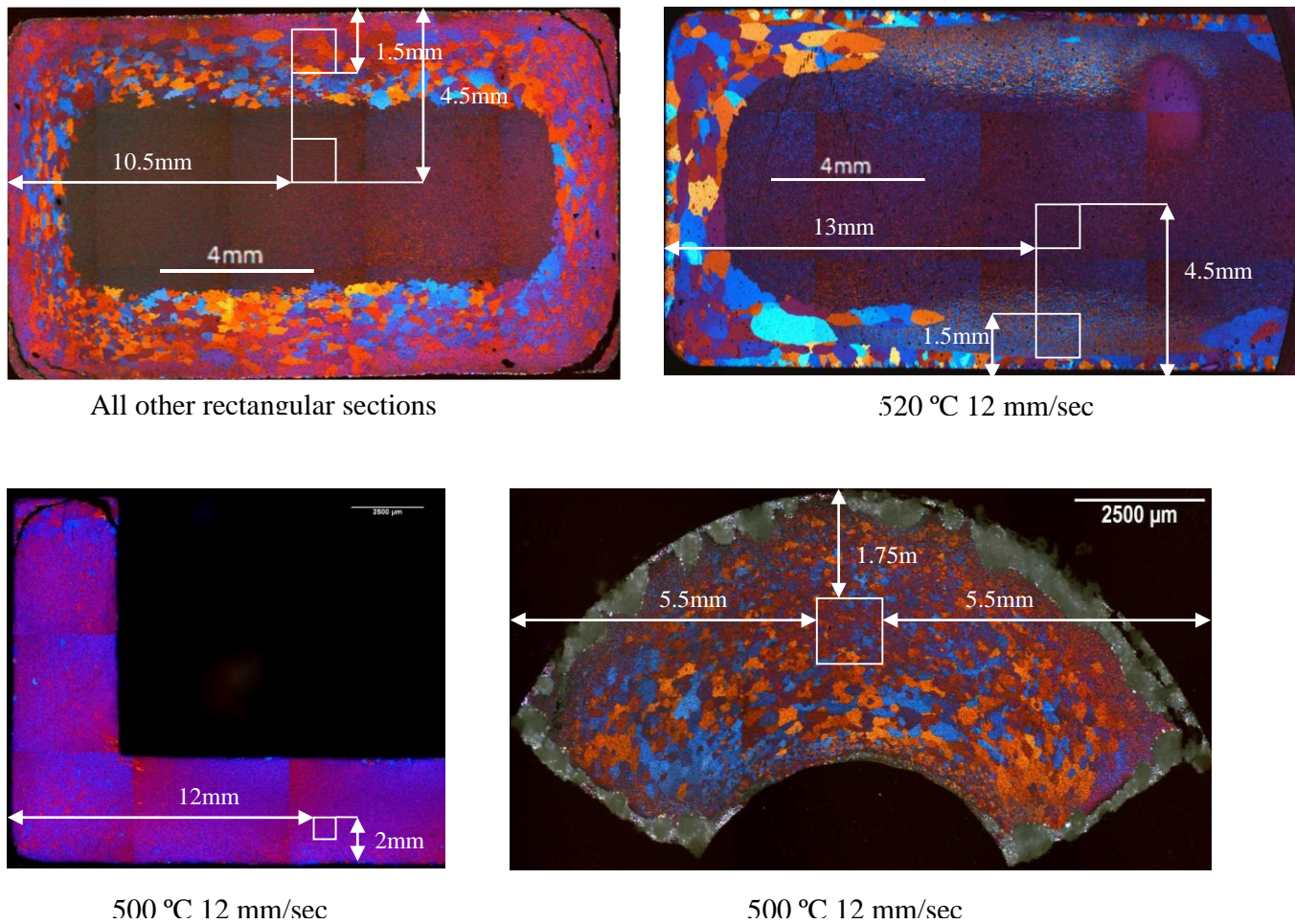


Figure 6.12 The location of the sample position for the EBSD investigations.

The results of sample, 520 °C 12 mm/sec, should be dealt with caution. In this case the cooling was possibly ineffective.

### 6.2.2.2 Effect of extrusion temperature

Sheppard and Titcher (1980) have reported the importance of the subgrain size and orientation which very much determines the metal response to the solution and ageing sequence. During the extrusion, the stored deformation energy within the extrudate ensures that some static recrystallisation occurs after extrusion and during the soaking process.

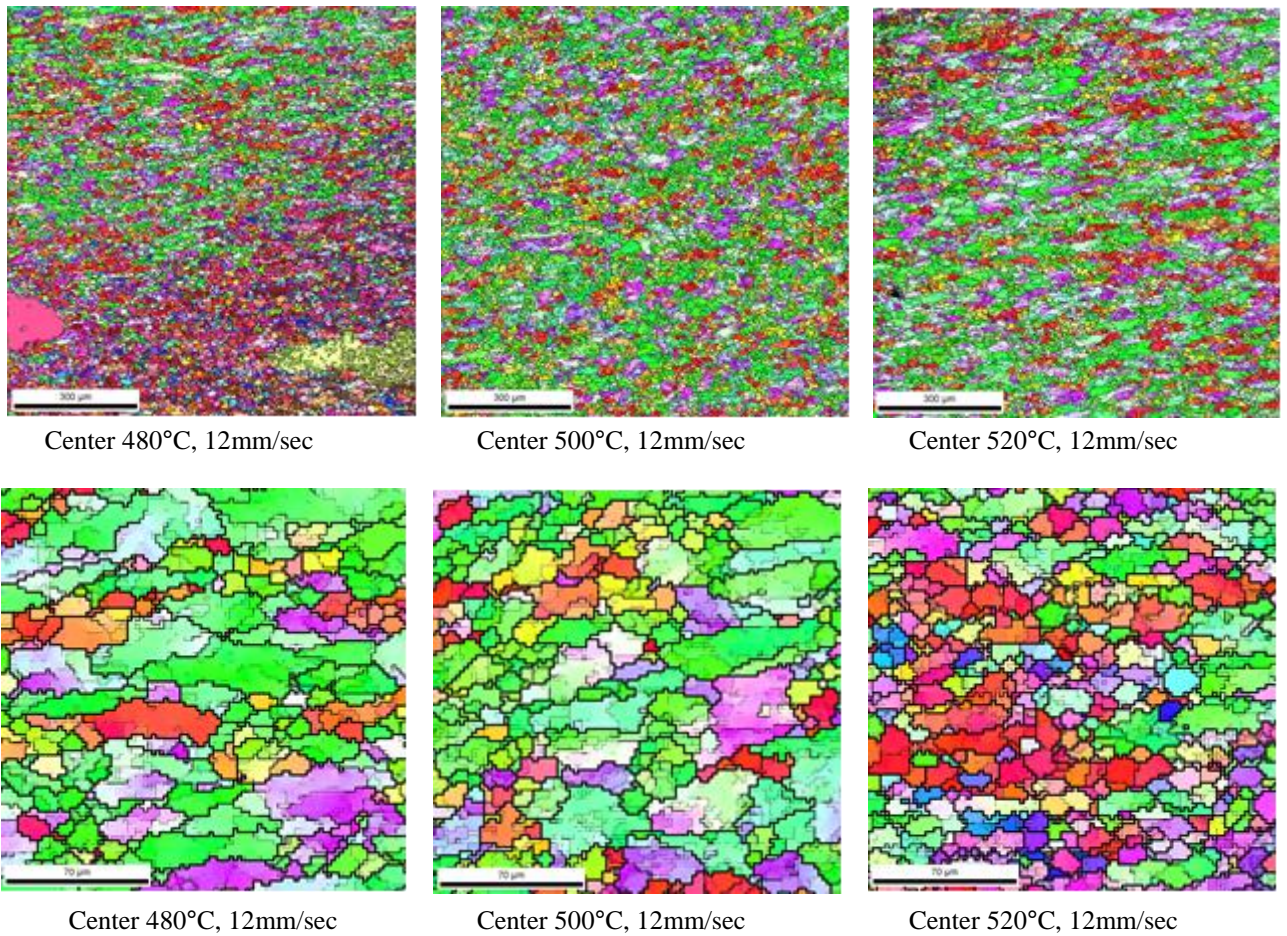
In this case there is no separate soaking process. Extrusion of solid bars that at low ram speed (2mm/sec) have been reported to be predominately unrecrystallised regardless of the billet temperature. (Parson et al. 2004).

As the ram speed is increased, the depth of the recrystallised surface layer will increase, and finally recrystallisation will be initiated in the core. The critical temperature at which this occurs will increase with higher initial billet temperature. Further increase of the ram speed will produce full recrystallisation of the cross section of the samples. Figure 6.13 show the EBSD result of the center part of the rectangular sections with increasing temperature whilst the speed remains constant. The depth of the fully recrystallised zone is expected to be greater with increasing ram speed and a lower billet temperature will result in a smaller recrystallized zone.

The top three EBSD graphs in Figure 6.13 show the internal structure at lower magnification. Sample 480°C, 12mm/sec looks different from the other two graphs in this figure. The presence of one larger grain in the center of 480°C and 12mm/sec indicates that at least some recrystallisation has occurred. This large recrystallised grain is probably the result of subgrain coalescence. Smaller subgrains are visible around this large grain. (Figure 6.14A).

The bottom three graphs in Figure 6.13 show the grain structure at larger magnification. The graph (520°C, 12mm/sec) show substantially smaller grains than graph (480°C and 500°C, 12mm/sec). In this case the cooling was probably insufficient.

Figure 6.13 show the EBSD results for the rectangular sections with constant speed and increased temperature. All EBSD graphs are representing the cross section.

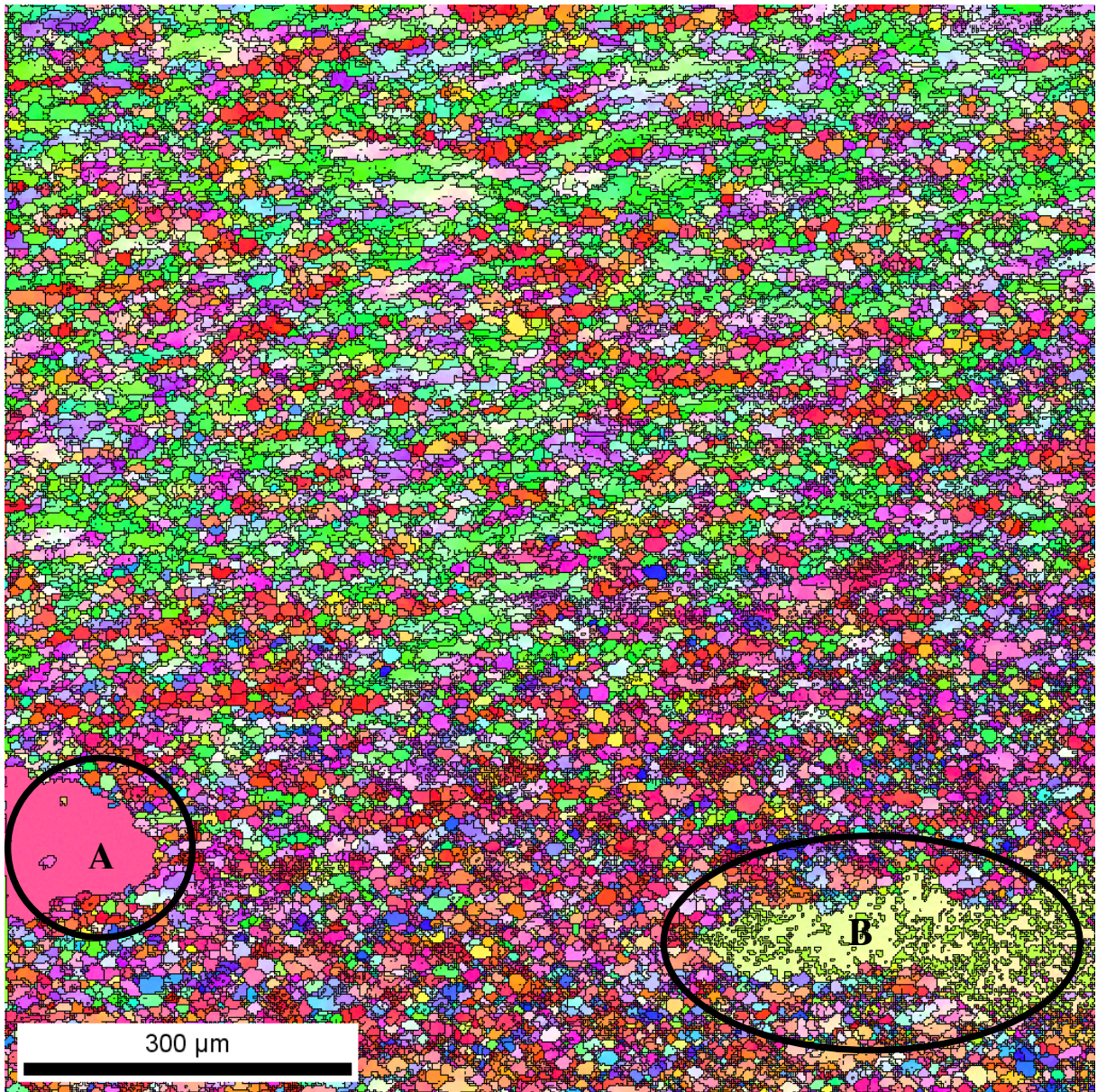


*Figure 6.13* EBSD graphs of the rectangular sections in the center with temperature increase. (Courtesy of Hydro Aluminium Mr. John Rasmus Leinum)

Figure 6.14 and 6.15 show an enlarged view of EBSD graph (480°C, 12mm/sec and 520°C, 12mm/sec) in the center. Although these structures may appear very similar a closer observation in the enlarged view, show that they are quite different.

The area in Figure 6.14B, visible as a yellow zone, is a recrystallised grain with presumably subgrains within it. The area of Figure 6.14B is probably just prior to the formation of a large grain as a result of subgrain coalescence. There is probably a relation between recrystallized area and the presence of intermetallics.



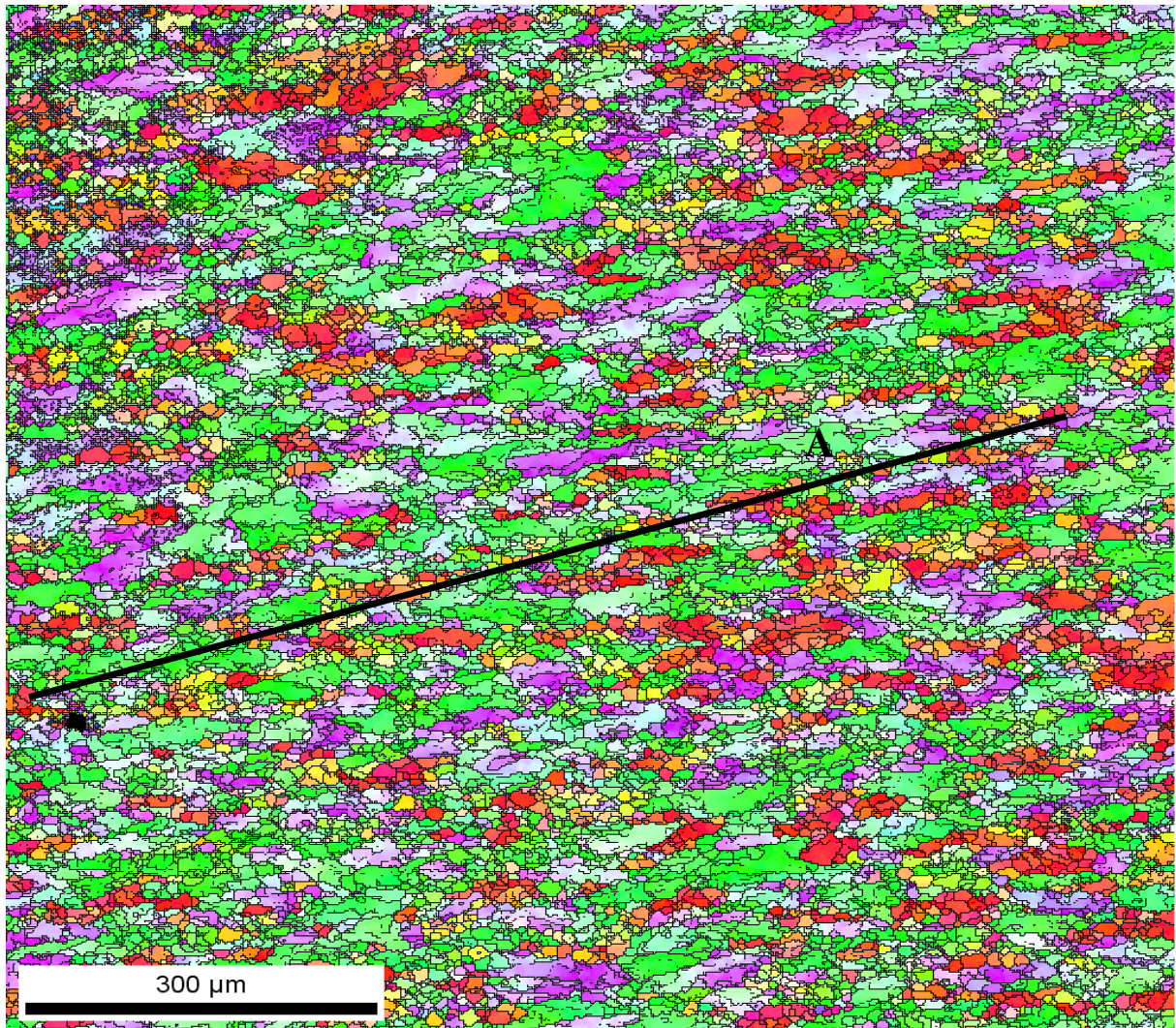


*Figure 6.14* Enlarged view of EBSD graph of rectangular section 480°C and 12mm/sec in the center of the sample. (Courtesy of Hydro Aluminium Mr. John Rasmus Leinum)

The structure revealed in Figure 6.15 (520°C, 12mm/sec) is not very regular. It clearly shows bands of grains deformed in the lateral direction usually surrounded by clusters of much smaller grains. The overall structure EBSD graph in Figure 6.14 (480°C and 12mm/sec) is more regular and has a much higher number of smaller grains.



The number of larger grains seems to be much less and they appear to be smaller, except for the two very large grains. This is an indication that the temperature increase will have affected the grain size and distribution. The presence of grains with abundant subgrains indicates that partial recrystallisation occurred.

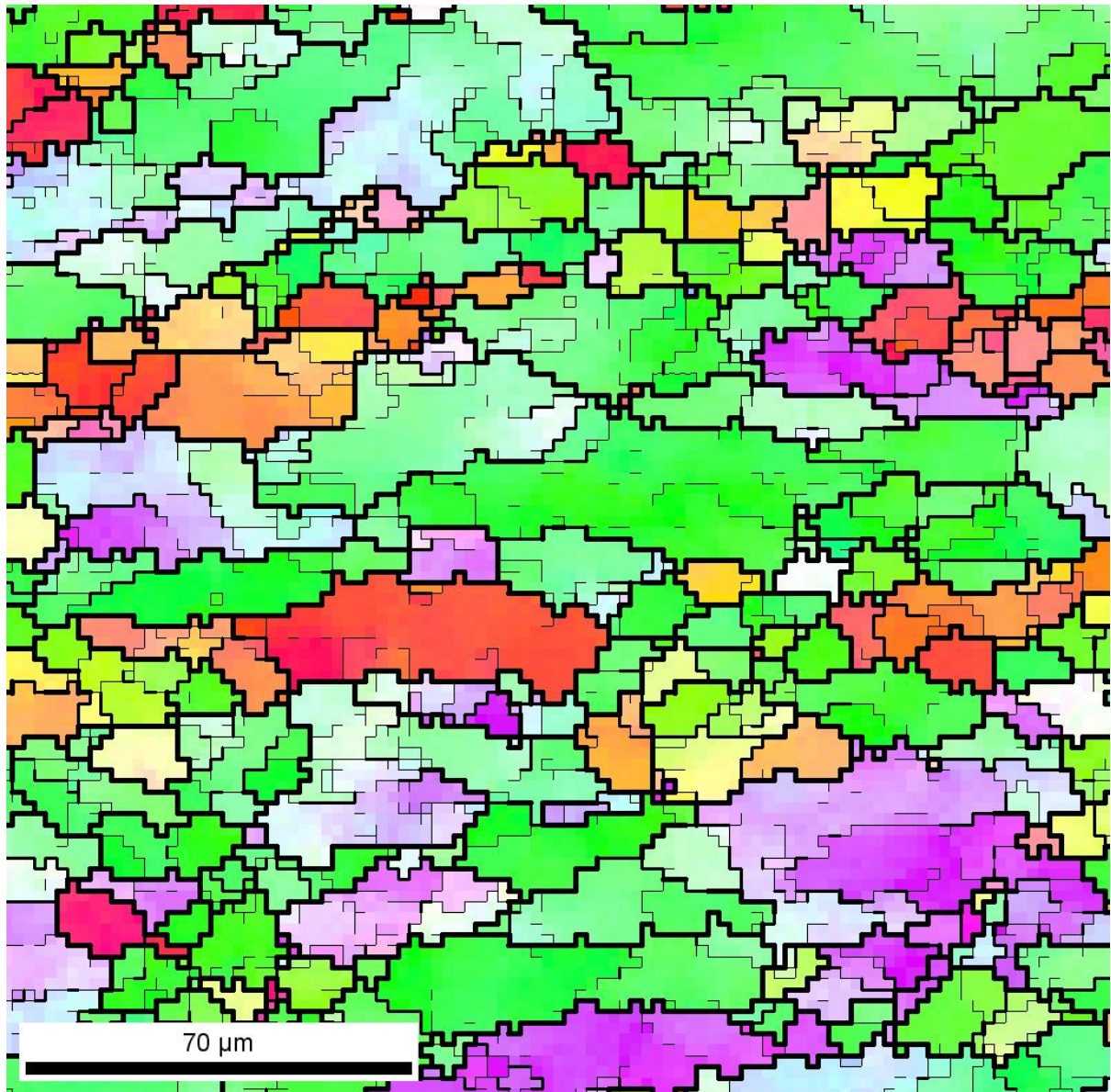


*Figure 6.15* Enlarged view of EBSD graph of the rectangular section 520°C and 12mm/sec in the center of the sample. (Courtesy of Hydro Aluminium Mr. John Rasmus Leinum)

The EBSD graphs at higher magnifications clearly reveal more of the sub structure than the lower magnifications does. Figure 6.16 and 6.17 show an enlarged view of EBSD graph (480°C, 12mm/sec and 520°C, 12mm/sec) in the center.

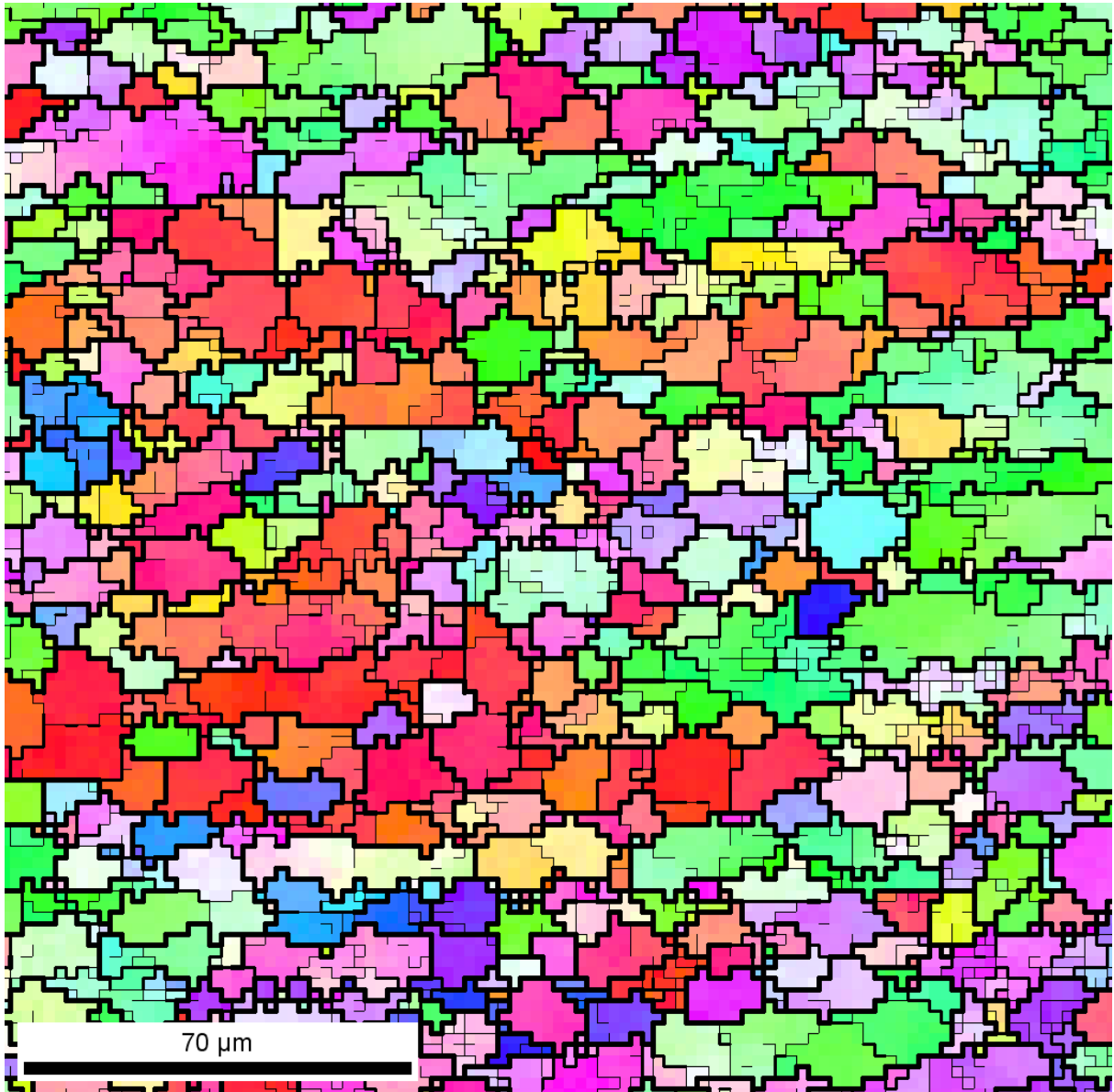


The bands appear to be perpendicular to the extrusion direction. There is deformation within the interior of the section not necessary in the extrusion direction. There seem to be a preferred deformation in the direction indicated by the line A in Figure 6.15.



*Figure 6.16* Enlarged view of EBSD graph of the rectangular section 480°C and 12mm/sec in the center of the sample. (Courtesy of Hydro Aluminium Mr. John Rasmus Leinum)

The EBSD graph in Figure 6.17 (480°C, 12mm/s) predominantly show more or less more uniform shaped smaller grains. In both Figure 6.16 and 6.17, there are subgrains present which can be identified by the thinner lines.

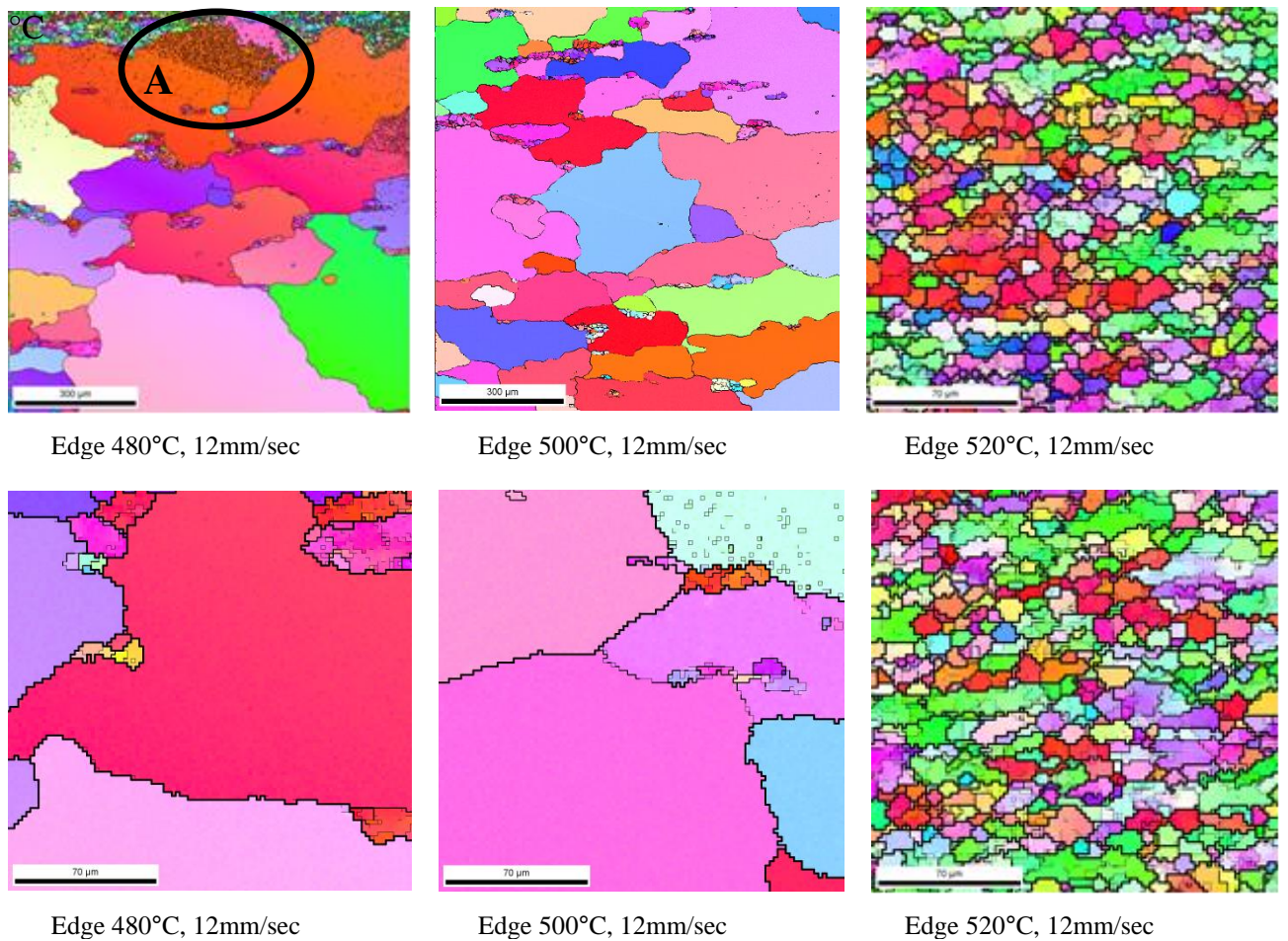


*Figure 6.17* Enlarged view of EBSD graph of the rectangular section 520°C and 12mm/sec in the center of the sample. (Courtesy of Hydro Aluminium Mr. John Rasmus Leinum)

The EBSD graph in Figure 6.16 (520°C, 12mm/s) show a structure which consists of much

larger grains. Figure 6.16 show larger grains which are predominantly deformed in the lateral direction. There seem to be more subgrain boundaries present in the (520°C, 12mm/s) graph. The EBSD graphs indicate that the temperature increase will have affected the grain size. EBSD graph 520°C, 12mm/s reveals a structure with courser grains compared to the lower temperatures. Table 6.2 include quantitative results of the subgrain size based upon EBSD data.

Figure 6.18 show the EBSD result of the edge of the rectangular sections with increasing temperature whilst the speed remains constant.



*Figure 6.18* EBSD graphs of the rectangular sections in the edge with temperature increase. (Courtesy of Hydro Aluminium Mr. John Rasmus Leinum)



The EBSD graphs in Figure 6.18 show the structure in the edge part of the rectangular sections with increasing extrusion temperature and constant speed. The EBSD graph at 500°C, 12mm/s are quite different possibly due to insufficient cooling. At the EBSD graph. 480°C, 12mm/s a cluster of subgrains can be seen at the position of Figure 6.18A. This is a recrystallised grain with presumably a cluster of dislocations within it. The area of Figure 6.18A is probably just prior to the formation of a large grain as a result of subgrain coalescence. The increase in temperature seems to coincide with the reduction of subgrains visible. At 480°C, 12mm/s a large number of subgrains can be seen in between larger grains. At 500°C, 12mm/s and larger magnification the presence of subgrains can be seen within a larger grain. Quantified conclusions regarding the subgrains can only be made after application of the calculation method to all the numerical data as a result of the EBSD analysis.

The EBSD results for subgrain size and misorientation with increased extrusion temperature are presented in table 6.2.

Average subgrain size, misorientation angle from EBSD analysis				
rectangular	average subgrain size	average grain size	average misorientation subgrain	average misorientation grain
480°C, 12mm/s	5.44	15.19	5.53	29.9
500°C, 12mm/s	5.35	15.63	5.35	30.15
520°C, 12mm/s	4.72	16.18	5.05	31.64

*Table 6.2* EBSD results for subgrain size ( $\mu m$ ) and misorientation ( $^{\circ}$ ) for the rectangular sections with increased extrusion temperature.

The numerical data presented in Table 6.2 indicate that the average subgrain size and misorientation of the subgrains in the center of the rectangular sections decreases with increased extrusion temperature. The average grain size and misorientation increases with increasing extrusion temperature. These results support the theory that subgrain size can be affected by extrusion temperature.

Table 6.2 presents' average values for the subgrain size and a trend of decreasing subgrain size with increasing extrusion temperature is visible. However should we wish to have quantitative data regarding the percentage of smaller (sub)grains present in the investigated area presented in the EBSD map, statistical data can help. Figure 6.18 show the statistical data regarding (sub) gerain size with increasing extrusion temperature.

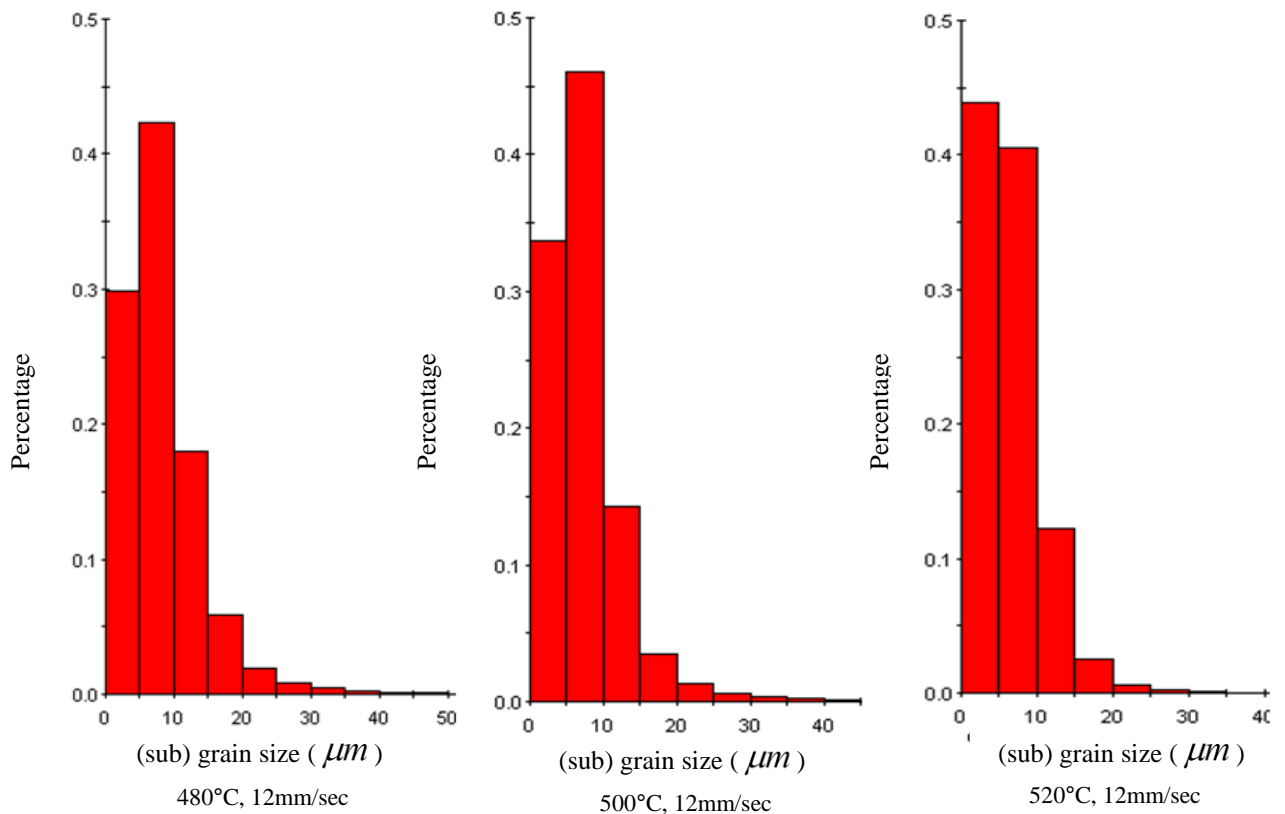


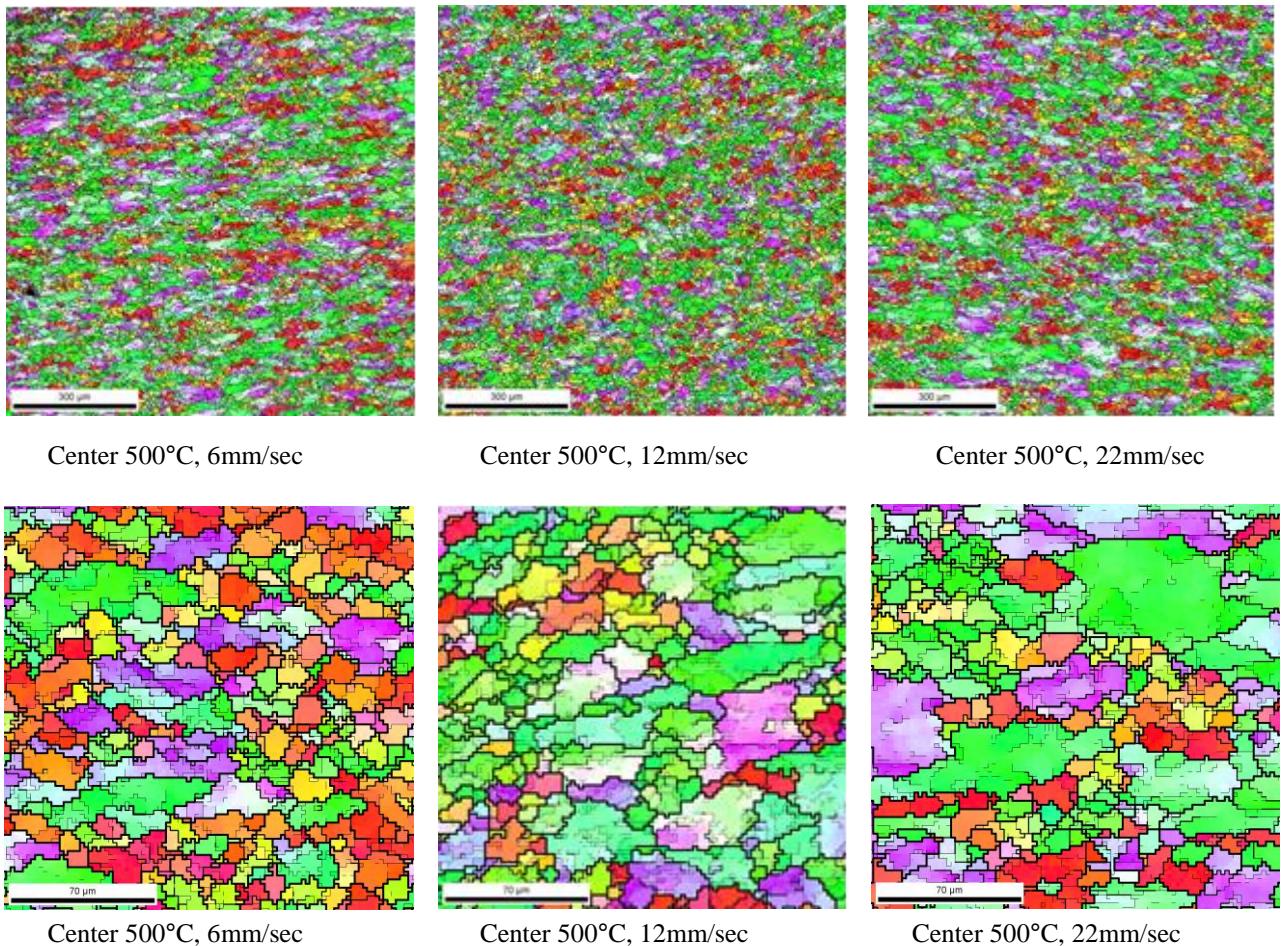
Figure 6.19 (sub) grain size ( $\mu m$ ) distribution with increasing extrusion temperature (Courtesy of Hydro Aluminium Mr. John Rasmus Leinum)

The graphs in Figure 6.19 show the distribution of (sub) grains as a percentage of the total number of (sub) grains in the sample area investigated by means of EBSD. The percentage of (sub) grains smaller than  $10 \mu m$  in the center area of the rectangular samples increases with increasing extrusion temperature (480°C- 73%, 500°C- 79%, 520°C- 84%).

The dimensional difference between grains and subgrains is probably somewhere between 5 and 10  $\mu\text{m}$ . Since larger subgrains can occur the trend was made visible by the 10 $\mu\text{m}$  mark.

### 6.2.2.3 Effect of ram speed

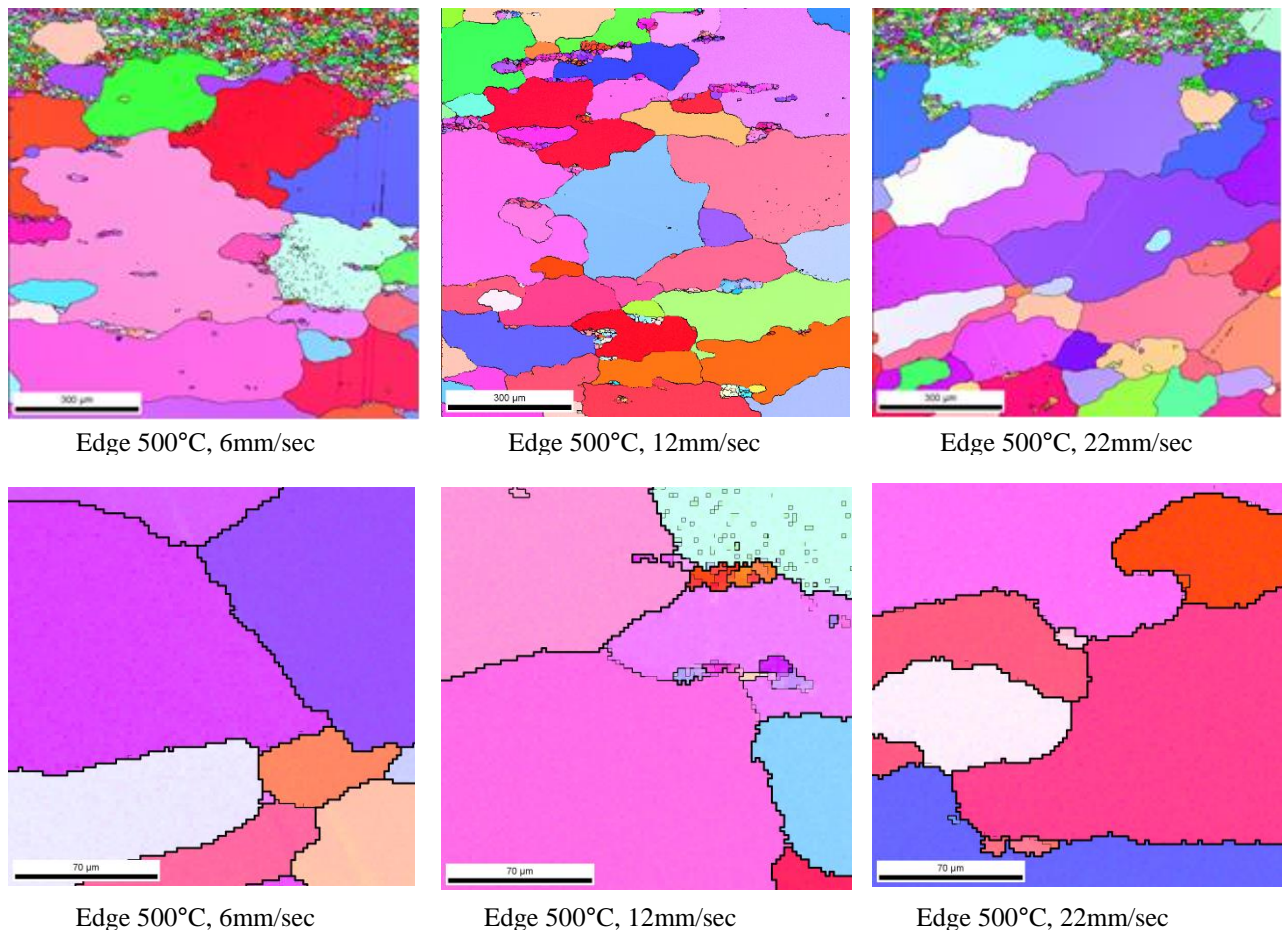
Optical micrographs in Chapter 6.2.1 have indicated that there is a noticeable effect of extrusion speed on the structure. EBSD analysis was performed to evaluate if this effects with respect to subgrain size and misorientation. Figure 6.19 show the EBSD results for the rectangular sections with constant extrusion temperature and increased extrusion speed.



*Figure 6.20* EBSD graphs of the rectangular sections in the center with ram speed increase.  
(Courtesy of Hydro Aluminium Mr. John Rasmus Leinum)

The top three EBSD graphs show a similar pattern to the optical micrographs. They indicate a structure of smaller grains in the center and increased extrusion speed seems to have an increasing effect on the visible grain structure. Figure 6.20 show the EBSD result of the center part of the rectangular sections with increasing speed whilst the temperature remains constant. These EBSD output clearly show the increase of recrystallization with increasing speed.

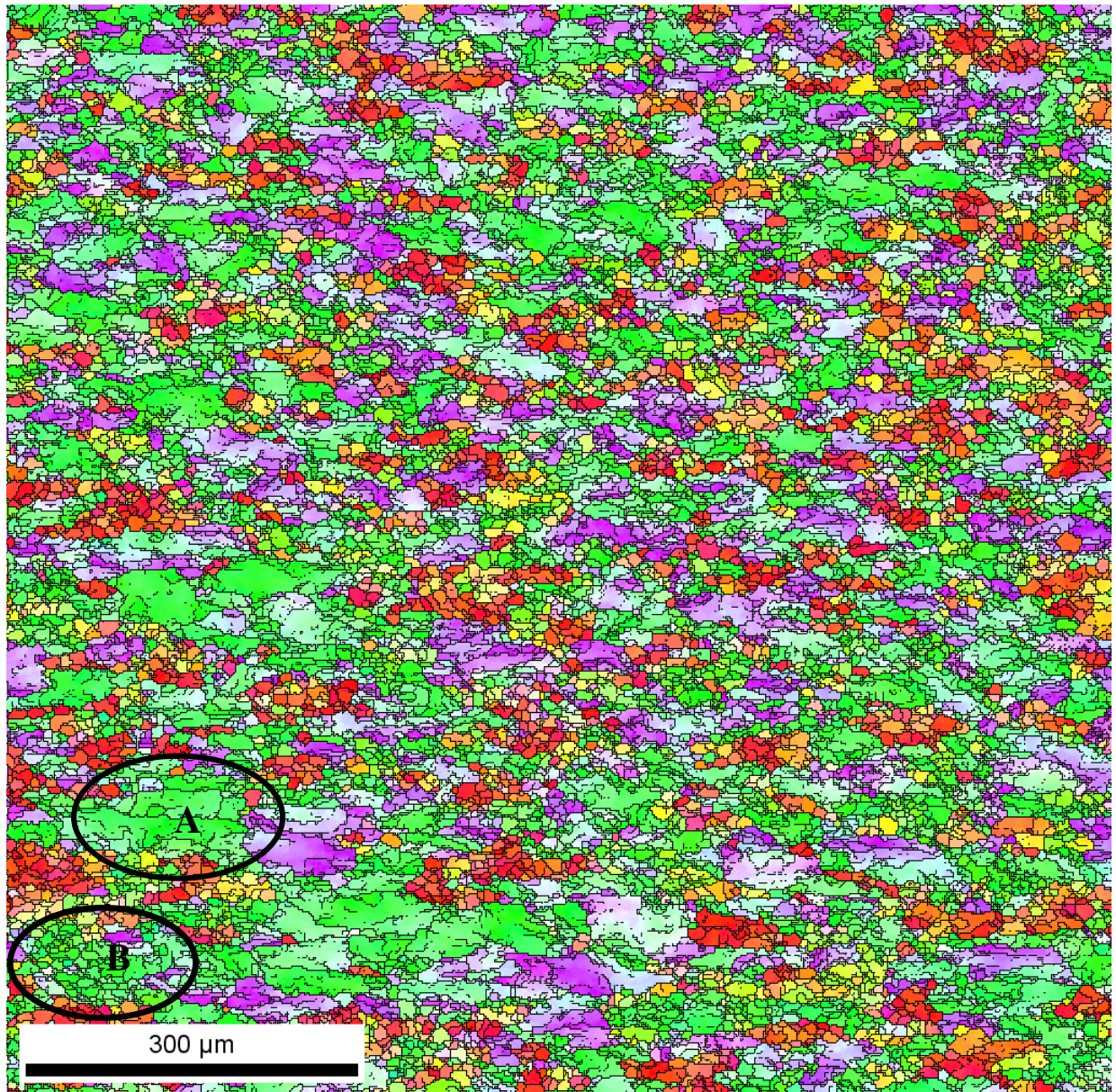
Figure 6.21 show the EBSD result of the center part of the rectangular sections with increasing speed whilst the temperature remains constant. The EBSD graphs are similar to those of the rectangular section with increased temperature.



*Figure 6.21* EBSD graphs of the rectangular sections in the edge with ram speed increase. (Courtesy of Hydro Aluminium Mr. John Rasmus Leinum)



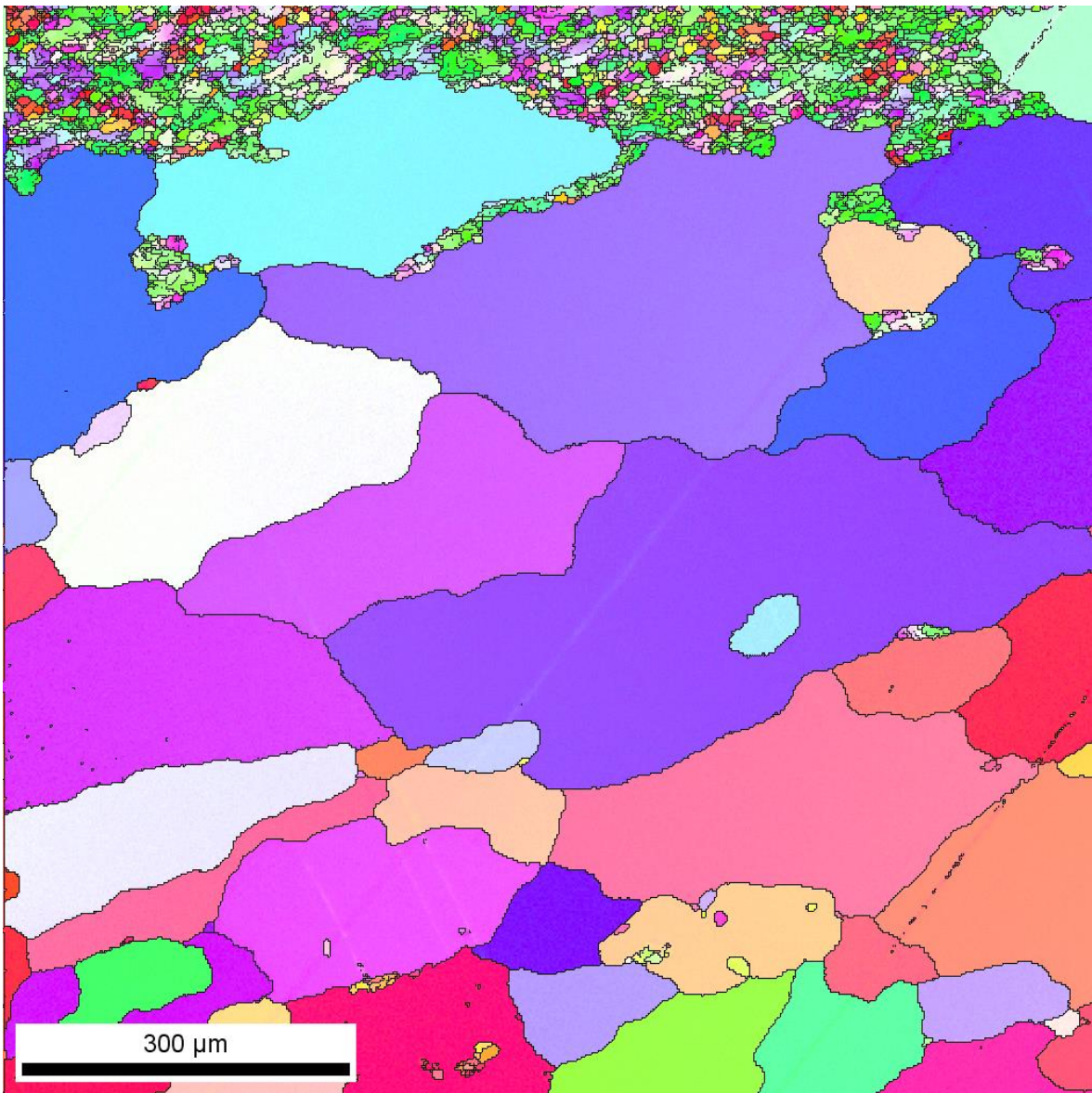
The top three EBSD graphs in Figure 6.21, show a band of substantially smaller grains towards the extrudates surface which most likely is caused by cooling effects. The bottom three EBSD graphs in figure 6.20 show a noticeable reduction in subgrain size with increasing extrusion speed.



*Figure 6.22* Enlarged view of EBSD graph of the rectangular section 500°C and 22mm/sec in the center of the sample. (Courtesy of Hydro Aluminium Mr. John Rasmus Leinum)



Figure 6.23 show a more detailed enlarged view of EBSD graph 500°C and 22mm/sec.



*Figure 6.23* Enlarged view of EBSD graph of the rectangular section 500°C and 22mm/sec in the edge of the sample. (Courtesy of Hydro Aluminium Mr. John Rasmus Leinum)

In figure 6.22 an enlarged view of EBSD graph (500°C and 22mm/sec) is presented. This EBSD graph show a mixed structure of larger and smaller grains. The larger grains seem to be elongated in extrusion direction. There is a large concentration of smaller grains.

Within the larger grains the subgrain boundaries are clearly visible. The nature of the subgrain morphology is following the deformed grain. Figure 6.22A show the forming of grains by subgrain coalescence. Figure 6.22B show an example of the situation at Figure 6.22A but then a few moments earlier in the forming process of the structure. Structure control therefor depends on extrusion conditions. High strength or low Z regions correspond with partial or un-recrystallised substructures whilst the low strength levels are associated with completely recrystallized structures. Figure 6.22 show a partial recrystallize structure from the center of the sample. This would suggest that there is a variation in the mechanical properties of the rectangular sections.

EBSD graph of the rectangular section (500°C and 22mm/sec) showing maximum extrusion speed is selected since it seem to show a large number of subgrain boundaries. The EBSD graph does show a large number of smaller grains. The optical evaluation of this graph may be misleading since it is difficult to distinguish between thinner and thicker lines with smaller grains. The increase in speed seems to coincide with the reduction of subgrains visible in the EBSD graphs. Quantified conclusions regarding the subgrains can only be made after application of the calculation method to all the numerical data as a result of the EBSD analysis. The EBSD results for subgrain size and misorientation with increased extrusion speed are presented in table 6.3.

Average subgrain size, misorientation angle from EBSD analysis				
rectangular	average subgrain size	average grain size	average misorientation subgrain	average misorientation grain
500°C, 6mm/s	5.53	15.89	5.38	29.01
500°C, 12mm/s	5.35	15.63	5.35	30.15
500°C, 22mm/s	5.27	15.93	5.47	29.7

Table 6.3 EBSD results for subgrain size ( $\mu m$ ) and misorientation ( $^{\circ}$ ) for the rectangular sections with increased extrusion speed.

The numerical data presented in Table 6.3 support the trend that the average subgrain size and misorientation of the subgrains in the center of the rectangular sections decreases with

increased extrusion speed. The average grain size and misorientation increases with increasing extrusion speed. These results support the theory that process parameters such as extrusion temperature influence the substructure.

Table 6.3 presents' average values for the subgrain size and a trend of decreasing subgrain size with increasing extrusion temperature is visible. However should we wish to have quantitative data regarding the percentage of smaller (sub)grains present in the investigated area presented in the EBSD map, statistical data can help. Figure 6.24 show the statistical data regarding (sub) grain size with increasing extrusion speed.

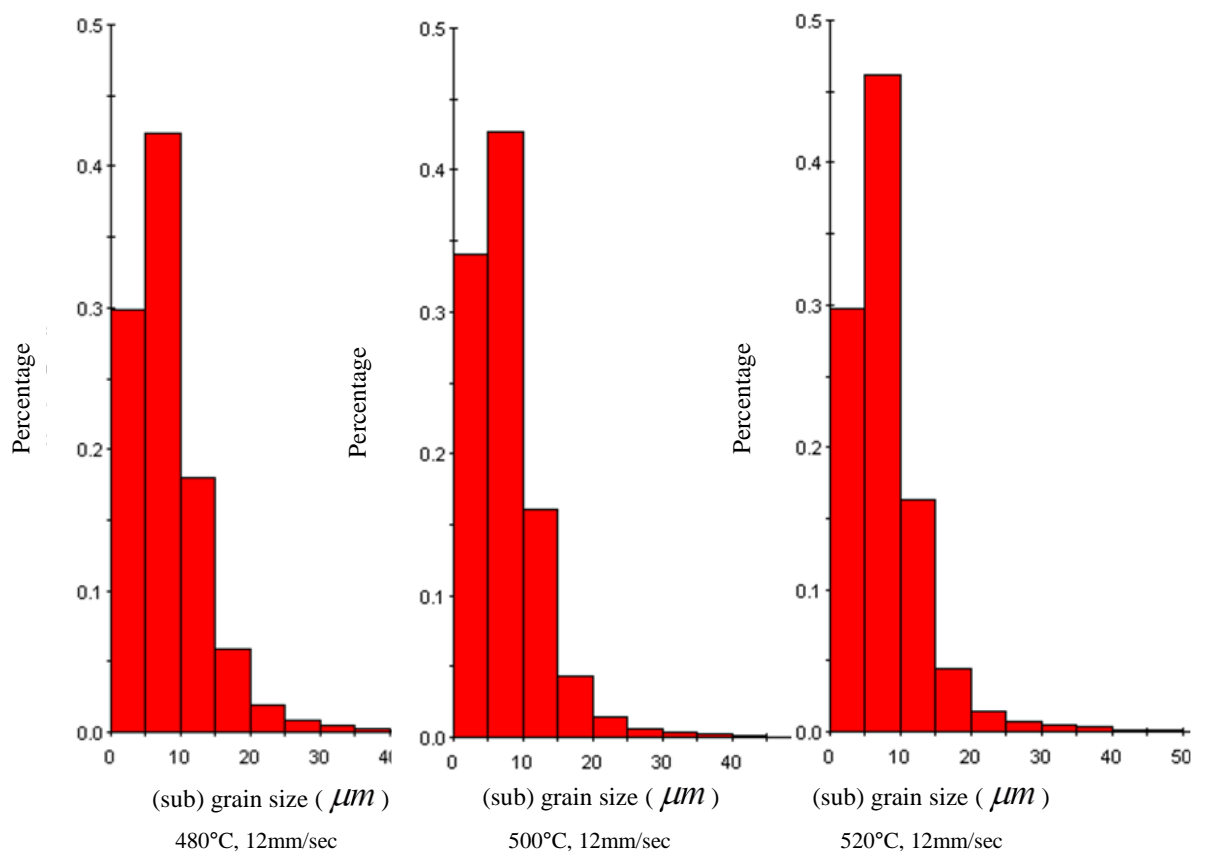


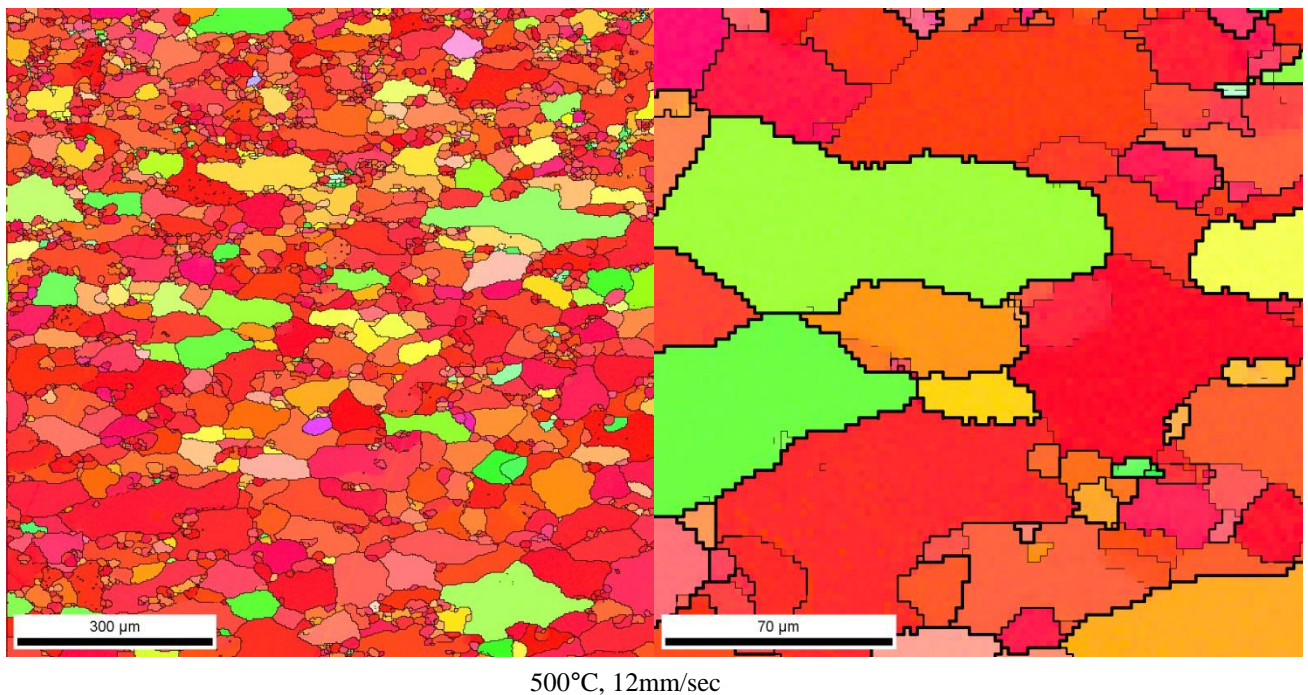
Figure 6.24 (sub) grain size ( $\mu\text{m}$ ) distribution with increasing extrusion speed (Courtesy of Hydro Aluminium Mr. John Rasmus Leinum)



The graphs in Figure 6.24 show the distribution of (sub) grains as a percentage of the total number of (sub) grains in the sample area investigated by means of EBSD. The percentage of (sub) grains smaller than  $10\ \mu\text{m}$  in the center area of the rectangular samples increases with increasing extrusion temperature ( $480^\circ\text{C}$ - 73%,  $500^\circ\text{C}$ - 77%,  $520^\circ\text{C}$ - 78%). The dimensional difference between grains and subgrains is probably somewhere between 5 and  $10\ \mu\text{m}$ . Since larger subgrains can occur the trend was made visible by the  $10\ \mu\text{m}$  mark. (Poschmann, McQueen, 1998).

#### 6.2.2.4 Effect of section geometry

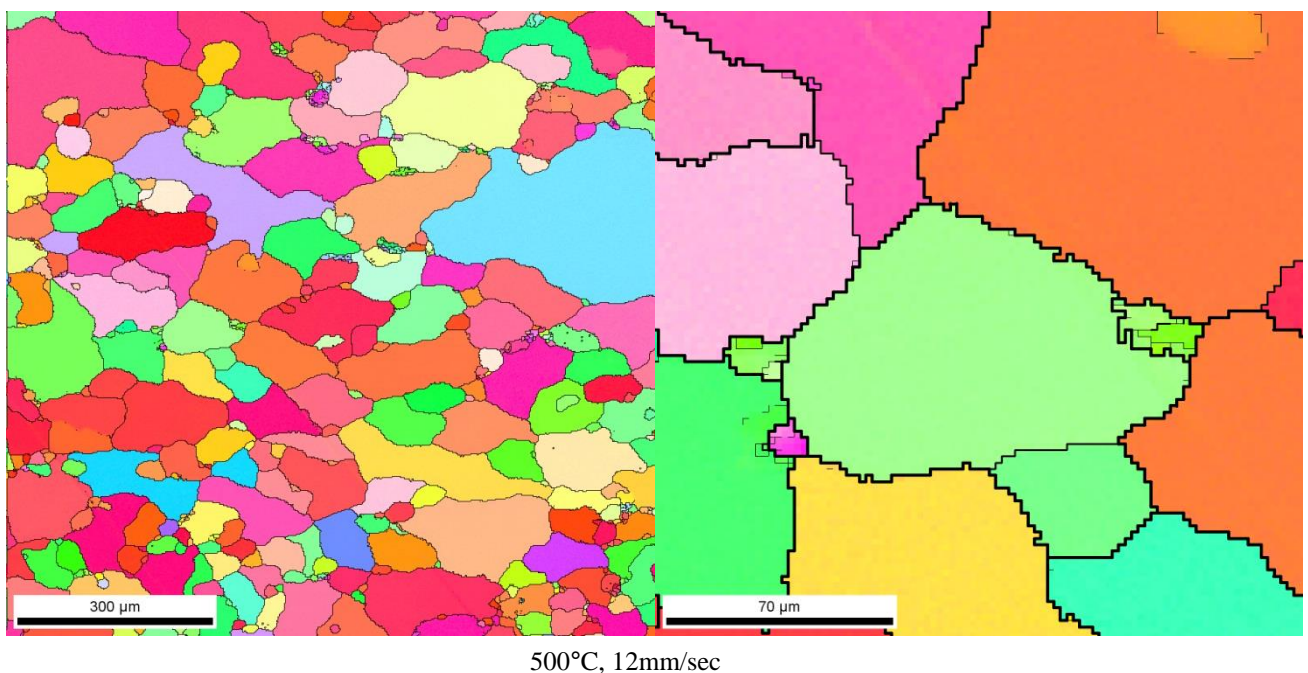
Optical micrographs in chapter 6.2.1.3 have illustrated that the U-shaped section and the tube show a different structure compared to the rectangular section. Differences between the rectangular sections and the U-shaped section and the tube were mainly reduced wall thickness and increased extrusion ratio. The investigated area is given in Figure 6.12.



*Figure 6.25* EBSD graphs of the U-shaped sections. (Courtesy of Hydro Aluminium Mr. John Rasmus Leinum)

The optical micrographs of the U-shaped section indicated a fully (or almost fully) recrystallised structure where effects of details in the geometry and the distance to the extrudate surface would influence the internal structure. The EBSD graphs for the U-shaped section are presented in Figure 6.25

The EBSD graph of the U-shaped section show a more or less regular structure of a mixture of larger and smaller grains. The larger grains seem to be not uniformly deformed. The smaller grains appear as coalescence of subgrains. At greater magnification the EBSD graph is supporting this impression. The smaller grains are accompanied by subgrain boundaries which indicate that the structure is not fully recrystallised. This supports the conclusion from the optical micrographs that the structure is not fully recrystallised. The optical micrographs of the tube section show a very regular structure in the center of the feeder hole. The grain size seems to increase towards the inner wall. In the area close to the position of the bridge the grain structure show an increased grain size over almost the whole wall thickness. Close to the outer section surface smaller grains are visible. The optical micrographs indicate that the structure is fully recrystallised. The EBSD graphs for the tube section are presented in Figure 6.26.



*Figure 6.26* EBSD graphs of the tube sections. (Courtesy of Hydro Aluminium Mr. John Rasmus Leinum)

The EBSD graph of the tube section show a more regular structure with larger grains compared to the U-shaped structure. There is less indication of a preferred orientation for the grain geometries. They seem to be more regular and random oriented. Coalescence of subgrains cannot be detected in the tube. All the grains are larger than the grains in the U-shaped structure. At greater magnification the EBSD graph is showing very few subgrain boundaries. The presence of only a few subgrain boundaries indicate that the structure is probably fully recrystallised. This supports the conclusion from the optical micrographs that the structure is fully recrystallised. In table 6.4 the EBSD results for subgrain size and misorientation are presented for the U-shaped section and the tube.

Average subgrain size, misorientation angle from EBSD analysis				
sample	average subgrain size	average grain size	average misorientation subgrain	average misorientation grain
u-shaped	5.74	24.17	7.31	12.91
tube	5.74	25.31	7.31	22.17

Table 6.4 EBSD results for subgrain size ( $\mu m$ ) and misorientation ( $^{\circ}$ ) are presented for the U-shaped section and the tube.

The average subgrain size and grain size for the U-shaped section and the tube are the largest in the experimental series. Table 6.4 presents' average values for the subgrain size. However should we wish to have quantitative data regarding the percentage of smaller (sub)grains present in the investigated area presented in the EBSD map, statistical data can help. Figure 6.27 show the statistical data regarding (sub) gerain size for the U-shaped section.

The graphs in Figure 6.27 show the distribution of (sub) grains as a percentage of the total number of (sub) grains in the sample area investigated by means of EBSD. The percentage of (sub) grains smaller then  $10 \mu m$  for the U-shaped section and he tube (U-shaped- 56%, tube - 55%) are substantially lower than in the rectangular geometry. The dimensional difference between grains and subgrains is probably somewhere between 5 and  $10 \mu m$ . Since larger subgrains can occur the trend was made visible by the  $10 \mu m$  mark.

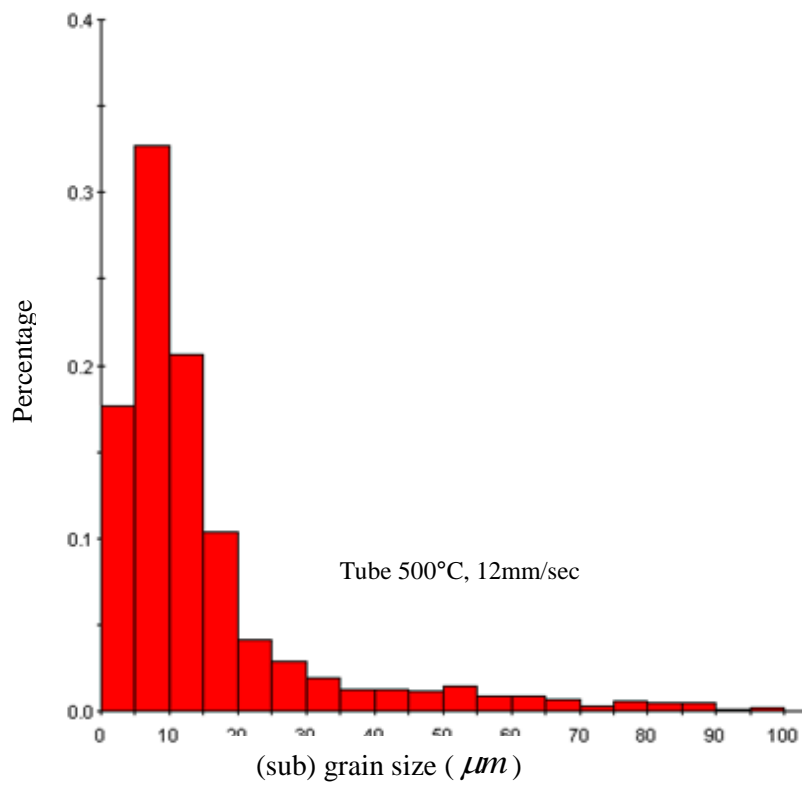
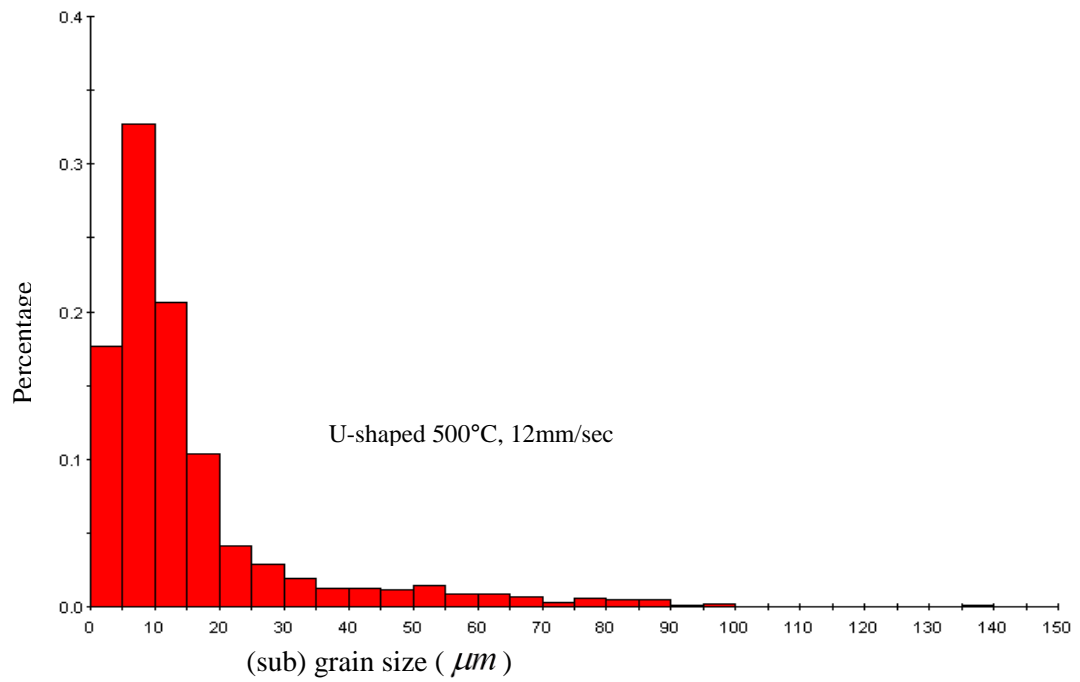


Figure 6.27 show the (sub) grain size ( $\mu m$ ) distribution for the U-shaped section and the tube. (Courtesy of Hydro Aluminium Mr. John Rasmus Leinum)

We have large margins because of the limits set in the software. These graphs can only be used to visualise the overall trend. Figure 6.26 show the subgrain size distribution for the U-shaped section and the tube.

#### 6.2.4 Simulation Results

The flow stress equation was initially proposed by Zener and Holloman (1944), later verified by Sellars et al. (1972) and subsequently rearranged by Sheppard and Wright (1979) is given below.

$$\bar{\sigma} = \frac{1}{\alpha} \ln \left[ \left( \frac{Z}{A} \right)^{\frac{1}{n}} + \sqrt{\left( \frac{Z}{A} \right)^{\frac{2}{n}} + 1} \right] \quad (6.1)$$

Where the parameters  $\alpha, A, n$  are material dependent constants. In this study the value for EN AW-6082 material are as follows: ( $\alpha = 0.052 m^2 MN^{-1}, A = 2.39 \times 10^8 s^{-1}, n = 2.976$ ). Nes et al. (1994) showed that equation (6.1) reduces to a power law when  $\alpha \bar{\sigma} < 0.8$ , but approximates an exponential relationship when  $\alpha \bar{\sigma} > 1.2$ .  $Z$  is the temperature compensated strain rate parameter also called the Zener-Hollomon parameter and is defined as follows:

$$Z = \dot{\epsilon} \exp \left( \frac{\Delta H}{RT} \right) \quad (6.2)$$

In which  $T$  is the temperature,  $R$  is the universal gas constant ( $8.31451 J * mol^{-1} * K^{-1}$ ), and  $\Delta H$  is the activation energy for hot deformation. It is generally accepted that the subgrain size  $\delta$  can be directly related to the temperature-compensated strain-rate or Zener-Hollomon parameter,  $Z$ , by the following equation:

$$\delta_{ss}^m = A + B \ln Z \quad (6.3)$$

Where  $A, B, m$ , are constants. ( $A = -0.455, B = 0.025, m = -1$ )

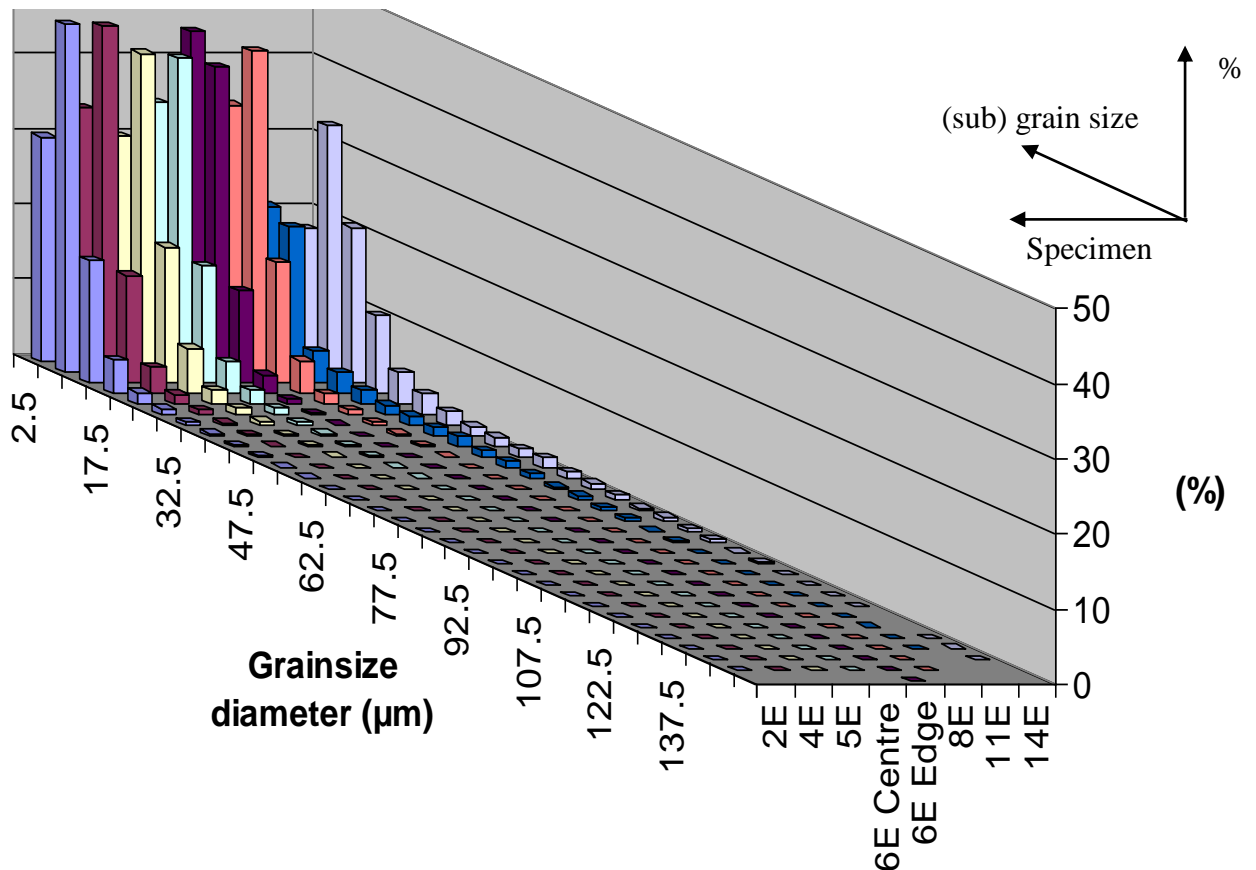


Figure 6.28 Graphical representations for all the EBSD results for grain size and subgrain size ( $\mu m$ ) from the center of the sample for the experimental geometries.

A good subgrain size fit could be obtained by varying exponent  $m$  within a range between -1.25 and -0.35 (Zaidi and Sheppard 1983). In fact, many researchers (Chanda et al. 2000); have chosen  $m = -1$  to produce accepted results. This is because obtainable subgrain size ranges, under hot working conditions, are very small when compared with the total subgrain size range. It should also be emphasized that equation (6.3) is not valid for prediction of subgrain size in a transient deformation. Prior to presenting the simulation results an overview is given for the EBSD results with respect to subgrain size and

misorientation. Figure 6.28 show a representation for the EBSD results for (sub) grain size of the center of all the experiments. EBSD measurements were performed for the (sub) grains visible in the marked areas in Figure 6.12. Figure 6.28 show the combined (sub) grain size as a function of the percentage present in the sample area for all experiments.

The rectangular sections (samples 2E, 4E, 5E, 6E and 8E) all show a comparable pattern. Subgrains smaller than or equal to a size of  $10\ \mu\text{m}$  are predominantly present in the sample. All the rectangular samples consist of a structure in which approximately 70-80% of all the (sub) grains present are smaller or equal to  $10\ \mu\text{m}$ . There are only very few grains present larger than  $22.5\ \mu\text{m}$  which is as could be expected since the sample area is from the center of the specimen. The EBSD results for (sub) grain size of the U-shaped section and the tube (11E and 14E), show a different pattern. Approximately 50-55% of the (sub) grains are smaller than or equal to  $10\ \mu\text{m}$ . At least 30% of the grains are between 10 and  $20\ \mu\text{m}$ . And between 15 and 20% of the grains are larger than  $20\ \mu\text{m}$ .

These figures are consistent with the almost completely recrystallised structure present in the U-shaped section and the tube. There are even grains which are larger than  $70\ \mu\text{m}$ . This is even more predominant for the tube section. This agrees with the fully recrystallised structure which Figure 6.5 show. Observing rectangular section samples (6E, 5E and 4E) in Figure 6.28 which were extruded at 12mm/s and increasing extrusion temperature (480, 500 and  $520^\circ\text{C}$ ) show that increasing the extrusion temperature whilst the extrusion speed is kept the same will reduce the average subgrain sizes.

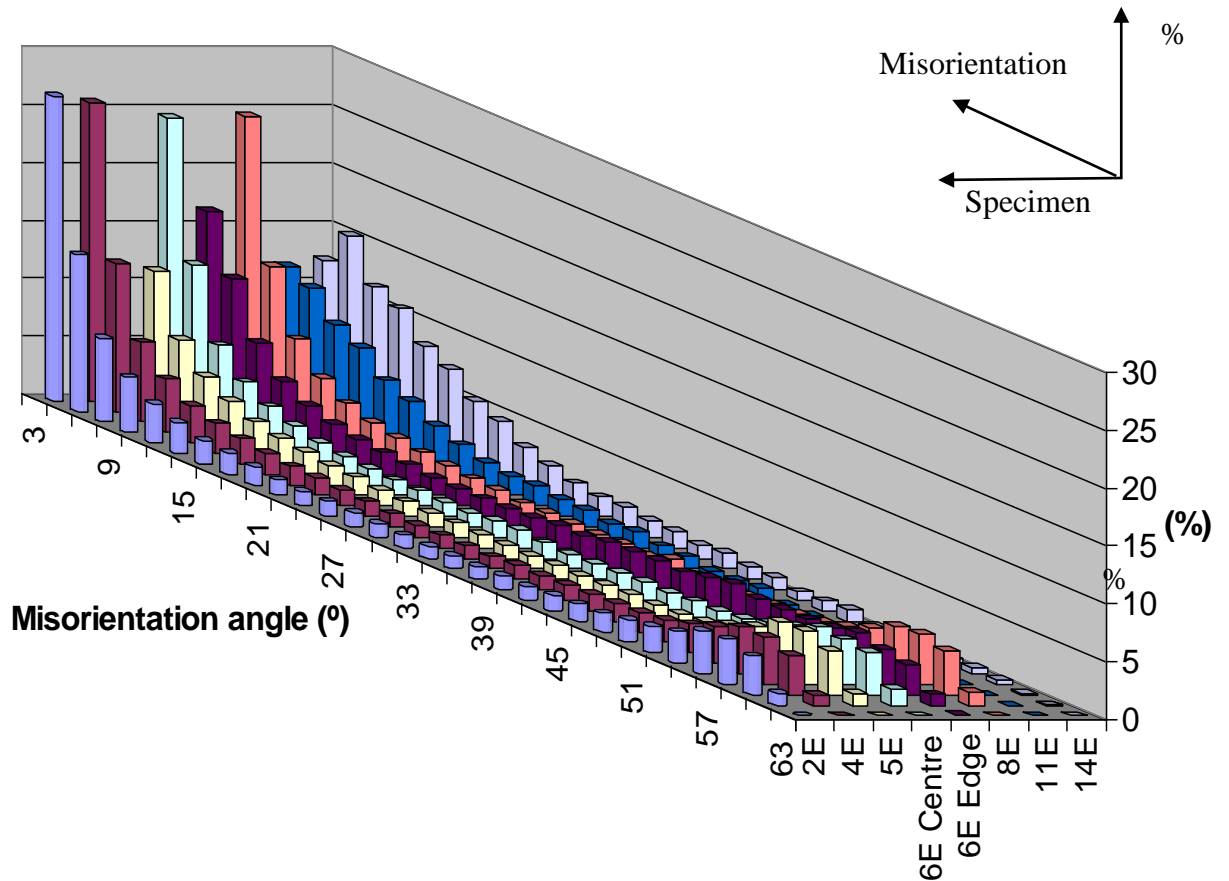


Figure 6.29 Graphical representations for all the EBSD results for misorientation ( $^{\circ}$ ) from the center of the sample for the experimental geometries.

The rectangular section samples in Figure 6.28 samples (2E, 5E and 8E) extruded at 6, 12 and 22 mm/s and  $500^{\circ}\text{C}$  show that when the extrusion temperature is kept the same and the extrusion speed is increased, the subgrain size is reduced. Figure 6.29 show a representation for the EBSD results for misorientation of all the experiments. EBSD measurements are performed for the (sub) grains visible in the marked areas in Figure 6.12. Figure 6.29 show the combined misorientation for all experiments as a function present in the extruded test samples. The rectangular sections (samples 2E, 4E, 5E, 6E and 8E) in Figure 6.29 all show a comparable pattern. Misorientation angles smaller than or equal to  $6^{\circ}$  are predominantly present in the sample. Approximately 40% of the (sub) grains show a misorientation angle of smaller than or equal to  $5^{\circ}$ . Approximately 60% of the (sub) grains have a misorientation angle of smaller than or equal to  $15^{\circ}$ .



The shape of the misorientation curve is more or less like a bath tub curve. The decrease is followed by a relative large range of more or less constant percentage followed by an increase. In other words, all rectangular sections show a relative constant picture with approximately 25% of (sub) grains showing misorientation angles between 15 to 50°. Only a few (sub) grains show misorientation angles larger than 50°. Samples 11E and 14E in Figure 6.29, which are the U-shaped section and the tube, show a different pattern.

Approximately 70-80% of the grains have a misorientation angle larger than 9° and approximately 12% of the subgrains have a misorientation smaller than 5°. The tube section has very few subgrains with very small misorientation angles. This agrees with the fully recrystallised structure which can be found in Figure 6.5. The simulated values for subgrain size are presented in Figure 6.30 for all the samples in the experimental sequence. The EBSD results for subgrain size and misorientation and simulated results for subgrain size are presented in Table 6.5.

Average subgrain size, misorientation angle from EBSD analysis and simulation						
section geometry	extrusion condition	EBSD subgrain size	simulated subgrain size	average grain size	average misorientation subgrain	average misorientation grain
rectangular	480°C, 12mm/s	5.44	5.66	15.19	5.53	29.9
rectangular	500°C, 12mm/s	5.35	5.28	15.63	5.35	30.15
rectangular	520°C, 12mm/s	4.72	4.88	16.18	5.05	31.64
rectangular	500°C, 6mm/s	5.53	5.38	15.89	5.38	29.01
rectangular	500°C, 12mm/s	5.35	5.28	15.63	5.35	30.15
rectangular	500°C, 22mm/s	5.27	5.31	15.93	5.47	29.7
u-shaped	500°C, 12mm/s	5.74	6.17	24.17	7.31	12.91
tube	500°C, 12mm/s	5.74	6.28	25.31	7.31	22.17

Table 6.5 The EBSD results for subgrain size ( $\mu m$ ) and misorientation ( $^{\circ}$ ) and simulated results for subgrain size.

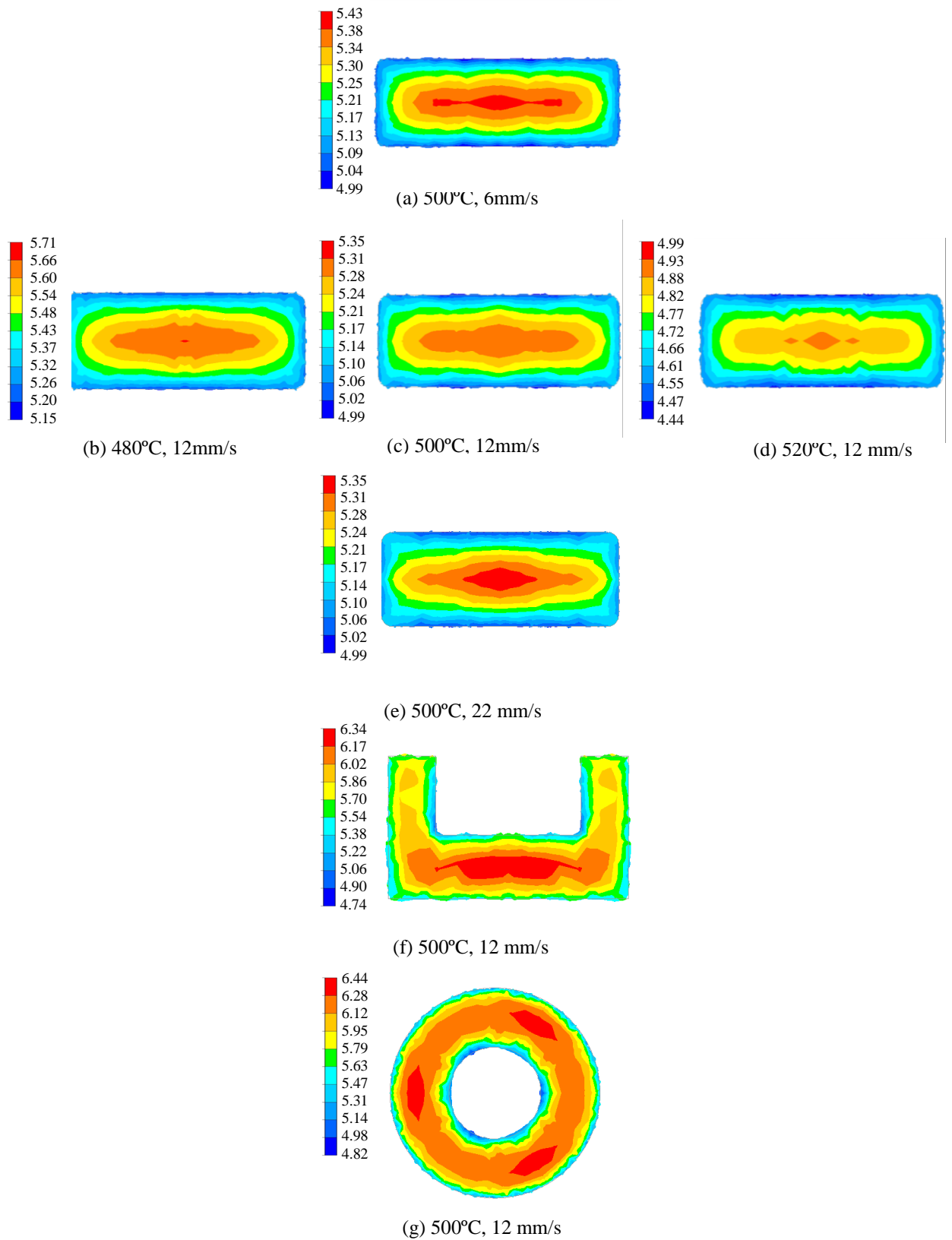


Figure 6.30 simulated subgrain sizes ( $\mu\text{m}$ ) for the experimental samples.

The experimental (EBSD) and simulated values from the center part of the rectangular sections show a decrease in average subgrain size with increased extrusion temperature and extrusion speed. Table 6.6 show the EBSD and simulated results for subgrain size with increased extrusion temperature. Table 6.7 show the EBSD and simulated results for subgrain size with increased extrusion speed. This decrease in subgrain size with increased extrusion temperature and speed is as could be expected and is supported by the EBSD graphs and optical micrographs of these sections. Table 6.8 show the EBSD and predicted values for subgrain size for the U-shaped section and the tube. The correlation between experimental (EBSD) values and simulated values is reasonable and within acceptable deviations.

section geometry	extrusion condition	EBSD subgrain size	simulated subgrain size
rectangular	480°C, 12mm/s	5.44	5.66
rectangular	500°C, 12mm/s	5.35	5.28
rectangular	520°C, 12mm/s	4.72	4.88

Table 6.6 EBSD and simulated results for subgrain size ( $\mu m$ ) with increased extrusion temperature.

section geometry	extrusion condition	EBSD subgrain size	simulated subgrain size
rectangular	500°C, 6mm/s	5.53	5.38
rectangular	500°C, 12mm/s	5.35	5.28
rectangular	500°C, 22mm/s	5.27	5.31

Table 6.7 EBSD and simulated results for subgrain size ( $\mu m$ ) with increased extrusion speed.

section geometry	extrusion condition	EBSD subgrain size	simulated subgrain size
u-shaped	500°C, 12mm/s	5.74	6.17
tube	500°C, 12mm/s	5.74	6.28

Table 6.8 EBSD and simulated results for subgrain size ( $\mu m$ ) for the U-shaped section and the tube.

### 6.3 Dislocation density

For steady state deformation a generally recognised equation relating subgrain size to internal dislocation density can be written as:

$$\rho_i^{\frac{1}{2}} \delta_{ss} = C \quad (6.4)$$

$$\frac{1}{\delta_{ss}} = A \ln Z - B \quad (6.5)$$

Where  $\delta_{ss}$  is the subgrain size at steady state and C a constant which is reported to range from 5 to 30 (Sellars 1997) ( $A = -0.455$ ,  $B = 0.025$ ), (Duan and Sheppard 2003).

Transient dislocation evolution can be calculated in terms of dislocation density storage from work hardening. The dislocation density decreases by recovery. During plastic deformation internal random dislocations are created by work hardening and annihilated by dynamic recovery. We assume steady state for the simulations.

Extrusion is a process characterized by large and transient plastic deformations. EN AW-6082 material usually consist of a relatively high number of dislocations. The microstructure has a restricting effect on the movement of these dislocations. Higher numbers of dislocations have a negative effect on the surface quality of the alloy. Both factors affect extrudability.

Figure 6.30 show the simulated results for the dislocation density for all the experiments and Table 6.10 show the numerical simulated values for the dislocation density. The simulated values (using equation 6.2) show a reduction in dislocation density with increased extrusion temperature and extrusions speed which is in agreement with expectations. With the exception of rectangular section (500°C, 6mm/s) this trend can be seen in the simulation results presented in Table 6.9.

section geometry	extrusion condition	dislocation density ( $\times 10^{13}$ )
rectangular	480°C, 12mm/s	11.1
rectangular	500°C, 12mm/s	9.51
rectangular	520°C, 12mm/s	8.73
rectangular	500°C, 6mm/s	9.23
rectangular	500°C, 12mm/s	9.51
rectangular	500°C, 22mm/s	8.66
u-shaped	500°C, 12mm/s	7.7
tube	500°C, 12mm/s	7.37

Table 6.9 Simulated results for dislocation density ( $\times 10^{13}$ ) for all the geometries in the experiments

The simulated dislocation density values for the rectangular sections show a decrease dislocation density with increased extrusion temperature and ram speed which is as to be expected.

The effect of a band of lower dislocation density in sample, Figure 6.31 (500°C, 12mm/s) is most likely caused by software aberrations.

The U-shape section and the tube show an almost uniform dislocation density for most of the cross section. The dislocation density values for the U-shaped section and the tube are lower than those of the rectangular sections due to the higher extrusion ratio.

Measurements of dislocation density require Transmission Electron Microscopy (TEM) and specific operating expertise. At this stage there was no expertise or equipment available to perform these measurements.

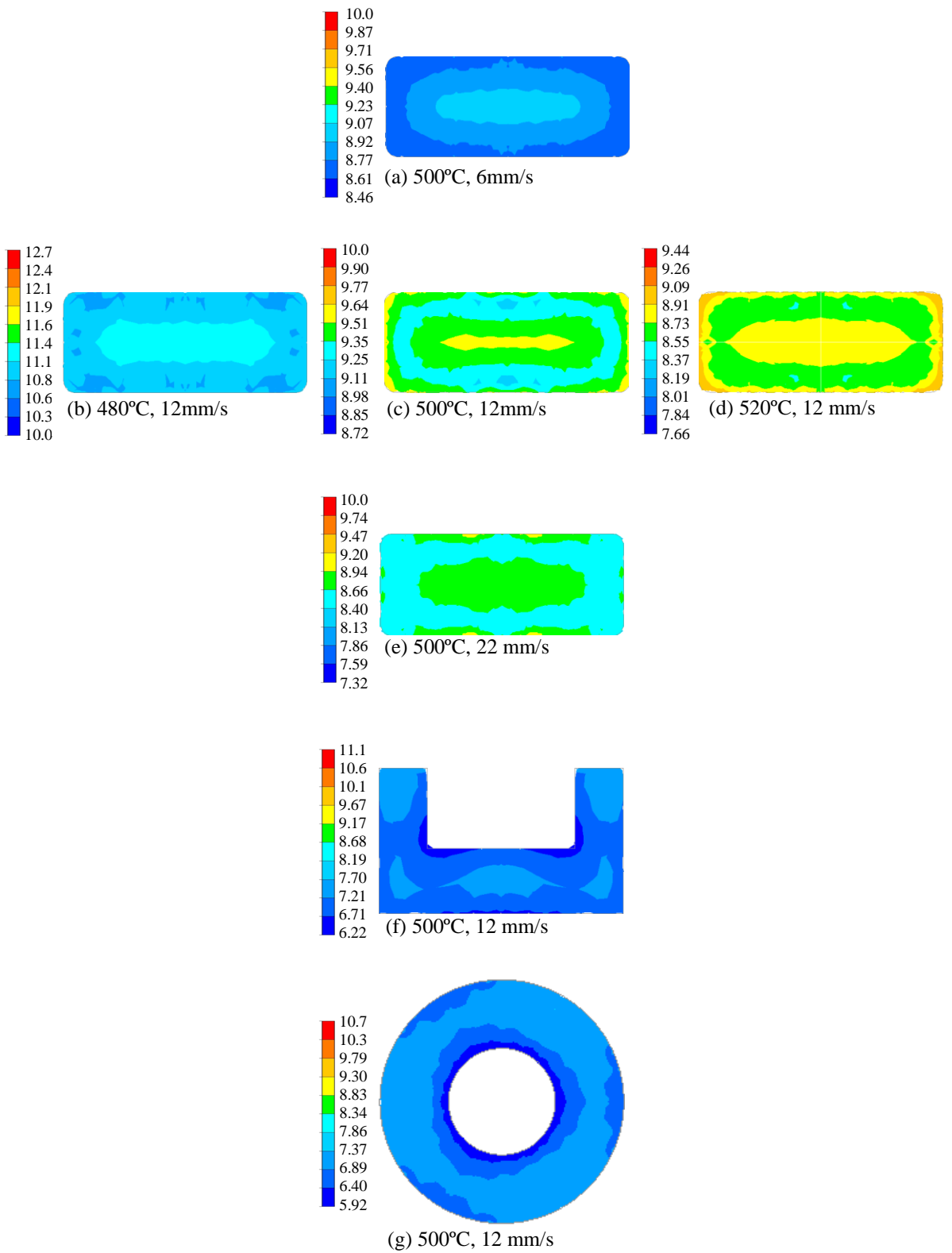


Figure 6.31 Dislocation density (x10<sup>13</sup>) for the experimental samples

## 6.4 Volume fraction recrystallized

With suitable quench conditions, the material can retain the (unrecrystallised) subgrain structure produced during extrusion. This yields the steady increase in mechanical properties (both yield strength and UTS) for material extruded at low temperatures compared to high temperature extrusion. There are practical implications involved in extruding at low temperatures and at low ram speeds. Both conditions would promote less recrystallisation and could yield mechanical properties. In some cases the specific pressure is insufficient to extrude under these conditions. In other cases there could be commercial restrictions extruding at low ram speeds. The challenge would be to find a commercial application for the improved properties or to alter the extrusion parameters such as cooling, stretching etc.

Cooling practice in extrusion plants is often far from ideal. To ensure sufficient cooling of extrusions of EN AW-6082 materials with wall thicknesses over 4mm usually require a water quench. In conventional extrusion plants this often results in deformed sections and water staining. Since this is not acceptable or leading to high levels of scrap in many cases air cooling is applied. This means that on the run out overhead cooling fans are applied and on the table underneath cooling. This leads to uneven and insufficient cooling. The industry requires a far more powerful and controllable air cool quench box which requires further research and investments. An ideal cooling unit should be able to control the cooling increment and compensate for geometrical effects.

Equation 6.4 is widely accepted to be used to calculate volume fraction recrystallised.

$$X_v = 1 - \exp\left\{-\frac{\ln 0.5}{(t_{50})^n} t^n\right\} = 1 - \exp\left\{-0.693\left(\frac{t}{t_{50}}\right)^n\right\} \quad (6.6)$$

According to Furu and i.e. Nes the Avrami exponent  $n$  has a value of 2 (Furu et al. 1999), (Shercliff 1997). The Avrami exponent for Al1Mn1Mg is reported to be 2.4 and for

Al1Mn0.5Mg to be 1.6. These values correspond with values commonly found for recrystallisation. There would appear to be no theoretical reason why  $n$  should vary or written as a mistake other than the fact to obtain acceptable fits to the equation.

According to Vatne et al. (1996)  $t_{50}$  can be calculated using:

$$t_{50} = \frac{C_t}{M_{GB} P_D} \left( \frac{1}{N_V} \right)^n \quad (6.7)$$

$C_t / M_{GB} = 7.82 \cdot 10^{13} N.S.m^{-5}$  at a deformation temperature of 623°C (Sheppard and Peng 2004). The most widely used equation, Huang and Humphreys (1999), Driver et al. (2005), for grain boundary mobility is:

$$M_{GB} = M_0 \exp\left(\frac{-Q_{GB}}{RT}\right) \quad (6.8)$$

In EN AW-6082 alloys the desired structure after extrusion is one exhibiting the least possible recrystallisation. This alloy is usually artificially aged to produce maximum mechanical properties.

Figure 6.32 show the simulation results for the geometries used in the experiments and Table 6.10 give the combined simulated and estimated values for volume fraction recrystallised. The effect of an increase of the initial billet temperature from 480 °C to 500 °C and ultimately to 520 °C of the rectangular section, whilst keeping the extrusion speed constant at 12 mm/sec, is an increase in the predicted volume fraction recrystallised from 69 to 88 and 98 at the outer area. The center will show an increase from 36 to 55 and 79 respectively. When the billet temperature remains at 500 °C and the extrusion speed is increased from 6 mm/sec to 12 mm/sec and finally to 22 mm/sec the volume fraction recrystallised is increased from 78 to 88 and finally 98 at the outer edge of the section. The center show an increase from 63 to 55 and 75.



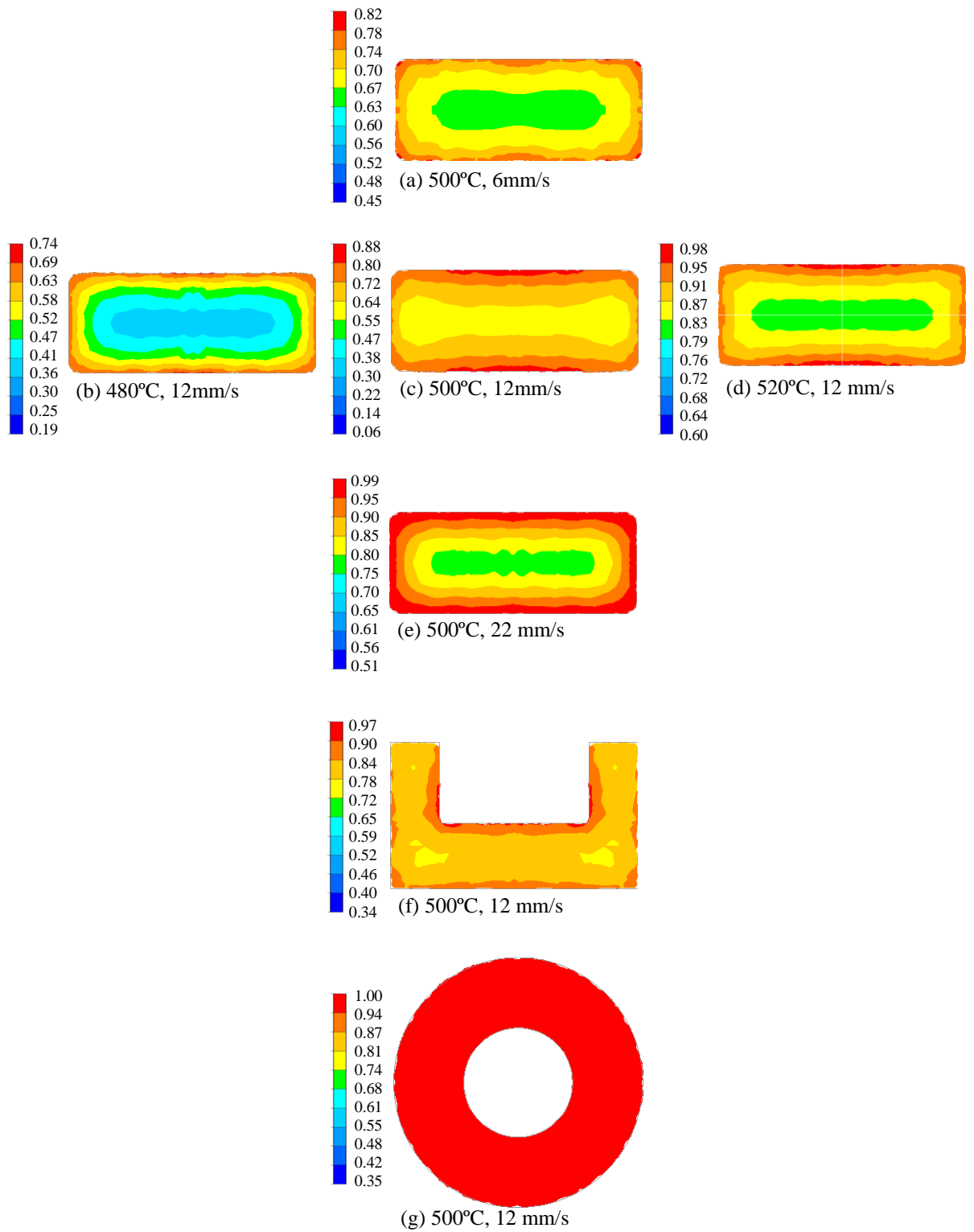


Figure 6.32 Volume fraction recrystallised (%) simulation results for the experimental samples.

The combinations of high initial billet temperature and high extrusion speed will lead to the higher values of volume fraction recrystallised. The initial billet temperature of 500 °C and an extrusion speed of 22 mm/sec results in a volume fraction recrystallised of 75 in the center and 99 at the edge. At the same time a similar result is obtained when the initial billet temperature is 520 °C and an extrusion speed of 12 mm/s results in a volume fraction recrystallised of 79 in the center and 98 at the edge. For the rectangular section extrusion lower initial billet temperature and medium extrusion speed will lead to a lower fraction recrystallised of 36 in the center of the section. See Figure 6.19b. High initial billet temperature combined with high extrusion speed will lead to a higher volume fraction recrystallised of 79 in the center of the section.

Extrusion of the U-shaped section show a higher level of recrystallisation over the whole cross section of the profile. The geometry of the U-shaped profile has a smaller wall thickness and a more complex nature due to its shape. Therefore it is likely to show higher level of recrystallisation and a more uniform recrystallisation compared to the rectangular sections. High levels of recrystallisation occur mainly at the corners of the section and surface areas where friction and deformation contribute to temperature increase. The U-shaped section show volume fraction recrystallised results of 78 in the center and 97 at the edge. The U-shaped section reveals a more uniform recrystallisation and an overall further recrystallised structure compared to the rectangular section. In Table 6.10 the combined simulated and estimated values for volume fraction recrystallised are presented.

The tube section show a fully recrystallised structure. Compared to the rectangular section the tube has a smaller wall thickness which will lead to temperature increase. Because of the hollow part the contact surface area is large compared to the rectangular section. This means that contact area with the die is also larger and the area generating friction which contributes to temperature increase is also larger. More important the extrusion of a hollow section is complex. The die consists of two parts and the material will have to flow across the die bridges to form a closed tube section. The complex extrusion process of extruding a tube will lead to increased extrusion temperatures compared to solid section extrusion. This has resulted in higher levels of recrystallisation as can be seen in Figure 6.32. The tube section show a fully recrystallised structure. The tube section is show 100% volume fraction

recrystallised over the whole cross section of the simulated section. Predicted values for volume fraction recrystallised  $X_V$  are given in Figure 6.32. In Table 6.10 the combined simulated and estimated values for volume fraction recrystallised are presented.

volume fraction recrystallised					
		simulated		EBSD	
section	extrusion condition	centre	edge	centre	edge
rectangular	480 °C, 12 mm/s	36	69	55	100
rectangular	500 °C, 12 mm/s	55	88	55	100
rectangular	520 °C, 12 mm/s	79	98	55	100
rectangular	500 °C, 6 mm/s	63	78	55	100
rectangular	500 °C, 12 mm/s	55	88	55	100
rectangular	500 °C, 22 mm/s	75	99	55	100
U-shape	500 °C, 12 mm/s	78	97	80	80
tube	500 °C, 12 mm/s	100	100	100	100

*Table 6.10* Volume fraction recrystallized (%) for the experimental and simulated geometries

Industrial application of aluminium extrusions often requires a compromise between high extrusion speed and high mechanical properties. In practical extrusion of EN AW-6082 material there is usually no separate solutionising process. It must be stated that in some industrial applications there is a separate solutionising cycle. During extrusion the soluble state will have to be reached by the combination of temperature and stress. Sufficient quenching will have to keep all precipitates in solution whilst preventing recrystallisation. Apparently this is not possible using air quenching. The preferred structure prior to ageing is fully solutionised without recrystallization which in this case could only be achieved by a much lower ram speed hence at much increased production cost.

## 6.6 Precipitation

Aluminium alloys from the 6000 series contain Si and Mg as the main alloying elements. These alloys are commonly used for structural components since they can obtain reasonable mechanical properties whilst they are relatively easy to extrude. The strengthening mechanism is precipitation of the  $Mg_2Si$  phase. Prior to extrusion the material has received a homogenising treatment to rearrange the structure and to partly dissolve the  $Mg_2Si$  particles. During pre-heating of the billets at the extrusion press the remainder of the  $Mg_2Si$  particles need to be fully dissolved. Extrusion followed by quenching will preserve the dissolved state and after artificial ageing the  $Mg_2Si$  will precipitate on the grain boundaries resulting in increased mechanical properties.

The material involved in the experiments (EN AW-6082) received a homogenising treatment (580°C for 4 hr). The variation in billet temperatures tested in the experiments would have led to a situation in which the  $Mg_2Si$  is fully dissolved in the matrix.

The obvious presence of (large)  $Mg_2Si$  particles prior to or during extrusion will have a detrimental effect on extrusion output. In most cases this leads to surface deterioration and slow extrusion speed. Moreover the achievable mechanical properties would be significantly lower.

The microstructure of EN AW-6082 alloys directly after casting is not suitable for extrusion. The inhomogeneous distribution of alloying elements severely limits the maximum extrusion speed below which the surface finish still meets practical requirements such as good appearance. Furthermore it causes poor mechanical properties of the extrudate, because of the low content of dissolved alloying elements available directly after extrusion. Solute alloying elements are required to form  $\beta''$  type precipitates after extrusion which give the alloy its required strength. Optimising the casting techniques as well as homogenising the material can improve the homogeneity of the material, Van de Langkruis (2000). Figure 6.33 show structure of experimental sections including precipitates and intermetallics. The sample area for the micrographs in Figure 6.33 are given in Figure 6.12. The center sample area were used for the rectangular samples.

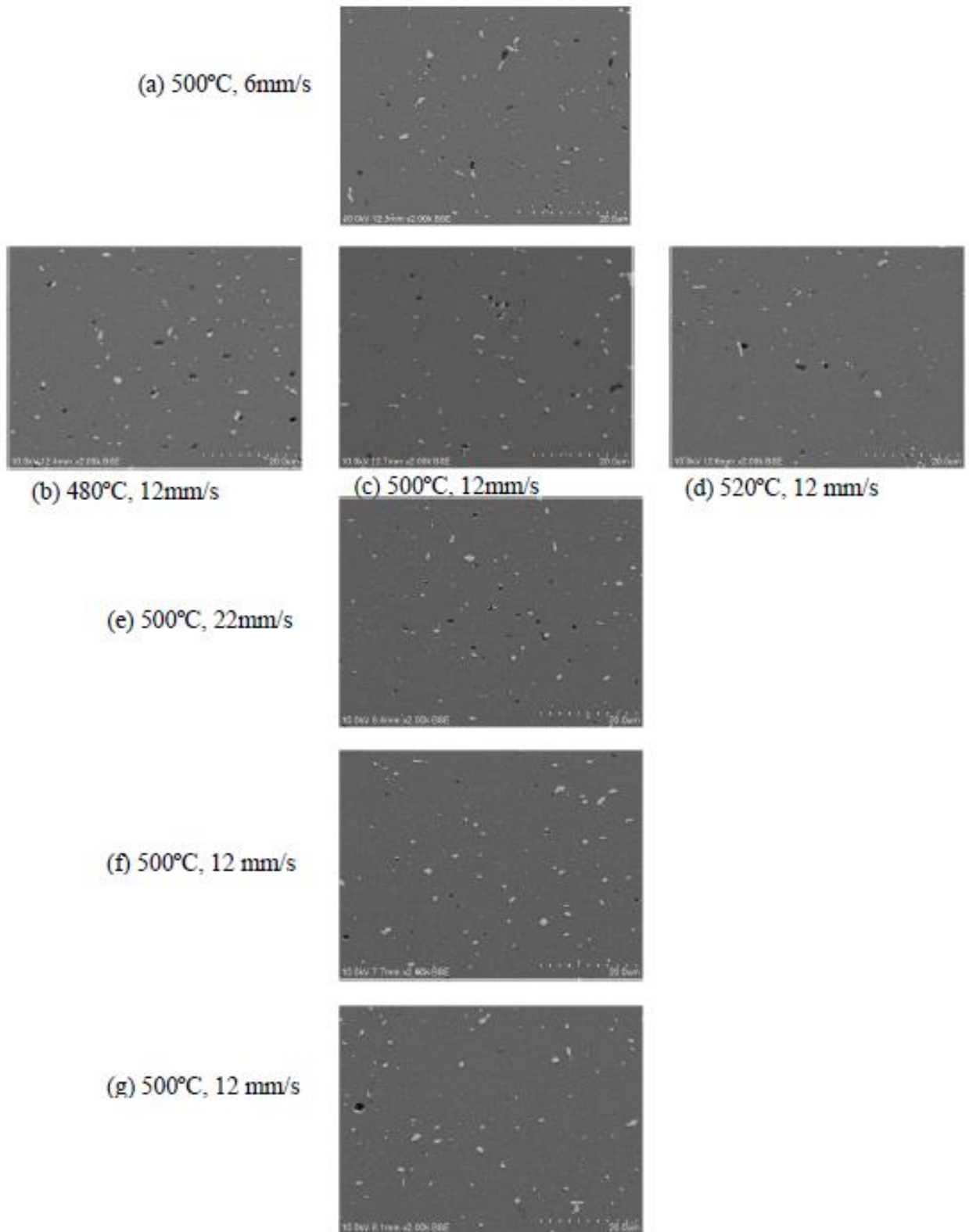


Figure 6.33 Micrographs at 1000x magnification using Backscatter Scanning Electron Microscope

After the billet is cast and solidified, then inhomogeneities are reduced by homogenising at a temperature which is high enough to enable dissolution and diffusion of secondary phases, precipitates, segregates and intermetallic compounds.

Most of the secondary phases consist of impurity elements or deliberately added alloying elements and are formed during solidification and subsequent cooling to room temperature. After homogenising the billet is cooled to room temperature (quenched) by means of forced or water.

Precipitates consist of the relatively fast diffusing alloying elements, typically the primary alloying elements. In EN AW-6082 alloys these are predominantly Mg and Si. Depending on the temperature regime during formation, the precipitates are of the stable  $\beta$  type, the meta stable  $\beta'$  type or the  $\beta''$  type. Rough estimates for the formation temperature regime and morphology parameters are according to Van de Langkruis (2000).

- $\beta$  type, (equilibrium phase  $Mg_2Si$ ), temperatures roughly 600K and higher, plate like shape, crystal structure fcc, Mg:Si ratio 2:1(at%), size ~0.1 to several  $\mu m$ .
- $\beta'$  type, temperature roughly in the range of 470-570K, lath like shape, crystal structure hcp, Mg:Si ratio 1.7:1 (at%), size 10-50 nm up to several  $\mu m$ .
- $\beta''$  type, temperature roughly in the range 400-500K, needle shape, crystal structure monoclinic, Mg:Si ratio 5:6 (at%), size ~5 nm width and 0.2 nm length.

Particles containing primary alloying elements Mg and Si influence extrudability by reducing solute levels in grains. During extrusion an excessively high solute content is undesirable since solute atoms act as obstacles to dislocations being in motion and therefore increase the high temperature strength of the alloy resulting in high extrusion pressure.

Figure 6.34 show structure of experimental sections including precipitates and intermetallics at magnification of 2000x.

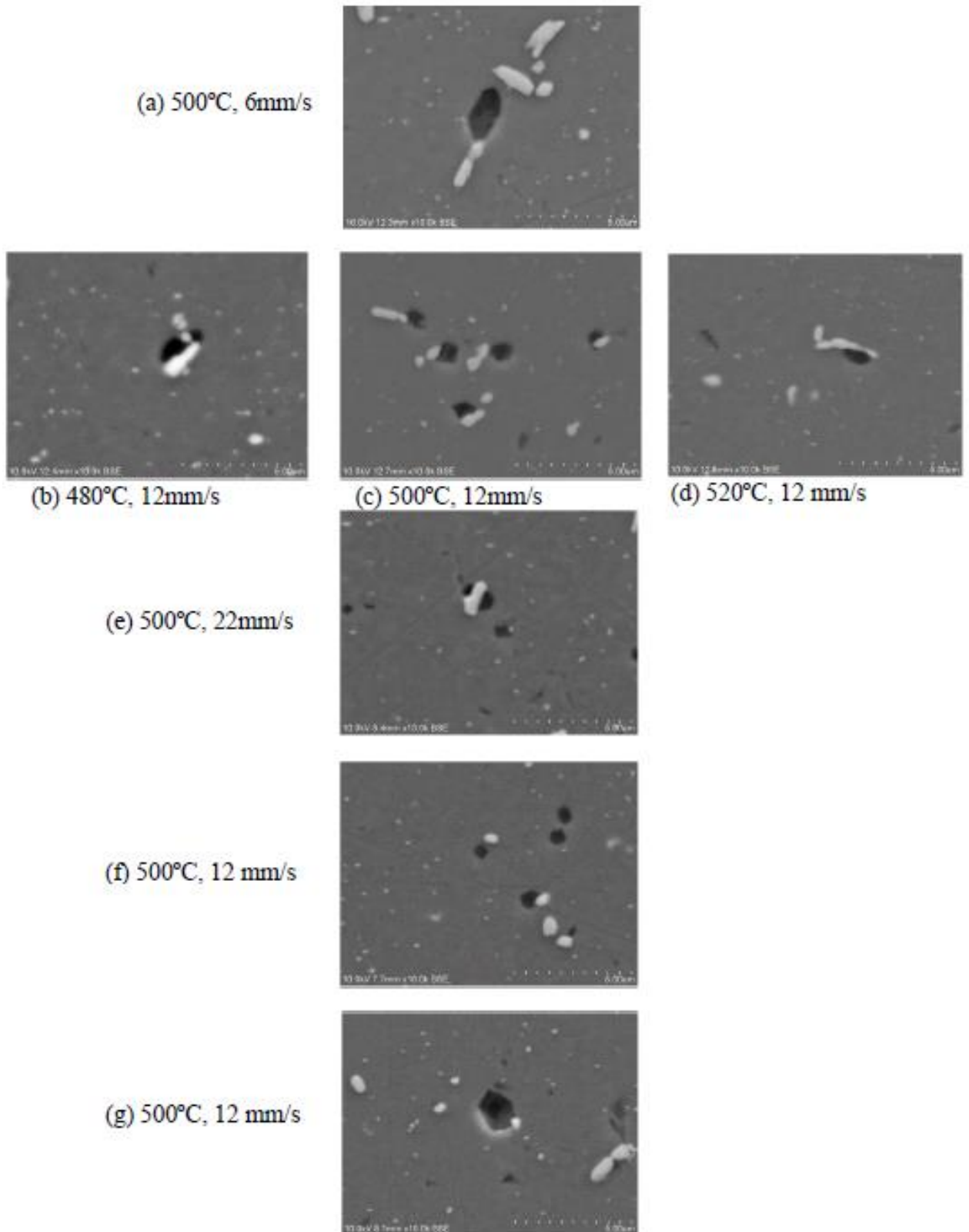


Figure 6.34 Micrographs at 2000x magnification using Backscatter Scanning Electron Microscope

For this reason the presence of  $Mg_2Si$  particles in the extrudate is investigated by means of Backscatter Scanning Electron Microscope. Images are represented for 1000x magnification in Figure 6.33 and 2000x magnification in Figure 6.34.

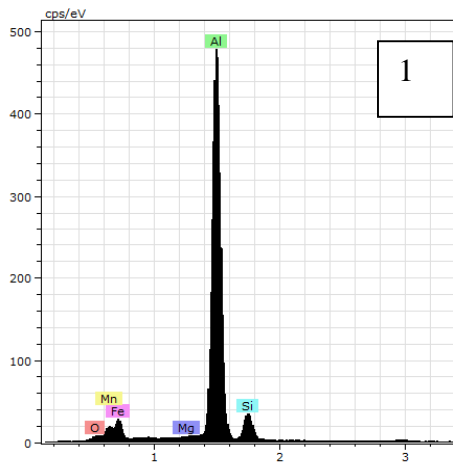
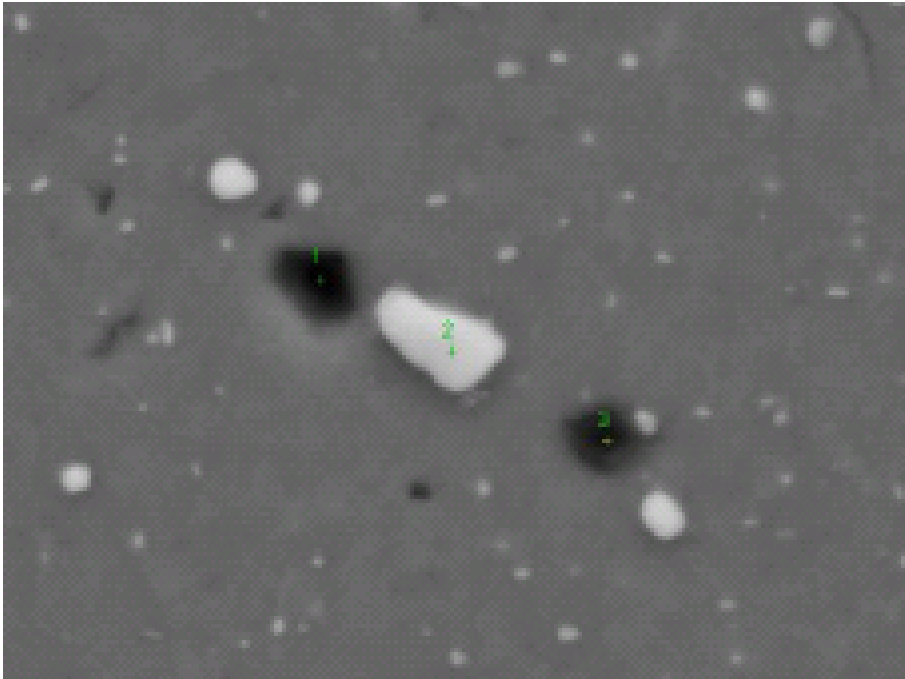
In 6000 series alloy the presence of Fe will lead to AlSiFe particles which are present in the material as intermetallics. These intermetallics cannot dissolve and precipitate. However some of the particles which exist in the material from solidification can transform from a dendrite form into a globular form. The homogenising treatment followed by billet pre heat should have contributed to the transformation of the Fe containing particles into the globular shape. On the other hand a high solute content at the beginning of artificial ageing is preferred since it results in more strengthening  $\beta''$  type particles, therefore can result in higher mechanical properties. To a limited extent the extrudability of an EN AW-6082 alloy can be controlled by controlling the amount of alloying elements in solid solution.  $Mg_2Si$  particles which dissolve during extrusion, decrease the required extrusion pressure and increase extrusion speed. Large  $Mg_2Si$  particle which do not dissolve should be avoided to achieve optimal surface appearance.

According to Van de Langkruis (2000),  $\beta''$  type precipitates in the initial microstructure have no significant effect on flow stress at elevated temperatures or on peak hardness after deformation.  $\beta''$  type precipitates significantly influence flow stress at 673K by precipitation hardening and significantly reduce peak hardness after deformation at 673K by retaining solute from the aluminium matrix. These effects are absent at 773K.

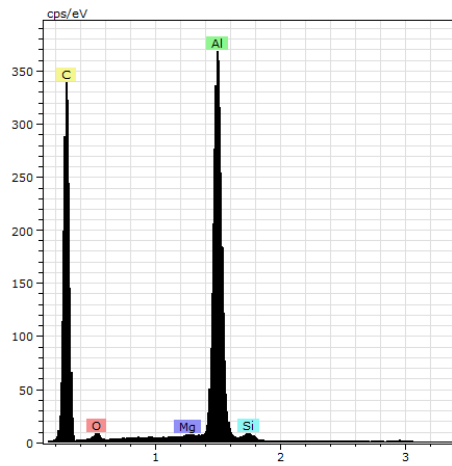
$\beta$  type precipitates result in reduction of both flow stress at elevated temperatures and final peak hardness by reducing the solute content during deformation.

In Figure 6.35 an analysis is given at 10000x magnification of some of the particles which are visible in the material. As can be seen in Figure (6.33) at 1000x magnification the homogenizing heat treatment has been successful since there are only a very few particles visible. At least no large  $Mg_2Si$  particles are present.

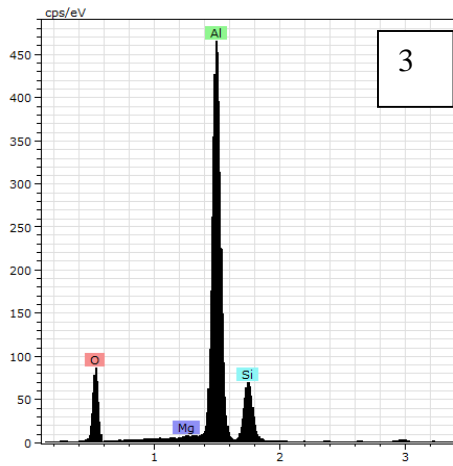




1



2



3

Figure 6.35 EDX analysis of sample 2E, 1) AlSiMnFe, 2) carbon, 3) Oxidised Mg<sub>2</sub>Si

A small oxidized  $Mg_2Si$  particle can be observed in Figure 6.35. Sign of oxidization are visible and possibly prevented the particle being dissolving. An AlSiFe particle in globular form which is also contains Mn can be found as is to be expected. Since the extrusion temperature was above 600K and the size of the particle is several  $\mu m$ . It is safe to conclude that the particle in Figure 6.35(3) is a  $\beta$  type  $Mg_2Si$  precipitate.

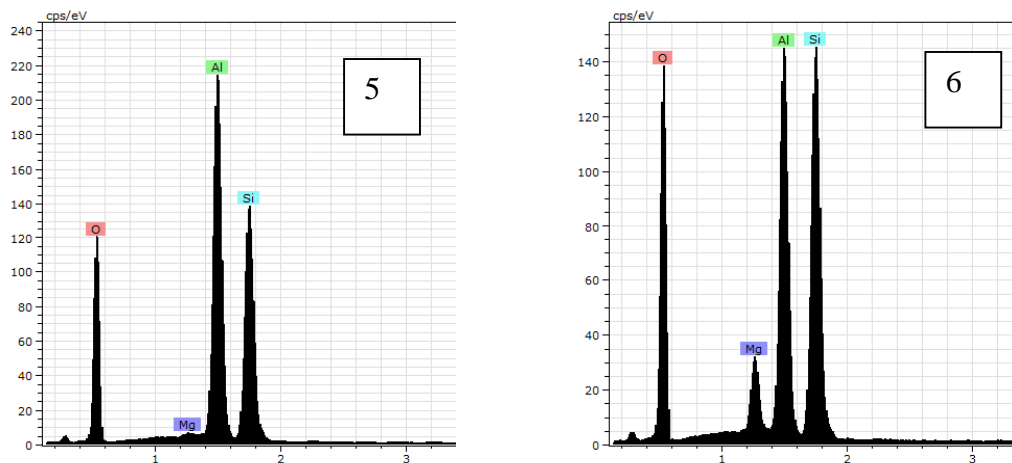
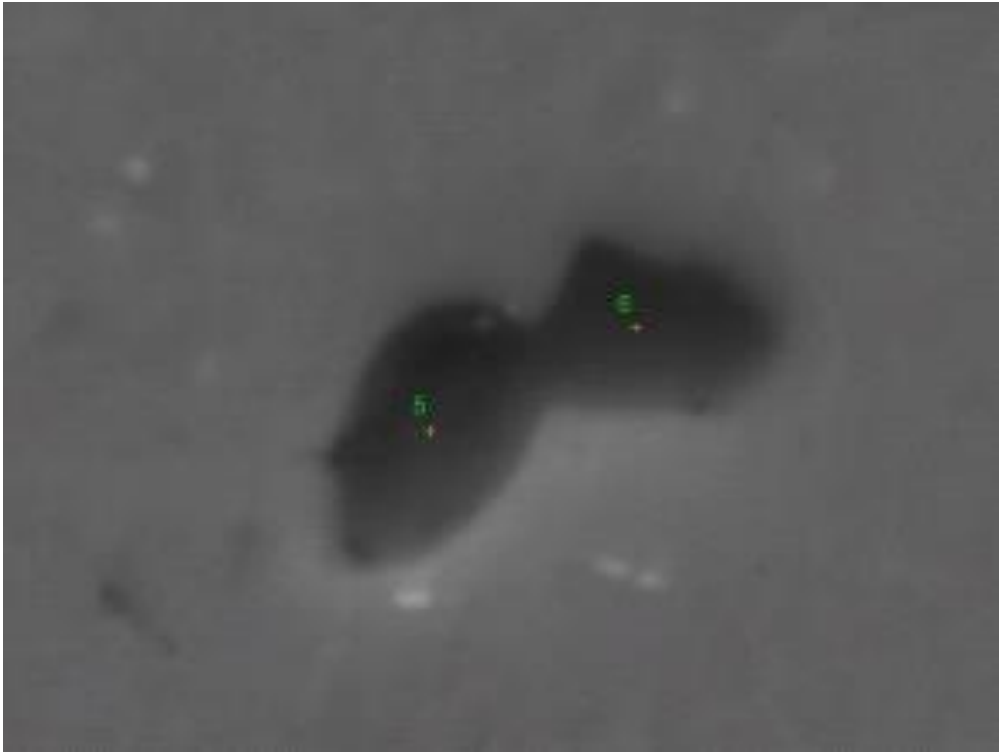


Figure 6.36 EDX analysis of phases in sample 5E: 5) Oxidized  $Mg_2Si$ , 6) Oxidized  $Mg_2Si$  with Mg-residue

The oxidation of the  $Mg_2Si$  particles is most likely caused by sample preparation and subsequent etching and is not expected to bear any relation with the extrusion process. The particles in Figure 6.36 are several  $\mu m$ . It is also safe to conclude that these particles are  $\beta$  type  $Mg_2Si$  precipitates.

## 6.7 Conclusions

The result of extruding solid high strength EN AW-6082 alloys often led to a partially recrystallised structure. The rectangular geometry revealed a recrystallised surface layer and an unrecrystallised center area. The depth of the recrystallised surface layer depends on the value of the temperature compensated strain rate. Hence increasing the billet temperature or increasing the extrusion speed both influenced the recrystallised layer.

Variations in billet temperature and extrusion speed produced variations in subgrain size and misorientation. Dislocation density decreased with increasing temperature and extrusion speed. At lower strain rates there was less time available for the dislocation rearrangement and at higher temperatures, with increased thermal activation, there was an increased dislocation annihilation. Larger subgrains and lower internal dislocation densities were therefore produced.

In the U-shaped section and the Tube section an (almost) fully recrystallised structure was observed. This was caused by the complex die geometry and high extrusion ratio. This led to a greater temperature increase. Simulated volume fraction recrystallised in the center of the U-shapes section was 84%, and on the edge 97%. The measured value was 87%. With sufficient pressure the welding after the bridge of the hollow section contributed to the temperature increase which produces a fully recrystallised structure in the tube section. This agrees with simulated results (Forge2009®) as well as measured values (EBSD).

EBSD results were in reasonable accord with simulation results and those available in the literature. In general the substructure was homogeneous in the unrecrystallised regions and showed evidence that subgrain coalescence was the recrystallization mechanism. There was little evidence of any precipitation or residual intermetallics.

## 7. Conclusions and further research

### 7.1 Conclusions

1. The material flow during the extrusion of complex shapes were predicted by the Forge2009® program. Hence the affect of die design variations could be investigated. It was observed that alteration in the cross section of a bridge during tube extrusion substantially influenced the material flow in the welding chamber which changed the optimisation of the processing parameters required. The extrusion of solid shapes were also affected by die design. Varying the depth of the sink altered the velocity profile across the extrudate providing the die designer with an extra tool to improve the performance of the die.
2. The load predicted by the simulation of the profiles used in the experiments was within 7 % of experimental results. The influence of the variation of extrusion parameters as well as section geometry on temperature and load was in reasonable agreement for the geometries investigated. The prediction of the extrusion temperatures was close to those predicted and within 3% of simulated values. Section geometry and extrusion ratio influenced the extrusion temperature and load.
3. Material flow throughout the ram stroke was well predicted using Forge2009®. Differences in metal flow for the various shapes could all be satisfactory modelled using the program. The complex material flow across the bridge of a hollow die was modelled taking into account the inaccuracies due to temperature effects.
4. The cracking simulations were performed with the implicit finite element code Forge2009® with user input written in Visual Fortran®. Surface cracking experiments show that the speed and temperature had a significant influence on cracking phenomena during extrusion. Using these values and the induced stress state allowed preliminary prediction of surface deterioraton. Increased section complexity was obseved to enhance the occurrence of cracking.

5. The result of extruding solid high strength EN AW-6082 alloys often led to a partially recrystallised structure. The rectangular geometry revealed a recrystallised surface layer and an unrecrystallised center area. The depth of the recrystallised surface layer depends on the value of the temperature compensated strain rate. Hence increasing the billet temperature or increasing the extrusion speed both influenced the recrystallised layer.
6. Variations in billet temperature and extrusion speed produced variations in subgrain size and misorientation. Dislocation density decreased with increasing temperature and extrusion speed. At lower strain rates there was less time available for the dislocation rearrangement and at higher temperatures, with increased thermal activation, there was an increased dislocation annihilation. Larger subgrains and lower internal dislocation densities were therefore produced.
7. In the U-shaped section and the Tube section an (almost) fully recrystallised structure was observed. This was caused by the complex die geometry and high extrusion ratio. This led to a greater temperature increase. Simulated volume fraction recrystallised in the center of the U-shapes section was 84%, and on the edge 97%. The measured value was 87%. With sufficient pressure the welding after the bridge of the hollow section contributed to the temperature increase which produces a fully recrystallised structure in the tube section. This agrees with simulated results (Forge2009®) as well as measured values (EBSD).
8. EBSD results were in reasonable accord with simulation results and those available in the literature. In general the substructure was homogeneous in the unrecrystallised regions and showed evidence that subgrain coalescence was the recrystallization mechanism. There was little evidence of any precipitation or residual intermetallics.

## 7.2 Further research

In the present work the effect of variation of two design features was investigated. It is clear that design changes will influence the extrusion process. Further optimisation of design features such as the bridge and the welding chamber is required to improve the practical extrusion process by means of reducing scrap and improving productivity.

The research could be expanded to include more design features in the research, such as bearing length and feeder holes. Solid dies would need to be improved with respect to shape prediction and the reduction of scrap. The combined effect of variation in bearing length and sink in geometry could be investigated. The research work could be expanded to include the relationship between die design and processing conditions such as extrusion temperature, ram speed and quench.

Prediction of the recrystallised structure of extruded sections in combination with process parameters is required. The work could be extended to investigate the predicted effect of improved quench on the structure including the recrystallisation. Work would implicate the clarification of structural loci on extrusion limit diagram to enable the correct structure to be predicted.

Priority:

-Prediction of  $X_v$

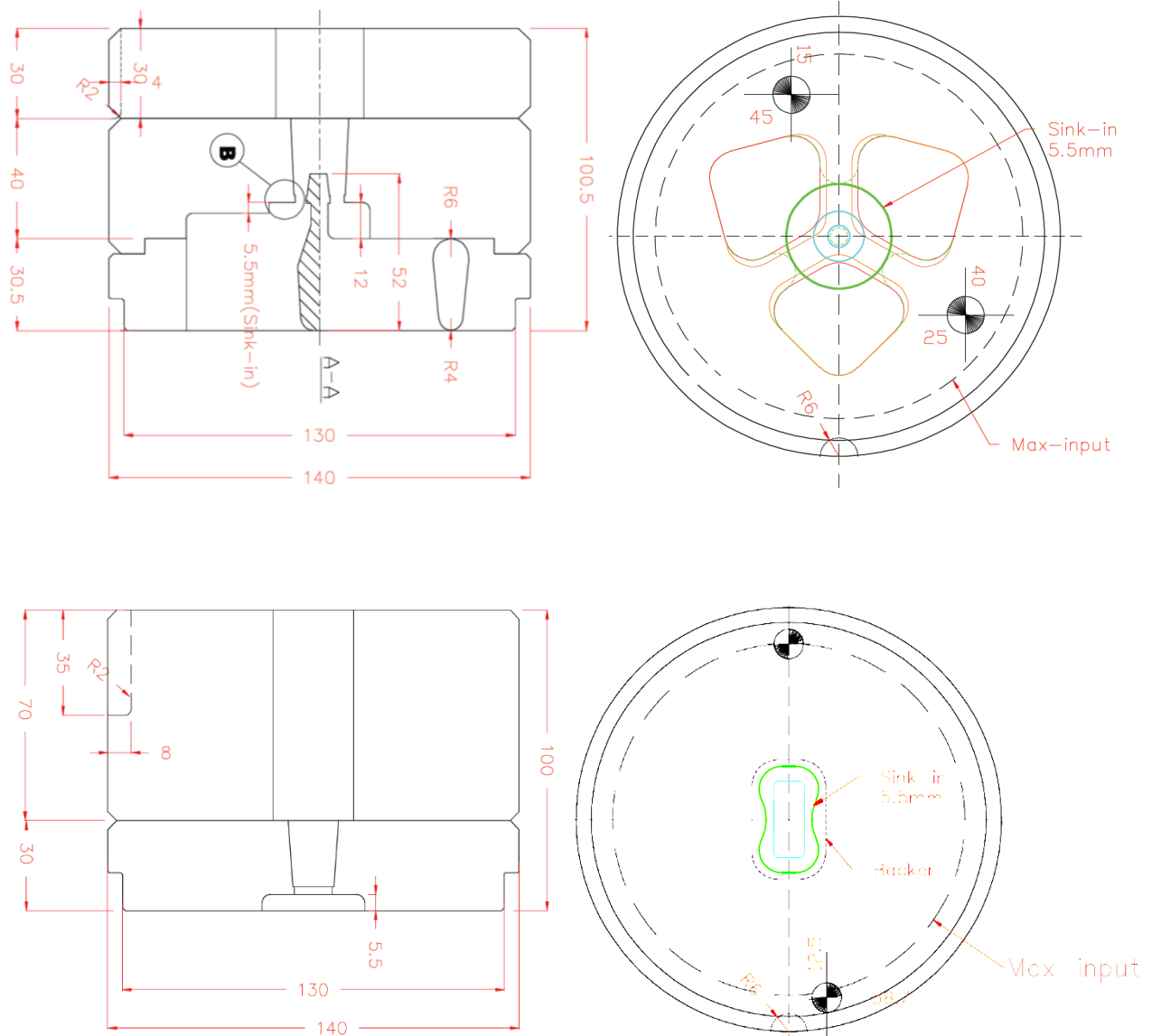
-Optimisation of  $V_{ram}$  and  $T_{exit}$

-Alter die design to optimise improvements

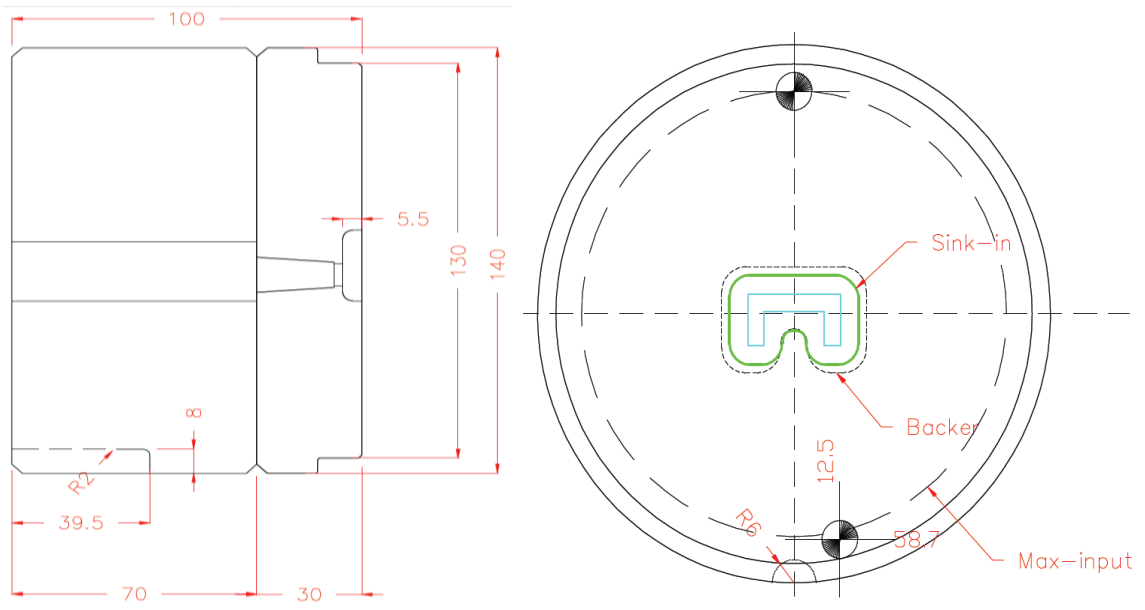
## 8 Appendix

### 8.1 Appendix 1

Die designs which were used in the experiments

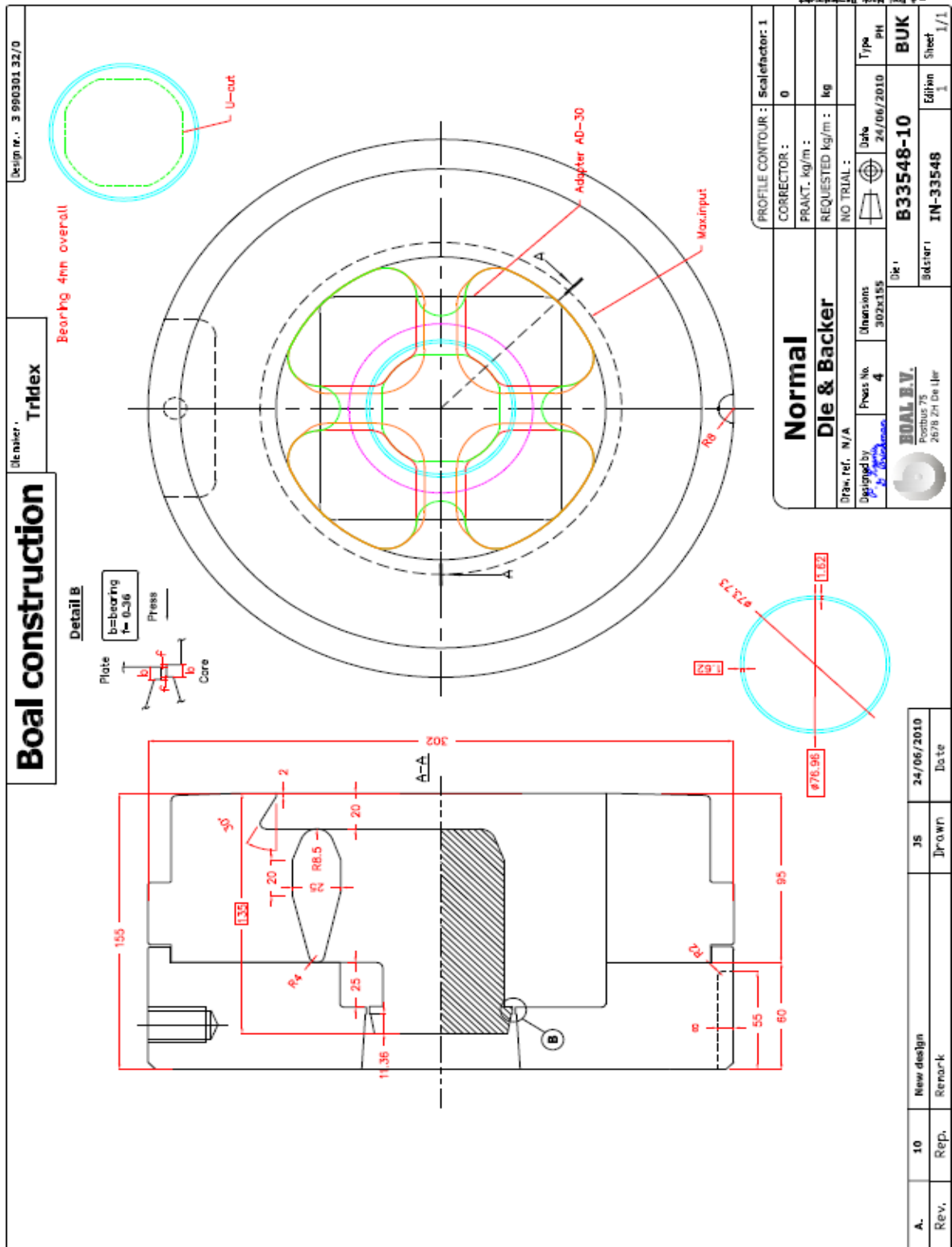


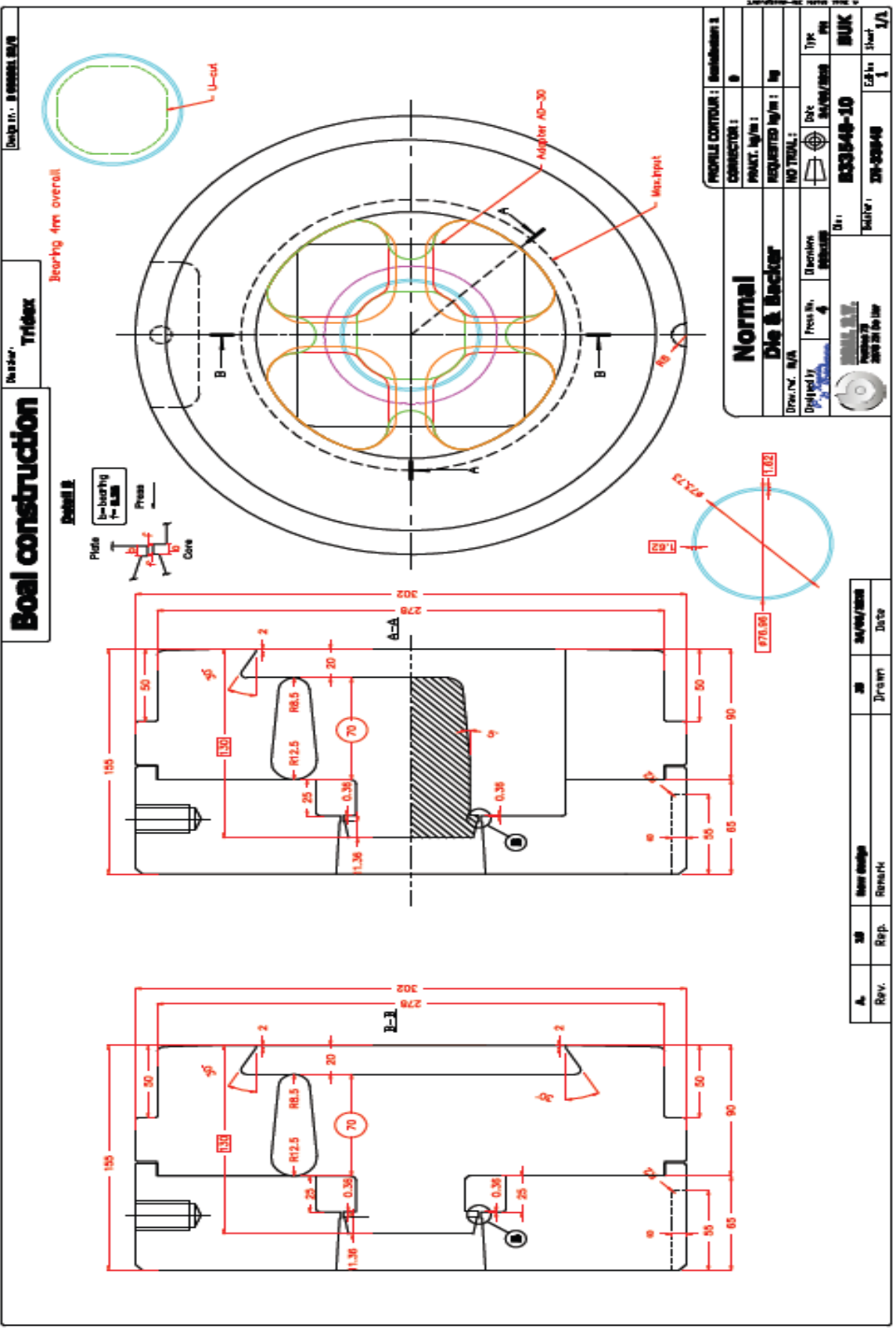




## 8.2 Appendix 2

Appendix 3; die design used in the simulations

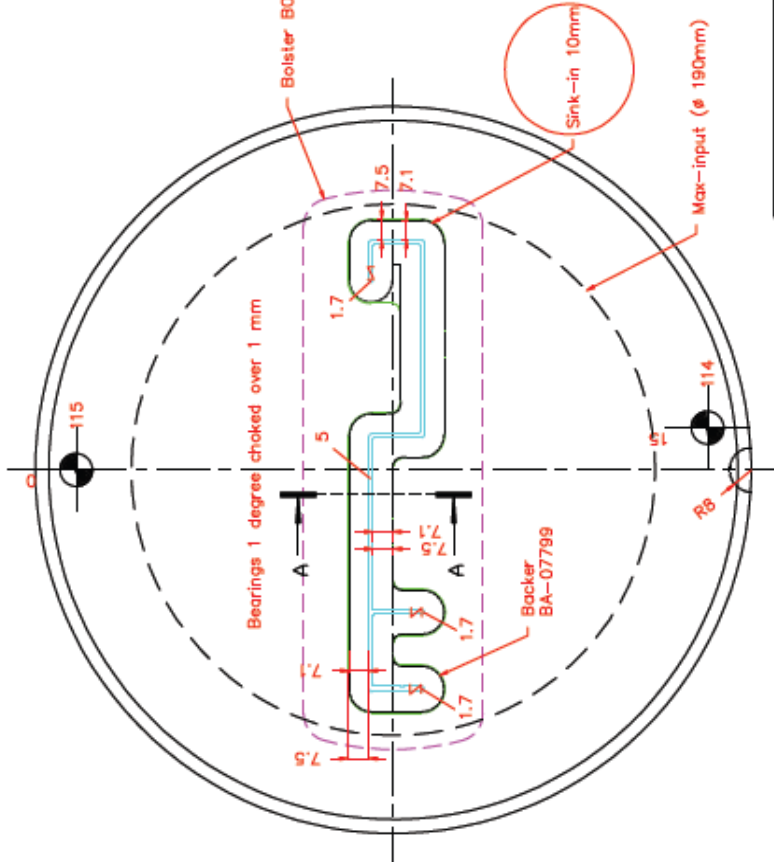
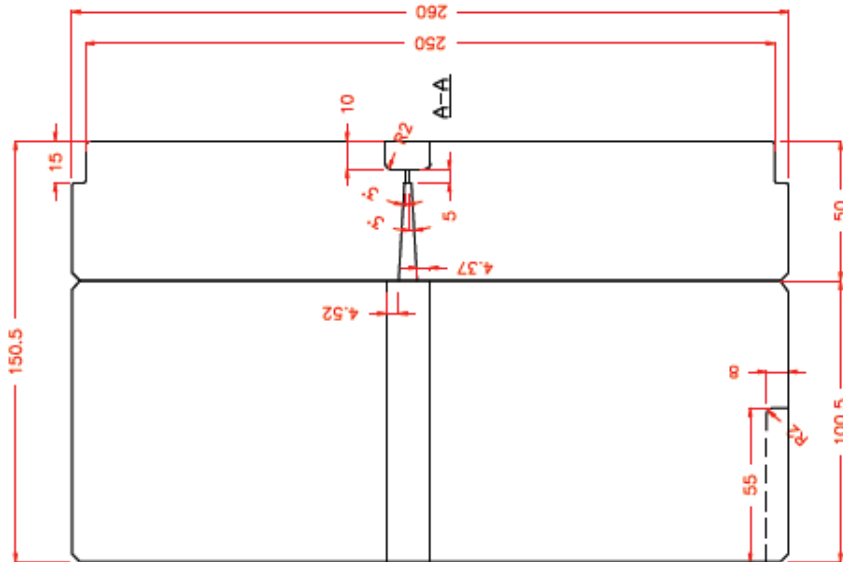




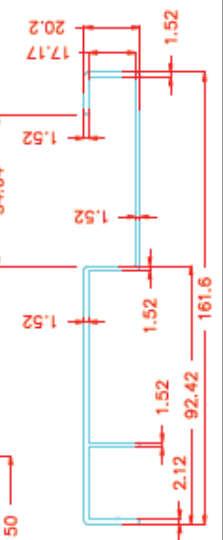
# Boal construction

Die maker: Phoenix NL

Design nr.: 2025.002.01/2



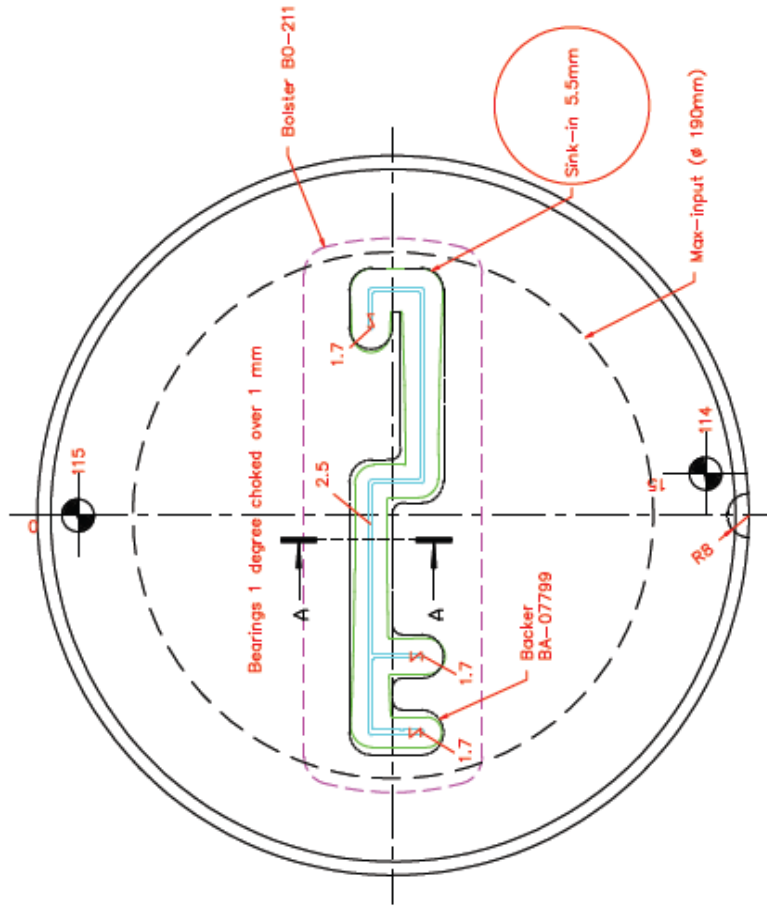
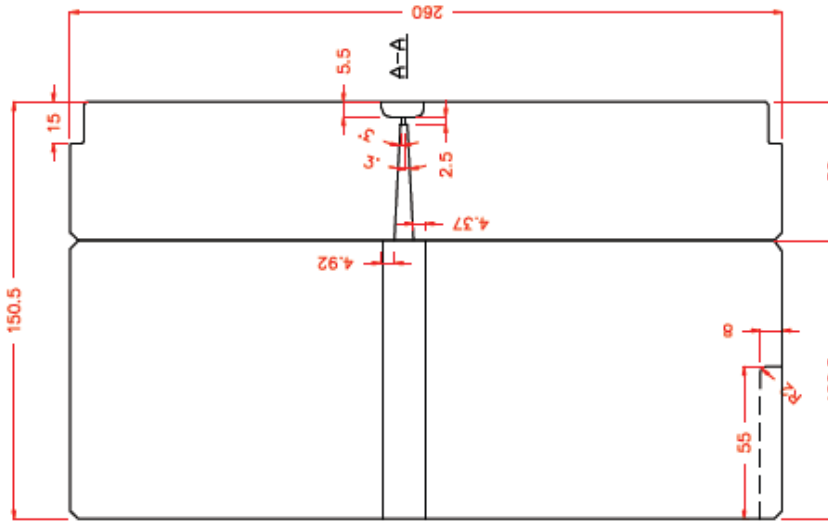
PROFILE CONTOUR : scalefactor 1	
CONNECTOR :	
PRAKT. kg/m :	
REQUESTED kg/m :	
NO TRIAL :	
Draw. ref. : 20-200-112/113	
Designed by : J. de Groot	
Press No. : 2	Dimensions : $\frac{25}{0.05/0.05/0.05}$
Date : 30/09/2025	Type : BK
Dr : B07799-8	BNL
Bolster : BO-211	Edition : 1
	Sheet : 1/1



# Boal construction

Die maker : **Phoenix NL**

Design nr. : **200502 01/3**



### 8.3 Appendix 3

```
! File Type:                FORGE2009® 2009® 3 V7.4 Data File
! Creator:                  GLpre  Version 3. 2. 0. 20-Release
! Project name:             rectanglel12m500
! Project description:      Empty_Generic_Project
! Simulation name:          U773
! Simulation description:   3D_Hot_Forging
! Author:                   Kjell
! Creation Date:            2011-05-28 11:21:09
! GLPre active language:   English
! System language:         English (UK)
! Data File Name:          u773.ref
! Data File Location:
      F:\User_Kjell\all\rectanglel12m500.tsv\U773\
!!!!!!!!!!!!!!!!!!!!!!!!!!!!!!!!!!!!!!!!!!!!!!!!!!!!!!!!!!!!!!!!!!!!!!!!!!!!
      !!!!!!!!!!!!!!!

!===== OBJECTS Block
.OBJETS
      ProjectName = rectanglel12m500
      SimulationName = U773

      Fout = u773.out
      Fres = results\u773.res
      Faux = results\u773.vtf

      NBSD = 1

      objet 1, NAME=Billet
      objet 1, FMAY=billet.may
      objet 1, NomGen=results\billet_
      objet 1, rheol=1

      outil 1, NAME=LowerDie
      outil 2, NAME=container
      outil 3, NAME=upperdie
.FIN OBJETS
!=====

!===== APPROXIMATION Block
.APPROXIMATION
      Periode_Meca = 1
.FIN APPROXIMATION
!=====

!===== UNITS Block
.UNITES
      MM-MPA-MM.KG.S
.FIN UNITES
!=====
```

!===== RHEOLOGY Block

.RHEOLOGIE

!!!!!!!!!!!!!!!!!!!!

MATERIAU 1 ! (object Billet)

!!!!!!!!!!!!!!!!!!!!

EVP

LOIV SIG0

ZENER-H

PAR DH = 153000.0d0

PAR R = 8.314d0

PAR alpha = 0.052d0

PAR n = 2.976d0

PAR A = 2.3853d8

FIN LOI

!Elasticity coefficients

Youngmodulus = 7.300000e+04

Poissoncoeff = 0.300000

!Thermal coefficients

mvolumique = 2.800000e-06 !Density

cmassique = 1.230000e+09 !Specific Heat

conductmat = 2.500000e+05 !Conductivity

epsilon = 5.000000e-02 !Emissivity

!-----

OUTIL1 ! LowerDie

File = lowerdie.tof

!Friction between deformable object and rigid die

Tresca

mbarre = 1.000000e-01

!Thermal Exchange between part and rigid die

! Unit = si

alphan = 2.000000e+03 ! Transfert coefficient

effus = 1.176362e+04 ! tool effusivity

Temp\_Die = 510.000000

FIN OUTIL

!-----

!-----

OUTIL2 ! container

File = container.tof

!Friction between deformable object and rigid die

Tresca

mbarre = 7.000000e-01

```

!Thermal Exchange between part and rigid die
  ! Unit = si
  alphas = 2.000000e+03      ! Transfert coefficient
  effus = 1.176362e+04 ! tool effusivity

  Temp_Die = 510.000000
FIN OUTIL
!-----

!-----
OUTIL3      ! upperdie
  File = upperdie.tof

  !Friction between deformable object and rigid die
  Tresca
  mbarre = 1.000000e-01

  !Thermal Exchange between part and rigid die
  ! Unit = si
  alphas = 2.000000e+03      ! Transfert coefficient
  effus = 1.176362e+04 ! tool effusivity

  Temp_Die = 510.000000
FIN OUTIL
!-----

  !Thermal Exchange between deformable object and ambient medium
  ! Unit = si
  AlphasExt = 10.000000e+00 ! Transfert coefficient
  TempExt = 50      ! Ambient Temperature

  ! Initial temperature has been set in mesh file: already exists
  in mesh file

!!!!!!!!!!!!!!!!!!!!!!!!!!!!
FIN MATERIAU
!!!!!!!!!!!!!!!!!!!!!!!!!!!!

! *** User Variable Law: BOX
LOIV UTIL
  BOX
  Par XMIN = -100
  Par XMAX = 100
  Par YMIN = -100
  Par YMAX = 100
  Par ZMIN = 25
  Par ZMAX = 100
  Par EQ_STRAIN = EXIST
  Eta EQ_STRAIN-BOX = 0.
FIN LOI

```



```

! *** User Variable Law: BOX
LOIV UTIL
  BOX
  Par XMIN = -100
  Par XMAX = 100
  Par YMIN = -100
  Par YMAX = 100
  Par ZMIN = -20
  Par ZMAX = -10
  Par EQ_STRAIN = EXIST
  Eta EQ_STRAIN-BOX = 0.
FIN LOI

! *** User Variable Law: Tens_Def
LOIV INTG
  Tens_Def
  Eta TDEF(6) = 0, 0, 0, 0, 0, 0
FIN LOI

! *** User Variable Law: SigmaCylZ
LOIV MECA
  SigmaCylZ
  Par STRESSTENSOR(6) = EXIST
  Var TENS_CYL(6) = 0, 0, 0, 0, 0, 0
FIN LOI

Stock=ZEN-HOLLOMON,TENS_CYL

! *** User Variable Law: PRINC_VAL_1

  LOIV MECA

    PRINC_VAL_1
    PAR TDEF(6) = EXIST

    VAR TDEF1= 0.d0
  FIN LOI

! *** User Variable Law: PRINC_VAL_2

  LOIV MECA

    PRINC_VAL_2
    PAR TDEF(6) = EXIST

    VAR TDEF2= 0.d0
  FIN LOI

! *** User Variable Law: PRINC_VAL_3

  LOIV MECA

```

```

PRINC_VAL 3
PAR TDEF(6) = EXIST

VAR TDEF3= 0.d0
FIN LOI

! *** User Variable Law: MY
LOIV MECA

MY

var Hydro= 0.d0

FIN LOI

Stock=TDEF1,TDEF2,TDEF3, Hydro

! *** User Variable Law: SV_NIU
LOIV UTIL
SV_NIU

PAR D0_GRN      = 50.0d-6
PAR TDEF1       = EXIST
PAR TDEF2       = EXIST
PAR TDEF3       = EXIST
PAR eq_strain=EXIST

ETA SV_NIU      = 0.d0
ETA SV_OLD      = 0.d0
ETA SV_New      = 0.d0
FIN LOI

! *** User Variable Law: MY_SUB
LOIV UTIL
MY_SUB

Par A6082 = -0.455d0
Par B6082 = 0.025d0
Par C6082 =40.0d0
par di_val=50.0
par eq_strain=EXIST

par cd_val=1.48d-4
par g_val1=2.05d10
par burgers=2.86d-10
par misori= 3.0d0
par misori_c=15.0d0

```

```

par  cmgb=3.07d11
    par  mgb_a=251.0
Par  STRAIN_RATE = EXIST
Par  DH_b = 152000.0d0
    par  cxv=0.693d0

    par  txv=3600.d0
    par  kxv=2.0d0
par  crex=2.347d0
par  delta_t=exist
par  Rg=2000.

par  SV_NIU= exist
par  ZEN-HOLLOMON= exist

Eta zener_1 = 1.d0
Eta subgrain = 1.d0
Eta D_Density = 1.d8
Eta pd01 = 1.d0
Eta pd02 = 1.d0

Eta pd03= 1.d0
Eta pd04 = 1.d0
Eta pd05 = 1.d0
Eta pd06= 1.d0
Eta pd= 1.d0

Eta SV_NIU2= 1.d0
Eta nv = 1.d0
Eta t50 = 1.d0
Eta t501= 1.d0
Eta t502= 1.d0

Eta t503 = 1.d0
Eta t504= 1.d0
Eta t505= 1.d0
Eta t506 = 1.d0
Eta t507= 1.d0

Eta t508= 1.d0
Eta t509 = 1.d0
Eta t510= 1.d0
Eta t511= 1.d0
Eta grain= 50.d-6

Eta xv = 1.d0
Eta xv1 = 1.d0
Eta xv2= 1.d0
Eta xv3 = 1.d0
Eta xv4 = 1.d0

Eta xv5= 1.d0
Eta xv6 = 1.d0
Eta xv7 = 1.d0
Eta xv8= 1.d0

```

Eta xv9 = 1.d0

Eta xv10 = 1.d0

Eta xv11= 1.d0

Eta subg1= 40.d-6

Eta subg2= 40.d-6

Eta subg3= 40.d-6

Eta subg4= 40.d-6

Eta subg5= 40.d-6

Eta subg6= 40.d-6

Eta subg7= 40.d-6

Eta subg8= 40.d-6

Eta subg9= 40.d-6

Eta subg10= 40.d-6

Eta subg11= 40.d-6

Eta subg12= 40.d-6

Eta subg13= 40.d-6

Eta subg14= 40.d-6

Eta subg15= 40.d-6

Eta misor1 = 0.01d0

Eta misor2 = 0.01d0

Eta misor3 = 0.01d0

Eta misor4 = 0.01d0

Eta misor5 = 0.01d0

Eta misor6 = 0.01d0

Eta misor7 = 0.01d0

Eta misor8 = 0.01d0

Eta misor9 = 0.01d0

Eta misor10 = 0.01d0

Eta misor11 = 0.01d0

Eta misor12 = 0.01d0

Eta misor13 = 0.01d0

Eta misor14 = 0.01d0

FIN LOI

!-----  
INTERFACE  
FIN INTERFACE  
!-----

```

.FIN RHEOLOGIE
!=====

!===== INCREMENT Block
.INCREMENT
    Deformation = 0.01
.FIN INCREMENT
!=====

!===== EXECUTION Block
.EXECUTION
    Inertia
    dtMin = 2.000000e-004
    dtMax = 1.000000e-002
    dhSto = 5.000000e-001
    Sans Marquage

    OBJET1
        NO Folds_Detection
    FIN OBJET
.FIN EXECUTION
!=====

!===== THERMAL Block
.THERMIQUE
.FIN THERMIQUE
!=====

!===== MESH BOXES Block
.BOITE

OBJET1
BOX 1
    Type=10          ! BOX
    Lagrangian
    Die= 3           ! upperdie
    Size= 4
    !Param Info: NbPar, Xmin, Ymin, Zmin, Length, Width, Height
    Parameters:, 6,0,0,0,76.6122,72.537,10
    Matrix:, 1, 0, 0, -2,
             0, 1, 0, -2.8365,
             0, 0, 1, -302,
             0, 0, 0, 1
END BOX
BOX 2
    Type=20          ! CYLINDER
    Lagrangian
    Die= 1           ! LowerDie
    Size= 5
    !Param Info: NbPar, Xcenter, Ycenter, Zcenter, Rext, Rint, H
    Parameters:, 6,0,0,0,50.978,38,331.02
    Matrix:, 1, 0, 0, 0,
             0, 1, 0, 0,
             0, 0, 1, -315.51,
             0, 0, 0, 1

```

```

END BOX
BOX 3
  Type=20          ! CYLINDER
  Lagrangian
  Die= 1           ! LowerDie
  Size= 3.5
  !Param Info: NbPar, Xcenter, Ycenter, Zcenter, Rext, Rint, H
  Parameters:, 6,0,0,0,8,0,331.02
  Matrix:, 1, 0, 0, 0,
           0, 1, 0, 0,
           0, 0, 1, -315.51,
           0, 0, 0, 1
END BOX
BOX 4
  Type=10          ! BOX
  Lagrangian
  Die= 1           ! LowerDie
  Size= 4
  !Param Info: NbPar, Xmin, Ymin, Zmin, Length, Width, Height
  Parameters:, 6,0,0,0,76.6122,72.537,100
  Matrix:, 1, 0, 0, -2,
           0, 1, 0, -2.8365,
           0, 0, 1, -15,
           0, 0, 0, 1
END BOX
BOX 5
  Type=10          ! BOX
  Lagrangian
  Die= 1           ! LowerDie
  Size= 2
  !Param Info: NbPar, Xmin, Ymin, Zmin, Length, Width, Height
  Parameters:, 6,0,0,0,28.8239,22.5917,80
  Matrix:, 1, 0, 0, -2,
           0, 1, 0, -2,
           0, 0, 1, -8.57644,
           0, 0, 0, 1
END BOX
BOX 6
  Type=10          ! BOX
  Lagrangian
  Die= 1           ! LowerDie
  Size= 1
  !Param Info: NbPar, Xmin, Ymin, Zmin, Length, Width, Height
  Parameters:, 6,0,0,0,20,12,60
  Matrix:, 1, 0, 0, -2,
           0, 1, 0, -2,
           0, 0, 1, -4,
           0, 0, 0, 1
END BOX
FIN OBJET
.FIN BOITE
!=====

!===== BOUNDARY CONDITIONS Block

```

```

.CONDLIM
.FIN CONDLIM
!=====

!===== DAMAGE CONDITIONS Block
.DAMAGE

OBJET1
      Name = EQ_STRAIN-BOX
      Trigger Value = 0.0001
FIN OBJET
.FIN DAMAGE
!=====

!===== REMESHING Block
.MAUTO

OBJET1
      periode = 20
      lbase = 1.3000000000000000e+001
FIN OBJET
.FIN MAUTO
!=====

!===== KINEMATICS Block
.CINEMAT_OUT
      Outil3      ! upperdie
      maitre
      Axe = 3
      Fin Outil
.FIN CINEMAT_OUT
!=====

!===== PILOT Block
.PILOT
      NbPass= 1
      Pass1
      Fin Pass
.FIN PILOT
!=====

!===== Analysis data Block
.INTERFACE_CIM
{ Analysis_Info=
  { Project=
    { Name= rectanglev12m500 }
  }
  { Simulation=
    { Name= U773 }
    { Location= F:\User_Kjell\all\rectanglev12m500.tsv\U773\ }
    { File= U773.tsf }
    { Software= FORGE2009@ 2009@ 3 }
    { Result_File_Extension= .fg3 }
    { Local_Results_Directory= results }
  }
}

```

```

}
{ Objects= Billet , LowerDie , container , upperdie }
{ Billet=
  { First= billet.may }
  { Outputs= Last }
  { Last=
    { IVType= None }
    { File= end_billet.may }
  }
}
{ LowerDie=
  { First= lowerdie.dou }
}
{ container=
  { First= container.dou }
}
{ upperdie=
  { First= upperdie.dou }
}
}
.FIN INTERFACE_CIM
!=====

```



## References

- Ahmed, H., Wells, M. A., Maijer, D. M., Howes, B. J., and Winden, M. R. V. D., 2005. Modelling of microstructure evolution during hot rolling of aa5083 using an internal state variable approach integrated into a FE model. *Materials Science and Engineering A-structural Materials Properties Microstructure and Processing*, 390 (1-2), 278-290.
- Avrami, M., 1939. Kinetics of phase change. I. General theory. *Journal of Chemical Physics*, 7 (12).
- Avrami, M., 1940. Kinetics of phase change.ii. Transformation-time relations for random distribution of nuclei. *Journal of Chemical Physics*, 8 (2).
- Avrami, M., 1941. Kinetics of phase change. Iii. Granulation, phase change, and microstructure. *Journal of Chemical Physics*, 9 (2).
- Argyris, J.H and Kelsey, S. *Energy theorems and Structural Analysis* Butterworth Scientific publications, London
- Baxter, G. J., Furu, T., Zhu, Q., Whiteman, J. A., and Sellars, C. M., 1999. The influence of transient strain-rate deformation conditions on the deformed microstructure of aluminium alloy al-1% mg. *Acta Materialia*, 47 (8), 2367-2376.
- Berezhnoy, V. L., Hahn, K. H., and Chang, J. Y., 1999. Extrusion defects: Conditions of formation and methods of prevention. *Light metal age*, 66-74.
- Bianchi, J. H., and Sheppard, T., 1987. A comparison of a viscoplastic finite-element model with slip-line field and upper-bound solutions for non-hardening material subjected to plane-strain and axisymmetrical extrusion. *International Journal of Mechanical Sciences*, 29 (1), 61-81.
- Bonet, J., and Wood, R. D., 1997. *Nonlinear continuum mechanics for finite element analysis* Cambridge University Press.
- Bourqui, B., Et Al., 2002. Improved weld seam quality using 3d fem simulation in correlation with practice. In: *The First EAA Extruder Division Congress*, Garda Hotel, Montichiari, Brescia, Italy.
- Bozzi, S., Vedani, M., Lotti, D., and Passoni, G., 2009. Extrusion of aluminium hollow pipes: Seam weld quality assessment via numerical simulation. *Metallurgical Science and Technology*, 27.
- Cahn, R.W., and Haasen, P., 1996, *Physical metallurgy* (three volume set) Fourth edition Noord Holland
- Carron, D., Bastid, P., Yin, Y., and Faulkner, R. G., 2010. Modelling of precipitation during friction stir welding of an al-mg-si alloy. *TECHNISCHE MECHANIK*, 1-3 (30), 29- 44
- Castle, A., Flory, R., and Gagg, J., 1988. Die design and construction in europe. In: *4th International aluminium extrusion technology seminar*, Chicago, Washington.
- Castle, A. F., 1974. *Continuum and structural aspects of aluminium alloy extrusion*. Thesis. Imperial College of Science and Technology, London, UK.
- Castle, A. F., 1992. Temperature control in aluminium extrusion. In: *5th International aluminium extrusion technology seminar*, Chicago, Washington.
- Castle, A. F., and Sheppard, T., 1976a. Development of product structure at commencement of extrusion. *Metals Technology*, 9 (3), 433-436.
- Castle, A. F., and Sheppard, T., 1976b. Pressure required to initiate extrusion in some al-alloys. *Metals Technology*, 2, 465-475.

- Chanda, T., Zhou, J., and Duszczyc, J., 2000. 3d fem simulation of thermal and mechanical events occurring during extrusion through a channel-shaped die. In: 7th International aluminium extrusion technology seminar, Chicago, Washington.
- Chen, B. K., Choi, S. K., and Thomas, P. F., 1991. Simulation of evolution of microstructure in a thermo-mechanical analysis of the hot rolling of aluminium. *Res Mechanica*, 31, 455-469.
- Chenot, J. L., and Chastel, Y., 1996. Mechanical, thermal and physical coupling methods in fe analysis of metal forming processes. *Journal Of Materials Processing Technology*, 60 (1-4), 11-18.
- Chenot, J. L., Coupez, T., Fourment, L., Ducloux, R., and Wey, E., 1999. Practical simulation of forging sequence of complex 3-d parts in industry. In: Geiger, M. ed. 6th International Conference on technology of plasticity, Nuremberg, Germany: Springer-Verlag Telos.
- Clif, S. E., Hartley, C.E., Sturgess, N. Rowe, G.W. . 1996. *International Journal of Mechanical Science*, 32, 1-17.
- Clode, M. P., 1992. Material flow and microstructural development during extrusion of aa6063. In: ET 1992, Chicago, Illinois: Aluminium Extrusion Technology Seminar.
- Cockroft, M. G., Latham, D.J. 1986. *Journal Institute of Metals*, 96, 2444-2477.
- Coupez, T., 1994, A mesh improvement method for 3d automatic remeshing. In: *Numerical Grid Generation in Computational Fluid Dynamics and Related Fields*. Pineridge Press.
- Crotaz, C. R., Shercliff, H. R., and Mackay, D. J. C., 2002. Advanced statistical modelling of processing of aluminium alloys. In: the 8th International Conference on Aluminium Alloys, CAMBRIDGE, ENGLAND.
- Daaland, O., and Nes, E., 1996. Recrystallization texture development in commercial al---mn---mg alloys. *Acta Materialia*, 44 (4), 1413-1435.
- Dashwood, R. J., Mcshane, H. B., and Jackson, A., 1996. Computer prediction of extrusion limit diagrams. In: 6th International aluminium extrusion technology seminar Chicago. Washington
- Dieter, G. E., 1987. *Metallurgical fundamentals*. 2nd Ed.
- Dobrzanski, L. A., and Trzaska, J., 2004. Application of neural networks to forecasting the cct diagrams. *Journal of Materials Processing Technology*, 157-158, 107-113.
- Doherty, R.D., Hughes, D.A., Humphries, F.J., Jonas, J.J., Jensen, D.J., Kassner, M.E., King, W.E., McNelly, T.R., McQueen, H.J., and Rollet, A.D., 1997. Current issues in recrystallisation: A review. *Materials science and Engineering, A* 238 (2), 219-274.
- Domanti, A. T., Horrobin, D.J., Bridgewater, J. 2002. *Journal of Mechanical Science*, 44, 1381-1410.
- Donati, L., and Tomesani, L., 2004. The prediction of seam welds quality in aluminum extrusion. *Journal of Materials Processing Technology*, 153-154, 366-373.
- Donati, L., and Tomesani, L., 2005. The effect of die design on the production and seam weld quality of extruded aluminum profiles. *Journal Of Materials Processing Technology*, 164–165 (0), 1025-1031.
- Driver, J. H., Lens, A., Maurice, C., 2005. Grain boundary mobilities during recrystallization of al-mn alloys as measured by in situ annealing experiments. *Materials Science and Engineering: A*, 403 (1-2), 144-153.
- Duan, X., 2001a. Some problems in hot rolling of al-alloys solved by the finite element method. Thesis. Bournemouth University, Bournemouth, UK.

- Duan, X., and Sheppard, T., 2002a. Influence of forming parameters on static recrystallization behaviour during hot rolling aluminium alloy 5083. *Modelling and Simulation in Materials Science and Engineering*, 10 (4), 363-379.
- Duan, X., and Sheppard, T., 2002b. Influence of forming parameters on the final subgrain size during hot rolling of aluminium alloys. *Journal of Materials Processing Technology*, 130-131, 245-249.
- Duan, X., and Sheppard, T., 2003. Computation of substructural strengthening by the integration of metallurgical models into the finite element code. *Computational Materials Science*, 27 (3), 250-258.
- Duan, X., Sheppard, T., 2001b. Prediction of temperature evolution by fem during multi-pass hot flat rolling of aluminium alloys. *Modelling and Simulation in Materials Science and Engineering*, 9 (6), 525-537.
- Duan, X., Sheppard, T., 2002. A new spread formula for hot flat rolling of aluminium alloys. *Modelling and Simulation in Materials Science and Engineering*, 10 (6), 597-610.
- Duan, X., Sheppard, T. 2003. Simulation and control of microstructure evolution during hot extrusion of hard aluminium alloys. *Materials Science and Engineering A-structural Materials Properties Microstructure and Processing*, 351, 282-292.
- Duan, X., Sheppard, T., Velay, X., 2004. Prediction of flow stress and recrystallization by the finite element method during the hot extrusion of aluminum alloys. In: 8th International aluminum extrusion technology seminar, Orlando, Illinois.
- Eshelby, J.D., Shockley. W. T. R., W., 1953. *Acta Materialia*, 1 (3), 251-259.
- Flitta, I., Sheppard, T., and Peng, Z., 2007. Fem analysis to predict development of structure during extrusion and subsequent solution soak cycle *Materials Science and Technology*, 23 (5), 582-592.
- Furu, T., Shercliff, H. R., Baxter, G. J., and Sellars, C. M., 1999. The influence of transient deformation conditions on recrystallization during thermomechanical processing of an al-1% mg alloy. *Acta Materialia*, 47 (8), 2377-2389.
- Garofalo, F., 1963. An empirical relation defining stress dependence of minimum creep rate in metals. *Transactions of the Metallurgical Society of Aime*, 227 (2), 351-365.
- Grong, and Shercliff, H. R., 2002. Microstructural modelling in metals processing. *Progress In Materials Science*, 47 (2), 163-282.
- Haupp, H.-J., and Roll, K., 1999. Future perspectives and limits for the mathematical modelling of metal forming processes in automotive industry. In: Geiger, M. ed. 6th International Conference on technology of plasticity, Nuremberg, Germany: Springer-Verlag Telos.
- Hamzah, H., 2000. Weld integrity on a die. In: ET 2000, Chicago Illinois: International Aluminium Extrusion seminar.
- Herba, E. M., and McQueen, H. J., 2004. Influence of particulate reinforcements on 6061 materials in extrusion modeling. *Materials Science and Engineering A-structural Materials Properties Microstructure and Processing*, 372 (1-2), 1-14.
- Hill, R., 1950, *the mathematical theory of plasticity*, Oxford, Clarendon Press.
- Hirsch, J., 2006. Virtual fabrication of aluminum products: Microstructural modeling in industrial aluminum production.
- Hirst, J., Ursell, D.H., 1958. Limit diagrams. *Metal treatment*.
- Holt, D. L., 1970. Dislocation cell formation in metals. *Journal of Applied Physics*, 41 (8), 3197-3201.

- Huang, Y., and Humphreys, F. J., 1999. Measurements of grain boundary mobility during recrystallization of a single-phase aluminium alloy. *Acta Materialia*, 47 (7), 2259-2268.
- Huang, Y., and Humphreys, F. J., 2000. Subgrain growth and low angle boundary mobility in aluminium crystals of orientation  $\{110\}\langle 001\rangle$ . *Acta Materialia*, 48 (8), 2017-2030.
- Humphreys, F. J., 1992. A network model for recovery and recrystallization. *Scripta Metallurgica Et Materialia*, 27 (11), 1557-1562.
- Humphreys, F. J., and Hatherly, M., 2004. *Recrystallization and related annealing phenomena*. Elsevier.
- Ingraldi, L., Giacomelli, V. Pedersoli, M. 1992. Design and correction of hollow dies in Europe. In: *Proceedings Fifth International Aluminium Extrusion Technology Seminar*
- Iwata, K., Fujino, S., and Osakada, K., 1972. Analysis of hydrostatic extrusion by finite element method. *Journal of Engineering for Industry*, 94 (2).
- Johnson, W., and Kudo, H., 1962, *The mechanics of metal extrusion*,. Manchester University Press.
- Jonas, J. J., Sellars, C. M., and McQueen, W. J., 1969. Strength and structure under hot-working conditions *International Metallurgical Reviews*, 130, 1-23.
- Jones, M. J., and Humphreys, F. J., 2003. Interaction of recrystallization and precipitation: The effect of Al<sub>3</sub>Sc on the recrystallization behaviour of deformed aluminium. *Acta Materialia*, 51 (8), 2149-2159.
- Jowett, C., Parson, N., and Fraser, W., 2000. Simulation of billet surface into the extruded product. In: *7th International aluminium extrusion technology seminar*, Chicago. Washington
- Kobayashi, S., Oh, S., and Alta, T., 1989. *Metal forming and the finite element method*. New York: Oxford University press.
- Lee, C. K. Automatic metric 3D surface mesh generation using subdivision surface geometrical model. Part 2: Mesh generation algorithm and examples. *International Journal for Numerical Methods in Engineering* vol. 56 issue 11 21 March 2003. p. 1615 - 1646
- Li, Q., Smith, C. J., Harris, C., and Jolly, M. R., 2003. Finite element modelling investigations upon the influence of pocket die designs on metal flow in aluminium extrusion: Part ii. Effect of pocket geometry configurations on metal flow. *Journal of Materials Processing Technology*, 135 (2-3), 197-203.
- Libura, W., Richert, J., Pacanowski, J., and Senderski, J., 2000. Temperature-speed parameters in extrusion of thin-walled sections from aluminium alloys. In: *7th International aluminium extrusion technology seminar*, Chicago, Washington.
- Liu, G., Zhou, J., and Duszczek, J., 2008. Fe analysis of metal flow and weld seam formation in a porthole die during the extrusion of a magnesium alloy into a square tube and the effect of ram speed on weld strength. *Journal Of Materials Processing Technology*, 200 (1-3), 185-198.
- Liversley, R. K., 1983. Some aspects of structural computing: 1943-1983. In: *the Michael R. Horne conference*, Manchester Dobbs Ferry: London; New York : Granada.
- Lof, J., 2000. *Developments in finite element simulations of aluminium extrusion*. Thesis (Ph.D). University of Twente, Enschede, Netherlands.

- Lotzenhiser, C., 1977. Die lay out and die design. In: ET 77, Chicago Illinois: International Aluminium Extrusion Seminar.
- Machado, P. T. F., 1992. Extrusion die design. In: ET 92, Chicago Illinois: International Aluminium Extrusion Seminar.
- Marthinsen, K., Holmedal, B., Abtahi, S., Valle, R., Chen, S., and Nes, E., 2003. Coupled fem and microstructure modeling applied to rolling and extrusion of aluminium alloys. *Thermec'2003, Pts 1-5*, 426-4, 3777-3782.
- Marthinsen, K., and Nes, E., 1997. A general model for metal plasticity. *Materials Science and Engineering A*, 234-236, 1095-1098.
- Marthinsen, K., and Nes, E., 2001. Modelling strain hardening and steady state deformation of al-mg alloys. *Materials Science and Technology*, 17, 376-387.
- Mcclintock, F. A., Kaplan, S. M. Berg, C.A. . 1996. *International Journal of Mechanical science*, 2, 614-628.
- Mclaren, A. J., and Sellars, C. M., 1992. Modeling distribution of microstructure during hot-rolling of stainless-steel. *Materials Science and Technology*, 8 (12), 1090-1094.
- Miles, N., Evans, G. Middleditch, A. 1996. Automatic bearing length assignment using the medial axis transform. In: ET 96, Chicago Illinois: International Aluminium Extrusion Seminar.
- Miles, N., Evans, G. Middleditch, A. 1997. Bearing lengths for extrusion dies: Rational current practice and requirements for automation. *Journal of material processing technology*, 72, 162-176.
- Moe, P. T., Lefstad, M., Flatval, R., and Storen, S., 2003. Measurement of temperature and die face pressure during hot extrusion of aluminium. *International journal of forming processes*, 6 (3), 241-270.
- Mooi, H. G., 1996. Finite element simulations of aluminium extrusion. Thesis (PhD). Technische Universiteit Twente.
- Mueller, K. M., Liu, M., and Burns, S. A., 2002. Fully stressed design of frame structures and multiple load paths. *Journal Of Structural Engineering-asce*, 128 (6), 806-814.
- Nes, E., 1997. Modelling of work hardening and stress saturation in fcc metals. *Progress in Materials Science*, 41 (3), 129-193.
- Nes, E., 1998. Influence of recovery recrystallization and texture on the structure and properties of aluminum alloys. Paper presented at the Proceedings of the 8th International Light Metals Congress, Leoben, Vienna.
- Nes, E., Holmedal, B., Evangelista, E., and Marthinsen, K., 2005. Modelling grain boundary strengthening in ultra-fine grained aluminum alloys. *Materials Science and Engineering: A*, 410-411, 178-182.
- Nes, E., and Marthinsen, K., 2002. Modeling the evolution in microstructure and properties during plastic deformation of fcc-metals and alloys - an approach towards a unified model. *Materials Science and Engineering A-structural Materials Properties Microstructure and Processing*, 322 (1-2), 176-193.
- Nes, E., Marthinsen, K., and Brechet, Y., 2002. On the mechanisms of dynamic recovery. *Scripta Materialia*, 47 (9), 607-611.
- Nes, E., Marthinsen, K., and Holmedal, B., 2004. The effect of boundary spacing on substructure strengthening. *Materials Science and Technology*, 20 (11), 1377-1382.
- Nes, E., Vatne, H. E., Daaland, O., Furu, T., Ørsund, R., and Marthinsen, K., 1994. Physical modelling of microstructural evolution during thermomechanical processing of aluminium alloys. Trondheim, Norway SINTEF (STF24 S94003).

- Niu, L., 2010. Numerical modeling of the aluminium extrusion process when producing complex sections. Thesis (PhD).
- Oyane, M., Sato, T. Okimoto, K. Shima, S. 1980. Journal of Mechanical Working Technology, 4, 65-79.
- Parson, N. B., S: Shalanski, a; Jowett, C., 2004. Control of grain structure in al-mg-si extrusions. In: ET 2004, Orlando, Florida: Aluminium Extrusion Technology Seminar.
- Parson, N. C., Hankin, J. D., and Bryant, A. J., 1992. The metallurgical background to problems occurring during the extrusion of 6xxx alloys. In: 5th International aluminium extrusion technology seminar, Chicago, Washington.
- Pashley, D.W., Rhodes, J. W. and Sendorek, A., J. Inst. Metals, 41, 94, 1966.
- Paterson, S. J., 1981. The direct and indirect extrusion of aluminium alloys. Thesis (Ph.D). University of London, London, UK.
- Peng, Z., 2005. Numerical modelling of the aluminium extrusion process. Thesis (Ph.D). Bournemouth University, Bournemouth, UK.
- Peng, Z., and Sheppard, T., 2004. Study of surface cracking during extrusion of aluminium alloy aa2014. Materials Science and Technology, 20 (9), 1179-1191.
- Peng, Z., and Sheppard, T., 2004 Prediction of static recrystallization during shaped extrusion. In: 8th International aluminum extrusion technology seminar, Orlando, Illinois.
- Poschmann, I.McQueen, H. J., '*Maney Online*', Volume 14 Issue 11 (01 November 1998), pp. 1101-1108
- Reddy, J. N., 2006. An introduction to the finite element method. McGraw-Hill Higher Education.
- Reinikainen, T., Welo, T., Korhonen, A. S., and Kivivuori, S., 1994. Comparison of 2 commercial fem codes in cold-extrusion simulation. Journal of Materials Processing Technology, 42 (2), 137-146.
- Robbins, M., 1996. Advanced design and manufacturing of hollow dies for improved extrusion speeds. In: ET 96, 6th International Aluminium Extrusion Seminar, Chicago Illinois.
- Rossi, P. L. O., and Sellars, C. M., 1997. Quantitative metallography of recrystallization. Acta Materialia, 45 (1), 137-148.
- Schikorra, M., Donati, L., Tomesani, L., and Kleiner, M., 2007. The role of friction in the extrusion of aa6060 aluminum alloy, process analysis and monitoring. Journal Of Materials Processing Technology, 191 (1-3), 288-292.
- Sellars, C. M., 1986. Modelling of structural evolution during hot working processes. In: the Seventh Risø International Symposium on Metallurgy and Materials Science, Roskilde, Denmark.
- Sellars, C. M., 1990. Modelling microstructural development during hot rolling. Materials Science and Technology, 6, 1072-1081.
- Sellars, C. M., 1997. An internal state variable approach to modelling microstructural evolution during thermomechanical process. In: Chandra, T., and Sakai, T. eds. Thermec'97 international conference on thermomechanical processing of steels & other materials University of Wollongong, Australia.
- Sellars, C. M., Tegart, W., and Mcg, J., 1972. Hot workability. International Metallurgical Reviews, 17 (1), 1-24.

- Sellars, C. M., and Zhu, Q., 2000. Microstructural modelling of aluminium alloys during thermomechanical processing. *Materials Science and Engineering A-structural Materials Properties Microstructure and Processing*, 280 (1), 1-7.
- Sheppard, T., 1984, Metallurgical aspects of direct and indirect extrusion. In: 3rd International aluminium extrusion technology seminar, Atlanta, Washington.
- Sheppard, T., 1993. Extrusion of AA2024 alloy. *Materials Science and Technology*, 9, 430-440.
- Sheppard, T., 1999a. Extrusion of aluminium alloys. Dordrecht, Netherlands: Kluwer Academic Publishers.
- Sheppard, T., 1999b. Temperature changes occurring during extrusion of metals: Comparisons of bulk, numerical, and integral profile predictions with experimental data. *Materials Science and Technology*, 15, 459-463.
- Sheppard, T., 2008. Innovative methodologies to increase productivity by simulating development of structure during extrusion and solution soaking. In: ET '08: The conference for innovations in aluminum extrusion, Gaylord Palms, Orlando, FL., U.S.
- Sheppard, T., and Duan, X., 2002. Modelling of static recrystallisation by combining fem with empirical models. *Journal of Materials Processing Technology*, 130-131, 250-253.
- Sheppard, T., Niu, L., Velay, X., 2012c. On the effect of differing symmetries in fem solutions for tube extrusions. *Journal of materials Science*
- Sheppard, T., and Patterson, S.J., 1982, Direct and indirect extrusion of aluminium alloys, *Metals Technology*, 9 (Jul), 274-281.
- Sheppard, T., and Raghunathan, N., 1989. Modification of cast structures in al-mg alloys by thermal treatments. *Materials Science and Technology*, 5 (3), 268-280.
- Sheppard, T., and Raghunathan, N., Hot Worked and Annealed Microstructures in Al-Mg Alloys, in 'Aluminium Technology '86', (Ed.T.Sheppard) publ. 1986, Institute of Metals, London., pp.357-372
- Sheppard, T., and Raybould, D., 1973. Load and temperature rise during extrusion of superpure al, al-zn, and al-zn-mg alloys. *Journal Of The Institute Of Metals*, 101 (Feb), 33-44.
- Sheppard, T., Tunnicliffe, P. J., and Patterson, S. J., 1982. Direct and indirect extrusion of a high strength aerospace alloy (aa 7075). *Journal of Mechanical Working Technology*, 6 (4), 313-331.
- Sheppard, T.; Tatcher, M. G.; Flower, H. M., Development of recovered dislocation substructures during plastic flow, *Metal science*, Volume 13, Number 8, August 1979, pp. 473-481(9)
- Sheppard, T., and Tatcher, M. G., 1980. Development of duplex deformation substructure during extrusion of a commercial al-5mg-0.8mn alloy. *Metal Science*, 14 (12), 579-589.
- Sheppard, T., Velay, X., 2007. Innovative methodologies for the simulation of static recrystallisation during the solution soaking process of shape extrusion. In: Extrusion Workshop 2007 and 2nd Extrusion Benchmark Bologna, Italy
- Sheppard, T., and Wood, E. P., 1980. Effect of section geometry on extrudability of al-cu alloy. *Metals Technology*, 7 (Feb), 58-66.

- Sheppard, T., and Wright, D. S., 1979. Determination of flow-stress .1. Constitutive equation for aluminum-alloys at elevated-temperatures. *Metals Technology*, 6 (Jun), 215-223.
- Sheppard, T., Velay, X. 2012d. On material flow and aspects of structural modification during direct and indirect extrusion of aluminium alloy. *Material Science and Technology*, 28 (4), 397-405.
- Shercliff, H. R. 1997. *Modelling and materials processing*: Cambridge University
- Shercliff, H. R., and Lovatt, A. M., 1999. Modelling of microstructure evolution in hot deformation. *Philosophical Transactions of the Royal Society A: Mathematical, Physical and Engineering Sciences*, 357 (1756), 1621-1643.
- Siebel, E., Fangmeier, E., 1931. *Mitt. Kais. Wilh.Eisenhof.*13, 28.
- Stockdale, C. O., 1992. The application of cad/cam to extrusion die design. In: ET 92, Chicago Illinois.
- Subramaniyan, J., 1989. Extrusion of 2024 aluminium alloy sections. Thesis. University of London, London.
- Talamantes-Silva, J., Abbod, M. F., Cabrera, E. S. P., Howard, I. C., Beynon, J. H., Sellars, C. M., and Linkens, D. A., 2009. Microstructure modelling of hot deformation of al-1%mg alloy. *Materials Science and Engineering: A*, 525 (1-2), 147-158.
- Thomma, M., Reissner, J. Lombardi, Z. . 1996. The use of a planning system to support the design of extrusion dies. In: ET 96, Chicago Illinois: International Aluminium Extrusion Seminar.
- Tibbetts, B. R., and Wen, J. T. Y., 1998. Extrusion process control: Modeling, identification, and optimization. *Ieee Transactions on Control Systems Technology*, 6 (2), 134-145.
- Transvalor. 2009a. Forge 2009 documentation - datafile forge2v44.
- Transvalor. 2009b. Forge 2009 documentation - datafile forge3v74.
- Transvalor. 2009c. Forge 2009 documentation - user routines.
- Tuschy, E., 1971. Differences in flow behaviour during extrusion of various materials. *Zeitschrift Fur Metallkunde*, 62 (7), 513-516.
- Valberg, H., 1996. A modified classification system for metal flow adapted to unlubricated hot extrusion of aluminum and aluminum alloys. In: 6th International aluminium extrusion technology seminar Chicago. Washington
- Valberg, H., 2002, Extrusion welding in aluminium extrusion. *international journal of Materials and Product Technology*, 17(7), 497-556.
- Van De Langkruis, J., 2000. The effect of thermal treatments on the extrusion behaviour of almg alloys. Thesis (Ph.D.). Technische Universiteit Delft.
- Vaneker, T.H.J., 2001. Development of an integrated design tool for aluminium extrusion dies. Thesis (Ph.D.). Universiteit Twente.
- Van Geertruyden, W. H., Misiolek, W. Z., and Wang, P. T., 2006. Grain structure evolution in a 6061 aluminum alloy during hot torsion. *Materials Science and Engineering A-structural Materials Properties Microstructure and Processing*, 419 (1-2), 105-114.
- Vatne, H. E., Furu, T., Ørsund, R., and Nes, E., 1996. Modelling recrystallization after hot deformation of aluminium. *Acta Materialia*, 44 (11), 4463-4473.
- Vierod, R. P., 1983. The effect of copper additions on the deformation processing of aluminium alloys. Thesis (Ph.D.). University of London, London, UK.



- Wetherill, N.P., and Hassan, O., 1994, Efficient three dimensional Delauney triangulation with automatic point creation and imposed boundary constraints. *Int J. Numer. Methods Eng* 37, 2005-2037.
- Zaidi, M. A., and Sheppard, T., 1983. Recrystallization mechanisms in commercial al-2mg alloy. *Metal Science*, 17 (5), 219-228.
- Zener, C., and Hollomon, J. H., 1944. Effect of strain rate upon plastic flow of steel. *Journal of Applied Physics*, 15 (1), 22-32.
- Zhu, Q., Abbod, M. F., Talamantes-Silva, J., Sellars, C. M., Linkens, D. A., and Beynon, J. H., 2003. Hybrid modelling of aluminium-magnesium alloys during thermomechanical processing in terms of physically-based, neuro-fuzzy and finite element models. *Acta Materialia*, 51 (17), 5051-5062.
- Zhu, Q., and Sellars, C. M., 2000. Microstructural evolution of aluminium-magnesium alloys during thermomechanical processing. *Aluminium Alloys: Their Physical and Mechanical Properties*, Pts 1-3, 331-3, 409-420.
- Zhu, Q., and Sellars, C. M., 2001. Evolution of microbands in high purity aluminium-3% magnesium during hot deformation testing in tension-compression. *Scripta Materialia*, 45 (1), 41-48.
- Zhu, Q., Sellars, C. M., and Bhadeshia, H. K. D. H., 2007. Quantitative metallography of deformed grains. *Materials Science and Technology*, 23 (7), 757-766.
- Zhu, Q., Shercliff, H. R., and Sellars, C. M., 1997, Jul 07-11. Modelling hot deformation behaviour based on evolution of dislocation substructures. Paper presented at the 2nd International Conference on Thermomechanical Processing of Steels and Other Materials (THERMEC 97), Wollongong, Australia.
- Zienkiewicz O. C and Taylor R L *The Finite Element Method for Solid and Structural Mechanics*, ISBN 978-0-7506-6321-2 ,1967, McGraw Hill, New York
- Zienkiewicz, O. C., 2004. The birth of the finite element method and of computational mechanics. *International Journal For Numerical Methods In Engineering*, 60 (1), 3-10.
- Zienkiewicz, O. C., Taylor, R. L., and Zhu, J. Z., 2005. *The finite element method: Its basis and fundamentals*. Butterworth-Heinemann publications.